Fluid structure interaction in piston diaphragm pumps

van Rijswick, Rudolfus

DOI
10.4233/uuid:2f24e261-003f-4e80-ba4e-0b0c1caecdf7

Publication date
2017

Document Version
Final published version

Citation (APA)
van Rijswick, R. (2017). *Fluid structure interaction in piston diaphragm pumps*. [Dissertation (TU Delft), Delft University of Technology]. https://doi.org/10.4233/uuid:2f24e261-003f-4e80-ba4e-0b0c1caecdf7

FLUID STRUCTURE INTERACTION IN PISTON DIAPHRAGM PUMPS

FLUID STRUCTURE INTERACTION IN PISTON DIAPHRAGM PUMPS

Proefschrift

ter verkrijging van de graad van doctor
aan de Technische Universiteit Delft,
op gezag van de Rector Magnificus prof. ir. K.C.A.M. Luyben,
voorzitter van het College voor Promoties,
in het openbaar te verdedigen op donderdag 16 maart 2017 om 12:30 uur

door

Rudolfus Johannnes Adeleida van Rijswick

Werktuigkundig Ingenieur,
Technische Universiteit Eindhoven, Nederland
geboren te Nijmegen, Nederland

Dit proefschrift is goedgekeurd door de

promotor: Prof. dr. ir. C. van Rhee
copromotor: Dr. ir. A.M. Talmon

Samenstelling promotiecommissie:

Rector Magnificus,	voorzitter
Prof. dr. ir. C. van Rhee	Technische Universiteit Delft
Dr. ir. A.M. Talmon	Technische Universiteit Delft
Onafhankelijke leden:	
Prof. dr. ir. B.J. Boersma	Technische Universiteit Delft
Prof. dr. ir. M.L. Kaminski	Technische Universiteit Delft
Prof. dr. ir. E.H. van Brummelen	Technische Universiteit Eindhoven
Prof. dr. ing. E. Schlücker	Friedrich-Alexander-Universität Erlangen-Nürnberg, Deutschland
Prof. D. MacKenzie	University of Strathclyde, Scotland, UK

Keywords: Fluid structure interaction, Piston diaphragm pump, Positive displacement pump

Printed by: 24-Proefschriften.nl

Front & Back: Vortex structure in pump chamber during last part of suction stroke

ISBN 978-9-49-183715-9

An electronic version of this dissertation is available at
http://repository.tudelft.nl/.

to my parents

CONTENTS

SUMMARY

Piston diaphragm pumps are used world-wide to transport abrasive and/or aggressive slurries against high discharge pressures in the mining, mineral processing and power industries. Limitation of excessive deformation of the diaphragm is of utmost importance for eliminating fatigue failures of the diaphragm and thereby obtaining a high reliability of the piston diaphragm pump. The deformation shape of the diaphragm is the result of a complex 2-way Fluid Structure Interaction (FSI) mechanism within the pump chamber between the propelling fluid, the diaphragm and the pumped slurry. The understanding of this FSI mechanism has improved in the last decades but is still limited. Load and deformation analysis of the diaphragm is currently based quasi-static assumptions. This is however an over-simplification, especially for the larger piston diaphragm pumps used in the mining and mineral processing industries. In these applications, fluid momentum loading by both convective as well as unsteady fluid acceleration become important to consider. For improved analysis of the diaphragm deformation a numerical model is required. The objective of this study is therefore:

Development of an experimentally validated numerical Fluid-Structure-Interaction model for the prediction of, operating condition induced, diaphragm deformation in piston diaphragm pumps

In this thesis the working principle and applications of the piston diaphragm pump are introduced first, followed by a introduction of the basics of crankshaft driven positive displacement pumps. Then the state of the art in pump diaphragm deformation analysis is described followed by a summary of solid and fluid mechanics theory which is used in the numerical model.

A dimensional analysis of the fluid structure interaction problem showed that the fluid compressibility and the 2 phase character of the pumped slurry can be neglected which allows the fluid around the diaphragm to be modelled as a incompressible homogeneous mixture. The flow is furthermore highly unsteady and momentum dominated which makes accurate modelling of viscous and turbulent stresses less important. Dimensionless numbers have been derived which allow scaling of the fluid structure interaction problem. These dimensionless numbers have been used to eventuate field experiences with hundreds of piston diaphragm pumps gained over the last 4 decades. Scaling using the dimensionless numbers allowed to identify limitations in reliable diaphragm operation which can be used in robust diaphragm selection guidelines. However, these guidelines only apply for geometrically similar pump chamber and diaphragm designs and can therefore not be used for geometric optimization of the diaphragm and its housing. In order to allow geometric optimization, a numerical fluid structure interaction model has been developed in this study.

The numerical model is based on the Immersed Boundary Method (IBM) which uses a fixed grid to model the fluid flow in which the rigid and deformable structures are immersed. The presence of the immersed structures is modelled with appropriately scaled body forces in the computational cells of the flow solver. The flow solver explicitly solves Navier-Stokes equations on a Cartesian grid using a Total Variation Diminishing (TVD) scheme for the advection of momentum which allows Large Eddy Simulations to be performed. The diaphragm is modelled as a Kirchhoff-Love thin shell model using a Finite Element(FE) discretization on triangular elements. An immersed boundary method using feedback forcing is used for modelling the 2-way interaction between the diaphragm and the fluid flow around it. The nodes of the FE mesh are immersed in and advected by the fluid flow and the nodal reaction forces are supported in the fluid by appropriately scaled body forces. The presence of the rigid pump chamber wall is modelled by a immersed boundary method which uses direct forcing. The complete model has been developed from scratch and has been implemented in the Matlab® programming environment.

An experimental set-up has been developed for validation of the numerical model. A transparent window in the pump chamber of the experimental set-up allows visual observation of the diaphragm deformation under dynamic conditions while pumping water. A laser triangulation sensor was used to successive measure the diaphragm displacement on different locations from which 3D deformation shapes of the diaphragm could be reconstructed. The results showed an increase in higher order deformation shapes with increasing flow rate.

Experimental validation of the results of the numerical model showed reasonable agreement. In some instances the numerical model showed higher order deformation modes which were not as severe in the experimental results. This was mainly when the diaphragm was approaching the pump chamber wall and when high flow velocities parallel to the diaphragm surface were present. This difference is expected to be caused by limitations in the fluid grid resolution which does not allow steep gradients in the boundary layer between the fluid low and the diaphragm surface. Grid refinement is restricted by the fluid structure interaction stability criterion which required the time step to be scaled with the grid size to the power 2.5. This restriction is caused by the thin shell model and could be improved when using a thick shell model which includes shear deformation.

SAMENVATTING

Zuigermembraanpompen worden wereldwijd gebruikt om abrasieve en/of agressieve slurries tegen hoge persdrukken te verpompen in de mijnbouw, mineraal verwerkende en kracht industrie. Beperking van overmatige vervorming van het pompmembraan is van het hoogste belang om vermoeiingsschades te voorkomen en daardoor een hoge betrouwbaarheid van de zuigermembraanpomp te garanderen. De vervorming van het membraan is het gevolg van een complex 2-richtingen vloeistof structuur interactie mechanisme in de pompkamer tussen de aandrijf vloeistof, het membraan en de te verpompen slurrie. Begrip van dit vloeistof structuur interactie mechanisme is in de laatste decennia verbeterd maar is nog steeds beperkt. Belasting- en vervormingsanalyse van het membraan zijn momenteel gebaseerd op quasi-statische aannames. Dit is echter een te vergaande vereenvoudiging, zeker voor de grotere zuigermembraanpompen die ingezet worden in de mijnbouw en mineraalverwerkende industrie. In deze toepassingen is het belangrijk om belastingen door vloeistof impuls door zowel convectieve als instationaire vloeistof versnellingen mee te nemen. Voor een verbeterende analyse van de membraanvervoming is een numeriek model nodig. De doelstelling van deze studie is dan ook:

Ontwikkeling van een experimenteel gevalideerd numeriek vloeistof structuur interactie model ten behoeve van de voorspelling van, bedrijfsconditie geïnduceerde, membraanvervorming in zuigermembraanpompen

In dit proefschrift worden eerst het werkingsprincipe en de toepassingen van de zuigermembraanpomp geïntroduceerd, gevolgd door een inleiding in de grondbeginselen van krukasgedreven verdringerpompen. Vervolgens wordt de stand der techniek van pompmembraan vervormingsanalyse beschreven gevolgd door een samenvatting van de theorie van vaste stof mechanica en stromingsleer welke in het numeriek model zijn gebruikt.

Een dimensie analyse van het vloeistof structuur interactie probleem laat zien dat de samendrukbaarheid en het 2-fase karakter van de verpompte slurrie verwaarloosd kan worden hetgeen toelaat om de vloeistof om het membraan als een onsamendrukbaar homogeen mengsel te beschrijven. De stroming is verder sterk instationair en traagheid gedomineerd waardoor het nauwkeurig modelleren van viskeuze en turbulente spanningen minder belangrijk is. Dimensieloze kentallen zijn afgeleid die het mogelijk maken om het vloeistof structuur interactie probleem te verschalen. Deze dimensieloze kentallen zijn gebruikt om veldervaringen met honderden zuigermembraanpompen, verzameld in de laatste 4 decennia, te evalueren. Verschaling met de dimensieloze kentallen maakt het mogelijk om grenzen van betrouwbaar membraanbedrijf te identificeren welke gebruikt kunnen worden in robuuste membraanselectierichtlijnen. Echter, deze richtlijnen zijn alleen van toepassing op geometrisch gelijkvormige pompkamer-

en membraanontwerpen en kunnen daarom niet gebruikt worden voor een geometrie optimalisatie van de het ontwerp van het membraan en zijn pompkamer. Om geometrische optimalisatie mogelijk te maken is een numeriek structuur interactie model ontwikkeld in deze studie.

Het numeriek model is gebaseerd op de 'ondergedompelde rand methode' waarin een vast rooster wordt gebruikt om de vloeistofstroming te modelleren waarin de starre en flexibele structuren zijn ondergedompeld. De aanwezigheid van ondergedompelde structuren wordt gemodelleerd met op de juiste wijze geschaalde volume krachten in de rekencellen van het stromingsmodel. In het stromingsmodel worden de Navier-Stokes vergelijkingen expliciet opgelost op een Cartesisch rooster, gebruikmakend van een 'totale variatie verminderend' schema voor de advectie van impuls waardoor een 'grote wervels simulatie' mogelijk wordt. Het membraan is gemodelleerd als een Kirchhoff-Love dunne schaal model middels een Eindige Elementen discretisatie op driehoekselementen. Een ondergedompelde rand methode met terugkoppel forcering is gebruikt om om de 2-richtingen interactie tussen het membraan en de omringende vloeistof te modelleren. De knooppunten van het eindige elementen rooster zijn ondergedompeld en worden geadvecteerd door de vloeistofstroming en de knooppuntreactiekrachten worden afgesteund in de vloeistof middels op de juiste wijze geschaalde volumekrachten. De aanwezigheid van de starre wanden van de pompkamer zijn gemodelleerd door een ondergedompelde rand methode met directe forcering. Het volledige model is van de grond af ontwikkeld en geïmplementeerd in de programmeeromgeving Matlab®

Een experimentele opstelling is ontwikkeld ten behoeve van validatie van het numerieke model. Een transparant venster in de pompkamer van de experimentele opstelling maakt visuele observatie van het pompmembraan onder dynamische omstandigheden tijdens het verpompen van water mogelijk. Een laser triangulatie sensor is gebruikt om achtereenvolgens de membraanverplaatsing te meten op verschillende locaties waaruit een 3D deformatievorm van het membraan kan worden gereconstrueerd. De resultaten laten een verhoging van hogere orde deformatievormen zien met toenemende volumestroom.

Experimentele validatie van de resultaten van het numerieke model laat een redelijke overeenstemming zien. In sommige gevallen laat het numerieke model hogere orde vervormingsmodi zien welke niet zijn waargenomen in de experimentele resultaten. Dit gebeurd voornamelijk wanneer het membraan de wand van de pompkamer nadert en wanneer hoge stromingssnelheden parallel aan het membraanoppervlak aanwezig zijn. Vermoedelijk wordt dit verschil veroorzaakt door beperkingen in de resolutie van het vloeistofrooster welke geen steile gradiënten in de grenslaag tussen de vloeistofstroming en het membraan toelaat. Verfijning van het rooster wordt verhinderd door het vloeistof structuur interactie stabiliteitscriterium welke een verschaling van de tijdstap met de rooster grootte tot de macht 2.5 eist. Deze voorwaarde wordt veroorzaakt door het dunne schaal model en zou verbeterd kunnen worden door het toepassen van een dikke schaal model waarin vervorming door afschuiving is inbegrepen.

PREFACE

This thesis is a result of my work on the subject of fluid structure interaction in piston diaphragm pumps since the commence of my PhD project in March 2010. The project was executed under supervision of the the dredging engineering department of the Delft University of technology, led by my promoter Prof. dr. ir. Cees van Rhee. The project has been fully funded by WEIR minerals Netherlands b.v., manufacturer of GEHO® piston diaphragm pumps, where I'm employed as the chief engineer for the piston diaphragm pump line.

In this project I could rely on decades of experience with the design and operation of piston diaphragm pumps gathered within WEIR Minerals Netherlands. The research and development activities within WEIR Minerals Netherlands were led by my father, Ger van Rijswick, since the early 70's when the GEHO® piston diaphragm pump was introduced, until his retirement in 2009. It was him who got me interested in technology in the first place from a rather young age, and later on, without any push, inspired me to study mechanical engineering. I worked under his supervision at WEIR Minerals Netherlands on piston diaphragm pumps as a trainee from the Eindhoven University of technology in 1999 and 2000 and from 2004 to 2009 as a full-time research and development engineer. During this period he taught me about every aspect of piston diaphragm pumps which gave me a solid knowledge basis on piston diaphragm pumps which has been essential in this work. This work is a continuation of the research and development activities with respect to diaphragm deformation led by him since the early 70's. Here the contribution of my colleague Jan Stroeken on diaphragm deformation analysis in the decade before the start of this study is to be mentioned as well.

It was on the Hydrotransport 17 conference in Capetown South Africa in may 2007 where I was presenting a paper on pressure pulsation analysis in crankshaft driven positive displacement pumps were I first met my promotor Prof. dr. ir. Cees van Rhee. It was there were we first discussed the idea of doing a PhD in part-time construction while working in industry. After convincing myself, my girlfriend, now wife, Yvonne, my manager Gregor Timmermans and our managing director Jan-Peter van Leeuwen that this was a good idea, I started with great enthusiasm in March 2010.

Ralph van Rijswick
Lottum, October 2016

1

INTRODUCTION

1.1. WORKING PRINCIPLE AND APPLICATIONS OF PISTON DIAPHRAGM PUMPS

A piston diaphragm pump is a positive displacement pump in which a piston displaces an intermediate fluid which is used to displace a flexible diaphragm which displaces the fluid to be pumped. The study presented in this thesis focuses on the larger crankshaft driven piston diaphragm pumps as used in the mining and mineral processing industry. A cross-section of such a pump is shown in Figure 1.1. A crankshaft (1) is driven by an external drive which is often a variable speed electric motor with a gearbox. Via a connecting rod (2) a reciprocating motion of the cross head (3), cross head rod (4), piston rod (5) and piston (6) is generated. The piston (6) displaces the intermediate fluid, referred to as the propelling fluid (7), which is often a mineral oil. The propelling fluid displaces the diaphragm (8). The diaphragm displaces the pumped fluid (9), which in the applications of interest in this study, is a mixture of water with suspended solid particles, called a slurry. With the help of self-acting non-return valves on the suction (10) and discharge (11) side, a positive displacement pump acting is enabled. A common arrangement is a so-called triplex single acting arrangement, (ANSI/HI, 1994), in which 3 single acting pistons with 3 pump chambers are arranged in parallel. The crankshaft phases the pistons by 120° to even out the flow fluctuation generated by a single pump chamber. The pump is often equipped with a gas filled dampeners on the suction and discharge (12) side to attenuate the residual flow pulsation generated by the pump. A leakage compensation system is used to keep the volume of the propelling fluid within certain limits in order to keep the diaphragm position within limits. A monitoring rod (13) is connected to a central plate in the diaphragm whose position is monitored by the pump controller. When the position of the central plate is outside its allowable operating limits, filling or relieving of a small amount of propelling fluid by an auxiliary hydraulic system is initiated by the pump controller.

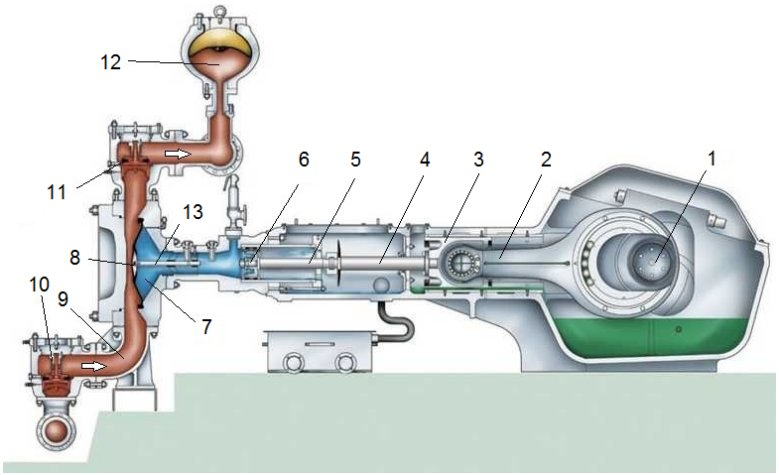

Figure 1.1: Cross-section of the GEHO® piston diaphragm pump

The main function of the diaphragm is to hermetically seal the pumped fluid from the ambient environment and the driving mechanism of the pump. Due to the hydraulic actuation principle, pressure levels are more or less equal on both sides of the diaphragm. This enables the generation of relatively high discharge pressure levels without over-stretching the diaphragm by high pressure loads. Piston diaphragm pumps are used in multiple applications ranging from small volume dosing applications in laboratory or chemical processes with an hydraulic output of a few W, to high volume slurry transportation in the mining and mineral processing industry with an hydraulic output of several MW, (Eifler *et al.*, 2009). Primary considerations for using a piston diaphragm pump are:

- Hermetical sealing of pumped fluid which,
  - creates a hermetic seal of toxic, corrosive and/or aggressive fluids to the ambient environment
  - eliminates abrasive wear of piston and liner due to abrasive solids present in the pumped fluid
- Hydraulic actuation of the diaphragm by positive displacement of intermediate fluid which, compared to mechanically or air actuated diaphragm pump,
  - generates a highly accurate flow rate
  - makes it suitable for higher discharge pressures

Piston diaphragm pumps as shown in Figure 1.1 are used in the mining, mineral processing and power industry to transport slurries, predominantly when pressures higher than 2.5 MPa are required. Elimination of abrasive wear of the piston and liner are the

primary reason for the use of this pump type in the mining and mineral processing industry. The pump shown in Figure 1.1 is of the GEHO® brand which is developed, produced and marketed by WEIR Mineral Netherlands b.v. and will by used as the study object throughout this study. The applications of this pump can be categorised as follows:

Long distance pipeline transport. When a mineral ore has a, or is ground to, a small enough particle size which is typically < 100 µm, it can be transported as a slurry across long distances reliably and efficiently. Piston diaphragm pumps are used as mainline pumps in long distance slurry transport pipelines for mineral concentrates such as iron, copper and bauxite which can have lengths of several 100 kilometres.

Process feed. The extraction of minerals from some ore types is executed using aqueous solutions which process is called hydrometallurgy. This often involves leaching with caustic or acidic aqueous solutions in high pressure and high temperature process vessels. Piston diaphragm pumps are used to feed the mineral ore as a slurry into the process vessels. Sometimes the slurry is already mixed with the caustic or acidic solution and preheated. Examples are feeding bauxite mixed with a 25 g/l caustic soda solution into a bauxite digester using the Bayer process, (Habashi, 2005), with a slurry temperature of 95 °C or feeding nickel laterite slurry at 200 °C into a High Pressure Acid Leaching (HPAL) autoclave in which sulphuric acid is added for leaching out the nickel.

Tailing disposal. After the extraction of the mineral from the ore a so-called mine tailing remains which needs to be disposed of. Traditionally these mine tailings are transported as a dilute slurry to a tailing disposal site using centrifugal pumps. The trend is towards higher concentration tailing disposal, as more and more focus is present on restricting water use and on making reclaimable tailing disposal sites. As these tailings often include fine clay type particles, higher viscosity slurries arise when concentrated. These higher viscosity slurries require higher discharge pressures for which piston diaphragm pumps are often used. Also disposal of fly ash slurries from power stations fall into this category and when considering dirty mine water as a tailing, mine de-watering from deep underground mines could be included in this category as well.

1.2. MOTIVE AND OBJECTIVE OF THESIS

An approximate operating envelope of current piston diaphragm pumps in the mining and mineral processing industry ranges from volumetric flow rates per pump of 25 to 800 m^3/h, discharge pressures of 2.5 to 25 MPa and hydraulic power output from 25 to 2200 kW per pump. The maximum size of these piston diaphragm pumps has increased continuously over the last 4 decades as mining and mineral processing operations have increased in size and new applications have been entered by the piston diaphragm pump technology. The gradual increase in maximum hydraulic power output and flow rate of produced GEHO® piston diaphragm pumps can be seen in Figure 1.2. Both the maxi-

mum hydraulic power as well as the maximum flow rate have gradually increased with a rate of approximately 60 % per decade, or a doubling every 15 years .

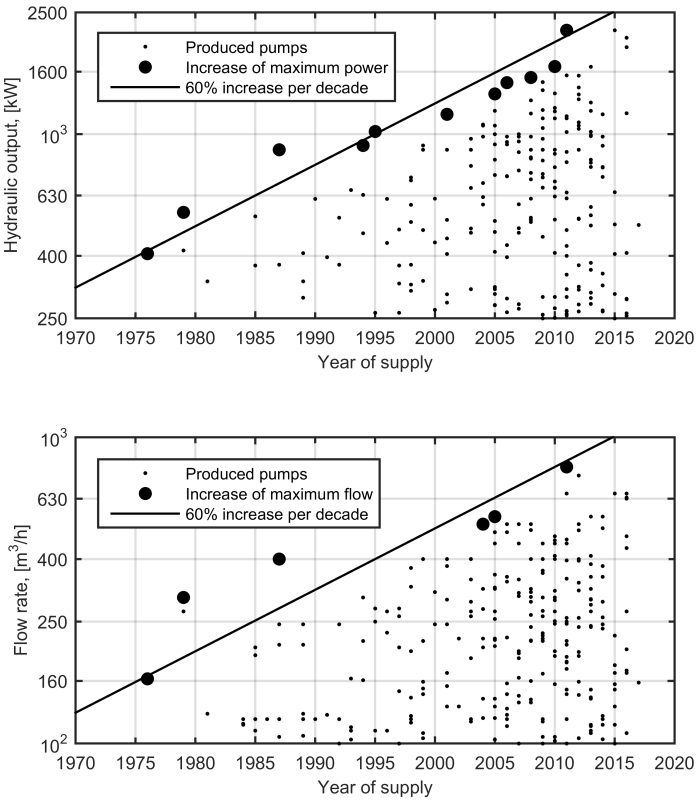

Figure 1.2: Historical increase in hydraulic power output (top) and flow rate (bottom) of produced GEHO® piston diaphragm pumps over the last 4 decades, van Rijswick *et al.* (2010)

This trend is expected to continue as the size of mining and mineral processing operations are expected to increase, driven by to the economics of scale. Furthermore, a trend towards high density tailing disposal is present in the mining and mineral processing industries driven by restrictions on water use and requirements for geotechnically more stable and potentially reclaimable tailing disposal areas. The higher density tailing disposal requires higher discharge pressures because of the increased viscous losses in the pipeline transport. This provides new application areas for piston diaphragm pumps in high volume tailing applications, larger than 2000 m^3/h, as present in the iron, copper and oil sands industry. Expansion of the operating envelope of piston diaphragm pumps with respect to flow rate requires a further increase in size of the diaphragm as examples of current largest pump stations already use 10 of the largest pumps available in parallel

operation as shown by van Rijswick *et al.* (2010).

Historically, piston diaphragm pumps used in slurry transport are operated at a relatively low stroke rate in order to minimize the wear of the self-acting valves in the severe slurry duty, limited to approximately 60 strokes per minute. The historical increase in flow rate as show in Figure 1.2 has mainly been achieved by increasing the size of the pumps while maintaining the stroke rate around the same level. For the smaller size pumps this is far from any dynamic limitation. But when increasing the size of these pumps while operating at similar stroke rates, dynamics issues started to arise which showed themselves by decreased suction performance, increased pressure pulsation and vibration levels and reduced diaphragm life. Understanding of the physics behind these dynamic limitations is required for an economical design and selection of a piston diaphragm pumps such that the pumps can be operated as close to these limitations as possible reliably. Development of 1D distributed and 0D lumped parameter simulation models describing the fluid transients in and around the pump have provided the necessary tools for reliable pump design and selection from a pressure pulsation point of view as shown by van Rijswick (2007). The understanding of the diaphragm deformation however is still rather limited. The current shape of the diaphragm as used in GEHO® piston diaphragm pumps, has been developed in the early 70's by trail-and-error and has not changed since. All diaphragm sizes used in the GEHO® piston diaphragm pump series, have been derived from this early design and are approximately geometrically similar. Despite the presence of over 40 years of field experience with this diaphragm shape, the exact diaphragm deformation shape during pump operation is still not known. As long as the diaphragm deformation shape is not known or can not be predicted, a reliable pump selection from a diaphragm loading point of view can currently only be achieved by the use of selection limits based on properly scaled field experiences as will be shown in section 5.4. The reliability of the current selection guidelines can only be guaranteed for geometrically similar designs. This blocks the geometric optimization of the diaphragm and its housing as the current level of reliability can only be guaranteed by selecting a geometrically similar designs as are present in the available field experience.

A further increase of the flow rate of a piston diaphragm pump by simply increasing the size of the diaphragm would be possible. However,this further increase in size requires a reduction in stroke rate as well, as the current largest size diaphragm are operating against their stroke rate limit. This limits the economic viability of a larger size piston diaphragm pump. Increasing the stroke volume and/or stroke rate limit of a certain size diaphragm would improve the economic viability of the piston diaphragm pump in larger volume applications.

Limitation of the strain levels in the elastomer of the diaphragm is of utmost importance for eliminating fatigue failures of the diaphragm and thereby obtaining a high reliability of the piston diaphragm pump. The actual strain levels in the diaphragm are the result of a complex Fluid Structure Interaction (FSI) mechanism within the pump chamber between the propelling fluid, the diaphragm and the pumped slurry. The understanding of this fluid structure interaction mechanism has improved in the last decades but is still limited. The main diaphragm deformation driver is the volumetric displacement of the piston. The volumetric displacement of the diaphragm is prescribed by the

piston displacement but its deformation shape however, is not. The deformation shape of the diaphragm is a result of the local fluid loads acting on the diaphragm while being constrained by the volumetric displacement of the propelling fluid by the piston. The following sources for diaphragm deformation can be considered:

- Volumetric displacement by the piston displacement
- Hydrostatic fluid loads by density differences between the propelling fluid and the pumped slurry
- Fluid momentum load by convective and unsteady fluid acceleration
- Viscous fluid loads by shear stresses in the boundary layers

The volumetric displacement generates a uniform pressure load on the diaphragm, but the other loads generate non-uniform pressure loads which besides the hydrostatic load can not be described analytically and are of a transient nature. As the geometry of the fluid domain is determined by the deformed shape of the diaphragm, which deformed shape is a result of the flow field itself, a 2-way FSI analysis is required for the determination of these loads and their effect on the deformation of the diaphragm.

The objective of the study described in this thesis is therefore:

Development of an experimentally validated numerical Fluid-Structure-Interaction model for the prediction of, operating condition induced, diaphragm deformation in piston diaphragm pumps

With the help of such a numerical model the geometry of the diaphragm and the pump chamber could be optimized such that the limits on stroke volume and stroke rate can be increased. When the numerical model is properly validated with experiments, reliably diaphragm design and selection guidelines can be derived for a new optimized design without the need for extensive field trials and re-gathering of decades of field experience.

1.3. OUTLINE OF THE THESIS

In chapter 2 the basics of crankshaft driven positive displacement pump operation are presented which are considered to be required for proper understanding of the choices made, the approach followed and the benefits of the application of the results. In chapter 3 a short overview of the state of the art in pump diaphragm deformation analysis is presented. As the public domain literature on this specific subject is quite limited, an overview of the GEHO® pump diaphragm development history is given which is considered to represent the current state of the art of elastomeric pump diaphragm deformation analysis. This chapter concludes with a brief overview of numerical modelling approaches for Fluid Structure Interaction (FSI). Here the basic choice within this study to use an Immersed Boundary Method (IBM) for modelling the FSI mechanism is introduced. In chapter 4 the continuum mechanics theory used for modelling the fluid

flow and structural deformation is introduced. Also approximate models for turbulence modelling and shell deformation are introduced. After the theoretical model is introduced, a dimensional analysis of the FSI problem is presented in chapter 5. Based on this dimensional analysis the validity of the use of an incompressible single phase fluid model is argued. Furthermore the lower relevance of accurate turbulence and boundary layer modelling is motivated based on the dimensional analysis. Basic dimensionless numbers are derived which are important in describing the FSI process within the piston diaphragm pump. These dimensionless numbers are then used to evaluated field experience data of diaphragm performance gathered over the last 40 years. The numerical implementation of the FSI model is described in chapter 6. Here the Finite Volume (FV) implementation of the fluid solver and the Finite Element (FE) implementation of a rotation-free triangular shell model are presented before combining both in a FSI model using the IBM. Finally some implementation details and the overview of the program procedure are given. In chapter 7 the experimental program and its results are presented which includes a spectral analysis of the results. The experimental results are furthermore used in chapter 8 to validate the results of the numerical model. Next to the validation cases, some industrial relevant cases with high density and high viscosity slurries are shown. Final conclusions and recommendations are given in chapter 9.

2

BASICS OF CRANKSHAFT DRIVEN POSITIVE DISPLACEMENT PUMP OPERATION

In this section some background is given on the operation of positive displacement pumps, especially of the crankshaft driven type as this is the object of this study. This background is considered to be required for proper understanding of the choices made, the approach followed and the benefits of the application of the results. Not all of it can be found in public domain literature, hence some part comes from the personal experience of the author in the subject.

2.1. CRANK KINEMATICS

The complete pump cycle is driven by the displacement of the piston. In Figure 2.1 the crank mechanism of a crankshaft driven positive displacement pump is shown schematically.

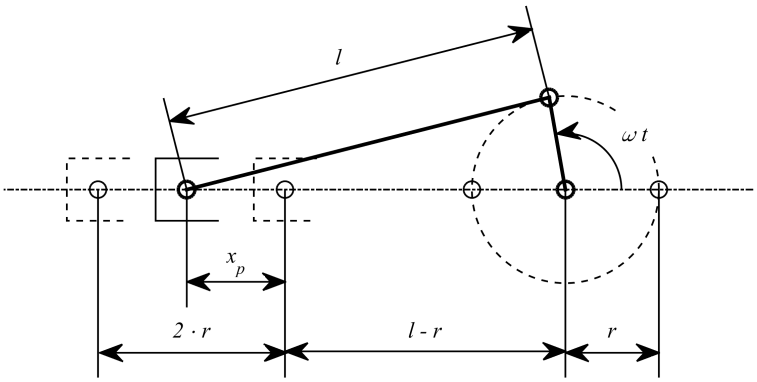

Figure 2.1: Crank mechanism

From a kinematic analysis of the crank mechanism shown in Figure 2.1 the following relationship can be derived for the piston position x_p assuming a constant angular velocity ω of the crankshaft, (Eifler *et al.*, 2009)

$$x_p(t) = r\left[1 - \cos(\omega t) - \frac{\lambda}{2}\sin^2(\omega t)\right] \tag{2.1}$$

with crank radius r and $\lambda = \frac{r}{l}$ with connecting rod length l. After applying a Taylor expansion and differentiation with respect to time of the first 2 harmonics, the following approximation is obtained for the piston velocity $\dot{x}_p$, (Eifler *et al.*, 2009)

$$\dot{x}_p(t) \approx r\omega\left[\sin(\omega t) - \frac{\lambda}{2}\sin(2\omega t)\right] \tag{2.2}$$

which after a second differentiation with respect to time yields the piston acceleration $\ddot{x}_p$

$$\ddot{x}_p(t) \approx r\omega^2\left[\cos(\omega t) - \lambda\cos(2\omega t)\right] \tag{2.3}$$

The piston position, velocity and acceleration are shown as a function of the crank angle ωt in the 3 top rows of Figure 2.2.

2.2. PUMP CYCLE

In combination with the self-acting suction and discharge valves, a cyclic pump chamber pressure is generated by the piston motion. The chamber pressure varies between the suction and discharge pressure present in respectively the suction and discharge manifolds of the pump. The pump chamber is defined as the volume between the piston and the suction and discharge valve. In the pump cycle several phases (1-6) and events (a-f) can be identified as shown in the bottom row of Figure 2.2 where the chamber pressure is shown as a function of the crank angle ωt. The pump cycle starts at the beginning of the discharge stroke (a) with the piston in the retracted position, referred to as the Bottom Dead Centre (BDC), following internal combustion engine terminology. At the BDC

the suction valve has not jet closed as the piston has just finished its suction stroke. This closing delay of the suction valve (1) is typically 5 to 10 degrees of crank angle and is a result of fluid drag around the moving valve body. During this phase, fluid is displaced from the pump chamber back into the suction manifold by the piston at a pressure approximately equal to the suction pressure. The chamber is compressed from the suction pressure towards the discharge pressure once the suction valve has closed (b). The pressure rises roughly linear with the piston displacement during this compression phase (2) giving a non-linear pressure increase in time due to the non-linear relationship of the piston position with time. The discharge valve opens (c) when the chamber pressure has reached the discharge pressure present in the discharge manifold. The opening delay of the discharge valve is typically between 20 and 45 degrees of crank angle depending on the fluid compressibility, discharge pressure level and stroke volume to chamber volume ratio. During the remainder of the discharge stroke (3), fluid is displaced from the pump chamber into the discharge manifold following the piston velocity at a pressure approximately equal to the discharge pressure. At the end of the discharge stroke (d), referred to as the Top Dead Centre (TDC), the piston reverses it direction of motion in order to start the suction stroke. A closing delay of the discharge valve (4) of typically 5 to 10 degrees is present here as well. During this phase fluid is displaced from the discharge manifold back into the pump chamber manifold at a pressure approximately equal to the discharge pressure following the piston motion. Once the discharge valve has closed (e), the chamber is decompressed from the discharge pressure towards the suction pressure. A decompression curve similar to the compression curve is present in the decompression phase (5). The suction valve opens (f) when the chamber pressure has reached the suction pressure present in the suction manifold. The opening delay of the suction valve is typically between 20 and 45 degrees, similar to the opening delay of the discharge valve. During the remainder of the suction stroke (6), fluid is displaced from the suction manifold into the pump chamber following the piston velocity at a pressure approximately equal to the suction pressure. At the end of the suction stroke (a) the BDC is reached again and the cycle is started all over again.

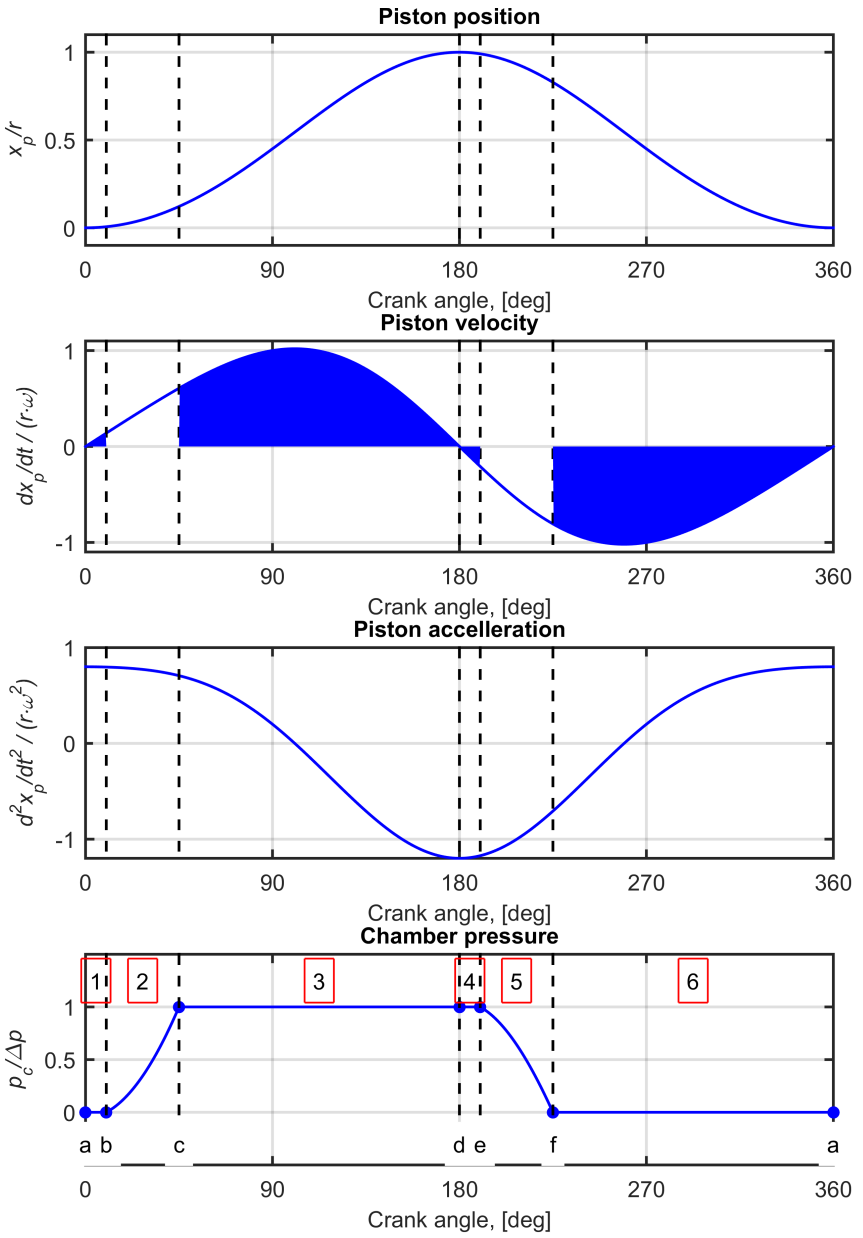

Figure 2.2: Crank kinematics and chamber pressure with identified phases (a-f) and events 1-6)

2.3. VOLUMETRIC AND ENERGETIC EFFICIENCY

It is clear from Figure 2.2 that the closing and opening delays of the suction and discharge valves create a deviation from the theoretical ideal operation with instant valve closing

and opening at the BDC and TDC. A deviation of the actual mean flow rate delivered by a single pump chamber from the theoretical one based on the piston displacement results. This is effect is normally quantified by a volumetric efficiency which is defined as the ratio between the actual and theoretical flow rate which is equal to 1 minus the ratio of the volumetric losses V_{loss} and the piston displacement or stroke volume V_S. The volumetric losses are composed of a leakage volume V_{leak} and a compression volume V_{comp}.

$$\eta_{\text{vol}} = \frac{Q_{\text{act}}}{Q_{\text{theo}}} = 1 - \frac{V_{\text{loss}}}{V_S} = 1 - \frac{V_{\text{leak}} + V_{\text{comp}}}{V_S} \tag{2.4}$$

The leakage losses generally include back-flow through the suction and discharge valve and leakage across the piston. However, leakage across the piston can normally be neglected such that only a volume loss due to back-flow through suction and discharge valves due to their closing delay remains. For 5 to 10 degrees closing delay this is 0.2 to 1 % of the stroke volume for each valve. The compression loss is a result of the fluid compression from the suction to the discharge stroke. The compressibility of a fluid is defined as its relative volumetric change as a response on a pressure change.

$$\kappa = -\frac{1}{V}\frac{\Delta V}{\Delta p} \tag{2.5}$$

Often the bulk modulus K is used to quantify the fluid compressibility which is simply the inverse of the compression coefficient κ. The volume of fluid which needs to be compressed at the beginning of the discharge stroke is equal to the stroke volume V_S plus a so-called dead volume V_0 which is defined as the remaining fluid volume in the pump chamber at the end of the discharge stroke. For the compression volume then holds:

$$V_{\text{comp}} = \frac{V_0 + V_S}{K_{\text{eff}}}\Delta p \tag{2.6}$$

with Δp the difference between the suction and discharge pressure and K_{eff} the effective bulk modulus which is a weighted average of the bulk moduli of the propelling fluid and the pump fluid which is furthermore corrected for the mechanical compliance of the pump chamber. The dead volume is typically 5 to 10 times the stroke volume for the piston diaphragm pumps used in this study. With discharge pressures ranging from 2.5 to 25 MPa and using an effective bulk modulus of 1.5 GPa a range of volumetric efficiencies from 98.5 % down to 80 % results. The majority of the pumps however, operate with a volumetric efficiency lager than 90 % as the dead volume to stroke volume ratio is considered more critically in higher pressure pump configurations.

It should be noted that this volumetric efficiency is different from and only has a limited effect on the energetic efficiency of the pump as the leakage flows over the valves during their closing delay have a very low pressure drop and the energy required to compress the pump chamber is recuperated during the decompression phase. The hydraulic efficiency of the pump is typically larger than 99 % as the frictional losses of the fluid flow within the pump are typically less than 1 % of the pressure differential across the pump due to the relatively high pressure differential across the pump compared to for example centrifugal pumps. The energetic pump efficiency is effected most by frictional losses

in the piston and the crank mechanism. Pump efficiencies of 95 % at the rated duty point are typical for larger size piston diaphragm pumps. When the efficiency of the external gearbox, electric motor and frequency converter are considered as well, an overall efficiency of typically 85 % results at the rated duty point. These high efficiencies are typical for the lager size crankshaft driven piston diaphragm pumps. For smaller size high pressure plunger pumps they can be somewhat lower due to increased friction losses in the plunger sealing. The relatively low volumetric efficiency is also typical for piston diaphragm pumps as the diaphragm construction results is larger dead volumes compared to for example high pressure plunger pumps where the dead volume can be bought back to the order of the stroke volume, or even a fraction of that, when using specific arrangements of the suction and discharge valves, (Eifler *et al.*, 2009). The low leakage losses are typical for all crankshaft driven positive displacement pumps with self-acting valves. This compared to plunger pumps used in fluid power applications where the volumetric efficiency is dominated by leakage flows around the plungers and the in- and outlet port phasing plate. In these fluid power pumps the volumetric efficiency does have a large impact on the energetic efficiency as these leakage flows have a high pressure drop as they are leakage flows from the discharge pressure to the suction or ambient pressure.

2.4. FLOW AND PRESSURE PULSATIONS

Crankshaft driven positive displacement pumps inherently generate a fluctuating flow due to the kinematics of the crack mechanism. The flow rate generated by a single pump chamber is obtained by multiplying the piston velocity with the piston area before modulating it with the valve timing. This is shown by the filled area under the velocity curve in Figure 2.2. In a multi chamber pump the flow profiles are have a phase shift from each other due to a phase shift between the individual crank throws of the crankshaft which evens out the flow fluctuation generated by the individual chambers as much as possible. In Figure 2.3 the flow fluctuation of a typical crankshaft driven triplex single acting positive displacement pump is shown.

The flow rate with its fluctuation as generated by the pump can be seen as a boundary condition for the connected hydraulic system. Depending on the hydraulic response of the connected system, a certain pressure pulsation results. This hydraulic response can have capacitive, inductive as well as resistive effects generated respectively by fluid compressibility, inertia and fiction which can can have lumped as well as distributed parameter behaviour, (van Rijswick, 2007). As shown in Figure 1.1, gas filled dampeners are installed on the pump to absorb the flow fluctuation. Such dampeners are normally sized such the pressure variation in the dampener by adiabatic compression and expansion of the gas in the dampener is within limits, typically between 1 and 10 % of the discharge pressure, depending on the application. The hydraulic response of a dampener can be obtained by modelling it as a hydraulic capacitance C for which holds

$$\dot{p} = \frac{1}{C} Q_{\text{net}} \tag{2.7}$$

in which $\dot{p}$ is the time derivative of the pressure in the volume, Q_{net} the net inflow into the volume. For an ideal gas filled dampener $C = C_{\text{gas}}$ for which holds

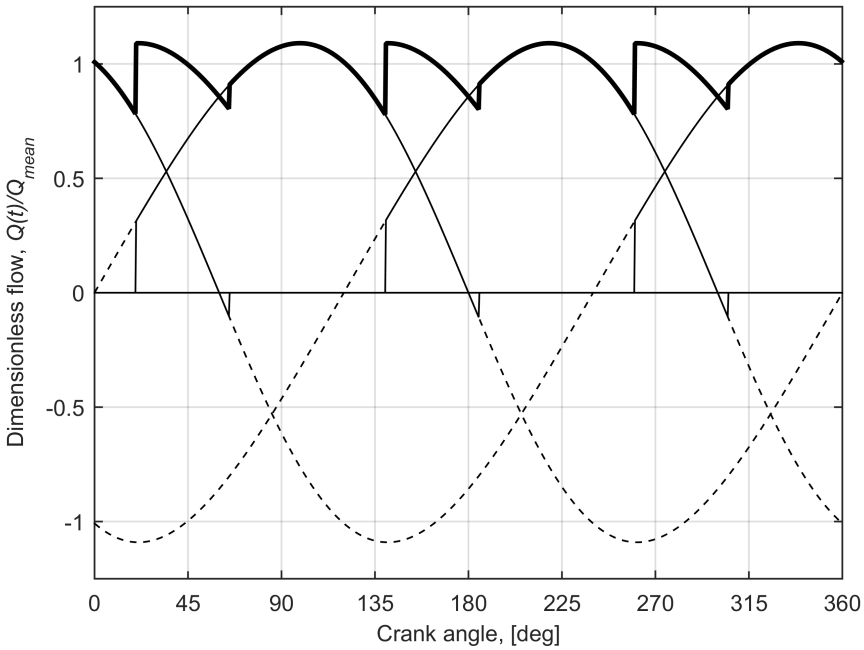

Figure 2.3: Flow fluctuation of a typical crankshaft driven triplex single acting positive displacement pump with a valve opening and closing delay of respectively 20 and 5 degrees ($\eta_{\text{vol}} = 97\%$). Dashed lines show the velocity profile of the individual pistons, thin solid lines show the discharge flow generated by a single piston and thick solid line shows the total flow generated by the pump obtained by summation of the individual piston flows

$$C_{\text{gas}} = \frac{V_m}{p_m \gamma} \tag{2.8}$$

The relationship for gas volume capacitance C_{gas} is found by linearising the polytropic pressure-volume relationship for an ideal gas around a mean volume V_m and mean pressure p_m using the compression coefficient γ. For liquid volumes where the volumetric change is limited, $C = C_{\text{liquid}}$ is used for which holds

$$C_{\text{liquid}} = \frac{V}{K} \tag{2.9}$$

with volume V and bulk modulus K. The volume fluctuation to be absorbed by the dampener can be found by integrating the flow fluctuation around its mean value from which the pressure fluctuation can be obtained by dividing this fluctuating volume with the dampener capacitance. This assumes full absorption of the pump flow fluctuation by dampener which implies a zero flow fluctuation downstream of the dampener. The integrating action of the dampener attenuates the higher frequency components of the flow fluctuation. The high frequency components in the flow fluctuation can be quite pronounced, especially when the valve opening delay is large which introduces a large

step in the flow rate upon valve opening. In Figure 2.4 the volume fluctuation to be absorbed by the dampener as generated by the flow fluctuation of the triplex single acting pump shown in Figure 2.3 is shown, both in the time as well as in the frequency domain.

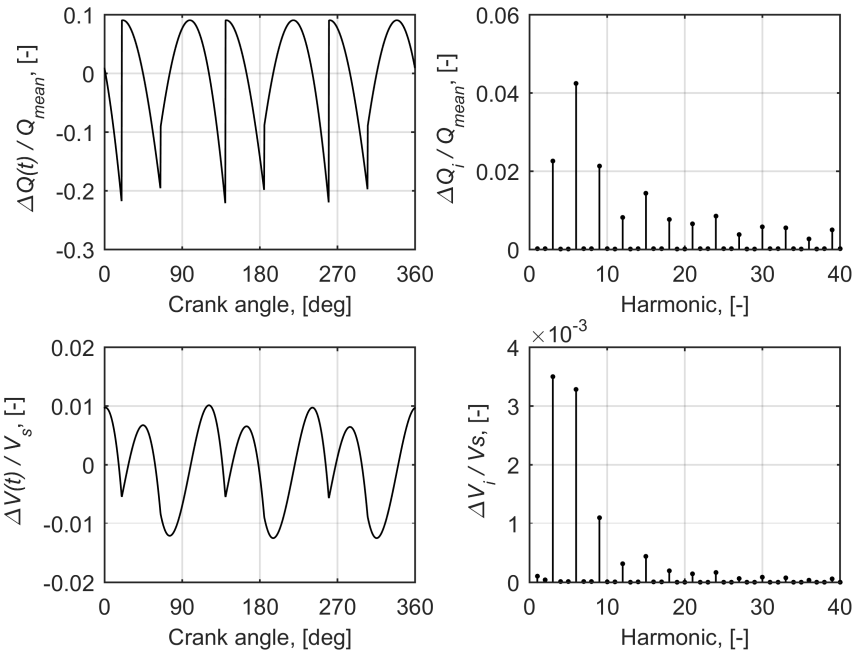

Figure 2.4: Pump flow fluctuation (top row) and dampener volume fluctuation (bottom row) of triplex single acting pump as per Figure 2.3 shown as waveform in the time domain (left column) and as amplitude spectrum in the frequency domain (right column).

In Figure 2.4 one can see that the flow and volume fluctuation are periodic and are composed of frequencies which are a multiple of the 3rd harmonic of the pump stroke rate. In the volume fluctuation to be absorbed by the dampener, and hence in the pressure fluctuation, the higher frequency components are largely attenuated, such that it is dominated by the 3rd and 6th harmonic with only a small contribution of the 9th harmonic the pump stroke rate. This analysis would indicate that a flat pressure profile can be obtained in the suction and discharge connection, and hence in the pump chamber during the suction and discharge stroke, by selecting a large enough dampening volume. Experience has shown that actual pressure pulsations do include higher frequency pulsation than what one would expect from the basic ideal dampener analysis as shown by actual pressure pulsation measurements in Figure 2.5.

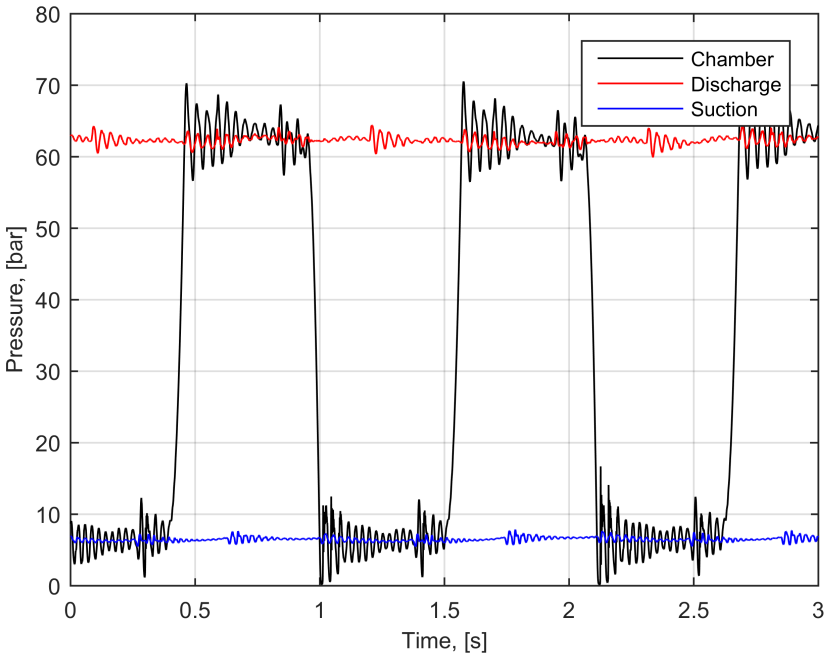

Figure 2.5: Typical pressure measurements on triplex single acting piston diaphragm pump, (van Rijswick, 2008)

The pressure measurements in Figure 2.5 show higher frequency pressure pulsations upon valve opening than what would be expected based on the ideal dampener approximation. The ideal dampener approximation assumes that every flow fluctuation generated by the pump is fully accumulated in the gas volume. However, the non-zero lengths of the fluid passages between the piston and the dampener gas volume poses a limit to this assumption. Upon the valve opening, fluid in these passages has to be accelerated in order to adapt to the flow rate generated by the piston. This typically generates a pressure oscillation upon valve opening due to a combination of capacitive and inductive effects of the fluid in-between the piston and the dampener. Numerical modelling using 1D distributed and 0D lumped parameter fluid transient models of the fluid passages allows reasonable prediction of these higher frequency pressure pulsations as shown by van Rijswick (2007). Deviations from the ideal pressure profile in the pump chamber are further shown in Figure 2.6 in which a pseudo-indicator diagram of the same measured chamber pressure is shown. In this pseudo-indicator diagram the chamber pressure is plotted against the crank angle from 0 to 180 degrees for the discharge stroke and back from 180 to 0 degrees for the suction stroke compared to the chamber pressure versus piston position in a actual indicator diagram.

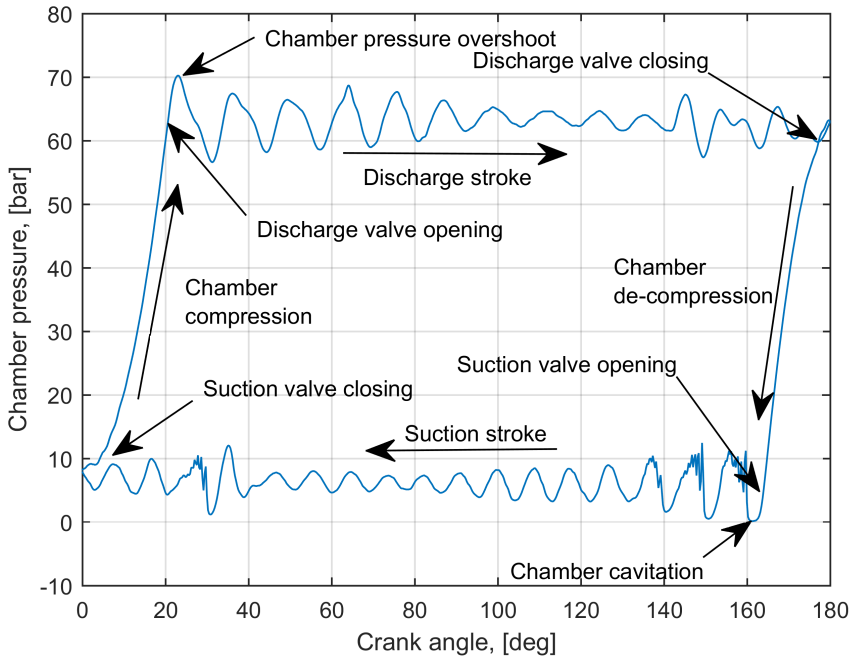

Figure 2.6: Pseudo-indicator diagram of chamber pressure measurement shown in Figure 2.5

In the pseudo-indicator diaphragm all important events and phases of the pump cycle can be identified. Next to the events and phases described before, the pressure overshoot and following pulsation upon discharge and suction valve opening can be seen. The frequency of these pressure pulsation is dependent on the dimensions of the pump and the arrangement of the suction and discharge manifold and the arrangement of the dampeners and is typically between 10 and 100 Hz (27 Hz in Figure 2.5), with a frequency typically decreasing with increasing pump size. Also cross-talk between individual chambers is observed. The negative pressure overshoot upon opening of the suction valve can furthermore initiate cavitation in the pump chamber when it reaches vapour pressure.

Further deviations from ideal dampener approximation are possible due to a hydraulic response of connected system more complex than ideal dampener assumption, for example due to the presence of hydraulic resonances in the connected system. Excitation of these hydraulic resonances can result in increase of pressure pulsation levels up to a factor 5 compared to non resonant conditions. Here numerical modelling of the connected hydraulic system using 1D distributed and 0D lumped parameter fluid transient models has shown to give reasonable predictions as well as shown by van Rijswick (2007). The susceptibility for resonance excitation increases when multiple pumps are operated in parallel. Minimization of the resonance excitation is possible by controlling the phase shift between the crankshaft of the individual pumps as shown by van Rijswick (2007), van Rijswick *et al.* (2010).

3

STATE OF THE ART IN PUMP DIAPHRAGM DEFORMATION ANALYSIS

3.1. PUBLIC DOMAIN LITERATURE ON PUMP DIAPHRAGM DEFORMATION ANALYSIS

3.1.1. DIAPHRAGM MATERIALS

Generally speaking 3 material classes are used as diaphragm material in piston diaphragm pumps; metals, plastomers such as PolyTetraFluoroEthylene(PTFE) and elastomers or rubbers. The advantage of metal and PTFE diaphragms is the high chemical and temperature resistance compared to elastomer diaphragms. The allowable cyclic strain levels which can be endured without fatigue failures, ϵ_{edu}, on the other hand, increases successively from metal to PTFE to elastomer by 2 order of magnitude with $O(\epsilon_{\text{edu}}) \approx 0.1\%, 1\%, 10\%$ respectively. The stroke and therefore the stroke volume that diaphragms of these different materials can endure increases from approximately 3% to 12-14% to 30% of the diaphrgam diameter for respectively metal, PTFE and elastomeric diaphragms, (Eifler *et al.*, 2009). PTFE diaphragms are the current standard in the chemical industry where piston diaphragm pumps are used for the transport of chemically aggressive and/or toxic fluids because of their hermetically sealed operation. In the mining and mineral processing industry however, elastomeric diaphragms are used almost exclusively. In these applications elimination of the abrasive wear of the piston and cylinders by the transported slurry is the primary motivation for selecting a piston diaphragm pump while the pumped fluid is normally within the allowable chemical and temperature limits of elastomers. The volumetric flow rates in this industry are often much larger than typically present in the chemical industry which limits the use of PTFE also from a economic perspective as well. Metal diaphragms have been used in the past in the chemical industry but have nowadays largely been superseded by PTFE diaphragms. Only in

specific applications with temperatures and pressures outside the range of PTFE, metal diaphragm are still being used, (Eifler *et al.*, 2009).

3.1.2. PUMP DIAPHRAGM DEFORMATION RESEARCH

The public domain literature on diaphragm deformation analysis of pump diaphragm is very limited. The only academic research on pump diaphragm deformation analysis known to the author has been performed at the Erlangen University in Germany in the 80's and 90's. Georgiadis (1988) describes a experimental and numerical study on metal diaphragms with the objective of determining stress levels in the diaphragm. Völkl (1992) also describes an investigation of metal diaphragms but specifically looked at clamping effects which showed to be the most critical location in the diaphragm. Schlücker (1993) investigated the deformation behaviour of PTFE diaphragms, both experimentally as well as numerically. In the numerical investigation 3D shell and 2D axisymmetric Finite Element (FE) models were used. Simulations were limited to quasi-static calculations using pressure load driven deformation analysis. Simulation of preformed diaphragms with snap-through effects could not be performed due to numerical instabilities. Because of the higher strain levels in the PTFE diaphragms, measurement of strain levels with strain gauges, as was done with metal diaphragms, could not be performed. An experimental set-up with an optically accessible diaphragm was used in which the diaphragm displacement was measured with a laser triangulation sensor. The working principle of the set-up used by Schlücker (1993) is shown in Figure 3.1

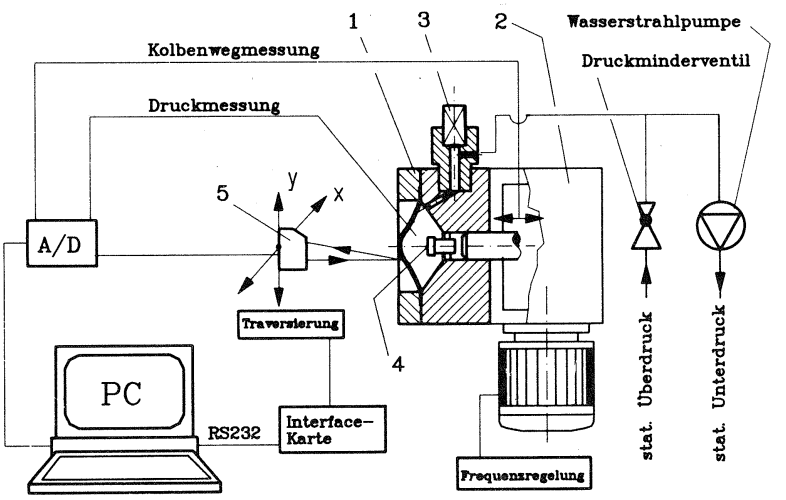

Figure 3.1: Experimental set-up for determining PTFE diaphragm deformation as used by Schlücker (1993), reprinted with permission

In this set-up the diaphragm was hydraulically displaced by a propelling fluid displaced by a piston. An open cover was used such that no pumped fluid was present and only ambient air was in between the laser triangulation sensor and the diaphragm. Although not specifically mentioned by Schlücker (1993) this assumes the presence of only quasi-static and uniform pressure loads on the diaphragm required to deform it. Only viscoelastic material behaviour was considered important. During the operation of the experimental set-up, the laser triangulation successively measures the diaphragm displacement waveform in Z-direction on different XY positions. As the piston displacement is measured simultaneously, reconstruction of a specific deformed diaphragm shape is possible by gathering all diaphragm positions measured at a specific piston position from the successively measured diaphragm displacements waveforms.

3.1.3. DIAPHRAGM DESIGN GUIDELINES

Literature on deformation analysis of elastomeric diaphragms is limited to information that can be found in handbooks for designing elastomeric and rubber components such as Schmitt (1987), Simrit (2007). The methods described are very basic analytical procedures either estimating stresses due to pressure loads in mechanically actuated diaphragms or estimating bending strains in hydraulically actuated diaphragms based on assumed deformed shapes. In the latter situation a deformed shape is estimated based on the assumption of an un-stretched mid-plane of the diaphragm, implying an absence of membrane stresses and strains. With this assumption only bending stresses and strains need to be considered. Rough estimates of the change of the radius of curvature from the manufactured shape to the deformed shape can then be made, potentially in combination with a deformation limitation of the diaphragm by the housing which might be present near the clamping area. From the change of the radius of curvature ΔR, the bending strain ϵ_b can be estimated according:

$$\epsilon_b = \frac{\Delta R h}{2} \tag{3.1}$$

with h the local thickness of the diaphragm. It is clear that such an approach can be highly inaccurate and is also limited to a quasi-static deformation analysis assuming uniform pressure loads and axisymmetric diaphragm deformation. Especially near the critical clamping area on the circumference of the diaphragm it is hardly possible to estimate the diaphragm deformation analytically when a deformation limitation by the housing is not present.

3.2. DEVELOPMENT HISTORY OF GEHO® PUMP DIAPHRAGM

As the public domain information of diaphragm design and development is rather limited, a short summary of the GEHO® pump diaphragm development history is given here. This shows how much trail-and-error went into the initial development, simply because numerical models were non-existing during the initial development. The current state of the deformation analysis described in this section is furthermore considered to be the current state of the art for elastomer diaphragms. A flat top cone, dish shaped or so-called conical frustum as shown in Figure 3.2, was selected as the diaphragm shape

during the original development of the GEHO® pump diaphragm. This diaphragm shape has a higher allowable stroke volume then a flat shaped diaphragm of equal diameter.

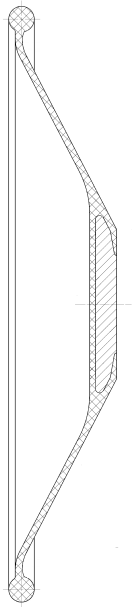

Figure 3.2: Original GEHO® pump diaphragm design as developed in early 70's

During the initial development of the GEHO® piston diaphragm pump in the early 70's, issues with diaphragm fatigue failures near the clamping area were experienced. By geometric optimization of the transition to the camping area by trail-and-error the fatigue strength was finally increased. The basic design of the GEHO® diaphragm has not changed since this initial geometrical optimization in the 70's. Only the size range has expanded since, but all new designs of larger diaphragms are more or less geometrically similar to the original ones which were optimized in the 70's by trial-and-error. The first pumps used rather conservative stroke volumes for a specific diaphragm size. In the 80's limitations on allowable stroke volume were determined based on experimentally determined diaphragm deformation shapes under static volumetric displacements in a set-up as shown in Figure 3.3. Changes of the local radius of curvature and hence bending strains could be estimated from these experimentally obtained deformed shapes, from which stroke volume limits could be derived.

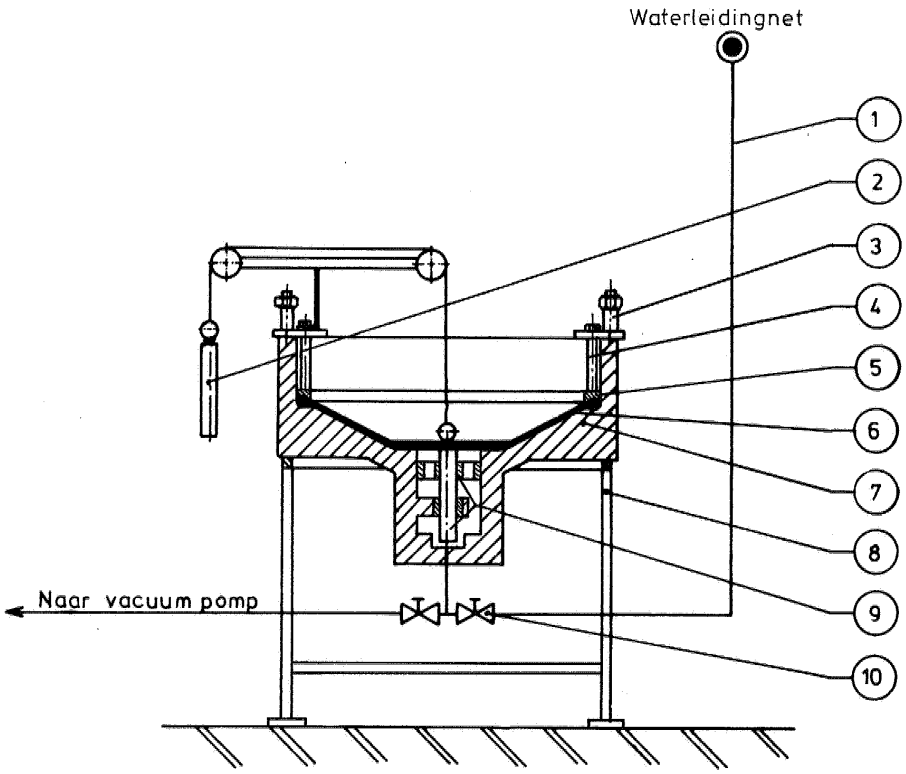

Figure 3.3: Experimental set-up for determining static diaphragm deformation shapes, (Segers, 1986).

When experience was gathered with the operation of larger size and hence larger flow rates piston diaphragm pumps in the 90's, issues with reduced diaphragm life were experienced again. From observation of failure locations it was concluded that asymmetric loads were acting on the diaphragm. This was not anticipated before and had and still have not been described in public domain literature so far besides some more recent publications by the author as part of this study, (van Rijswick *et al.*, 2012, 2014, 2016). The asymmetric fluid loads were initially considered to be caused by differences in hydrostatic pressure in the propelling fluid and the pumped slurry due to the density difference between them. Later it was recognised that convective fluid acceleration within the pump chamber played a role as well. This led to the introduction of slurry density and stroke rate dependent corrections on the allowable stroke volume of a certain size diaphragm. These corrections were largely based on field experiences gathered. In the late 90's non-linear Finite Element Analysis (FEA) became available which allowed to numerically simulate quasi-static deformed diaphragm shapes based on assumed non-uniform pressure loads as shown in Figure 3.4

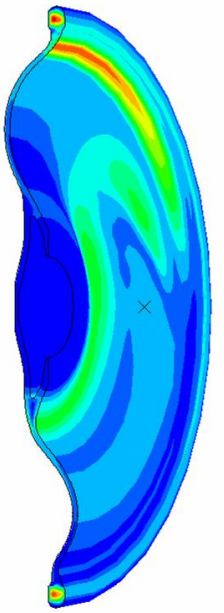

Figure 3.4: Result of non-linear quasi-static 3D FEA of pump diaphragm with non-uniform pressure load, (Stroeken, 2004).

Important to mention here is that these quasi-static FEA's indicated a uniform pressure load necessary to deform the diaphragm of $O(p) = 1000\,\text{Pa}$. This is used later to evaluate the importance of different sources of fluid loads in the deformation analysis of the diaphragm. Although these quasi-static 3D FEA's gave much insight in the diaphragm deformation and the critical locations in the diaphragm, its ability to quantitatively explain all field experiences was limited. This is considered to be caused by both the complexity of the FSI mechanism, as well as the limitations of the structure-only FEA's used. Issues are:

- Uncertainty of the magnitude and distribution of the estimated fluid loads, especially when considering fluid momentum loading
- Assumption of quasi-static fluid loads neglects influence of unsteady fluid acceleration
- Diaphragm displacement is neither load nor displacement driven. The diaphragm displacement is a result of the pressure load acting on the diaphragm while its volumetric displacement is constrained by the piston displacement. Combined with the snap-through behaviour of the diaphragm it is difficult to analyse the mid-stroke diaphragm positions in a quasi-static FEA.

The limitations of these structure-only FEA's show that the actual diaphragm displacement is linked much more intimately to the fluid flow around it than can be de-

scribed by a structure-only calculation. In a quasi-static sense this is due to the volumetric constraint of the diaphragm displacement. In a dynamic sense this is due to a 2-way coupling between the flow path and the diaphragm deformation as the geometry of the flow path is dependent on the deformed diaphragm shape whose shape is again dependent on the flow path dependent fluid loads. A proper numerical analysis of the diaphragm deformation behaviour therefore requires the analysis of the FSI mechanism which has to include a 2-way coupling between the fluid flow around and the structural deformation of the diaphragm. As far as known to the author, such a FSI analysis with the application to piston diaphragm pumps is non-existing in public domain literature. The development of such a numerical model is therefore subject of this study.

3.3. FLUID STRUCTURE INTERACTION

Pump diaphragm deformation is normally not considered to be a result of a complex 2-way Fluid Structure Interaction (FSI) process and is regarded as a quasi-static deformation process. As a result, public domain literature on FSI of pump diaphragms is non-existing. As discussed in chapter 1 and in the previous section however, a 2-way FSI process is considered to be present in the larger piston diaphragm pumps used in the mining and mineral processing industries. Although public domain literature on FSI of pump diaphragm deformation is non-existing, the public domain literature on general FSI research and numerical modelling of FSI phenomena is rather large and is growing fast, indicating it is an active field of research, see e.g. Hou *et al.* (2012) for an overview. First major application areas of FSI are discussed followed by a short discussion on numerical approaches followed for modelling FSI phenomena.

3.3.1. APPLICATION AREAS OF FLUID STRUCTURE INTERACTION

Although the field of FSI is quite large, when scanning the literature, it seems that 2 major application areas dominate in which a 2-way fluid structure interaction is important to consider. The first application is vortex-induced vibrations in both hydro as well as aerodynamics applications where vortex shedding can result in structural vibrations which require a 2-way FSI analysis when the vibration amplitudes are large enough to influence the vortex shedding, see e.g. Sarpkaya (2004). The other main application area is in biological flows. Of specific interest for this study is the field of hemodynamics in which the blood flow in animal hearts and arteries and around natural or artificial heart valves is researched, see e.g. Thiriet (2008). Here rather flexible structures are present which can have relative large structural displacements as a result of the fluid loads present. Other biological flow examples with large structural displacements are encountered in the analysis of the flight of birds an insects and the swimming of fish, see e.g. Mittal *et al.* (2008). But it seems that in most situation these situations are handled using prescribed structural motion implying the lower relevance of the 2-way interaction. It seems therefore that the applications which require a 2-way FSI approach with relatively large structural displacements of relatively flexible structures are limited to the field of hemodynamics. At first hand this seems to be a completely different field than the field of positive displacement slurry pumps, however there are quite some similarities. First of all an animal heart is a positive displacement pump which uses self-acting valve in its

operation as well. The blood which is being pumped is a 2 phase solid water mixture which has non-Newtonian rheological properties similar to some fine particle slurries. Furthermore the flow in a part of the connected system, the cardiovascular system in the animal, is of pulsating nature as well. With respect to FSI it is interesting to note that the Elastic modulus of artery wall material is of $O(E) = 0.1$ to 10 MPa, (Thiriet, 2008), depending on the direction fibre reinforcements, which is of similar magnitude as the elastic modulus of elastomers used as pump diaphragm material. A typical stroke rate of human heart is similar to the stroke rate used in piston diaphragm pump. Only the geometric scale of the fluid flow in a piston diaphragm is roughly an order of magnitude larger than what is present in a human heart. This comparison suggest that the underlying physics in the FSI phenomena present in blood flow in animal hearts and main arteries is quite similar to the physics which play a role in the FSI phenomena in a piston diaphragm pump.

3.3.2. NUMERAL MODELLING OF FLUID STRUCTURE INTERACTION

Numerical modelling of FSI phenomena requires the combination of numerical methods applied in structural mechanics and fluid mechanics. Numerical methods applied in structural mechanics and fluid dynamics have developed quite separately from each other.

The Finite Element Method (FEM), which evolved within the field of structural mechanics, is the default approach for numerical analysis of structural problems, (Zienkiewicz *et al.*, 2005a). Although the basis of present day finite element procedures were developed in the late 50's and early 60's, a wide spread application in general industry for 3D solid mechanics outside specific industries like the aerospace industry, was not until the late 80's and early 90's when commercial FEA software and low cost computing power became more readily available. But even then it was still mainly limited to linear elastic stress analysis. The development and application of non-linear FEA for structures roughly lagged behind a decade.

In fluid mechanics the Finite Volume Method (FVM), based on the control volume approach which is typically applied in fluid mechanics, has initially developed as the default approach for the numerical analysis of fluid mechanics problems. This field is called Computational Fluid Dynamics (CFD). Only later the FEM developed for structural mechanics was applied to fluid mechanics problems as well, (Zienkiewicz *et al.*, 2005b). Numerical analysis of fluid mechanics of industrially relevant fluid flows is normally considered to be more complex than the numerical analysis of structural mechanics problems. This is mainly due to turbulent phenomena in the fluid flow which have such a wide range of scales that a Direct Numerical Simulation (DNS) of the Navier-Stokes equitations of industrial flows is not possible with today's computational resources, (Ferziger and Peric, 2002). This has led to the development of turbulence models which focusses on modelling the effect of turbulence without actually resolving the turbulent flow. This is different from structural mechanics where the physical approximations are typically limited to the definition of boundary conditions such that one only has to care about the mathematical and numerical approximations which are typically been taken care of by a convergence check on a finer numerical mesh. The physical modelling involved in CFD requires a much deeper understanding of the underlying physics and the

approximations made in the turbulence modelling by the numerical analyst for fluid mechanics problems than what is typically required for structural mechanics problems. The physical approximations also requires more attention for experimental validation than what is typically considered to be required for structural mechanics problems. Furthermore the flow field is more complex which typically requires a numerical model with a higher number of Degrees Of Freedom (DOF) and hence typically requires more computational resources. This is the main reason why widespread industrial application of CFD outside the aerospace industry was delayed to the beginning of the 21st century and is still not as common as the application of structural FEA.

For the numerical analysis of the FSI problem the structural FEA and CFD approaches need to be combined. One of the earliest attempt for numerical analysis of FSI phenomena is described by Peskin (1972, 1977), for the application of modelling FSI phenomena around heart valves. Peskin developed the so-called Immersed Boundary Method (IBM) in which the fluid flow is modelled using a Eulerian formulation for the fluid flow on a non-deforming Cartesian grid. The structure is immersed in the fluid domain and is modelled using a Lagrangian formulation on a deforming grid. Finite Difference Methods (FDM) were used for the dicretization of both the fluid as well as the structural equations. The structural nodes are immersed in the fluid and are advected each time step to a new location by an interpolated fluid velocity. Based on the new positions of the structural nodes, structural reaction forces are calculated on each node which are supported in the fluid flow as body forces which are used in the solution of the flow field at the next time step. The advantages of the IBM approach are its relative simplicity, largely due to the use of a Cartesian grid flow solver, and the ability to handle extremely large structural displacements without any requirements for the deformation of the computational fluid grid. Despite some disadvantages with respect to numerical instabilities when analysing FSI phenomena with stiff structures and the inability to use unstructured body fitted grids with a nice grid refinement in boundary layers, the method is still being used and researched, especially in the field of biological flows, (Griffith, 2012). The advantages with respect to its simplicity and the ability to handle large structural displacements, in combination with the presence of relatively flexible structure in biological flows, are the basis why this approach is still used and is the reason why it is used in this study as well.

Next to the mentioned IBM the so-called Arbitrary Lagrangian Eulerian (ALE) approach is used quite often for the numerical analysis of FSI phenomena, see e.g. Bungartz and Schäfer (2006), Hou *et al.* (2012). In the ALE approach the computational domain is divided in a structural domain and a fluid domain which are both allowed to deform. In the fluid domain, fluid is allowed to flow through the computational grid while this grid can move and deform in space as well. This requires a description of the fluid equations in a combination of Lagrangian and Eulerian formulations which gives the method its name. The advantage is that unstructured body-fitted fluid grids can be used which allow nice grid refinements near the boundaries of the fluid domain required for accurate description of boundary layers. The disadvantage is however, the deforming fluid grid which can become too deformed when very large structural displacements need to be followed. This is the area where the IBM is most powerful as it does not require any deformation of the fluid grid. Literature on the field of ALE approaches for FSI analysis is quite extensive and a full evaluation of it is considered outside the scope of

this study as this study will focus on the IBM because of its strengths in handling very large structural displacement which are present in piston diaphragm pump. The maximization of the structural displacement of the diaphragm with respect to the dimensions of the pump chamber is actually the objective of a pump chamber and diaphragm design optimisation.

4

THEORY

The Fluid Structure Interaction (FSI) process present within the pump chamber involves the interaction between the structural deformation of the pump diaphragm and the fluid flow around the diaphragm on both the propelling fluid side as well as on the pumped fluid side. For the numerical analysis of the FSI mechanism both a solid mechanics model as well as a fluid mechanics model is required. In this chapter the basis of the both models is described, starting from a continuum mechanics approach. After the basic continuum description is presented some approximate models for turbulence modelling and shell approximation will be presented. In chapter 6 the numerical implementation and the interaction between the solid and fluid mechanics models will be described.

4.1. CONTINUUM MECHANICS

Most of this section is a summary of general continuum mechanics theory as described by Belytschko *et al.* (2000). When not specifically mentioned, this reference applies as an general source of the information presented in this section. Most of the continuum mechanics theory presented applies to both solid as well as fluid mechanics.

4.1.1. KINEMATICS OF MOTION AND DEFORMATION

MOTION

Consider a moving body in space which has undergone some deformation as shown in Figure 4.1.

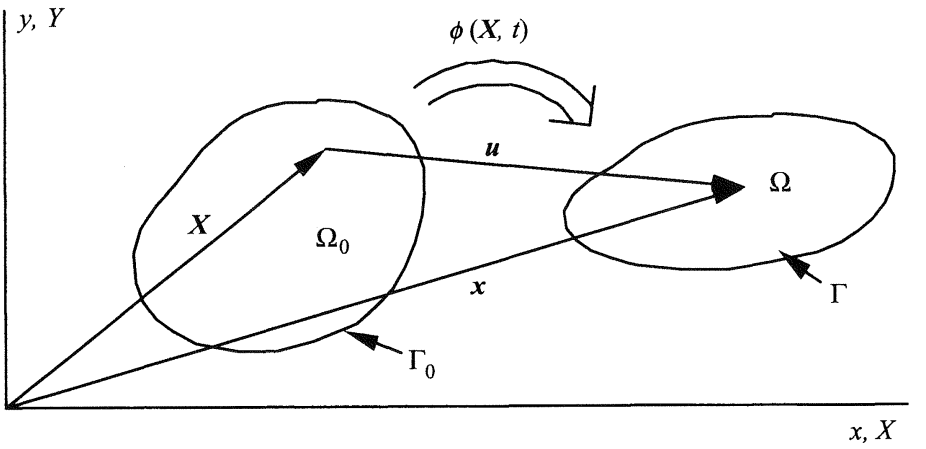

Figure 4.1: Deformation and motion of a body of a fixed material volume in space, with Lagrangian coordinates **X** in the undeformed reference configuration Ω_0 with boundary Γ_0 and corresponding Eulerian coordinates **x** in the deformed configuration Ω with boundary Γ, (Belytschko *et al.*, 2000), Copyright ©2000 John Wiley & Sons, Ltd, reprinted with permission.

The body is defined as a fixed material volume indicted by Ω. In Figure 4.1 both the undeformed reference configuration Ω_0 as well as the deformed configuration Ω are shown. The body can be either a fixed portion of a solid or a material volume of a fluid. The coordinates of a material point in the reference configuration are identified with the Lagrangian coordinate **X** while the same material point in the deformed configuration has a Eulerian coordinate **x** which are related to each other via the mapping function $\boldsymbol{\phi}(\mathbf{X}, t)$

$$\mathbf{x} = \boldsymbol{\phi}(\mathbf{X}, t) \tag{4.1}$$

When deriving governing equations for the solid deformation and the fluid flow both Lagrangian as well as Eulerian description can be used. In a Lagrangian description the independent variables are the Lagrangian or material coordinates **X** and time t while in a Eulerian description the independent variables are the Eulerian or spatial coordinates **x** and time t. In solid mechanics the Lagrangian description is most widely used as the stresses normally depend on the deformation history from the reference configuration which is most easily described in Lagrangian coordinates. In fluid mechanics on the other hand, a Eulerian formulation is normally used as stresses normally depend on the deformation rate and not on the deformation history and fluid deformation is normally too large to be described in Lagrangian coordinates. The displacement of a material point **u** is simply the difference between its current position and the original position

$$\mathbf{u} = \mathbf{x} - \mathbf{X} \tag{4.2}$$

The velocity of a material point is the rate of change of its position vector which is called the material time derivative for which holds

$$\mathbf{v}(\mathbf{X},t) = \frac{\partial \boldsymbol{\phi}(\mathbf{X},t)}{\partial t} = \frac{\partial \mathbf{u}(\mathbf{X},t)}{\partial t} \equiv \dot{\mathbf{u}} \tag{4.3}$$

The acceleration of a material point is the rate of change of the its velocity which is called the material time derivative of the velocity for which holds

$$\mathbf{a}(\mathbf{X},t) = \frac{\partial \mathbf{v}(\mathbf{X},t)}{\partial t} = \frac{\partial^2 \mathbf{u}(\mathbf{X},t)}{\partial t^2} \equiv \dot{\mathbf{v}} \tag{4.4}$$

When the velocity is expressed in the spatial coordinates in a Eulerian description, the material time derivative of the velocity is obtained by applying the chain rule which gives

$$\frac{D\mathbf{v}(\mathbf{x},t)}{Dt} = \frac{\partial \mathbf{v}}{\partial t} + \mathbf{v}\cdot\nabla\mathbf{v} \tag{4.5}$$

The first term is the spatial time derivative or unsteady term and the second term is the convective or transport term.

DEFORMATION

For describing the stress response of the solid and fluid a description of its deformation or deformation rate are required respectively. The deformation in a body can be characterized by the deformation gradient tensor **F** which is defined as

$$\mathbf{F} = \frac{\partial \mathbf{x}}{\partial \mathbf{X}} \text{ or } F_{ij} = \frac{\partial x_i}{\partial X_j} = \nabla_0 \mathbf{x}^T \tag{4.6}$$

In non-linear solid mechanics different strain measures are used. An essential property of these strain measures is their invariance under rigid body motion also called objectivity. Here the Green-Lagrange strain tensor **E** is defined.

$$\mathbf{E} = \frac{1}{2}\left(\mathbf{F}^T\cdot\mathbf{F} - \mathbf{I}\right) \text{ or } E_{ij} = \frac{1}{2}\left(F_{ik}^T F_{kj} - \delta_{ij}\right) \tag{4.7}$$

with $\mathbf{F}^T\cdot\mathbf{F} = \mathbf{C}$ with the right Cauchy-Green deformation tensor **C**, identity tensor **I** and Kronecker delta δ_{ij} which is 1 when $i = j$ and 0 otherwise. The Green-Lagrange strain tensor can also be expressed in terms of displacement gradients by

$$\mathbf{E} = \frac{1}{2}\left((\nabla_0\mathbf{u})^T + \nabla_0\mathbf{u} + \nabla_0\mathbf{u}\cdot(\nabla_0\mathbf{u})^T\right) \text{ or}$$

$$E_{ij} = \frac{1}{2}\left(\frac{\partial u_i}{\partial X_j} + \frac{\partial u_j}{\partial X_i} + \frac{\partial u_k}{\partial X_i}\frac{\partial u_k}{\partial X_j}\right) \tag{4.8}$$

For small deformations ($\nabla_0\mathbf{u} \ll 1$) this is equal to infinitesimal strain tensor $\boldsymbol{\epsilon}$

$$\mathbf{E} \underset{\nabla_0\mathbf{u}\ll 1}{\approx} \boldsymbol{\epsilon} = \frac{1}{2}\left((\nabla_0\mathbf{u})^T + \nabla_0\mathbf{u}\right) \text{ or } \epsilon_{ij} = \frac{1}{2}\left(\frac{\partial u_i}{\partial X_j} + \frac{\partial u_j}{\partial X_i}\right) \tag{4.9}$$

In constitutive models for isotropic hyper-elastic materials the left Cauchy-Green deformation tensor or Finger tensor **B** is often used

$$\mathbf{B} = \mathbf{F} \cdot \mathbf{F}^T \text{ or } B_{ij} = \frac{\partial x_i}{\partial X_k} \frac{\partial x_j}{\partial X_k} \tag{4.10}$$

For describing the deformation rate in fluid mechanics the velocity gradient tensor **L** is defined first

$$\mathbf{L} = \frac{\partial \mathbf{v}}{\partial \mathbf{x}} = (\nabla \mathbf{v})^T \text{ or } L_{ij} = \frac{\partial v_i}{\partial x_j} \tag{4.11}$$

The velocity gradient tensor can be split into a symmetric part **S** and skew-symmetric part **Ω**

$$\mathbf{L} = \mathbf{S} + \mathbf{\Omega} \tag{4.12}$$

with the rate-of-deformation tensor **S**

$$\mathbf{S} = \frac{1}{2}\left(\mathbf{L} + \mathbf{L}^T\right) = \frac{1}{2}\left((\nabla \mathbf{v})^T + \nabla \mathbf{v}\right) \text{ or } S_{ij} = \frac{1}{2}\left(\frac{\partial v_i}{\partial x_j} + \frac{\partial v_j}{\partial x_i}\right) \tag{4.13}$$

and the spin or rate-of-rotation tensor **Ω**

$$\mathbf{\Omega} = \frac{1}{2}\left(\mathbf{L} - \mathbf{L}^T\right) = \frac{1}{2}\left((\nabla \mathbf{v})^T - \nabla \mathbf{v}\right) \text{ or } \Omega_{ij} = \frac{1}{2}\left(\frac{\partial v_i}{\partial x_j} - \frac{\partial v_j}{\partial x_i}\right) \tag{4.14}$$

STRESS

In non-linear continuum mechanics also different stress measures are used. Here the true stress or Cauchy stress tensor $\boldsymbol{\sigma}$ is mentioned only. The Cauchy stress tensor $\boldsymbol{\sigma}$ is defined by Cauchy's law

$$\mathbf{n} \cdot \boldsymbol{\sigma} \, \mathrm{d}\Gamma = \mathbf{t} \, \mathrm{d}\Gamma \tag{4.15}$$

in which **t** is the traction force per unit area or stress vector working on the boundary Γ and **n** the boundary normal vector. The Cauchy stress is called the true stress as it is defined on the deformed geometry. The Cauchy stress can be split in a deviatoric part and a hydrostatic part giving the deviatoric stress tensor $\boldsymbol{\tau}$ and the pressure p

$$\boldsymbol{\tau} = \boldsymbol{\sigma} - \frac{1}{3}\mathrm{tr}\,(\boldsymbol{\sigma})\,\mathbf{I} = \boldsymbol{\sigma} + p\mathbf{I} \tag{4.16}$$

USE OF INVARIANTS

Often invariants of the tensor quantities introduced in this section are used in continuum mechanics, for example in determining principle stresses and strains and in the definition of constitutive equations. In the latter case the invariants represent scalar measures of characteristic deformation types for which models can be derived which can be fitted to experimental data. Furthermore the invariants are frame invariant which means such that they can be used as objective measures of deformation. The 3 invariants of a second-order tensor **A** are defined as

$$I_A = \mathrm{tr}(\mathbf{A}) = A_{ii} = \lambda_1 + \lambda_2 + \lambda_3 \tag{4.17}$$

$$II_A = \frac{1}{2}\left[\mathrm{tr}(\mathbf{A})^2 + \mathrm{tr}\left(\mathbf{A}^2\right)\right] = A_{ii}^2 - A_{ij}A_{ji} = \lambda_1\lambda_2 + \lambda_2\lambda_3 + \lambda_3\lambda_1 \tag{4.18}$$

$$III_A = \det(\mathbf{A}) = \lambda_1\lambda_2\lambda_3 \tag{4.19}$$

with λ_1, λ_1, λ_1 being the principle or eigen values of $\mathbf{A}$. For the left Cauchy green deformation tensor $\mathbf{B}$ for example, they are equal to the principle extension ratios $\lambda = \frac{l}{l_0}$. For an incompressible solid $J = \det(\mathbf{F}) = 1$ holds which gives $III_B = J^2 = 1$ which applies for the elastomer of the diaphragm in this study as well. For an incompressible fluid $I_S = 0$ holds. In fluid mechanics the square root of the absolute value of the second invariant of 2 times the rate-of-strain tensor $II_{2\mathbf{S}}$ is used to define the effective the effective shear rate $|\mathbf{S}|$ which is equal to shear rate $\dot{\gamma}$ in a simple shear flow. As the rate-of-strain tensor is symmetric, $S_{ij} = S_{ji}$, a simplification of its second invariant is possible for an incompressible fluid, $S_{ii} = 0$, which gives

$$\sqrt{|II_{2\mathbf{S}}|} = \dot{\gamma} = |\mathbf{S}| \underset{\substack{S_{ij}=S_{ji} \\ S_{ii}=0}}{=} \sqrt{2S_{ij}S_{ij}} \tag{4.20}$$

In the analysis and visualisation of turbulent flows the rotation of the flow is often important as well which can be described by the spin or rate-of-rotation tensor $\mathbf{\Omega}$. As $\mathbf{\Omega}$ is skew-symmetric and has a zero trace $II_{\mathbf{\Omega}} = \frac{1}{2}\Omega_{ij}\Omega_{ij}$ holds, which can be seen as an effective rotation rate. Both shear and rotation are included in the velocity gradient tensor $\mathbf{L}$. In the WALE turbulence model, (Nicoud and Ducros, 1999), which will be discussed in section 4.2, invariants of the square of the velocity gradient tensor are used. The second invariant of the velocity gradient tensor is also used for vortex visualization as shown by Dubief and Delcayre (2000) where it is called the Q-criterion. As the velocity gradient can be split in the symmetric deformation rate tensor $\mathbf{S}$ and the anti-symmetric rotation rate tensor $\mathbf{\Omega}$, the Q criterion can also be written as

$$Q = II_{\mathbf{L}} = \frac{1}{2}\left(\Omega_{ij}\Omega_{ij} - S_{ij}S_{ij}\right) \tag{4.21}$$

and therefore indicates the balance between the rotation rate $\mathbf{\Omega}^2 = \Omega_{ij}\Omega_{ij}$ and the rate of deformation $\mathbf{S}^2 = S_{ij}S_{ij}$. In areas where Q is positive, the rotation of the flow dominates over the deformation or shear of the flow. A vortex can then be identified by a zone in which the Q-criterion is larger than some threshold value.

4.1.2. CONSERVATION EQUATIONS

Now the kinematics of motion and deformation have been described, the governing equation can be derived using the basic conservation laws which are:

- Conservation of mass
- Conservation of linear momentum
- Conservation of energy

- Conservation of angular momentum

In deriving the conservation equations two important theorems are used; the Gauss's divergence theorem and the Reynolds transport theorem. The Gauss's divergence theorem states that the integral of the divergence of a tensor field **g** over domain Ω is equal to outward flux of that tensor field through the boundary Γ of that domain which gives

$$\int_{\Omega} \left(\nabla \cdot \mathbf{g}\right) \mathrm{d}\Omega = \int_{\Gamma} \left(\mathbf{g} \cdot \mathbf{n}\right) \mathrm{d}\Gamma \tag{4.22}$$

with **n** the outward pointing normal. The Reynolds transport theorem states that the rate of change of the integral of a property **g** in a material domain Ω_M is equal to integral of the rate of change property **g** in a control domain Ω_C plus the flux of property **g** through the control domain boundary Γ_C,Ferziger and Peric (2002).

$$\frac{D}{Dt}\int_{\Omega_M} \mathbf{g}\,\mathrm{d}\Omega = \int_{\Omega_C} \frac{\partial \mathbf{g}}{\partial t}\,\mathrm{d}\Omega + \int_{\Gamma_C} \mathbf{g}\left(\mathbf{v} - \mathbf{v}_b\right) \cdot \mathbf{n}\,\mathrm{d}\Gamma \tag{4.23}$$

The material domain Ω_M moves with the material while the control domain Ω_C can be fixed in space but also moving in space and deforming indicated by the boundary velocity of the control volume $\mathbf{v}_b$.

CONSERVATION OF MASS

For the conservation of mass m holds that the change of mass, or volume integral of density ρ, in a material volume is zero which, in combination with the Reynolds transport theorem and divergence theorem, gives

$$\frac{Dm}{Dt} = \frac{D}{Dt}\int_{\Omega} \rho\,\mathrm{d}\Omega = \int_{\Omega} \left(\frac{D\rho}{Dt} + \rho \nabla \cdot \mathbf{v}\right) \mathrm{d}\Omega = 0 \tag{4.24}$$

Mass conservation is straight forward in a Lagrangian description as used in solid mechanics as a material volumes are tracked. The density in the deformed geometry is then related to the original density ρ_0 by the determinant of the deformation gradient tensor **F**

$$\rho \det\left(\mathbf{F}\right) = \rho J = \rho_0 \tag{4.25}$$

For an incompressible material $J = 1$ holds which implies $\rho = \rho_0$. In a Eulerian description as used in fluid mechanics, the last form of the mass conservation in Equation 4.24 is used which also holds for a fixed control volume which gives the continuity equation after inserting the definition of the material time derivative.

$$\frac{\partial \rho}{\partial t} + \nabla \cdot \left(\rho \mathbf{v}\right) = 0 \tag{4.26}$$

In an incompressible flow the term $\frac{D\rho}{Dt}$ in Equation 4.24 is 0 which gives

$$\nabla \cdot \mathbf{v} = 0 \tag{4.27}$$

which also holds for a variable density flow which can be seen when deriving it from Equation 4.24.

CONSERVATION OF LINEAR MOMENTUM

The conservation of linear momentum is equal to Newton's second law of motion which states that the acceleration of a body is equal to the sum of all forces acting on that body

$$\frac{D}{Dt}\int_{\Omega}\rho\mathbf{v}\,\mathrm{d}\Omega = \int_{\Omega}\rho\mathbf{b}\,\mathrm{d}\Omega + \int_{\Gamma}\mathbf{t}\,\mathrm{d}\Gamma \tag{4.28}$$

with body force per unit volume **b** and traction force per unit area or stress vector **t**. By applying Reynolds transport theorem and inserting the continuity equation it can be shown that the following is mathematically equivalent

$$\frac{D}{Dt}\int_{\Omega}\rho\mathbf{v}\,\mathrm{d}\Omega = \rho\int_{\Omega}\frac{D\mathbf{v}}{Dt}\,\mathrm{d}\Omega \tag{4.29}$$

Applying Gauss's Theorem on Cauchy's law gives

$$\int_{\Gamma}\mathbf{t}\,\mathrm{d}\Gamma = \int_{\Gamma}\mathbf{n}\cdot\boldsymbol{\sigma}\,\mathrm{d}\Gamma = \int_{\Omega}\nabla\cdot\boldsymbol{\sigma}\,\mathrm{d}\Omega \tag{4.30}$$

After inserting Equation 4.29 and Equation 4.30 in Equation 4.28, which holds for an arbitrary domain Ω, the momentum equation results

$$\rho\frac{D\mathbf{v}}{Dt} = \nabla\cdot\boldsymbol{\sigma} + \rho\mathbf{b} \tag{4.31}$$

In a Eulerian description used in fluid mechanics the material derivative of the velocity is written out and the stress is decomposed in a hydrostatic pressure p and a deviatoric stress tensor $\boldsymbol{\tau}$ which gives the Navier-Stokes momentum equation.

$$\rho\left(\frac{\partial\mathbf{v}}{\partial t} + \mathbf{v}\cdot\nabla\mathbf{v}\right) = -\nabla p + \nabla\cdot\boldsymbol{\tau} + \rho\mathbf{b} \tag{4.32}$$

The above form of the Navier-Stokes equations is the so-called non-conservation form. The so-called strong conservation form, Ferziger and Peric (2002), is obtained when the density is remained in the difference operator and the hydrostatic pressure remains in the stress tensor.

$$\frac{\partial\left(\rho\mathbf{v}\right)}{\partial t} + \nabla\cdot\left(\rho\mathbf{v}\mathbf{v}\right) = \nabla\cdot\boldsymbol{\sigma} + \rho\mathbf{b} \tag{4.33}$$

Mathematically both forms are equivalent, but after discretization for obtaining a numerical solution the strong conservation form is often preferred within fluid mechanics as it has better conservation properties in for example the finite volume method.

CONSERVATION OF ENERGY

The conservation of energy requires the rate of change of the total energy of a material volume, both internal as well as kinetic energy, to be balanced by the power done by the external forces and the energy added by heat conduction and any heat sources. The equations describing conservation of energy are not further discussed here as thermodynamic processes are not considered to be of importance in this study.

CONSERVATION OF ANGULAR MOMENTUM

The conservation of angular momentum is obtained by taking the cross product of each term in Equation 4.28 with the position vector **x** which then only requires the Cauchy stress tensor to be symmetric.

$$\boldsymbol{\sigma} = \boldsymbol{\sigma}^T \tag{4.34}$$

4.1.3. CONSTITUTIVE EQUATIONS

The momentum equations describe the relationship between the motion and the stresses acting on a material volume. In order to solve these equations a relationship between these stresses and the deformation or rate of deformation is required. In solid mechanics the stresses are typically related to the deformation of a material volume while in fluid mechanics they are typically related to the rate of deformation.

CONSTITUTIVE EQUATIONS FOR SOLID MECHANICS

A linear small strain, small displacement constitutive model for isotropic materials can be derived by applying Hook's law in 3 dimensions, see e.g. Ugural and Fenster (1995), which gives in tensor notation

$$\boldsymbol{\sigma} = 2\mu\boldsymbol{\epsilon} + \lambda \operatorname{tr}(\boldsymbol{\epsilon})\mathbf{I} \tag{4.35}$$

with the Lamé coefficients $\mu = G$ and $\lambda = K - \frac{2}{3}G$ with shear modulus G and bulk modulus K. The shear and bulk modulus can also be expressed in terms of the elastic modulus E and Poisson's ratio ν by $G = \frac{E}{2(1+\nu)}$ and $K = \frac{E}{3(1-2\nu)}$. For a incompressible solid $\nu \rightarrow \frac{1}{2}$ and $K \rightarrow \infty$. The infinitesimal strain tensor $\boldsymbol{\epsilon}$ relates the deformation to the reference configuration Ω_0 while the Cauchy stress tensor is related the deformed configuration Ω. In a small strain, small displacement and small rotation situation however, these are approximately identical such that the use of the Cauchy stress tensor in combination with the infinitesimal strain tensor is considered correct.

In this study the deformation behaviour of the elastomer diaphragm needs to be described in which material volumes for sure undergo large displacements and rotations and potentially also large deformations. For the constitutive modelling of elastomer materials so-called hyper-elastic material models are most often used, (Macosko, 1994), for which a stored energy function exist which is load path independent. For isotropic hyper-elastic materials the stored strain energy function can be written as a function of the invariants of the left Cauchy-Green deformation tensor **B**.

$$\psi = \psi(I_B, II_B, III_B) \tag{4.36}$$

The following constitutive equation then holds for every incompressible isotropic hyper-elastic material

$$\boldsymbol{\sigma} = -p\mathbf{I} + 2\frac{\partial \psi}{\partial I_B}\mathbf{B} - 2\frac{\partial \psi}{\partial II_B}\mathbf{B}^{-1} \tag{4.37}$$

When the function ψ is expanded as a power series in terms of I_B and II_B, the strain energy function at small strain levels must have the form

$$\psi = C_1 I_B + C_2 I I_B \tag{4.38}$$

which is called the Mooney-Rivlin equation, (Gent, 2001), which gives the Mooney-Rivlin constitutive model

$$\boldsymbol{\sigma} = -p\mathbf{I} + 2C_1\mathbf{B} - 2C_2\mathbf{B}^{-1} \tag{4.39}$$

For infinitesimal strains this should give the same result as the small strain, small displacement model in Equation 4.35 which gives $G = 2(C_1 + C_2)$. When C_2 is assumed to be zero the Neo-Hookean model is obtained which is an extension of Hooke's law for larger deformations.

$$\boldsymbol{\sigma} = -p\mathbf{I} + G\mathbf{B} \tag{4.40}$$

The Neo-Hookean model has shown to give good correlation with experimental data of uni-axial tensile test of rubbers up to approximately 40 % strain while the Mooney-Rivlin model gives good correlation up to 100 % strain but with limited accuracy in compression, (Gent, 2001). For good correlation at higher strain levels, higher order, non-linear versions of the strain energy function are required, but this is considered outside the range of interest for analysis of the diaphragm deformation in this study.

CONSTITUTIVE EQUATIONS FOR FLUID MECHANICS

In fluid mechanics the stress is related to the rate of deformation. For an incompressible Newtonian fluid the following constitutive equation holds

$$\boldsymbol{\tau} = \mu 2\mathbf{S} \text{ or } \tau_{ij} = \mu 2S_{ij} = \mu\left(\frac{\partial v_i}{x_j} + \frac{\partial v_j}{x_i}\right) \tag{4.41}$$

with the Newtonian dynamic viscosity μ. A general incompressible viscous fluid with non-Newtonian rheology is normally described with an apparent viscosity $\mu(|\mathbf{S}|)$ which depends on the effective shear rate $|\mathbf{S}|$, (Macosko, 1994).

$$\boldsymbol{\tau} = 2\mu(|\mathbf{S}|)\,\mathbf{S} \tag{4.42}$$

High concentration fine particle slurries which are being transported by piston diaphragm pumps often exhibit non-Newtonian rheology. This non-Newtonian behaviour is normally shown in a graph in which the shear stress is plotted as a function of the applied shear rate which is called a rheogram. Non-Newtonian effects which are considered here are shear thinning and plastic behaviour. In a shear thinning fluid the apparent viscosity decreases with increasing shear rate. The shear thinning effect is typically modelled with a power law model in which the apparent viscosity is modelled as a power law function of the shear rate. Fluids with visco-plastic behaviour have a yield stress, τ_y, which has to be applied before shearing of the fluid can take place. Below the yield stress the fluid behaves like an elastic solid. A widely used rheological model for fluid flow with plastic behaviour is the Bingham plastic model in which the shear stress is equal to the yield stress plus a part which proportional with the applied shear rate. The power

law and Bingham plastic model can be combined into the Herschel-Bulkley model, (Macosko, 1994).

$$\boldsymbol{\tau} = 2\left[\frac{\tau_y}{|\mathbf{S}|} + m|\mathbf{S}|^{(n-1)}\right]\mathbf{S} \text{ for } II_\tau \geq \tau_y^2 \tag{4.43}$$

with the apparent viscosity between square brackets. When $\tau_y = 0$ the power law model results. When $\tau_y > 0$ and when $n = 1$ the Bingham plastic model results with the plastic viscosity $m = \mu_\infty$, the asymptotic value of the apparent viscosity at infinite shear rate. The elastic behaviour of the fluid below the yield stress poses numerical challenge but is a somewhat theoretical assumption as well. The discontinuity at zero shear rate due to the yield stress can be removed by limiting the apparent viscosity to a large but finite Newtonian viscosity at small shear rates which gives a bi-viscosity model. When using a Bingham plastic model, $n = 1$, the transition between the Newtonian model and the Bingham plastic model can be smoothed with an exponential function, as shown by Papanastasiou (1987), by replacing the yield stress in Equation 4.43 with

$$\tau_y \rightarrow \tau_y\left(1 - e^{-\alpha|\mathbf{S}|}\right) \tag{4.44}$$

This gives a Newtonian viscosity at small shear rates for which holds

$$\lim_{|\mathbf{S}|\rightarrow 0} \mu(|\mathbf{S}|) = \mu_\infty + \alpha\tau_y \tag{4.45}$$

The value of α should be selected such that the Newtonian viscosity at small shear rates is much larger, e.g. 2 orders of magnitude, than the apparent viscosity which is present in the sheared regions of the flow of interest. Although proposed in Macosko (1994), this smoothing does not work for Herschel-Bulkley models with $n < 1$, as the power law term in the apparent viscosity goes to infinity at small shear rates when $n < 1$. In this case a simple limiter on the apparent viscosity can be used as is done in the bi-viscosity model.

4.2. TURBULENCE MODELLING

Viscous effect are included in the Navier-Stokes equations by a viscous stress tensor which describes the viscous stresses which arise because of laminar shearing of the fluid. For a correct description of the viscous dissipation all scales at which the viscous dissipation need to be resolved by a numerical model. This is normally only possible for a laminar flow. When modelling a turbulent flow this requires fully resolving all turbulent scales including the smallest scales where the viscous dissipation takes place. The required resolution is not realistic for any real life industrial flow problem. In a turbulent flow vortices are formed which are transported with the mean flow and which transport their angular momentum down to smaller and smaller scales until it can be dissipated at the smallest scales by viscous dissipation. The turbulence introduces an unsteadiness in the flow with a more or less chaotic character with velocity fluctuations around a mean value. The flow velocity $\mathbf{v}$ can be decomposed in a steady or slowly varying mean flow velocity $\overline{\mathbf{v}}$ and a fluctuating component $\mathbf{v}'$

$$\mathbf{v} = \overline{\mathbf{v}} + \mathbf{v}' \tag{4.46}$$

The vortical structures in a turbulent flow transport momentum across moving layers of fluid perpendicular to the mean flow direction due to the perpendicular velocity component introduced by the rotation of the vortices. When a velocity gradient is present in the mean flow, faster moving layers will be decelerated and slowing moving layers will be accelerated by this momentum transport. This momentum exchange between layer of fluid generates additional turbulent stresses which are called Reynolds stresses. Modelling of these Reynolds stresses is the subject of turbulence modelling. In the Computational Fluid Dynamics (CFD) literature one generally finds three approaches followed for turbulent flow calculations, see e.g. Versteegh and Malalasekera (2007):

Reynolds Averaged Navier Stokes (RANS). When using a RANS approach, the focus is on the mean flow and the effect of turbulence on the mean flow properties. A time or ensemble averaged version of the Navier-Stokes equations is used which introduces an additional term, called the Reynolds stresses, describing the interaction between the various turbulent fluctuations. In a RANS approach a turbulence model is used to model the Reynolds stresses. The most basic one is Prandtl's mixing length model and the most widely used method for industrial CFD is the $k-\epsilon$ model. In both models the Reynolds stresses are modelled with an eddy viscosity which is added to the molecular viscosity following the Boussinesq eddy viscosity hypothesis. In the Prandtl's mixing length model the spatial variation of the eddy viscosity is assumed to be known *a priori* while in the $k-\epsilon$ model the eddy viscosity is a function of the turbulent kinetic energy k and its dissipation rate ϵ for which two additional transport equations need to be solved and boundary conditions need to be given.

Large Eddy Simulation (LES). While in a RANS approach one attempts to remove the unsteadiness due to the turbulent fluctuations from the solution, one attempts to include the larger turbulent fluctuations in a LES while modelling the smaller ones. Instead of a time or ensemble averaged version of the Navier-Stokes equations, a spatially averaged version is used which is obtained by applying a spatial filter. Just like in the RANS approach an additional stress term arises which is called the Sub-Grid-Scale (SGS) stress for which a turbulence model is required. In the Smagorinsky-Lilly SGS model and the Wall Adapting Local Eddy (WALE) viscosity model, (Nicoud and Ducros, 1999), the SGS stresses are modelled using a linear eddy viscosity model. The eddy viscosity adds dissipation which represents the physical dissipation in the unresolved scales. An alternative to using a physical model for this dissipation is to use the dissipation of the numerical method as the SGS turbulence model which is called an Implicit Large Eddy Simulation (I-LES), (Grinstein *et al.*, 2007). It is argued that some dissipation, either physical or numerical, is required to keep the method stable when not all turbulent scales can be resolved. As kinetic energy cascades towards the smallest scales in a turbulent flow where it is finally dissipated, all the SGS stresses do is dissipate the energy at the unresolved scales which otherwise would make the model unstable. When a numerical method is used which is designed to be unconditionally stable, its numerical dissipation could be used as the SGS turbulence model. Especially when the numerical model only adds numerical dissipation where and when required,

it might mimic the physical reality quite well.

Direct Numerical Simulation (DNS). In a DNS no turbulence model is used and one attempts to resolve all the turbulent scales down to the Kolmogorov scale where the viscous dissipation takes place. This requires a very fine grid which is the reason why DNS is normally only used within fundamental turbulence research and is generally considered unrealistic to be used for industrial applications.

In order to provide estimates of the impact of the turbulent behaviour on the flow and the requirement to model it correctly in this study, some basic characteristics of wall bounded turbulent flows are presented here which are mainly based on Pope (2000). When a solid boundary is present, a boundary layer with thickness δ will form between the free stream flow and the boundary where the mean flow velocity decreases to zero to fulfil the no-slip boundary condition. Near the wall the flow is influenced by viscous effects and is not influenced by free stream parameters. The mean flow velocity in the boundary layer $\overline{v}$ then only depends on the distance from the wall y, density ρ, viscosity μ and wall shear stress τ_w. From these parameters appropriate velocity and length scales are defined. These are the friction velocity v_τ

$$v_\tau = \sqrt{\frac{\tau_w}{\rho}} \tag{4.47}$$

and the viscous length scale δ_μ

$$\delta_\mu = \frac{\mu}{\sqrt{\rho \tau_w}} = \frac{\mu}{\rho v_\tau} \tag{4.48}$$

These scales are then used to scale the mean velocity in the boundary layer $\overline{v}$

$$v^+ = \frac{\overline{v}}{v_\tau} \tag{4.49}$$

and the distance from the wall y giving the so-called wall units y^+

$$y^+ = \frac{y}{\delta_\mu} = \frac{\rho v_\tau y}{\mu} \tag{4.50}$$

which have to be related based on dimensional grounds which gives the law of the wall

$$v^+ = f\left(y^+\right) \tag{4.51}$$

The law of the wall is a universal function for the velocity profile in the boundary layer, independent on the free stream velocity and the boundary layer thickness δ and is considered to be universally applicable to the so-called inner layer, $y/\delta < 0.1$, and seems to hold for both channel and pipe flow as well as for general boundary layers. Very close to the wall, $y^+ < 5$, a viscous sub-layer is present in which the shear stress is equal to the wall shear stress τ_w which, in combination with the no-slip boundary condition at the wall, dictates a linear velocity profile which gives

$$v^+ = y^+ \tag{4.52}$$

Further away from the wall, $y^+ > 30$, the so-called log-law seems to hold universally within the inner layer, $y/\delta < 0.1$.

$$v^+ = \frac{1}{\kappa}\ln y^+ + B \tag{4.53}$$

with the von Kárman constant $\kappa = 0.41$ and constant $B = 5.2$. The transition region from $y^+ = 5$ to $y^+ = 30$ is called the buffer layer.

For a pipe flow with mean or bulk velocity $\overline{V}$, the wall shear stress can be estimated from empirical relationships for the (Darcy-Weisbach) friction factor f_D

$$f_D = \frac{\Delta p D}{\frac{1}{2}\rho \overline{V}^2 L} = \frac{4\tau_w}{\frac{1}{2}\rho \overline{V}^2} \tag{4.54}$$

The friction factor for an industrial water flow in a steel pipe is normally in the range of 0.01 to 0.03, but typically around 0.015 (e.g. 5 m/s in DN200 ($\mathrm{Re} = 10^6$) with 46 µm roughness), (Fox and McDonald, 1998). For the viscous length scale δ_μ holds

$$\delta_\mu = \frac{\mu}{\sqrt{\rho \tau_w}} = \frac{\mu}{\rho \overline{V}\sqrt{f/8}} \tag{4.55}$$

For the example above $\tau_w = 47$Pa which gives $\delta_\mu = 4.6$ µm which indicates a viscous sub-layer thickness of 23 µm ($y^+ = 5$) and a start of the log-region at 138 µm ($y^+ = 30$) from the wall. These values are important when the boundary layer needs to be described accurately in a CFD analysis. The first computational point needs to be within the viscous sub-layer if the mean velocity profile of the flow in the boundary layer needs to be resolved. This is an un-practical requirement for a normal industrial CFD analysis which is normally circumvented by using wall-functions. These wall functions use the universal law of the wall to apply a wall shear stress on first computational cell which obeys the law of the wall. The first computational cell then has to be within the valid log-region for which a limit of $y^+ = 500$ is can be used, (Versteegh and Malalasekera, 2007). For the example above this gives 2.3 mm. In a CFD analysis using an unstructured grid this is practically possible to achieve by using a properly refined grid in the boundary layer. For the anticipated approach in this study, which uses a uniform Cartesian grid in combination with an Immersed Boundary Method, such refinement is not considered practical. Next to the impractically large number of computational cells that would result, wall functions have not been developed for IBM approaches to the authors knowledge. However, the friction factor relates the magnitude of the shear stresses due to the turbulent flow to the inertial forces in the flow. The typical value of the friction factor indicates that the shear stresses due to the turbulent flow are more than 2 orders of magnitude smaller than the dynamic pressure. These shear stresses are important in the production, dissipation and transport of turbulent kinetic energy turbulent and needs to be considered when interested in the transport and mixing characteristics of a turbulent flow. In this study however, the focus is on the deformation of the diaphragm. The diaphragm deforms as a response on fluid loads acting on the diaphragm. These loads can be decomposed in normal stresses due to the pressure as well as shear stresses

due to viscous shear in the boundary layers. In chapter 3 it was mentioned that the a quasi-static displacement of the diaphragm requires pressures of $O(p) = 1000\,\text{Pa}$. The expected shear stresses due to turbulent flow are estimated to be 2 orders of magnitude smaller. The dynamic pressure in the flow and the hydrostatic pressure difference across the diaphragm on the other hand are of similar magnitude or even an order of magnitude larger than the quasi-static diaphragm displacement pressure. This suggest the lower relevance of accurate modelling of the turbulent boundary layers and is used here as an argument to omit any turbulence modelling or omit the use of wall-functions when turbulence modelling is applied. This argument will be supported further in chapter 5 where a dimension analysis of the FSI mechanism will be presented.

4.2.1. LES SGS TURBULENCE MODELLING

In a Large Eddy Simulation (LES), the largest turbulent structures are resolved in an unsteady flow simulation, while the contribution of the smaller turbulent structures is represented by a Sub-Grid-Scale (SGS) turbulence model. In deriving the SGS turbulence model spatial filtering is applied on the Navier-Stokes equations which give the Navier-Stokes equations of the filtered field variables with an additional term for the SGS stresses which have to be modelled by an LES turbulence model. The oldest and most basic one, the Smagorinsky-Lilly SGS model, uses an SGS viscosity which is proportional to the average strain rate $|S| = \sqrt{2S_{ij}S_{ij}}$ of the resolved flow:

$$\mu_{\text{SGS}} = \rho\,(C_S\Delta)^2\,|S| \tag{4.56}$$

This resembles the equation for the eddy viscosity in Prantl's mixing length model. The mixing length $l_m = C_S\Delta$ is assumed proportional to the filter length Δ, which is normally equal to the grid spacing ($\Delta = \sqrt[3]{\Delta_x\Delta_y\Delta_z}$), with proportionality constant for which values in the range of $C_S = 0.1 - 0.24$ are reported, (Versteegh and Malalasekera, 2007). The Smagorinsky model however gives unrealistically high eddy viscosity in shear flow near a wall which can turn the flow to laminar when C_S is not reduced near walls. A SGS turbulence model which is an improvement in this aspect, is the Wall Adapting Local Eddy viscosity (WALE) model as described by Nicoud and Ducros (1999). In the WALE model the SGS eddy viscosity automatically reduces in a shear dominated flow in which no rotation is present. The SGS eddy viscosity is determined by

$$\mu_{\text{SGS}} = \rho\,(C_W\Delta)^2\,\frac{\left(S^d_{ij}S^d_{ij}\right)^{3/2}}{\left(S_{ij}S_{ij}\right)^{5/2} + \left(S^d_{ij}S^d_{ij}\right)^{5/4}} \tag{4.57}$$

with $S^d_{ij} = \frac{1}{2}\left(g^2_{ij} + g^2_{ij}\right) - \frac{1}{3}\delta_{ij}g^2_{kk}$ and $S_{ij} = \frac{1}{2}\left(g_{ij} + g_{ji}\right)$ with the velocity gradient of the resolved grid velocities: $g_{ij} = \frac{\partial u_i}{\partial x_j}$. In this study $C_W = 0.55$ as proposed by Nicoud and Ducros (1999) is used when this model is applied. As the SGS eddy viscosity vanishes in shear dominated flow, the model can be applied in both laminar as well as turbulent flow situations and can be used to predict laminar to turbulent flow transition.

4.3. PLATE AND SHELL MODELLING

In section 4.1 a continuum mechanics approach was described which could be used for modelling the structural deformation of the diaphragm. In this section a reduced dimensional structural shell model is described which simplifies the structural model. The assumptions and limitations will be discussed such that the validity of the approach in this study can be argued.

In Figure 4.2 a cross section of a GEHO® pump diaphragm is shown. The pre-moulded shape of the diaphragm shape is essentially a conical frustum. In the center, a metal plate is moulded into the diaphragm to which a monitoring rod is connected which is used to monitor the position of the central plate in the diaphragm. When the central plate gets outside its allowable operating limits, propelling fluid is added or relieved. The monitoring rod furthermore guides the movement of the central plate and hence places a constraint on the motion of the central plate such that only translation in and rotation around the monitoring rod axis is allowed. The diaphragm has a constant thickness in the annular area with dimension $\Delta r \approx 0.3D$ between the clamping diameter with diameter D and the central plate with diameter $d \approx 0.4D$ of $h \approx 0.01D$ which a gradually increases up to $h \approx 0.05D$ near the central section and up to $h \approx 0.02D$ near the outer clamping diameter.

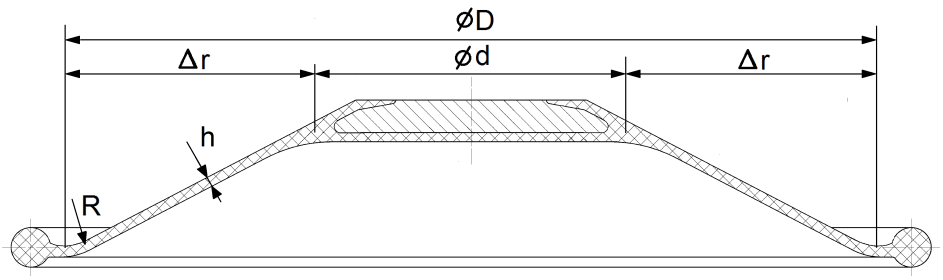

Figure 4.2: Cross section GEHO® pump diaphragm

The structural model should describe the structural deformation of the diaphragm and should interface with the fluid flow in order to model the Fluid Structure Interaction (FSI). The anticipated method for describing the FSI between the deformable diaphragm and the fluid flow is an Immersed Boundary Method (IBM) using feedback forcing, Mittal and Iaccarino (2005). In this approach the structure is represented by a Lagrangian mesh which is immersed in and advected by the fluid flow every time step. The structural model should respond with reaction forces on the computational nodes of the structure which can then be supported in the fluid flow as body forces in the computational cells of the flow solver.

In the original IBM developed by Peskin (1977), the structural model consisted of a system of elastic links in 2D, thereby only including membrane and no bending stiffness. More rigid structures were modelled as a truss structure. A more general approach was

followed by Peskin and McQueen (1980) by deriving the boundary forces as a derivative of the energy function. By applying the energy equation on a triplet of points rather than on a couple of points only, rigid structures, path constraints and bending stiffness could be introduced. The latter resembles a finite difference approximation of the beam bending equations on a curvilinear grid following the neutral axis of a beam. Peskin and McQueen (1989) extended the method to 3D by modelling the structure as an immersed system of elastic fibres, with only stiffness in the fibre direction. This gives a highly anisotropic material with only stiffness in the fibre direction which was considered adequate for the application of modelling a human heart wall. Here the fibres follow the natural muscle fibres and also allowed to include muscle action in the model. The lateral wall stiffness has actually been introduced by the incompressibility constraint of the fluid in which the structure is immersed, but resistance in shear was absent. In this study the diaphragm is a 3D solid structure with more or less isotropic properties, hence a continuum or solid mechanics based modelling approach seems more appropriate than the fibre approach as used by Peskin.

The question is whether the structural model needs to be based on a full 3D continuum description or that a reduced dimensional structural model based on plate and shell deformation theory suffices, a shell being a curved plate. In analytical approaches the benefit of plate and shell models lies in the reduced complexity of the problem which in some cases allows the development of analytical solutions, especially for flat square, rectangular or circular plates, see e.g. Roark and Young (1983). In a numerical approach the advantage lies in the elimination of the need for spatial discretization in the thickness direction of the plate or shell. This greatly reduces the degrees of freedom of the numerical model, especially when considering a thin shell in combination with the FE modelling requirement of roughly equilateral side lengths of the elements in the structural mesh.

Plate and shell models are derived from a continuum mechanics model with additional constraints on the kinematics of the deformation. Plate and shell theory is generally considered applicable when the thickness dimension is small compared to the in-plane dimensions such that bending deformation can be considered dominant. The shape of the plate or shell can then be represented by the shape of the mid-surface. In a pure bending deformation of plates and shells, the curvature of the mid-surface of the plate or shell changes while straight lines normal to the mid-surface remain normal and straight during the deformation. Two theoretical plate deformation models are typically used, the Kirchhoff-Love and Reissner-Mindlin theories for thin and thick plates respectively, see e.g. Zienkiewicz and Taylor (2005). These theories are extensions of the Euler and Timoshenko beam theories respectively. The Euler beam and Kirchhoff-Love plate theory only include bending deformation, and exclude transverse shear deformation. This is a result of the assumption that straight lines normal to the neutral axis or mid-surface remain straight and normal to the neutral axis or mid-surface during deformation. The Timoshenko beam and Reissner-Mindlin plate theory include transverse shear deformation as well by relaxing the requirement that straight lines normal to the neutral axis or mid-surface remain normal to the neutral axis or mid-surface. All theories do assume that straight lines normal to the neutral axis or mid-surface remain straight during deformation. Transverse shear deformation becomes important to consider when the

span to thickness ratio L/h becomes small. The difference between bending and shear deformation is shown in Figure 4.3.

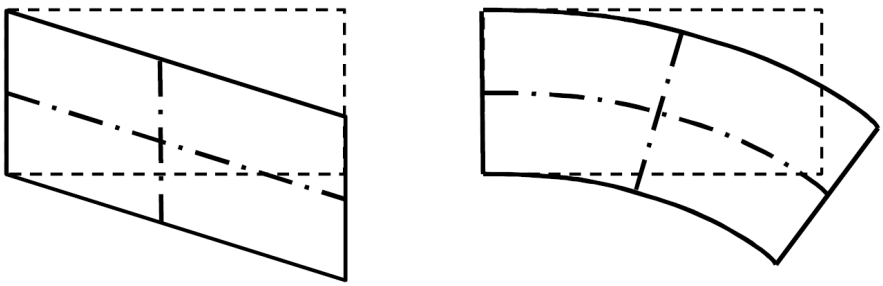

Figure 4.3: Shear (left) versus bending (right) deformation

For a cantilever with an end load and a rectangular cross section, with beam thickness h and span L it can be shown that the ratio of shear deflection to bending defection is roughly $\left(\frac{h}{L}\right)^2$, (Ugural and Fenster, 1995). For $L/h = 10$ the ratio is only 1% and even for $L/h = 5$ it is still limited to 4%. For plate deformation the ratio also scales with $\left(\frac{h}{L}\right)^2$, but the proportionality constant is roughly an order of magnitude higher as shown by numerical experiments by Zienkiewicz and Taylor (2005) (4.6 for square simply supported and 18 for square clamped plate). Thin plate theory is therefore considered accurate or $L/h > 100$ and thick plate theory seems to be the correct choice when the span to thickness ratio is $O(L/h) = 10$. The span to thickness ratio for the annular section in the diaphragm is $\Delta r/h \approx 30$, indicating that thin plate theory could give reasonable answers but the accuracy might by limited.

As beam and plate theory is derived for straight and flat beams and plates respectively, it can also be questioned whether the curvature of the shell is important to consider. As the curvature is mainly in the radial direction of the diaphragm, at least in its undeformed shape, a 1 dimensional evaluation based on beam theory is used to evaluate its effect. Analysis of curved beams described by Ugural and Fenster (1995) shows that, although plane sections remain plane during bending of curved beams, the stress and strain distribution along the height of the beam significantly differs from the linear one found in straight beams, roughly 10% for a radius of curvature to thickness ratio of $R/h = 4$. However, by using energy considerations it is shown that the deflection is not much different such that deformation analysis using straight beam theory is considered accurate for curved beams with a radius of curvature to thickness ratio of $R/h > 2$. The radius of curvature to thickness ratios in the diaphragm are larger than 3, hence a representation of the diaphragm by a shell consisting of an assembly of flat plate elements seems reasonable for determining the deformed shape of the diaphragm. However, care should be taken when evaluating stress and strain levels at the outer fibres.

When deriving constitutive equations for plates and shells, the kinematic constraints for plate and shell deformation need to be inserted in the constitutive models of the

continuum. A selection of the appropriate constitutive model for the continuum needs to be made first. In section 4.1 3 constitutive models for describing elastic behaviour of a continuum were presented; the linear elastic model for small strains and deformation following Hooke's law in 3D, and the hyper-elastic Neo-Hookean and Mooney-Rivlin model. When observing tensile test data for elastomer materials one could rapidly conclude that the material behaviour is strongly non-linear and that a non-linear material model is required. However when taking a closer look one recognizes that most of this non-linearity arises from the so-called geometric non-linearity. During a tensile test the geometry changes while the engineering stress normally reported from a tensile test normally uses the measured load divided by the cross sectional area in the undeformed reference configuration. Here 2 types of deformation are evaluated; simple extension with a load in the 1st principle direction while the other principle directions remain unloaded as present in a normal tensile test and constrained tension in which the 2nd principle direction is constrained. The latter is considered to be most representative for the bending of the diaphragm in the radial direction in which development of strains in the circumferential direction is largely constrained by the circular symmetry of the diaphragm. The deformation can be described by the principle extension ratio's, $\lambda = \frac{l}{l_0}$, which are related to the principle strain ϵ by $\epsilon = \lambda - 1 = \frac{l-l_0}{l_0}$. For simple extension $\lambda_1 = \lambda$ holds which gives $\lambda_2 = \lambda_3 = \lambda^{-1/2}$ by using the incompressibility constraint $\lambda_1\lambda_2\lambda_3 = 1$. For the constrained extension $\lambda_2 = 1$ holds which gives $\lambda_3 = 1/\lambda$ by using the incompressibility constraint. These extension ratios can be inserted in the constitutive models for obtaining relationships for the axial stress, σ_{11} as shown in Table 4.1.

Table 4.1: Cauchy stress σ_{11} for different constitutive models and deformation types, with extension ratio $\lambda = \frac{l}{l_0} = \epsilon + 1$

Constitutive model	**Simple extension**	**Constrained tension**
Hooke's law	$E(\lambda - 1)$	$\frac{E}{1-\nu^2}(\lambda - 1)$
Neo-Hookean	$G\left(\lambda^2 - \lambda^{-1}\right)$	$G\left(\lambda^2 - \lambda^{-2}\right)$
Mooney-Rivlin	$2\left(C_1 + C_2\lambda^{-1}\right)\left(\lambda^2 - \lambda^{-1}\right)$	$2\left(C_1 + C_2\right)\left(\lambda^2 - \lambda^{-2}\right)$

For evaluating the differences between the constitutive models the following relationships between the coefficients are used; $E = 3G$, $\nu = 1/2$, $G = (C_1 + C_2)/2$, which result from the requirement to give identical results with Hooke's law in the small strain limit and $C_2 = 0.25C_1$ which is given as a rule of thumb by Gent (2001). The relationships shown in Table 4.1 give the Cauchy stress which is the true stress acting on an area in the deformed configuration. Tensile test data are however often presented with the nominal or engineering stress as the dependent variable as this is the load measured during the tensile test divided by the undeformed cross sectional area. The nominal or engineering stress, P_{11}, can be obtained by dividing the Cauchy stress with the extension ratio, λ, as this is the ratio at which the cross sectional area changes during extension of an incompressible material. In Figure 4.4 the nominal stress is shown as a function of the extension ratio for the different constitutive models shown in Table 4.1. Next to the nominal stresses resulting from the different constitutive equations, the Cauchy stress

resulting from Hooke's law is shown as well which result from a linear elastic analysis in which the evaluated Cauchy stress is assumed to be present on the undeformed reference configuration which is a correct assumption only for small strains or extension ratios.

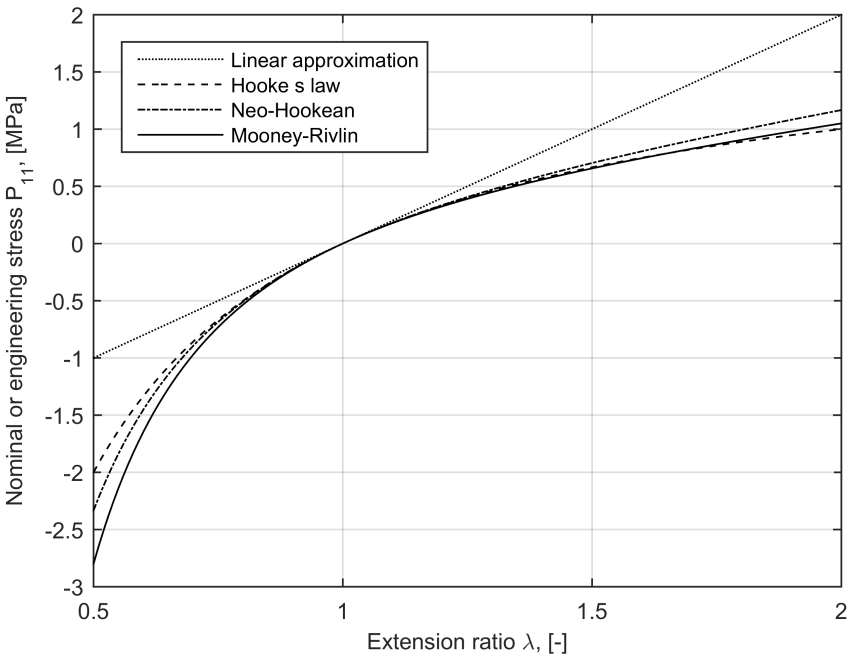

Figure 4.4: Nominal of Engineering stress $P_{11} = \sigma_{11}/\lambda$ as a function of the extension ratio $\lambda = L/L_0$ for simple extension with different constitutive models shown in Table 4.1 using $E = 2$Mpa, $\nu = 1/2$, $G = E/3 = (C_1 + C_2)/2$ and $C_2 = 0.25C_1$ showing a strongly non-linear response in a tensile test.

It is remarkable how little the 3 constitutive models differ, only the linear approximation shows larger deviations from the others at strain levels larger than 5 to 10 % but this is due to the incorrect assumption that the Cauchy stresses applies to the undeformed configuration as well. The non-linearity observed in the tensile test is therefore for the major part a result of the geometric non-linearity of the problem and to a much lessor extent a result of the non-linearity of the constitutive model. In order to explore the usability of Hooke's law the response of the Cauchy stress of the different constitutive models is evaluated for both the simple, extensional as well as the constrained tension deformation type as shown in Figure 4.5

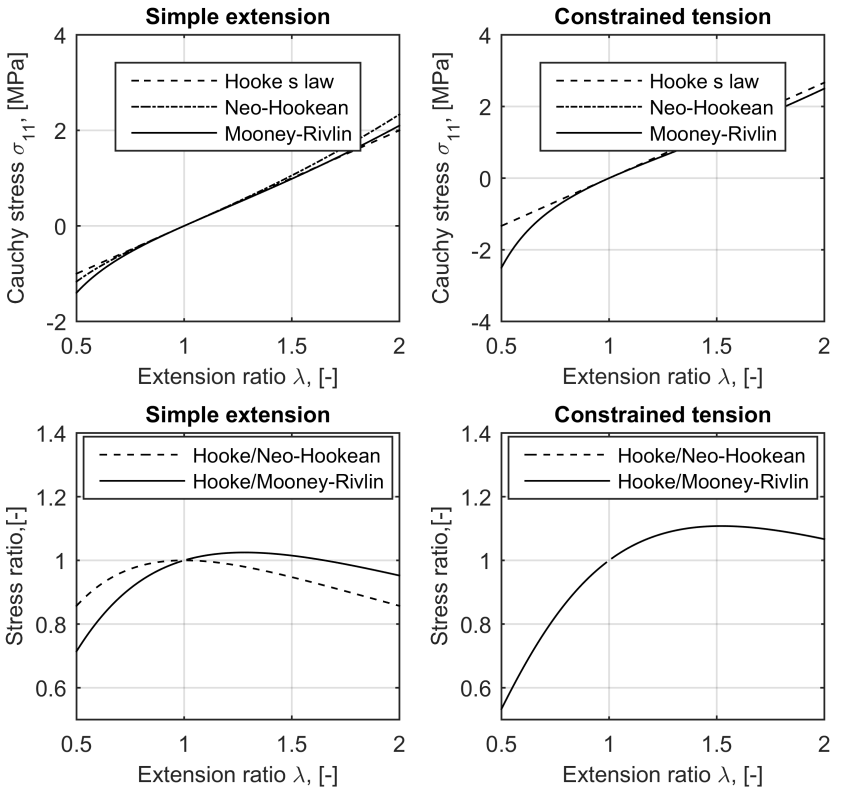

Figure 4.5: Comparison of the Cauchy stress response of the constitutive models shown in Table 4.1 for both simple extension as well as constrained tension

In the top row of Figure 4.5 one can see that the Cauchy stress response of the Neo-Hookean and Mooney-Rivlin material is much more linear than what one would expect from a tensile test curve as shown in Figure 4.4. In simple extension the deviation of the Mooney-Rivlin model is within ±5% for a strain up to 100 % in tension and 20 % in compression. For the constrained tension deformation type the deviation is limited to ±10% in this strain range. The strain in the diaphragm consists of an in-plane stretching and a bending part which are respectively called the membrane and bending strains. The membrane strains in the diaphragm are expected to be below 10 % as the diaphragm is designed with the assumption to operate with bending deformation only. In this range the deviation from Hooke's law is limited to ±5%. The maximum bending strains are expected to be in the range of 20 to 40 %, based on the experience described in chapter 3. These bending strains give a somewhat larger deviation from Hooke's law but the deviation of the stress is of opposite sign for tension and compression. The effect of this deviation on the stiffness of a plate or shell is however largely compensated when the stresses are integrated over the thickness of the diaphragm to obtain bending mo-

ments. It is therefore concluded that the use of a plate bending formulation using an infinitesimal strain constitutive model is a reasonable approximation for describing the deformation behaviour of the diaphragm up to bending strain in the range of 20 to 40 %. However it must be noted that the infinitesimal strain tensor $\boldsymbol{\epsilon}$ is not invariant for rigid body translations and rotations. This issue can be overcome by using a co-rotational formulation of the stresses and strain in the plate or shell model. The stresses and strains are then formulated in a local coordinate system which translates and rotates with the individual locations on the shell. The conservation equations then need to be evaluated in the deformed configuration in order to include the geometric non-linearity which is called an updated Lagrangian formulation.

The Kirchhoff-Love flat plate theory is applied on a flat thin plate in the xy-plane with a deflection w in z-direction as shown in Figure 6.6.

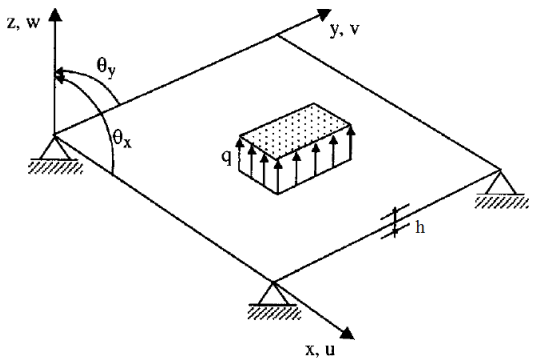

Figure 4.6: Plate model sign convention, (Oñate and Zárate, 2000), Copyright ©2000 John Wiley & Sons, Ltd, reprinted with permission.

The kinematic constraints used in the Kirchhoff-Love thin plate model are, (Ugural and Fenster, 1995):

- Deflection w of plate is small compared to its thickness h
- Straight lines normal to the mid-surface remain straight and normal during deformation
- No in-plane stretching of mid-surface
- No stress normal to mid-surface (plane stress state)

The plate model is derived by inserting these kinematic constraints into the infinitesimal strain tensor which allows the strains to be expressed as a function of second-order derivatives of the defection w of the mid-surface of the plate. The second-order derivatives of the plate deflection represent the local curvatures $\boldsymbol{\kappa}$ of the plate.This means that the strains are directly related to the local curvature of the plate. Through the use of Hooke's law, the stresses are expressed as a function of the strain and hence as a function

of the plate curvature. Bending and twisting moments **m** are obtained by integrating the moments of the stresses with respect to the mid-surface over thickness of the plate which gives the constitutive moment-curvature relationship.

The constitutive moment-curvature and curvature-deflection relationships according the Kirchhoff-Love theory for a thin flat plate as shown in Figure 6.6 are then in Voigt notation:

Constitutive equation

$$\{\mathbf{m}\} = [\mathbf{D}]\{\boldsymbol{\kappa}\} \tag{4.58}$$

Curvature deflection equation

$$\{\boldsymbol{\kappa}\} = \{\mathbf{L}\}w \tag{4.59}$$

with surface curvature $\{\boldsymbol{\kappa}\}$, deflection to curvature operator $\{\mathbf{L}\}$, moment $\{\mathbf{m}\}$ and plate rigidity $[\mathbf{D}]$ defined as:

$$\{\boldsymbol{\kappa}\} = \left[\kappa_x, \kappa_x, \kappa_{xy}\right]^T \tag{4.60}$$

$$\{\mathbf{L}\} = \left[-\frac{\partial^2}{\partial x^2}, -\frac{\partial^2}{\partial y^2}, -2\frac{\partial^2}{\partial x \partial y}\right]^T \tag{4.61}$$

$$[\mathbf{D}] = \frac{Eh^3}{12\left(1-\nu^2\right)}\begin{bmatrix} 1 & \nu & 0 \\ \nu & 1 & 0 \\ 0 & 0 & \frac{1-\nu}{2} \end{bmatrix} \tag{4.62}$$

with Elastic modulus E, Poisson's ratio ν and plate thickness h.

In chapter 6 a rotation-free Finite Element (FE) formulation of the thin plate model is presented. The allows the combination of the plate model with the Immersed Boundary Method (IBM) which can only support nodal forces related to nodal displacement and not nodal bending moments related to nodal rotations.

5

DIMENSIONAL ANALYSIS

This section describes a dimensional analysis of the Fluid Structure Interaction (FSI) problem in the piston diaphragm pump. First the effects of fluid compressibility and presence of solid particles are analysed to show the validity of an incompressible single phase fluid flow analysis for the fluid flow on a single side of the diaphragm. A scale analysis is performed on the incompressible Navier-Stokes equations before a set of dimensionless numbers is derived which includes the elasticity of the diaphragm as well. Finally field experiences will be analysed using the derived dimensionless numbers. Major parts of section 5.3 and section 5.4 have been published in van Rijswick *et al.* (2012, 2014, 2016).

5.1. EFFECT OF FLUID COMPRESSIBILITY

In this section the effect of fluid compressibility is evaluated in order to evaluate whether this needs to be included in the Fluid Structure Interaction (FSI) model. The compressibility of a fluid is defined as its relative density change at constant entropy s upon a pressure change. Often the bulk modulus K is used to quantify the fluid compressibility which is simply the inverse of the compression coefficient κ. The ratio of the bulk modulus and the density is furthermore related to the speed of sound c, (Fox and McDonald, 1998), which then gives

$$\kappa = \frac{1}{K} = -\frac{1}{\rho}\left(\frac{\partial \rho}{\partial p}\right)_s = \frac{1}{\rho c^2} \tag{5.1}$$

Inclusion of fluid compressibility in a fluid flow analysis is generally considered important in the following situations:

1. Compression of fluid such that significant density changes occur which need to be considered in the momentum equations
2. Time scales of the fluid flow are shorter than the propagation time of pressure and flow perturbations through the fluid domain with the speed of sound such that wave propagation needs to be considered

3. Compression of fluid such that volumetric flow rates and total transported volumes are significantly influenced

Significant density changes normally only occur in gas flows and can be a result of either pressure or temperature increases by external sources or a result of the flow itself. The latter is of importance when the flow velocity v is near or above the speed of sound a. A rule of thumb is that incompressible flow can be assumed when the flow velocity is less than 30% of the speed of sound, or indicated by a Mach-Number: $\text{Ma} = \frac{v}{c} < 0.3$, (Fox and McDonald, 1998). This condition obviously holds in the piston diaphragm pump where the velocities are of $O(v) = 1\,\text{m/s}$ and the speed of sound is of $O(c) = 10^3\,\text{m/s}$.

The time scales in the fluid flow within the pump chamber can be of a significant wide range. The primary time scale is obviously the stroke period of the pump cycle which is of $O(t_{\text{pump}}) = 1\,\text{s}$. But the most significant pressure oscillations which occur upon the delayed valve opening are of $O(t_{\text{pulsation}}) = 10^{-1} - 10^{-2}\,\text{s}$ for a pump with a chamber dimension of $O(L_{\text{chamber}}) = 1\,\text{m}$ as discussed in chapter 2. The pressure wave transit time in the pump chamber is of $O(t_{\text{wave}}) = O(L_{\text{chamber}}/c) = 10^{-3}\,\text{s}$ which is 1 to 2 orders of magnitude shorter. Therefore wave propagation seems to be unimportant for the flow analysis within the pump chamber when considering the most significant pressure pulsations up to 100 Hz.

The volumetric compression which occurs in the compression phase of the pump cycle when the fluid is compressed from the suction to the discharge pressure might be of greater importance. During the compression phase the entire chamber volume, which is the stroke volume plus a dead volume consisting of both propelling fluid as well as pumped slurry, has to be compressed from the suction pressure to the discharge pressure as discussed in chapter 2. In a piston diaphragm pump the dead volume is typically 4 to 8 times the stroke volume. With a discharge pressure in the range of 2.5 to 25 MPa and an effective bulk modulus of 1.5 GPa, a compression volume in the range of 1 to 13% of the stroke volume results. This means that some amount of the stroke volume, and hence diaphragm displacement volume, is lost in liquid compression. Inclusion of fluid compressibility in the FSI model is considered of lessor importance as it does not introduce any additional loads on the diaphragm as the pressure variation due to fluid compressibility is considered to be uniform within the pump chamber. The time scale of the pressure variations for which fluid compressibility is of importance is much longer than the wave propagation time in the chamber which results in a uniform pressure variation. Only the diaphragm displacement will be somewhat lower compared to the piston displacement. The loss in diaphragm displacement is roughly half the total compression loss in the pump chamber as both propelling fluid as well as pumped fluid are compressed, limiting it to only a few % in most situations, especially in the experimental set-up for validation which operates at low pressure.

5.2. EFFECT OF SOLID PARTICLES

The analysis described so far considered a single phase fluid. In this section the effect of the solid particles in the slurry is evaluated. A slurry is a 2 phase mixture consisting of a liquid with suspended solid particles in it. The first effect of the presence of the particles is the change of the mixture density compared to the liquid density. The mixture density

ρ_m can calculated from the density of the liquid ρ_l and the solid particles ρ_s using either a volumetric $C_v = \frac{V_s}{V_m}$ or mass concentration $C_m = \frac{m_s}{m_m}$ of solids, (Wilson *et al.*, 2006):

$$\rho_m = \frac{m_m}{V_m} = \rho_l + C_v(\rho_s - \rho_l) = \rho_l + \frac{\rho_l C_m(\rho_s - \rho_l)}{\rho_s - C_m(\rho_s - \rho_l)} \tag{5.2}$$

Solid particles tend to settle out from the fluid due to gravity as their density is normally higher than that of the suspending liquid. When a particle is settling, it reaches a terminal settling velocity resulting from a force equilibrium between the submerged weight of the particle and the drag forces acting on the particle. A slurry can be classified based on its settling behaviour, (Cooke and Paterson, 2008).

Non settling slurries. Slurries consisting of particles with a terminal settling velocity less than 0.1 mm/s ($d < 10\,\mu$m for sand density particles in water). The particles are than kept in suspension by Brownian motion. These very fine silt and clay particles can alter the rheology of the mixture significantly and can significantly increase the viscosity, even at low concentrations, and can generate non-Newtonian behaviour as well.

Slow settling slurries. Slurries consisting of particles with terminal settling velocity between 0.1 and 1 mm/s ($10\,\mu$m $< d < 32\,\mu$m for sand density particles in water). Particles are not sufficiently suspended by Brownian motion and require some turbulence to stay in suspension. In quiescent conditions particles settle out slowly.

Settling slurries. Slurries consisting of particles with a terminal settling velocities larger than 1 mm/s ($d > 32\,\mu$m for sand density particles in water). Particles need sufficient turbulence to stay in suspension and will rapidly settle out in quiescent conditions. In horizontal transport in a pipe a concentration gradient tends to form which increases towards the bottom of the pipe.

Mixed regime slurries. Slurries having a wider particle size distribution consisting of particles from a combination of the above categories. The finer particles in the mixture form a carrier fluid or vehicle in which the coarser particles are suspended. The carrier fluid can have an increased viscosity with possibly non-Newtonian rheology.

Most of the slurries handled by piston diaphragm pumps in the mining and mineral processing industries are of non or slow settling behaviour or are of the mixed regime type with a significant portion of fine particles resulting in a viscous, sometimes non-Newtonian, carrier fluid. But even for settling slurries with particle sizes limited to a few $100\,\mu$m as encountered by piston diaphragm pumps, the settling behaviour is of limited importance. The transport direction in the pump chamber is predominantly vertical which means that settling is less important when the terminal settling velocity is significantly below the vertical transport velocity and when the total settling time through the pump chamber is much smaller the period of the pump cycle. The first condition results in minor in-situ density changes due to the limited slip velocity between the particles and the liquid. The second condition makes sure that no significant particle settling

occurs in the low flow periods of around the stroke reversal points. The vertical transport velocities in the pump chamber are of $O(v) = 1\,\mathrm{m/s}$ and a typical stroke period is of $O(T_{\mathrm{pump}}) = 1\,\mathrm{s}$ for a pump chamber with a vertical dimension of $O(h_{\mathrm{chamber}}) = 1\,\mathrm{m}$. Both conditions indicate that a homogeneous fluid approximation is valid when the terminal settling velocity is $\ll 1\,\mathrm{m/s}$, let say $< 10\,\mathrm{mm/s}$, which corresponds to approximately 100 µm sand in water. Settling seems therefore only important when considering medium to coarse sand slurries without a viscous carrier fluid. From the brief analysis described above it is concluded that an homogeneous mixture approach seems valid for the diaphragm deformation analyses. The effect of solids can then included by using the mixture density and a homogeneous mixture rheology.

5.3. DERIVATION OF DIMENSIONLESS NUMBERS

The following assumptions are made for the dimension analysis analysis of the FSI problem in this study:

- Diaphragm and its housing scale geometrically uniform resulting in geometrically similar designs
- Incompressible flow on both sides of diaphragm
- Slurry can be modelled as a homogeneous mixture with Newtonian rheology
- Incompressible Neo-Hookean constitutive model can be applied for diaphragm
- Inertia of diaphragm, cone plate and monitoring rod can be neglected

In order to describe the diaphragm deformation problem, 9 independent parameters are then required which are shown in Table 5.1. The first parameter is the diaphragm diameter D. This is the only geometric dimension used in the analysis which assumes geometrically similar diaphragm and pump chamber designs. This scaling rule has been strictly applied in the design of different diaphragm sizes, but not in all housing designs, for which a correction has to be applied as will be shown later. The second parameter is the volumetric displacement of the piston or stroke volume V_S. This is a free parameter as the stroke volume is normally adjusted by changing the piston diameter in order to fit the stroke volume within the application dependent allowable stroke volume of a given diaphragm size but also to tune the piston rod load acting within the power end. The third parameter is the pump stroke rate f. Incompressible fluid flow with Newtonian rheology is assumed to be present on both sides of the diaphragm which gives 4 more fluid parameters being density and dynamic viscosity of the propelling fluid, ρ_1 and μ_1, and of the pumped fluid, ρ_2 and μ_2. The diaphragm compliance is next to its size D described by a single linear elastic modulus E, which holds as long as incompressible neo-Hookean material behaviour is assumed. Note that very large non-linear deformations can still be modelled with a single elastic modulus in a neo-Hookean material model, as long as the strain levels are relatively low, <40 %, (Gent, 2001). This is considered a valid assumption for the strain levels in a pump diaphragm. The deformation behaviour is then geometrically non-linear but the material behaviour itself might still be linear. As the propelling fluid and the pumped slurry can have significantly different densities,

differences in hydrostatic pressure on both sides of the diaphragm are to be included as well, which requires a gravitational acceleration g as the 9th and last parameter.

Table 5.1: Independent parameters which define diaphragm loading and deformation

Parameter	Symbol	Unit
Diaphragm diameter	D	m
Pump frequency	f	s^{-1}
Pump stroke volume	V_S	m^3
Density propelling fluid	ρ_1	kg/m^3
Dynamic viscosity propelling fluid	μ_1	Pa s
Density pumped fluid	ρ_2	kg/m^3
Dynamic viscosity pumped fluid	μ_2	Pa s
Elastic modulus diaphragm	E	Pa
Gravitational acceleration	g	m/s^2

The dimension and scale analysis described further in this section is built up in steps for simplifying the understanding of the physical phenomena present. An initial step is the analysis of a single fluid domain while assuming a prescribed diaphragm deformation. Then only the first 5 parameters remain. The fluid flow on one side of the diaphragm can then be described by the Navier-Stokes equation and continuity equation for incompressible Newtonian fluid flow as derived in section 4.1, which in non-conservation form are

$$\underbrace{\rho\frac{\partial \mathbf{v}}{\partial t}}_{\text{Unsteady acceleration}} + \underbrace{\rho\mathbf{v}\cdot\nabla\mathbf{v}}_{\text{Convective acceleration}} = \underbrace{-\nabla p}_{\text{Pressure gradient}} + \underbrace{\mu\nabla^2\mathbf{v}}_{\text{Viscous friction}} + \underbrace{\mathbf{b}}_{\text{Body forces}} \tag{5.3}$$

$$\underbrace{\nabla\cdot\mathbf{v}=0}_{\text{Incompressibility constraint}} \tag{5.4}$$

As indicated in Equation 5.3, the different terms describe different phenomena in the fluid flow. The body force term **b**, is used to include a gravitational effect and/or the presence of immersed boundaries in a numerical model as described in the chapter 6. However the body force is not required when analysing the fluid flow on a single side of the diaphragm while assuming a prescribed motion of the diaphragm. By using proper scaling parameters for the fluid domain dimensions (D), the fluid flow velocity (v_{ref}), the fluid flow time scale ($\frac{1}{f}$) and the pressure (ρv_{ref}^2), a dimensionless form of Equation 5.3 and Equation 5.4 can be derived as shown by Fox and McDonald (1998).

$$St\frac{\partial \mathbf{v}^*}{\partial t} + \mathbf{v}^*\cdot\nabla\mathbf{v}^* = -\nabla p^* + \frac{1}{Re}\nabla^2\mathbf{v}^* \tag{5.5}$$

$$\nabla \cdot \mathbf{v}^* = 0 \tag{5.6}$$

with $\mathbf{v}^* = \frac{\mathbf{v}}{v_{\text{ref}}}$ and $p^* = \frac{p}{\rho v_{\text{ref}}^2}$. Furthermore, two dimensionless numbers appear in Equation 5.5; the Strouhal number, St and the Reynolds number, Re. The Strouhal number and Reynolds number represent the ratio of respectively the unsteady acceleration forces and the viscous fluid forces with respect to the convective acceleration forces in the fluid flow and are defined by Equation 5.7, 5.8 and 5.9:

$$v_{\text{ref}} = \frac{f \cdot V_S}{D^2} \tag{5.7}$$

$$St = \frac{f \cdot D}{v_{\text{ref}}} = \frac{D^3}{V_S} \tag{5.8}$$

$$Re = \frac{\rho \cdot v_{\text{ref}} \cdot D}{\mu} = \frac{\rho \cdot f \cdot V_S}{\mu \cdot D} \tag{5.9}$$

5

These two dimensionless numbers define the relative importance of the individual terms in the Navier-Stokes equation. An order of magnitude analysis with $O(D) = 10^0\,\text{m}$, $O(V_S) = 10^{-1}\,\text{m}^3$, $O(f) = 10^0\,\text{s}^{-1}$, $O(\rho) = 10^3\,\text{kg/m}^3$, $O(\mu) = 10^{-3}\,\text{Pa s}$ gives $O(v_{\text{ref}}) = 10^{-1}\,\text{m/s}$, $O(St) = 10^1$ and $O(Re) = 10^7$. It should be noted that these estimates are very coarse order of magnitude estimates. For example the velocity order of magnitude is estimated to be 0.1 m/s while nominal velocities in the inlet and outlet ports can be $\gg 0.1$ m/s which would be obtained when taking a proportionality of the dimension of the effective flow area of 0.2 to 0.3 times the diaphragm diameter. This would roughly lower the Strouhal number with an order of magnitude to $O(St) = 10^0$ and increase the Reynolds number with and order of magnitude to $O(Re) = 10^8$ (note: acceleration length does not include the aforementioned proportionality factor). This indicates that both the unsteady as well as the convective acceleration are important to consider and that viscous effects might be of lower importance. However, in the definition of the Reynolds number, a shear rate of $O(\dot{\gamma}) = O(\frac{v_{\text{ref}}}{D})$ is assumed which assumes a distance across which the fluid is sheared equal to the size of the diaphragm D. This might be a valid approximation in a laminar flow condition, but in turbulent flow condition much smaller shear distances are present in the turbulent boundary layers resulting in much higher shear rates and hence higher shear stresses due to viscous shearing of the fluid. The viscous friction term in Equation 5.3 is equal to the divergence of the deviatoric stress tensor $\boldsymbol{\tau}$.

$$\mu \nabla^2 \mathbf{v} = \nabla \cdot \boldsymbol{\tau} \tag{5.10}$$

By scaling the stress tensor with ρv_{ref}^2, the viscous term in Equation 5.5 becomes

$$\frac{1}{Re} \nabla^2 \mathbf{v}^* = \nabla \cdot \boldsymbol{\tau}^* \tag{5.11}$$

with

$$\boldsymbol{\tau}^* = \frac{\boldsymbol{\tau}}{\rho v_{\text{ref}}^2} \tag{5.12}$$

The latter is similar to the definition of the skin friction coefficient which relates the wall shear stress τ_w to the dynamic pressure of the bulk flow velocity $\overline{V}$ according

$$C_f = \frac{\tau_w}{\frac{1}{2}\rho\overline{V}^2} \tag{5.13}$$

The skin friction coefficient C_f is equal to 1/4 of the Darcy-Weisbach friction coefficient f_D which is used for calculating friction losses in turbulent pipe flow. The order of magnitude of the dimensionless stress tensors is equal to the order of the skin friction coefficient or friction factor as the order of the magnitude of the shear stress tensor is equal to the wall shear stress. Typical levels for the friction factor indicate a wall shear stress which is 2 orders of magnitude lower than the dynamic pressure as discussed in section 4.2. This indicates a lower relevance of the turbulent stresses on the fluid loads acting on the diaphragm. In laminar flow of viscous Bingham type fluids, the order of the magnitude of the shear stress tensor will be equal to the order of the Bingham yield stress. Only when considering very viscous, paste type, slurries, with yield stresses of $O(\tau_y) = 10^2 - 10^3$ Pa, (Cooke, 2006), shear stress levels in the order of the acceleration pressures, $O(p_{\text{unsteady}}) = O(\rho \cdot D \cdot \nu \cdot f) = 1000\,\text{Pa}$ and $O(p_{\text{convective}}) = O(\rho \cdot \nu^2) = 1000\,\text{Pa}$ can be reached. Fluid loads need to be of this order to have a significant influence on the diaphragm deformation as the uniform pressure required to deform the diaphragm is of this order as well as shown by structure-only FEA's discussed in chapter 3. Therefore viscous losses seem only important to consider when considering paste type slurries. An further interesting result is that the Strouhal number is not dependent on the pump stroke rate f as both the unsteady acceleration as well as the convective acceleration scale similar to the pump stroke rate. The Strouhal number indicates the ratio of diaphragm volume to the stroke volume, which implies that the inverse of the Strouhal number represents the static loading of the diaphragm by the piston displacement.

A next step in the analysis of the FSI problem is to include the 2$^{\text{nd}}$ fluid domain and the diaphragm in the analysis. For clarity, viscous effects are neglected and the same fluid is initially assumed to be present on both sides of the diaphragm. With these assumptions, the viscosity and gravitational acceleration can be excluded and only 5 parameters result. According to the Buckingham Π theorem, (Buckingham, 1914), a physical problem is fully defined by $k = m - n$ independent dimensionless numbers, when the problem is defined by m basic physical parameters which can be built up from n basic physical quantities. In this system, the 3 basic physical quantities; linear dimension, mass and time, are relevant. These give, together with the 5 physical parameters, $5 - 3 = 2$ independent dimensionless numbers. The following dimensionless numbers are introduced which result by selecting the stroke rate and stroke volume as independent parameters within the 2 dimensionless numbers:

Dimensionless stroke volume:

$$V_S^* = \frac{V_S}{D^3} \tag{5.14}$$

Dimensionless stroke rate:

$$f^* = f \cdot D \cdot \sqrt{\frac{\rho_1}{E}} \tag{5.15}$$

When fluids with different density are used on both sides of the diaphragm, two additional parameters become important to consider: the density of the second fluid and the gravitational acceleration. These two parameters are included in two additional dimensionless numbers:

Dimensionless hydrostatic pressure:

$$p_g^* = \frac{\rho_1 \cdot g \cdot D}{E} \tag{5.16}$$

Density ratio:

$$R_\rho = \frac{\rho_2}{\rho_1} \tag{5.17}$$

As viscous effects were considered to be of lower importance, viscosity has been excluded but would otherwise require 2 more dimensionless numbers, for example 2 Reynolds numbers for the fluid flow on each side of the diaphragm. Then 6 dimensionless numbers are defined for describing the FSI problem with the 9 parameters shown in Table 1.

5.4. EVALUATION OF FIELD EXPERIENCE

In the last 4 decades vast experience has been gained by WEIR Minerals Netherlands with the operation of GEHO® piston diaphragm pumps in different slurry applications and with different pumps sizes under different operating conditions. Although most field experiences were positive in the sense that no issues with reduced diaphragm life were present, some experiences showed issues with reduced diaphragm life. In this section this field experience is evaluated using a dimensionless representation of the field experience data using the dimensionless numbers derived in section 5.3. The stroke volume naturally seems to be the most important driver in the diaphragm deformation as the volumetric displacement of the diaphragm is equal to the volumetric piston displacement. This is purely static loading. Field experience has further shown that the stroke rate has an influence on the diaphragm deformation as well, which can be explained by the unsteady and convective acceleration loads within the fluid flow. The first step in evaluation of the field experience is therefore to plot all the field experience data in a stroke volume versus stroke rate plot as shown in Figure 5.1.

Note: all the field experience data presented in this study are based on experience with GEHO® piston diaphragm pumps and all data have been normalized with an arbitrary value for confidentiality reasons.

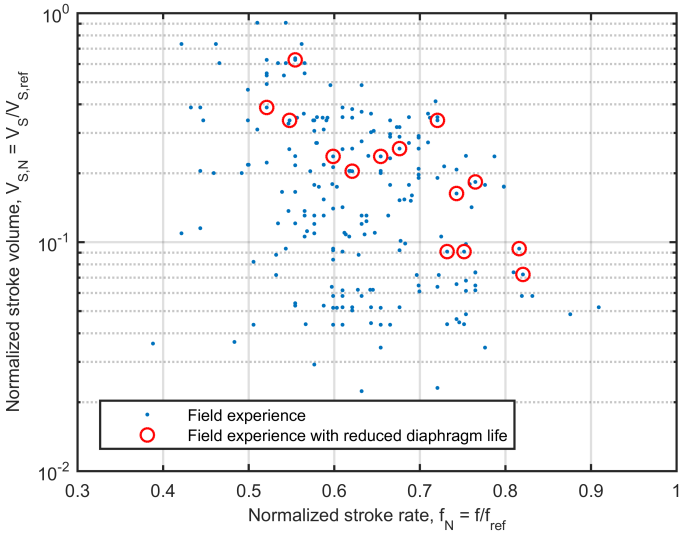

Figure 5.1: Normalised diaphragm field experience data. Note that the normalization procedure only scales the axis to unity which is done for confidentiality reasons.

The stroke volume range spans almost 2 orders of magnitude while the stroke rate range spans only a factor 2. This is a result of the traditional approach of selecting piston diaphragm pumps in the mining and mineral processing industry at a relatively low and fixed stroke rate in order to maximize the wear life of the self-acting valves within the pump. When these experiences are to be evaluated, some scaling is required for which the dimensional analysis described in section 5.3 has been used. Based on this analysis, 4 primary diaphragm loading mechanisms can be distinguished:

1. Static volumetric displacement by stroke volume,
2. Fluid momentum loading by unsteady and convective acceleration of fluid flow
3. Hydrostatic loading by density differences between propelling fluid and pumped slurry
4. Viscous fluid forces

The dimensional analysis has shown that 6 independent dimensionless numbers are required for a full description of the problem (i.e. includes 2 different fluids). This is a too large number for evaluation of the field experiences as no quantitative information is known on the individual diaphragm deformation. Only a binary evaluation on reported limited diaphragm life is possible. Therefore some reduction in parameters is required. Dimensional analysis has shown that the viscous fluid forces do not seem to be important in the total loading of the diaphragm for most non-paste like slurries. This allows the omission of the Reynolds numbers for the two fluid domains. What remains,

however, are 4 dimensionless numbers for describing the first 3 basic mechanisms mentioned above. This is the result of 2 different densities which can principally scale the acceleration and hydrostatic pressures on both sides of the diaphragm independently from each other. A further approximation is possible by assuming a single density in the fluid acceleration and only a density difference in the hydrostatic pressure, similar as is done in the Boussinesq approximation, (Fox and McDonald, 1998). In the Boussinesq approximation a mean density is used in the unsteady and convective acceleration terms of the Navier-Stokes equations while a density deviation from that mean density is used in the hydrostatic pressure calculation within the body force term. This is normally only valid when the density difference is small compared to the mean density. In this case the density difference can be of the same magnitude as the mean density, when using for example $\rho_1 = 900\,\mathrm{kg/m^3}$ for a mineral oil as propelling fluid and $\rho_2 = 2300\,\mathrm{kg/m^3}$ for an iron ore concentrate slurry. Nonetheless, the use of a single reference density in combination with a density difference still seems a reasonable approximation. The density of the slurry has been selected as the reference density because it is anticipated, based on field experience, that the fluid acceleration loads on the slurry side are most dominant. The following similar but slightly different dimensionless numbers, indicated by **, as presented before then result:

Dimensionless stroke volume

$$V_S^* = \frac{V_S}{D^3} \tag{5.18}$$

Alternative dimensionless stroke rate

$$f^{**} = f \cdot D \cdot \sqrt{\frac{\rho_{\mathrm{ref}}}{E}} \tag{5.19}$$

Alternative dimensionless hydrostatic pressure

$$p_g^{**} = \frac{\Delta\rho \cdot g \cdot D}{E} \tag{5.20}$$

with

$$\rho_{\mathrm{ref}} = \rho_2 \tag{5.21}$$

and

$$\Delta\rho = \rho_2 - \rho_1 \tag{5.22}$$

This definition of the dimensionless stroke rate and dimensionless hydrostatic pressure differs only in the used densities, respectively ρ_{ref} and $\Delta\rho$ instead of ρ_1, which is indicated by subscripted ** in the definition of f^{**} and p_g^{**}. A next step in the evaluation is to plot the field experience data as a function of the dimensionless numbers. In Figure 5.2 the data are plotted as a function of normalized dimensionless stroke rate and the normalized dimensionless stroke volume which are considered the primary drivers in the diaphragm deformation.

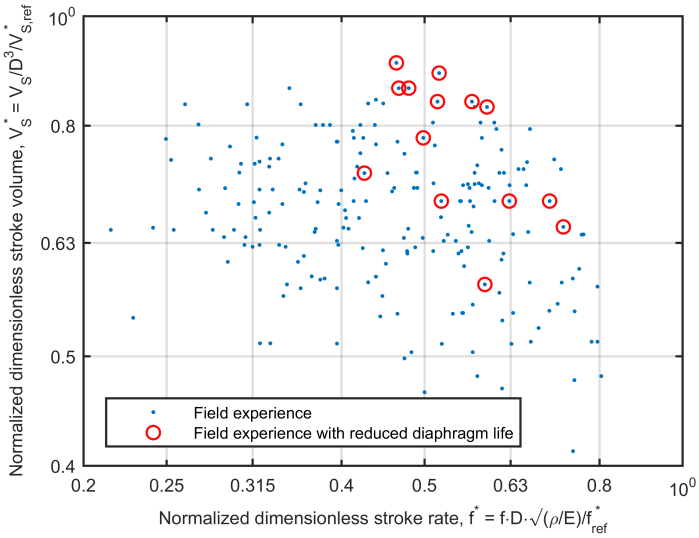

Figure 5.2: Normalised dimensionless diaphragm field experience data

This scaling step makes it possible to compare the field experience data of different diaphragm sizes in different operating conditions. However, the reported projects with diaphragm life issues are still relatively distributed within the plotted field of experiences. From the dimensional analysis it can be seen that the dimensionless hydrostatic pressure has not been used in the analysis of the field experiences so far. Furthermore the presented dimensional analysis only included a single geometric dimension D. When analysing the field experiences data it turned out that strict geometric uniform scaling had not been applied for all diaphragm housing designs in the past. As the loading by the unsteady and convective fluid acceleration scales with the fluid velocity, an effective flow area within the diaphragm housing A_{eff} has been estimated which gives an additional dimensionless number:

$$A^* = \frac{A_{\text{eff}}}{D^2} \tag{5.23}$$

In analysing the field experience data it was possible to derive 2 additional dimensionless correction factors for the dimensionless stroke and flow rate. The first is a function of the dimensionless hydrostatic pressure p_g^{**} and the second a function of the dimensionless flow area A^*. The functional relationship used in calculating the correction factors is not mentioned here for confidentiality reasons, hence only the general relationship is given:

$$K_A = f\left(A^*\right) \tag{5.24}$$

$$K_g = f\left(p_g^{**}\right) \tag{5.25}$$

The hydrostatic correction factor is used for correcting the dimensionless stroke volume as both are static diaphragm loads. The flow area correction factor is used for correcting the dimensionless stroke rate as both are dynamic diaphragm loads. When applying both correction factors, the field experience data can be plot again, now as a function of the corrected normalized dimensionless stroke rate and volume as can be seen in Figure 5.3.

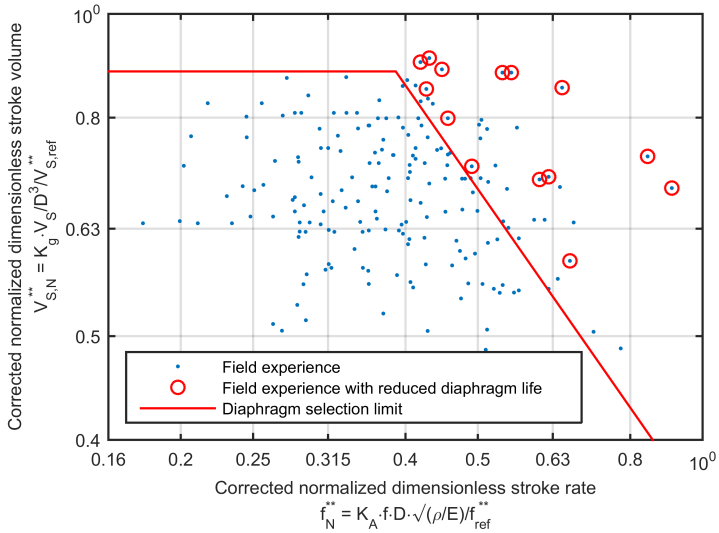

Figure 5.3: Corrected normalised dimensionless diaphragm field experience data

In Figure 5.3 one can see that by applying these corrections, the field experience data with reduced diaphragm life move to the boundary area of the operating envelope. This enables the derivation of a diaphragm selection limit by simply drawing an envelope curve around the field field experience data without reported diaphragm life issues. The selection limits basically consists of a limit on dimensionless stroke volume and a limit on the so-called dimensionless flow rate which is the product of the dimensionless stroke rate and stroke volume. The first is a horizontal line and the second a line with a -1 slope in a log-log plot of dimensionless stroke volume versus dimensionless stroke rate. It is noted that most of the reported diaphragm issues come from operations with pumps that were supplied in the 90's when the piston diaphragm pump technology was pushed forward for application within in the mining and mineral processing industries. Optimization of effective flow area within the diaphragm housings has eliminated these diaphragm fatigue failures since. Only after gaining valuable field experience, both good and bad, a robust diaphragm selection procedure can be derived. This requires a proper dimensional analysis for the appropriate scaling of all influencing factors. Therefore, selection of piston diaphragm pumps without having a database of field data, or selection pump operation outside the proven operating envelope is considered to be very risky. A specific piston diaphragm pump selection for a specific application can only be

considered reliable, from a diaphragm life point of view, when it is selected within the dimensionless experience envelope of the manufacturer. Such evaluation is therefore important for both the manufacturer as well as the operator. Operators and engineering companies should therefore challenge the pump manufacturers to show how their equipment falls within their experience envelope or what has been done to safely move outside their experience envelope.

6

NUMERICAL MODEL

6.1. APPROACH

In this chapter the development of a numerical Fluid Structure Interaction (FSI) model is described which is used to model the diaphragm deformation in a piston diaphragm pump. The numerical model is based on the theory and mathematical modelling as presented in chapter 4. In this section the basic requirements of the model are presented and an overview is given of different potential numerical approaches before describing the approach followed in developing the numerical model in this study.

6.1.1. BASIC REQUIREMENTS

The basic requirements for the model based on the analysis in previous chapters is as follows:

- A transient flow solver is required as the flow field is significantly unsteady as indicated by Strouhal number in dimensional analysis
- Flow solver should include 2 fluid domains, one for the propelling fluid and one for the pumped fluid
- In each fluid domain an incompressible single phase fluid flow needs to be described with individual fluid properties in each domain
- Model should include a structural model describing the deformation of the diaphragm
- Model should be able to model a non-rectangular 3D fluid domain within pump chamber
- Model should be able to handle 2-way interaction between each of the individual fluid domains and the structural model of the diaphragm

- Model should be able to handle large displacements of the diaphragm which are in the order of the fluid domain dimensions

Aspects which would be nice to have but are not considered absolutely necessary are:

- Accurate modelling of turbulence is considered of lessor importance as the forces due to turbulent stresses are of much lower magnitude than the forces due to fluid momentum and hydrostatic pressure differences between propelling fluid and pumped fluid.
- Inclusion of fluid compressibility is considered of lessor importance as it does not introduce any additional loads on the diaphragm as the pressure variation due to fluid compressibility can be considered to be uniform within the pump chamber as discussed in chapter 5.

6.1.2. OVERVIEW NUMERICAL APPROACHES

In this section a basic description of some general numerical approaches is given. This to give a reader who is not an expert in numerical analysis some background such that the approach followed in developing the FSI model can be followed.

LAGRANGIAN VERSUS EULERIAN FORMULATION

The FSI model requires the solution to a set of conservation equations which describe the fluid flow and the structural deformation. These equation are derived by applying principles of conservation of momentum, conservation of mass and using constitutive relations describing the relationship between the deformation and/or deformation rates and the internal stresses in the fluid and the structure. In the modelling of fluid flow and structural deformation, two basic mathematical formulations are generally used; the Lagrangian and the Eulerian formulation. The Lagrangian formulation uses a moving frame of reference which moves with the matter being modelled, while in the Eulerian formulation a fixed frame of reference is used through which the matter being modelled „flows". The Lagrangian approach is most suited for modelling of structural deformation while the Eulerian approach is most suited for modelling fluid flows.

STRUCTURED VERSUS UNSTRUCTURED GRIDS

The resulting model is a set of differential or integral equations which need to be discretized on a computational mesh or grid in order to be solved numerically. The vale of the dependent variables are only solved at discrete points in space which are called computational nodes or points. The computational grid can be structured or unstructured. Structured grids are based on a rectangular spatial domain which is subdivided in rectangular blocks or cells which can be deformed to fit the required computational domain. When the computational cells remain rectangular, and the grid lines remain orthogonal with respect to each other, the grid is called an orthogonal grid. When the grid spacing is constant in each dimension the grid is called a regular grid, when the grid spacing is equal in all spatial dimensions, the grid is called a Cartesian grid. In an unstructured grid, the computational domain is subdivided in a number of computational

cells which can be of arbitrary shape, e.g. quadrilaterals or triangles in 2D and hexahedron or tetrahedrons in 3D. The difference between structured and unstructured grids is shown in Figure 6.1.

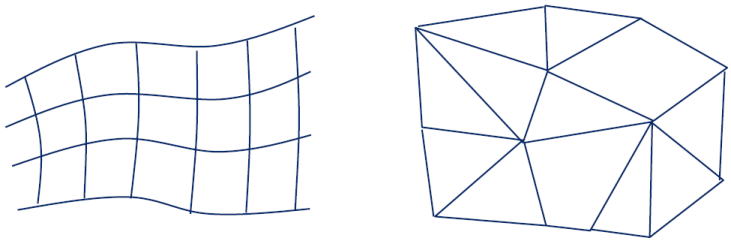

Figure 6.1: Structured versus unstructured grid

A structured grid is based on orthogonal lines running through the computational domain. The intersection of these grid lines are called vertices and the volumes that are defined by the grid lines are called computational cells. The computational nodes or points at which the dependent variables are calculated can either be vertex or cell-centred.

SPATIAL DISCRETIZATION METHODS

The following 3 different methods are commonly used for the spatial discretization of the differential and/or integral model equations:

Finite Difference (FD) method. See for example Heath (1997). This method uses the governing equations in differential form and uses finite differences to approximate the differential operators. Drawback of this method is that it can only be applied on structured grids and is not necessary conservative.

Finite Volume (FV) method. See for example Versteegh and Malalasekera (2007). This method uses the governing equations in integral form which are applied to discrete volumes in the computational grid. The rate of change of the conserved property is to be balanced by fluxes entering the control and internal sources and sinks. The method is rather intuitive as it is based on a control volume approach which is very common in engineering practice, especially when considering fluid flow. Strict conservation of the conserved property results as the fluxes leaving one cell enter a neighbouring cell. The finite volume method can furthermore be used on both structured as well as unstructured grids.

Finite Element (FE) method. See for example Zienkiewicz *et al.* (2005a). In this method the geometry is divided into elements in which the governing equations are evaluated. The elements have computational nodes, typically at the vertices of the elements and sometimes on edges and the interior of the elements depending on the type of element and the order of interpolation function used. A variational or

so-called weak form of the governing equations is used which is derived by applying variational or energy principles such as the principle of virtual work. The discrete solution values are evaluated at the computational nodes, while the continuous solution within the element is assumed to obey a polynomial interpolation function. The polynomial solution is then inserted in the variational form of the governing equations which are then integrated over the element to end up with a discrete set of equations which are only a function of the nodal quantities. The method is mathematically a bit more complex then FD or FV methods. The method has originally been developed and applied in structural and solid mechanics but has developed since for the use in a much wider range of physics including fluid flow. The method is naturally suited for unstructured meshes and is easier to extent to higher order interpolation, as the interpolation functions only uses nodal values of nodes belonging to a single element. This in comparison with FV methods which require cell values of neighbouring cells for evaluation of the fluxes at the cell boundary.

EXPLICIT VERSUS IMPLICIT TIME INTEGRATION

In explicit time integration the solution at the next time level is stated explicitly as a function of the solution of the current and potentially previous time levels and therefore does not require the solution of a system of equations. In implicit time integration the solution can not be stated explicitly as the solution depends on the information on the new time level as well and requires the solution of a system of equations. Implicit time integration is typically unconditionally stable which means that the integration is stable for any time step value. Explicit methods are only conditionally stable and require a time step small enough to ensure a bounded solution. The time step is limited by the typical transport time of the dependent variable across a single computational cell. Explicit time integration is therefore mainly used when dynamic transport processes are to be resolved in detail.

6.1.3. BASIC APPROACH NUMERICAL FSI MODEL

As discussed, two basic mathematical formulations can be used in the modelling of fluid flow and structural deformation; the Lagrangian and the Eulerian formulation. The Lagrangian approach is most suited for modelling of structural deformation while the Eulerian approach is most suited for modelling fluid flows. In FSI problems these two approaches need to be combined. An approach which is frequently followed for FSI simulations is the so-called Arbitary-Lagrangian-Eulerian (ALE) formulation of the fluid flow, see e.g. Bungartz and Schäfer (2006), Hou *et al.* (2012). In the ALE approach the fluid flows through the computational grid of the fluid domain while the computational grid is also allowed to deform. When solving an FSI problem, the structure is modelled on a Lagrangian mesh which is coupled to an ALE fluid grid. Displacement and pressure information is then exchanged between the fluid grid and structural mesh in order to solve the 2-way coupled FSI problem.

The FSI modelling using an ALE-formulation for the fluid flow has some advantages such as the possibility to use non-uniform, unstructured body fitted grids. However, a major disadvantage is the large deformation of the fluid domain and its computational

grid when the structural displacement is large compared to the dimensions of the fluid domain. This can result in severe distortion of the computational grid, which can make the calculations unstable and can require re-meshing during the computation. In piston diaphragm pumps the diaphragm displacement is typically large compared to the pump chamber dimensions, and the maximization of the stroke volume with respect to the chamber volume is even an objective of a design optimization. The numerical model used in this study therefore follows a different approach.

The approach used here is based on the so-called Immersed Boundary Method, Mittal and Iaccarino (2005). In the immersed boundary method the fluid is modelled on a fixed Eulerian grid in which the structure is immersed. For the interaction with deformable structures, in this case the pump diaphragm, an immersed boundary method as originally developed by Peskin (1977) is used. In this method the flexible structure is modelled using a Lagrangian discretization of the structure which can be finite difference, finite volume or finite element based. The computational nodes of the structure are immersed in and advected by the fluid flow. Depending on the deformation of the structure, nodal reaction forces acting on the computational nodes can be calculated which are then supported in the fluid by body forces in the fluid flow. Representing the presence of a structure in the fluid domain by appropriately calculated fluid body forces is the key aspect of the immersed boundary method. The main advantage is that a simple Cartesian or regular grid can be used. This eliminates the need for fluid grid deformation and therefore allows structural displacements which are large compared to the fluid domain. Furthermore grid generation is trivial, grid re-generation because of large fluid domain deformation is no longer necessary and very efficient flow solvers can be used.

As the fluid flow in the pump chamber in which the FSI takes place is an internal flow, the boundaries with the pump chamber need to be included as well. One could consider using an unstructured body fitted mesh, but this would eliminate many of the described advantages of a regular mesh. One could also consider to model the pump chamber boundary as a very stiff immersed boundary using the method described above. The above described immersed boundary method uses so-called feedback forcing, Mittal and Iaccarino (2005), which means that depending on the structural deformation a force is fed back in the fluid flow. For very stiff structures this can cause instabilities in the calculation, as shown by Fadlun *et al.* (2000). For rigid immersed objects, a different immersed boundary method called direct forcing can be used, as described by Fadlun *et al.* (2000). In this method the body forces are calculated explicitly from a known velocity of the solid boundary, which eliminates the mentioned stability issues. As far as know to the author, modelling of the interaction of a pump diaphragm with 2 different fluid domains within a pump chamber using a combination of two different types of immersed boundary methods has not been described before besides in publications by the author himself as part of this study, (van Rijswick *et al.*, 2012, 2014, 2016), and is therefore considered to be a novel approach.

Next to the basic approach of modelling the presence of both the flexible diaphragm as well as the rigid pump chamber wall using an IBM, the following choices have been made:

- FV discretization on a structured rectangular grid of the Navier-Stokes equations

- FE discretization of the structural model of the diaphragm which gives nodal reaction forces based on the nodal positions of the structure which can be supported as body forces in the computational cells of the flow solver.
- Explicit time integration of Navier-Stokes equations as the transient characteristics of the flow need to be resolved which requires small a time step anyhow.

6.2. FLOW SOLVER

A flow solver is required to solve the Navier-Stokes equations on a structured rectangular or regular grid. This regular grid makes the discretization of the flow equation relatively easy compared to using an unstructured grid. This choice has allowed the author to develop the flow solver code from scratch. As an implementation platform the high level programming environment Matlab® has been used whose implementation aspects are further discussed in section 6.5. The flow solver has to handle spatially variable fluid properties because 2 fluid domains, the propelling fluid and the pumped fluid domain, are captured on a single computational domain when using the IBM. The propelling fluid and pumped fluid can have different densities, and different viscosities. The density within a single fluid domain is considered to be uniform because a homogeneous mixture approach is followed. The viscosity is also uniform within a single fluid domain when considering Newtonian rheology and omission of a turbulent eddy viscosity, but is spatially variable within a single fluid domain when non-Newtonian rheology or turbulent eddy viscosity is included in the model. As discussed, fluid compressibility is neglected which means that the following form of the incompressible Navier-Stokes equations need to be solved with spatially variable fluid properties

$$\frac{\partial}{\partial t}\left(\rho\mathbf{v}\right)+\nabla\cdot\left(\rho\mathbf{v}\mathbf{v}\right)=-\nabla p+\nabla\cdot\boldsymbol{\tau}+\mathbf{b} \tag{6.1}$$

$$\nabla\cdot\mathbf{v}=0 \tag{6.2}$$

The presence of the immersed boundary will be modelled by locally scaling the body force field **f**. The presence of either slurry or propelling fluid in an computational cell can be set by changing the local fluid properties depending on the diaphragm position.

6.2.1. TEMPORAL DISCRETIZATION OF NAVIER-STOKES EQUATIONS

As a transient solution is sought, a choice for the time integration of the Navier-Stokes-equations has to be made. Explicit time integration has been chosen as all transient characteristics of the flow field in the diaphragm housing are to be resolved for accurately tracking the diaphragm deformation. The flow structures change with the displacement of the diaphragm which follows the fluid flow. It is furthermore considered that the displacement of the structural nodes within a single time step should be less than the size of a fluid cell for an accurate tracking of the immersed structure. This prohibits the use of larger time steps which might be allowed by an implicit method anyway. For simplicity, first-order Euler time integration has been chosen for the time integration of the flow field. Time steps smaller than allowed by the stability criteria of the fluid flow are

required anyhow as the stability criteria of the structural time integration of the flexible immersed structure are more stringent as will be shown in section 6.4.

The time integration of the Navier-Stokes equations is a little bit more complex than the time integration of an ordinary differential equation as one is looking for both a solution of the flow velocity $\mathbf{v}$ as well as the pressure p. In compressible flow the continuity equation can be used to calculate the change in density such that the pressure can be calculated from the equation of state. For incompressible flow this is not possible, but the pressure can be used to enforce the incompressibility constraint. The pressure needs to be solved at the new time level $n+1$ as one wants to enforce the incompressibility constraint on the new velocity field at time $n+1$. The following set of time discretized equations are to be solved:

$$\rho^n \frac{\mathbf{v}^{n+1}-\mathbf{v}^n}{\Delta t} + \nabla\cdot\left(\rho^n\mathbf{v}^n\mathbf{v}^n\right) = -\nabla p^{n+1} + \nabla\cdot\boldsymbol{\tau}^n + \mathbf{b}^n \tag{6.3}$$

$$\nabla\cdot\mathbf{v}^{n+1} = 0 \tag{6.4}$$

This is however a difficult system to solve as the continuity equation does not include the pressure. Here a fractional step approach is used in which an intermediate velocity is solved first by using the pressure at the current time level ($\beta = 1$) in the momentum equations:

$$\mathbf{v}^* = \mathbf{v}^n + \frac{\Delta t}{\rho^n}(-\nabla\cdot\left(\rho^n\mathbf{v}^n\mathbf{v}^n\right) - \beta\nabla p^n + \nabla\cdot\boldsymbol{\tau}^n + \mathbf{b}^n) \tag{6.5}$$

For the velocity at the new time level $n+1$ then holds:

$$\mathbf{v}^{n+1} = \mathbf{v}^* - \frac{\Delta t}{\rho^n}\nabla(p^{n+1} - \beta p^n) = \mathbf{v}^* - \frac{\Delta t}{\rho^n}\nabla\phi \tag{6.6}$$

with pressure correction $\phi = p^{n+1} - \beta p^n$. When Equation 6.6 is inserted in Equation 6.4 one obtains a Poisson equation for the pressure correction ϕ

$$\nabla\cdot\left(\frac{1}{\rho^n}\nabla\phi\right) = \frac{\nabla\cdot\mathbf{v}^*}{\Delta t} \tag{6.7}$$

The density can be taken out of the divergence operator and moved to the right-hand-side in case of constant density but is required to stay in the Poisson equation in case of variable density, resulting in a Poisson equation with variable coefficients. The Poisson equation is an elliptic equation which implicitly contains the pressure at the new time level p^{n+1} and therefore requires the solution of a system of equations. For the solution of the Poisson equation a multigrid solver is used which characteristics are described later.

6.2.2. SPATIAL DISCRETIZATION OF NAVIER-STOKES EQUATIONS

In the previous paragraph the temporal discretization of the Navier-Stokes equations has been described without considering spatial discretization of the individual terms. The finite volume approach is followed for the dicretization of the individual terms in the Navier-Stokes equation as it enforces conservation and is most intuitive, especially when

variable properties such as density and viscosity are to be included. In the finite volume method the Navier-Stokes equations are integrated over a control volume. Furthermore the Gauss divergence theorem is used to change volume integrals of the divergence of a vector or tensor field into a surface integral. The Gauss theorem states that the integral of the divergence of a tensor field **g** over a control volume V is equal to outward flux of that tensor field through the control volume surface S:

$$\int_V \left(\nabla \cdot \mathbf{g}\right) \mathrm{d}V = \int_S \left(\mathbf{g} \cdot \mathbf{n}\right) \mathrm{d}S \tag{6.8}$$

with **n** the outward pointing normal. As mentioned before, an orthogonal structured grid is used. Furthermore a staggered arrangement of computational nodes for the individual flow directions and pressure is used as is shown in Figure 6.2

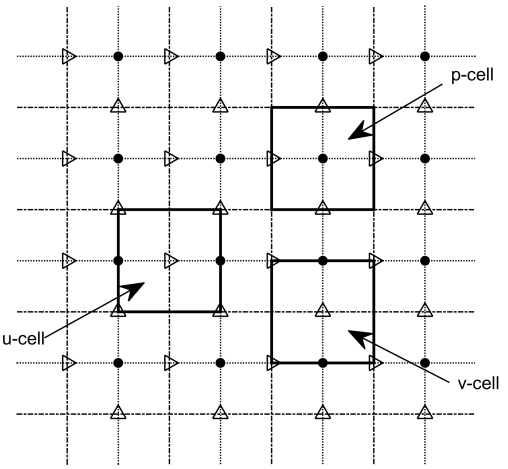

Figure 6.2: 2D staggered grid arrangement of p-points (•), u-points (▷) and v-points (△) with computational cell control volumes indicated with thick solid line

The advantage of using a staggered grid is the improvement of the pressure velocity coupling compared to a collocated grid in which the pressure nodes coincide with the velocity nodes. The pressure needs to be interpolated to the cell faces in a collocated grid when the pressure gradient needs to be evaluated over a computational cell. A high-low or checker board variation of pressure would give a zero pressure gradient when evaluated at the pressure cell boundaries using linear interpolation. The staggered arrangement is also a more natural and intuitive in a finite volume approach as the pressure nodes are located at the faces of the computational cells of the velocities for evaluating the momentum equations and the computational nodes of the velocities are located on the faces of the computational cells of the pressure for evaluating the continuity equation. Scalar properties of the flow field such as density and viscosity are also stored at the pressure nodes.

DISCRETIZATION OF VISCOUS TERM

In an incompressible fluid flow the following holds for the deviatoric stress tensor $\boldsymbol{\tau}$ in the diffusive term

$$\boldsymbol{\tau} = \mu\left(\nabla\mathbf{v} + (\nabla\mathbf{v})^T\right) \tag{6.9}$$

Here μ can be a uniform Newtonian viscosity, a non-uniform non-Newtonian viscosity or a non-uniform turbulent eddy viscosity. The divergence of the stress tensor in an incompressible fluid with a uniform Newtonian viscosity, can be written as

$$\nabla\cdot\left(\mu\left(\nabla\mathbf{v} + (\nabla\mathbf{v})^T\right)\right) \underset{\substack{\mu=const\\ \nabla\cdot\mathbf{v}=0}}{=} \mu\nabla^2\mathbf{v} \tag{6.10}$$

The latter form is convenient as it can be treated as a diffusion of momentum and can be handled as a scalar diffusion in a single direction of momentum. The term $(\nabla\mathbf{u})^T$ is considered to be small compared to the term $\nabla\mathbf{u}$ which allows the diffusion of momentum to be handled as a scalar diffusion also when the viscosity is spatially variable as is described by Versteegh and Malalasekera (2007) by

$$\nabla\cdot\left(\mu\left(\nabla\mathbf{v} + (\nabla\mathbf{v})^T\right)\right) \approx \nabla\cdot\left(\mu\nabla\mathbf{v}\right) \tag{6.11}$$

This approach is followed in this study as well. The finite volume integration of the diffusive term for a single direction i is then:

$$\int_V \left(\nabla\cdot\left(\mu\nabla v_i\right)\right)\mathrm{d}V = \int_S \left(\mu\nabla v_i\cdot\mathbf{n}\right)\mathrm{d}S \tag{6.12}$$

For correct evaluation of the surface integral both the velocity as well as the viscosity have to be interpolated to the cell face. For the velocity nodes this is a simple difference operation with neighbouring nodes while for the viscosity this requires tri-linear interpolation in 3D as the viscosity is stored at the pressure nodes. As the finite volume surface integral uses velocity information of both neighbouring cells it is equivalent to central differencing which is second-order accurate.

SPATIAL DISCRETIZATION OF CONVECTIVE TERM

The convective acceleration term for a single direction i is be cast into a finite volume integration:

$$\int_V \nabla\cdot\left(\rho v_i\mathbf{v}\right)\mathrm{d}V = \int_S \left(\rho v_i\mathbf{v}\right)\cdot\mathbf{n}\,\mathrm{d}S \tag{6.13}$$

Here the conserved or advected quantity is the momentum per unit mass or velocity v_i which is advected by the flow field $\mathbf{v}$. The surface integral could be evaluated by interpolating the advected momentum per unit mass to the cell faces and use an interpolated normal velocity on the cell faces. In this way a central difference equivalent is obtained for the advection of momentum as well. However when advection is dominant over diffusion, it is known to generate wiggles. A bounded and wiggle free operation of the central differencing approach is only obtained when the local cell-Peclet number is smaller than 2, see e.g. Versteegh and Malalasekera (2007),

$$\mathrm{Pe}_{\mathrm{cell}} = \frac{\rho v \Delta}{\mu} < 2 \tag{6.14}$$

with fluid density ρ, velocity v and grid spacing Δ. In the central difference approach, an equal amount of up and down stream information is used to evaluate the advected quantity at the cell face while the upstream information would logically have a stronger impact as this is the direction from which information is coming. An alternative is therefore to use the advected quantity upstream of the cell face which is then advected by the advective velocity at the cell face. This approach is called upstream or upwind differencing. It has the advantage that it satisfies the boundedness conditions unconditionally and does not show the wiggles which can arise when using central differencing. Also a combination of both is possible by locally switching between upwind and central differencing based on the local Peclet number. This is called hybrid differencing, see Versteegh and Malalasekera (2007) for implementation details. The drawback of upwind differencing is that it introduces a lot of numerical diffusion which acts as an additional numerical viscosity of $O(\mu_{\mathrm{num}}) = \rho v \Delta$ which actual value depends on the angle between the flow and major grid directions, (Ferziger and Peric, 2002). For a water flow at 1 m/s through a grid with a 10 mm spacing a numerical viscosity of $O(\mu_{\mathrm{num}}) = 10\,\mathrm{Pa\,s}$ results which is 10^4 times the dynamic viscosity of water. The effect on the outcome of a flow simulation could still be acceptable as the housing Reynolds number is of $O(Re) = 10^6$ and the housing Strouhal number is of $O(St) = 1$ which still indicates an acceleration dominated flow.

A further improvement is possible by using a Total Variation Diminishing (TVD) scheme. TVD schemes are a class of stable, non-oscillatory schemes which are monotonicity preserving which means that they don't create new under of overshoots in the solution and don't accentuate existing extremes. These TVD schemes evaluate the advected quantity by a weighted summation of the advected quantity evaluated by respectively upwind and central differencing. The following holds on the east cell face with subscript e when considering advection of the u-momentum in a flow field with positive u-velocity:

$$u_e = u_P + \frac{1}{2}\psi(u_E - u_P) \tag{6.15}$$

with u_P and u_E the cell centre values of respectively the computational cell whose flux is evaluated and its eastern neighbour. The weighting function ψ is a function of the ratio of the upwind-side over the downwind-side gradient of the computational cell

$$\psi = \psi(r) \tag{6.16}$$

with

$$r = \frac{u_P - u_W}{u_E - u_P} \tag{6.17}$$

For central differencing $\psi = 1$ and for upwind differencing $\psi = 0$. The weighting function $\psi(r)$ is called a flux limiter function and is constructed such that it results in a TVD scheme which means that the total variation of the discrete solution diminishes with time, (Versteegh and Malalasekera, 2007). Sweby (1984) has given necessary and

sufficient conditions for a scheme to be TVD in terms of the ψ - r relationship, requirements for second-order accuracy, a range of possible second-order schemes and introduced the symmetry property. The region for second-order TVD-schemes with some commonly used flux limiters is shown in Figure 6.3

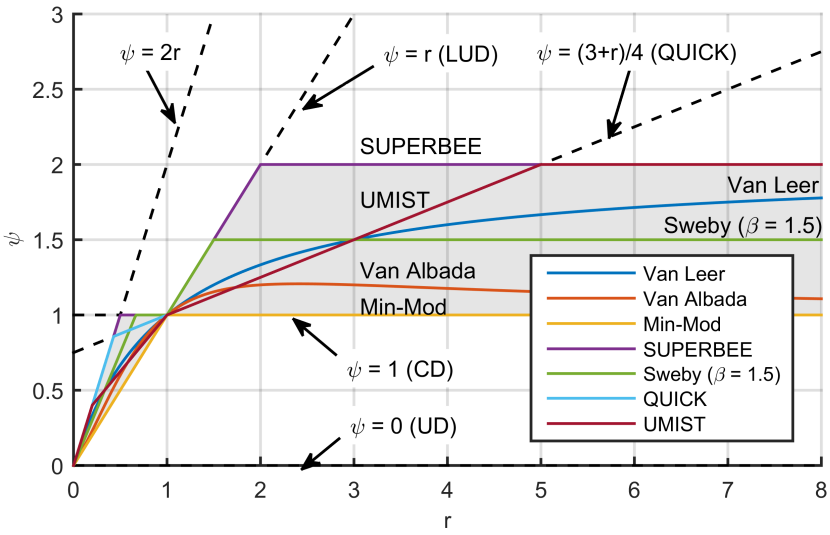

Figure 6.3: Second-order TVD region with some commonly used flux limiters

Versteegh and Malalasekera (2007) mention that the performance of the different second-order flux limiters is quite similar and that the selection of one would be a choice of personal preference. Some undocumented trials by the author with 1D waveform advection and 2D diagonal advection revealed a more diffusive behaviour of limiters which follow the lower boundary of the second-order TVD region such as the Min-Mod limiter compared to the more aggressive limiters which follow the upper region such as the SUPERBEE limiter. The more aggressive ones on the other hand introduce waveform steepening in 1D waveform advection; a sine deforms into a square wave when adected. Finally the UMIST limiter, Lien and Leschziner (1994), was selected to be used in further calculations as it seemed the most waveform preserving while having relatively low diffusion. The UMIST limiter is a symmetric version of the QUICK limiter, Leonard (1988), which is TVD version of the well-known QUICK differencing scheme, Leonard (1979). For more implementation details with respect to TVD schemes, see Versteegh and Malalasekera (2007).

SPATIAL DISCRETIZATION OF POISSON EQUATION

A finite volume discretization of the Poisson equation is obtained by taking the volume integral of Equation 6.7, followed by applying the divergence theorem to get a surface integral:

$$\int_S \frac{\nabla\phi}{\rho^n}\cdot\mathbf{n}\,\mathrm{d}S = \frac{1}{\Delta t}\int_S \mathbf{v}^*\cdot\mathbf{n}\,\mathrm{d}S \tag{6.18}$$

This surface integral is evaluated on a computational cell for the pressure. The normal gradient of the pressure correction ϕ on the cell face is obtained by the difference between the computational nodes on both sides of the face. The density is stored at the cell center and has to be interpolated to the cell face which in this case is a simple averaging operation. The intermediate velocities normal to the cell faces are directly available at the cell faces due to the staggered grid arrangement and don't need interpolation for their evaluation.

6.2.3. STABILITY CRITERIA

The time step which can be used in explicit time integration is limited because of stability considerations. These limitations can be derived by applying a Neumann stability analysis on the discretized equations, (Ferziger and Peric, 2002). The conditions which result, and are typically used for explicit Euler integration, are:

$$\Delta t < \left(\frac{\rho}{2\mu\left(\frac{1}{\Delta_x^2}+\frac{1}{\Delta_y^2}+\frac{1}{\Delta_z^2}\right)}, \frac{\Delta_x}{|u_{\max}|}, \frac{\Delta_y}{|v_{\max}|}, \frac{\Delta_z}{|w_{\max}|}, \Delta t_{\max,\,\mathrm{user}} \right) \tag{6.19}$$

The first is a limit imposed by the diffusion which states that the time step should be less than half the characteristic diffusion time $\rho\Delta^2/\mu$ for the 1D case. It should be noted that this limits scales with 2^{nd} power of the grid spacing which might make it overly restrictive in case of high viscosity μ. The 3 latter limitations are the famous Courant-Friedrichs-Lewy or CFL conditions which state that a fluid particle can not travel further than a single grid spacing within a single time step. The diffusive term can be treated explicitly when the CFL conditions are limiting, otherwise an implicit treatment of the diffusive terms is preferred as it would otherwise be overly restrictive on the required time step. For a 1D case the CFL condition can be equated with half the characteristic diffusion time in order evaluate when the diffusive term becomes limiting. For a 1D situation the diffusive term is then limiting the time step when

$$\frac{\rho v\Delta}{\mu} = \mathrm{Pe}_{\mathrm{cell}} < 2 \tag{6.20}$$

This is the same as the boundedness limit for the use of the central differencing discretization as shown before. For a flow with a density of $O(\rho) = 10^3\,\mathrm{kg/m^3}$, a flow velocity of $O(v) = 1\,\mathrm{m/s}$ and a grid spacing of $O(\Delta) = 10^{-2}\,\mathrm{m}$ a limiting dynamic viscosity of $O(\mu) = 10\,\mathrm{Pa\,s}$ results. Some estimates of dynamic viscosity used in different a approaches flow simulation are;

Newtonian viscosity in ILES In an Implicit Large Eddy Simulation (ILES) no turbulence model is included hence no additional eddy viscosity is added to the Newtonian fluid viscosity. Most fluids of interest here have a dynamic viscosity in the range of 1 to 100 mPas, which is 2 to 4 order of magnitude below the above described threshold at which diffusion is limiting the time step of the simulation

LES eddy viscosity The eddy viscosity in an explicit LES model can be estimated using the Smagorinksy Sub-Grid-Scale (SGS) eddy viscosity

$$\mu_{\text{SGS}} = \rho \left(C_S \Delta\right)^2 |S| \tag{6.21}$$

with a fluid density of $O(\rho) = 10^3\,\text{kg/m}^3$, a Smagorinsky constant of $O(C_S) = 10^{-1}$, a grid spacing of $O(\Delta) = 10^{-2}\,\text{m}$ and an average local rate of strain of the resolved flow of $O(|S|) = O(\frac{v}{\Delta}) = 100\,s^{-1}$, a SGS viscosity of $O(\mu_{\text{SGS}}) = 0.1\,\text{Pa s}$ results. This is 2 orders of magnitude below the above described threshold at which diffusion is limiting the time step of the simulation. If this order of magnitude analysis is inserted in Equation 6.20, $O(C_S) < 1$ results which generally holds. This means that for an explicit LES no implicit treatment of the viscous term is ever required.

RANS eddy viscosity An estimate of eddy viscosity in a RANS approach can be based on a values reported for DNS results of turbulent boundary layer by Pope (2000) which gives a maximum value of $\frac{\mu_{\text{RANS}}}{\rho v_\tau \delta} \approx 0.1$ at $\frac{y}{\delta} \approx 0.45$ which applies quite universal as the law of the wall is universally applicable for turbulent boundary layers. With $v_\tau = \sqrt{\frac{\tau_w}{\rho}}$ and $\tau_w = \frac{f_D}{8}\rho v^2$, $\mu_{\text{RANS}} = 0.1\,\rho v \delta \sqrt{\frac{f_D}{8}}$ results. With $O(\rho) = 1000\,\text{kg/m}^3$, $O(v) = 1\,\text{m/s}$, $O(\delta) = 0.1\,\text{m}$ and $O(f_D) = 0.01$, $O(\mu_{\text{RANS}}) = 1\,\text{Pa s}$ results. This is 1 order of magnitude below the above described threshold at which diffusion is limiting the time step of the simulation. This indicates that no implicit treatment of the viscous term is required at these conditions, but might be required at somewhat higher Reynolds number flows.

Laminar Bingham flow A paste type slurry with an yield stress of $O(\tau_y) = 100\,\text{Pa}$ flowing with a velocity of $O(v) = 1\,\text{m/s}$ through a channel with a width of approximately 10% of the fluid domain of $O(h_{\text{channel}}) = 0.1 \cdot O(L) = 0.1\,\text{m}$, has a bulk shear rate of $O(\gamma_{\text{bulk}}) \approx 10 \cdot O(\frac{u}{h_{\text{channel}}}) = 100\,\text{s}^{-1}$ which gives an apparent viscosity for the bulk flow of $O(\mu_{\text{bulk}}) = O(\frac{\tau_y}{\gamma_{\text{bulk}}}) = 1\,\text{Pa s}$. In the un-sheared core of the Bingham flow the apparent viscosity is theoretically infinite. When it is assumed that an adequate flow profile can be obtained when the apparent viscosity is allowed to rise 2 orders of magnitude above the apparent viscosity of the bulk flow, a maximum local viscosity of $O(\mu_{\text{max}}) = 100\,\text{Pa s}$ results. This is 1 order of magnitude above the threshold at which diffusion is limiting the time step of the simulation. This indicates that for simulation with these types of Bingham flows an implicit treatment of the viscous term could be advantageous. One should try to minimize the maximum viscosity which is allowed to develop at lower shear rates when the viscous term is treated explicitly as is done in this study.

From the viscosity estimates described above it is argued the for anticipated (I)LES approaches, diffusion will not be limiting the time step, hence no need is present to consider implicit treatment of the diffusive term as is often done when diffusion is limiting the time step. Only when considering a highly viscous laminar flow simulation of Bingham flow with yield stresses of $O(\tau_y) = 100 - 1000\,\text{Pa}$, viscosity will be limiting the time step in the explicit time integration. Only then implicit time integration of the diffusive

term will have a merit. The above described evaluation also applies for the evaluation whether central differencing of the advective term can be considered as the same grid Peclet number based criterion applies. It is therefore clear that for the anticipated (I)LES approaches upwind differencing or TVD schemes with flux limiters are required under all circumstances.

6.2.4. BOUNDARY CONDITIONS

In order to obtain a numerical solution, Boundary Conditions (BC's) are required on the boundary of the computational domain for the flow velocity components u, v, and w and for the pressure p. The computational domain is arranged such that the boundaries of the p-cells coincide with the physical boundary of the computational domain as shown in Figure 6.4. For the staggered grid arrangement this means that the u-points and the v and w-cell boundaries coincide with the East and West boundary, the v-points and the u and w-cell boundaries coincide with the North and South boundary and the w-points and u and v cell boundaries coincide with the Top and Bottom boundary (not shown). In order to simplify implementation of the boundary conditions a strip of so-called ghost cells is used outside the physical boundary for all cells whose boundary coincides with the physical boundary of the computational domain.

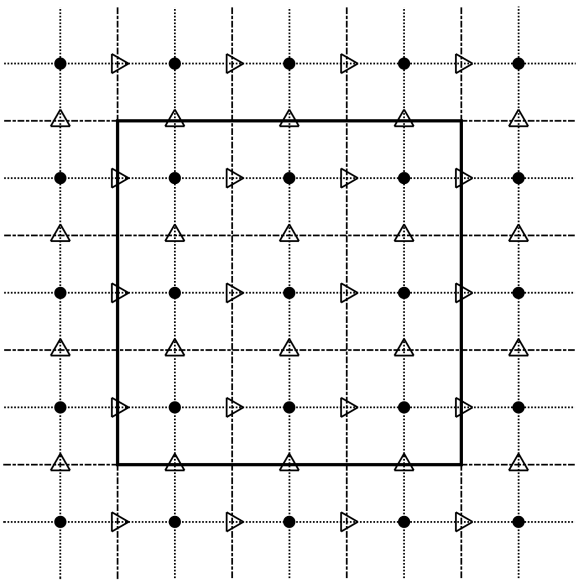

Figure 6.4: Physical domain boundary (thick solid line) coinciding with p-cell boundaries with strip of ghost cells outside physical domain used for implementation of boundary conditions,(•) p-points, (▷) u-points and (△) v-points

The boundary conditions for the momentum equation are set at the beginning of the explicit time integration in either the nodes coinciding with the boundary or in the nodes of the ghost cells. The finite volume integral of momentum equations is only evaluated in the interior cells while using the boundary or ghost cell nodes. The boundary conditions used are either of the Dirichlet or the Neumann type which respectively means that value of the solution or the derivative of the solution is specified on the boundary. They are called homogeneous when the specified value or derivative is zero.

BOUNDARY CONDITIONS FOR THE VELOCITY

The following boundary conditions are used for the velocity, as described by Griebel *et al.* (1998):

Inflow boundary On a inflow boundary all velocity components are prescribed with normal components set to some prescribed value and tangential components set to zero. As the nodes of the normal components coincide with the boundary, values can be simply set to the boundary nodes. The tangential components are set in the ghost cells such that the interpolated value on the boundary between the ghost cell and first interior cell is zero on the boundary. As explicit time integration is used this means enforcing of the tangential components on the old velocity values which means a non exact enforcement in the solution on the new time level. This boundary condition is used for the inlet or suction port of the pump chamber during the suction stroke and for the propelling fluid port during the discharge stroke of the pump cycle.

Outflow boundary On the outflow boundary the normal derivative of all velocity components is set to zero, which means no change of flow velocity across the boundary. For the normal components with the points on the boundary this means an upwind difference and for the tangential components a central difference across the boundary. Because of the explicit time integration a non-exact enforcement in the solution at the new time level results. This boundary condition is used for the outlet or discharge port of the pump chamber during the discharge stroke and for the propelling fluid port during the suction stroke of the pump cycle.

Free slip boundary On a free slip boundary the normal component is set to zero directly in the boundary node. For the tangential components the normal derivative is set to zero, this to enforce the shear stress to zero at the free slip boundary. This is done by equating the values in the ghost cell to the values in their first interior neighbours. Again this means no strict enforcement in the solution at the new time level. This boundary condition is used on the remaining part of the boundary to guarantee no fluid is entering the domain through this boundary. Constraint of the tangential velocity components is left to the body forces generated by the IBM which is used to model the solid geometry of the pump chamber.

No-slip wall On a no slip wall all velocity components are set to zero. The normal components can be set directly in the nodes on the boundary while the tangential components are set such that the interpolated value at the boundary is zero. For the tangential components this again means no strict enforcement in the solution at

the new time level. This boundary condition is used on the suction and discharge port of the pump chamber during respectively the discharge and suction stroke. It has furthermore been used when testing the flow solver for other flow situations such as the lid driven cavity and channel flow.

Periodic boundary A periodic boundary condition is used when periodicity is assumed to be present in the solution of the velocity field. For a periodic boundary the velocities at the 2 periodic boundaries need to be equated. The normal nodes on the periodic boundary can not be the boundary nodes of the computational domain as they need to be able to develop freely in time. A periodic grid therefore needs to overlap with 1 grid cell. The first interior node near a periodic boundary, which is a result of the numerical solution, is then copied to the boundary of the computational domain which is one grid spacing outside the other periodic boundary. For the tangential components with ghost cells this means copying the second interior point of the computational domain to the ghost cell on the other side of the computational domain. This boundary condition is not used in the FSI model of the piston diaphragm pump but has been used for testing the flow solver for channel flow situations and is mentioned here for completeness. Here it was used as an in and outlet boundary used to mimic an infinite length channel, required to model a fully developed channel flow.

The set of boundary conditions listed above apply to individual sections of the boundary of the computational domain, which also have to satisfy the divergence free condition of the entire flow field. This requires the surface integral over the boundary of the computational domain Γ of the normal velocities to be zero which follows by applying the divergence theorem on the divergence of the entire computational domain Ω:

$$\int_{\Omega} \nabla \cdot \mathbf{v} \, \mathrm{d}\Omega = \int_{\Gamma} \mathbf{v} \cdot \mathbf{n} \, \mathrm{d}\Gamma = 0 \tag{6.22}$$

Non zero normal boundary velocities are only present in the inflow, outflow and periodic boundaries. The boundary integral of the normal velocities is not guaranteed to be zero when only applying the boundary conditions listed above. In order to enforce this condition the outflow normal velocities need to be scaled such that the volumetric outflow matches the volumetric inflow:

$$\mathbf{v}|_{\Gamma_{\text{out}}} \cdot \mathbf{n} = (\mathbf{v}|_{\Gamma_{\text{out}}} \cdot \mathbf{n}) \frac{\int_{\Gamma_{\text{in}}} \mathbf{v} \cdot \mathbf{n} \, \mathrm{d}\Gamma_{\text{in}}}{\int_{\Gamma_{\text{out}}} \mathbf{v} \cdot \mathbf{n} \, \mathrm{d}\Gamma_{\text{out}}} \tag{6.23}$$

Enforcing the continuity condition on the boundary in essence means that a Dirichlet boundary condition is required for all normal velocities on the boundary. The Neumann boundary condition used on an outflow boundary is additional to required Dirichlet boundary condition on the entire boundary making it an Cauchy boundary condition. In the discrete implementation with explicit time integration, all velocity boundary conditions are actually implemented as a Dirichlet boundary conditions. Fixed values are set in the nodes on the boundary and in the ghost cells which remain fixed during a single time step of the explicit time integration.

BOUNDARY CONDITIONS FOR THE PRESSURE

The boundary conditions for the pressure in the incompressible Navier-Stokes equations are derived by applying the normal component of the momentum equations on the boundary as is described by Gresho and Sani (1987), which results in a Neumann boundary condition for the pressure:

$$\nabla p \cdot \mathbf{n} = \frac{\partial p}{\partial n} = \mathbf{n} \cdot \left(\nabla \cdot \boldsymbol{\tau} + \mathbf{f} - \rho \mathbf{v}\mathbf{v} - \rho \frac{\partial \mathbf{v}}{\partial t} \right) \tag{6.24}$$

For the time discretized equation on the boundary then holds

$$\frac{\nabla \phi}{\rho^n} \cdot \mathbf{n} = \frac{(\mathbf{v}^* - \mathbf{v}^{n+1}) \cdot \mathbf{n}}{\Delta t} \tag{6.25}$$

When inserted in the discrete implementation of the Poisson equation it can be shown that the normal of the intermediate velocity $\mathbf{v}^*$ on the boundary falls out of the discrete Poisson equation as $\mathbf{v}^*$ is present in both the right hand side of Equation 6.25 as well as Equation 6.18 which allows its value in Equation 6.25 to be selected freely. A logical choice is $v_n^* = v_n^{n+1}$ which results on a homogeneous Neumann boundary condition for the pressure correction, $\frac{\partial \phi}{\partial n} = 0$, on the entire boundary. The homogeneous Neumann BC for the pressure correction results in an ill-posed system as the underlying linear system is singular because the pressure is only determined up to an additive constant which value is physically irrelevant in a incompressible flow. This can give stability issues when the Neumann BC is inserted in the discrete Poisson equation. This situation can be improved when using a iterative solver by implementing the Neumann BC by equating the ghost cell value to the value of the first interior cell value, (Griebel *et al.*, 1998). The value in the ghost cells needs to be updated after every iteration in order to follow the development of the solution such that the Neumann BC is satisfied at the converged solution. Equating the ghost cell values to the first interior cell results in a central difference implementation of the boundary condition as the p-cells are aligned with the boundary. The second-order behaviour of the central differencing of the interior of the Poisson equation is then maintained. However, in the used implementation of the Multigrid Poisson solver, which is described in the next section, the Neumann BC is inserted in the discrete Poisson equation as this is useful for the cell-centred coarsening strategy used. This has not given any issues in this study, most likely due to the fact that the boundary conditions satisfy the incompressibility constraint up to machine accuracy by applying Equation 6.23 every time step before solving the Poisson equation.

6.2.5. POISSON SOLVER

The solution of the pressure field can be obtained by solving the Poisson equation for the pressure. Different methods exist, see e.g. Heath (1997), on which the introduction of this section is based. Direct methods solve the system of equations exactly within numerical precision, while iterative method approximately solve the system of equations within a single iteration which is improved every iteration. Direct solvers based on Gaussian elimination are not considered to be efficient solvers for large sparse matrices which result from the discretization of partial differential equations, and are especially

worse in 3D situations. FFT based Poisson solvers are very efficient but can only be applied to constant coefficient stencils which requires both a constant coefficient Poisson equation as well a equidistant grid. The latter condition is met in this case but the former is not when using a variable density. Basic iterative methods such as Gauss-Seidel and Jacobi are not considered efficient or even realistic for larger 3D systems as their computational cost is proportional with $k^5 \log k$ in 3D with k the number of grid points in a single direction. Conjugate gradient or preconditioned conjugate gradient methods are an improvement with a computational cost proportional with k^4 and $k^{3.5}$ respectively. But most efficient seem MultiGrid (MG) methods with a computational cost proportional with $k^3 \log k$ or even k^3 for respectively Multigrid V-cycle or Full MultiGrid (FMG) which is nearly optimal as the cost of writing the output is proportional to k^3. A Multigrid solver has therefore been developed for solving the Poisson equation in this study, whose characteristics are described next.

MULTIGRID POISSON SOLVER

In Multigrid methods a sequence of subsequently coarser grids is used to determine the solution on the finest grid. Their performance is based on the observation that basic iterative methods are only effective in reducing the high frequency error in the solution effectively. What remains after a single or a few iterations is a solution with a low frequency error. For this reason these basic iterative methods are called smoothers. However, the low frequency error becomes a high frequency error when represented on a coarser grid. A reduction of all frequencies in the error of the solution can be obtained by reducing the error on subsequently coarser grids. If $\hat{x}$ is a approximate solution to the system of equations $Ax = b$, with residual $r = b - A\hat{x}$, then the error $e = x - \hat{x}$ satisfies the equation $Ae = r$, which is called the residual equation. Approximate solutions of the error on a coarser grid, obtained by applying a smoother on the residual equation on a coarser grid, can be used to improve the solution on a finer grid. Transition of the residual from a finer to a coarser grid is called restriction or injection while transition of the error from a coarser to a finer grid is called prolongation or interpolation. When the successively coarser grids have geometric meaning, the method is called Geometric-Multigrid which can be understood quite intuitively. Basic choices and considerations in developing an Multigrid algorithm are; choice of smoother, coarsening strategy, method used for restriction and prolongation, method used for determining A on the coarser grids and strategy for cycling through the various grid levels. For more background see Briggs *et al.* (2000), Wesseling (1992). A short description of the choices made in this study is given here:

Smoother Many iterative methods can be used as a smoother in multigrid. See Wesseling (1992) for an overview of many methods. In this study the red-black Gauss-Seidel method is used as it has an improved smoothing capability over a basic Gauss-Seidel method in a constant coefficient Poisson equation and can be vectorized and parallelized as the update of the solution in the individual points within a single sweep over all red or black points is independent from other red points or back points respectively.

Coarsening strategy The coarsening can either be vertex-centred or cell-centred. In vertex-centred coarsening every other vertex in each direction is deleted while in

cell-centred coarsening unions of fine grid cells are used as shown in Figure 6.5. In this study cell-centred coarsening is applied as this gives a coarse grid in which the p-cell faces remain aligned with the boundary of the computational domain. This allows straightforward implementation of the Neumann boundary condition on the coarse grid level while maintaining a second-order accurate discretization of the Neumann boundary condition.

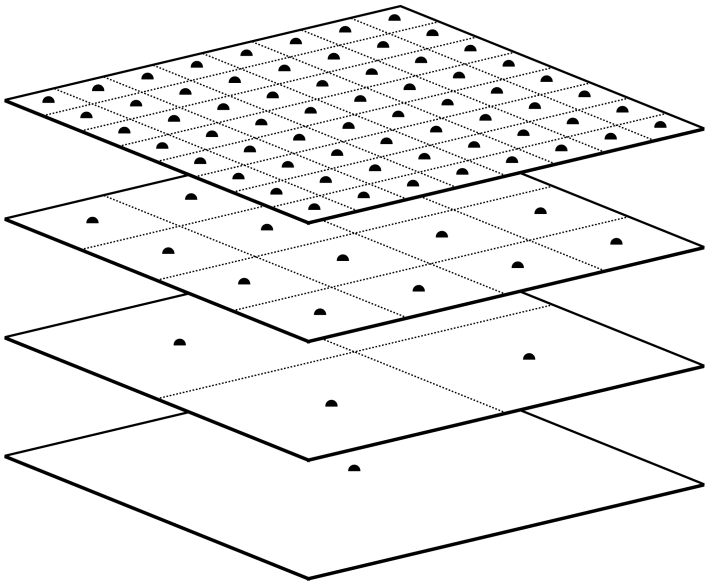

Figure 6.5: Cell-centred coarsening strategy employed in geometric multigrid Poisson solver in which p-cell faces remain aligned with domain boundary, 2D example.

Restriction and Prolongation The choice of the restriction and prolongation operators is based on the intuition of the author. Restriction of the fine grid residual to the coarse grid is obtained by simply averaging the fine grid cell values which are joined to form a new coarse grid cell. The coarse grid error is prolongated to the fine grid by trilinear interpolation in 3D . This approach seems more logical and is easier to implement than approaches mentioned in Wesseling (1992, 1988), and seems to work quite well.

Coarse grid coefficients The coarse grid approximation of $\overline{\mathbf{A}}$ is obtained by discretization of the partial differential equation on the coarse grid which is called Discrete Coarse grid Approximation (DCA). The variable coefficient in the Poisson equation is restricted to the coarser grid by averaging the face values of the fine grid which form a new larger face on the coarse grid. This requires 6x4 fine grid face values

to be restricted to 6 coarse grid values which showed improved convergence compared to restricting 8 cell center values as an average to a single coarse grid cell center. This approach is similar to the one described by Wesseling (1988), where it is shown to correspond to a Galerkin Coarse grid Approximation (GCA) in which the coarse grid matrix $\overline{\mathbf{A}}$ is obtained by multiplication of the restriction, fine grid coefficient and prolongation matrices **R**, **A** and **P** which gives $\overline{\mathbf{A}} = \mathbf{RAP}$.

Cycling method Here a basic multigrid V-cycle algorithm is used which starts at the finest grid level and then successively restricts the fine grid residuals to coarser grids before prolongation the coarse grid error back through the successively finer grids. Here 2 smoothing sweeps before restriction and 2 sweeps after the prolongation are used.

6.3. STRUCTURAL MODEL

6.3.1. FINITE ELEMENT METHOD FOR SOLID AND STRUCTURAL MECHANICS

For the numerical analysis of solid and structural deformation the Finite Element Method (FEM) is the most widely used discretization method. In the FEM, the structure is divided in elements with computational nodes on the boundary and sometimes in the interior of the element. In a structural analysis, the nodal quantities are position, velocity, acceleration and force. The FEM can easily be applied to unstructured meshes in non-rectangular domains, as the interpolation of the nodal quantities within an element normally only include nodal values of the element at hand. Use of unstructured meshes is not possible with finite difference methods, and is more complicated with Finite Volume Methods (FVM) as they require information of neighbouring cells to evaluate the cell face fluxes. The advantage of straight forward implementation of Eulerian mass conservation laws in finite volume methods is less relevant in a Lagrangian approach used in solid mechanics as the mesh follows material points such that no mass enters or leaves the computational elements anyway. The discretized structural FE equations are naturally suitable for the anticipated IBM using feedback forcing. The structural nodes are immersed in and advected by the fluid flow which results in a set of nodal positions. The external nodal reaction forces required to generate the nodal displacements are calculated using the FE discretization described in this section. These external nodal forces can then be fed back into the fluid solver as body forces.

The discrete FE equation can be derived by using the principle of virtual work as described by Belytschko *et al.* (2000), Zienkiewicz *et al.* (2005a), Zienkiewicz and Taylor (2005). These references are used as the basis of the following section when no specific reference is mentioned. By applying the principle of virtual work on the momentum equation, a relationship between the nodal displacements and nodal forces can be derived. In the FEM the principle of virtual work is typically applied on a single element which results in a relationship between the element nodal positions and the element nodal forces which are typically represented as column matrices. All nodal forces and positions in the complete FE model are normally gathered in global column matrix as well. As nodes can be shared between elements an assembly process is required. The element nodal positions have to correspond to the global nodal positions obviously.

The global nodal forces are obtained by summing the contribution of the element nodal forces.

The principle of virtual work states that the total work during a virtual displacement $\delta\mathbf{u}$ is zero which for a updated Langrangian formulation can be obtained by taking the product of the virtual displacement with the momentum equation and integrating it over a finite element in the current configuration Ω.

$$\int_{\Omega} \delta\mathbf{u}\left(\nabla\cdot\boldsymbol{\sigma}+\rho\mathbf{b}-\rho\ddot{\mathbf{x}}\right)\mathrm{d}\Omega \tag{6.26}$$

When splitting the virtual work contributions into work done by the internal stress, W^{int}, work done by external force, W^{ext} and work done by the inertial or kinetic force, W^{kin} the following balance results

$$\delta W = W^{\text{int}} - W^{\text{ext}} + W^{\text{kin}} = 0 \tag{6.27}$$

The work done by external forces includes both the contribution of body forces as well as external traction forces. The principle of virtual work applies on the continuous momentum equation but has to apply on the discrete momentum equation as well. The discrete version of the virtual work equation can be written as follows

$$\{\delta\mathbf{u}\}^T\left(\{\mathbf{f}\}^{\text{int}} - \{\mathbf{f}\}^{\text{ext}} + [\mathbf{M}]\{\ddot{\mathbf{x}}\}\right) = 0 \tag{6.28}$$

where $\{\delta\mathbf{u}\}$, $\{\mathbf{f}\}$ and $\{\ddot{\mathbf{x}}\}$ are column matrices containing the virtual nodal displacements, the nodal forces and the nodal accelerations respectively and $[\mathbf{M}]$ the mass matrix. This gives the discrete momentum equation as the virtual displacements are arbitrary.

$$[\mathbf{M}]\{\ddot{\mathbf{x}}\} - \{\mathbf{f}\}^{\text{int}} = \{\mathbf{f}\}^{\text{ext}} \tag{6.29}$$

Definition of the individual terms in the discrete virtual work equation are derived by relating the continuous variables in Equation 6.26 to the nodal quantities in the FE discretization. The motion within a single element is assumed to follow a polynomial interpolation function N_I which relates the internal coordinates $\mathbf{x}$ to the nodal coordinates $\mathbf{x}_I$ by

$$\mathbf{x}(\mathbf{X},t) = N_I(\mathbf{X})\,\mathbf{x}_I(t) \tag{6.30}$$

in which I is the element nodal index which by its repetition in N_I and $\mathbf{x}_I$ implies summation of the interpolated value of the individual nodes. The interpolation function can just as well be used to interpolate displacements, velocities and accelerations by replacing $\mathbf{x}$ in Equation 6.30 by respectively $\mathbf{u}$, $\dot{\mathbf{u}}$ or $\ddot{\mathbf{u}}$. The internal virtual work δW^{int} done by the internal nodal forces $\{\mathbf{f}\}^{\text{int}}$ by a virtual displacement $\{\delta\mathbf{u}\}$ must be equal to the work done by the stress $\{\boldsymbol{\sigma}\}$ in the element due to the same virtual displacement.

$$\delta W^{\text{int}} = \{\delta\mathbf{u}\}^T\{\mathbf{f}\}^{\text{int}} = \int_{\Omega}\{\delta\boldsymbol{\epsilon}\}^T\{\boldsymbol{\sigma}\}\,\mathrm{d}\Omega \tag{6.31}$$

Here the Voigt notation is used in which second-order symmetric tensors are written as column matrices, indicated by $\{\}$, and higher order tensors as rectangular matrices,

indicated by [] as this is often used in finite element implementations and publications. As the principle of virtual work is based on a virtual, arbitrary, but small displacement, the infinitesimal strain tensor $\{\boldsymbol{\epsilon}\}$ based on the gradient of the displacement field $\{\mathbf{u}\}$ can be used. Now a matrix $[\mathbf{B}]$ is introduced which relates the virtual displacement $\{\delta\mathbf{u}\}$ to the infinitesimal strain tensor $\{\boldsymbol{\epsilon}\}$ by

$$\{\delta\boldsymbol{\epsilon}\} = [\mathbf{B}]\{\delta\mathbf{u}\} \tag{6.32}$$

In an updated Lagrangian formulation as used in this study, the matrix $[\mathbf{B}]$ includes the spatial derivatives of the interpolation function with respect to the Eulerian coordinates in the form $N_{I,\mathbf{x}}$, organized such that Equation 6.32 holds. The stress $\{\boldsymbol{\sigma}\}$ in the element depends on the displacement field $\{\mathbf{u}\}$ as well through some constitutive model which relates the stress to some strain measure which is a function of the displacement field in the element. The interpolation function therefore allows the evaluation of the integral in Equation 6.31 which is typically evaluated using Gaussian quadrature in one or more integration points in the element depending on the order of the interpolation function used. As the virtual displacement $\{\delta\mathbf{u}\}$ is arbitrary it follows that

$$\{\mathbf{f}\}^{\text{int}} = \int_{\Omega} [\mathbf{B}]^T \{\boldsymbol{\sigma}\}\, \mathrm{d}\Omega \tag{6.33}$$

Element stiffness matrices $[\mathbf{K}]$ can be derived from Equation 6.33 which relate nodal displacements or increments in nodal displacements to the nodal forces by $\{\mathbf{f}\}^{\text{int}} = [\mathbf{K}]\{\mathbf{u}\}$ These element stiffness matrices are assembled into a system stiffness matrix required for the solution of the system of equations in a static or implicit transient analysis. When explicit time integration is used as in this study, no element stiffness matrices are required and one can work directly with Equation 6.33. The explicit time integration will give all nodal positions which then allow evaluation of Equation 6.33 for every element independent of each other. The nodal accelerations can be integrated in time to find the nodal positions and can be obtained from Equation 6.29 as follows

$$\{\ddot{\mathbf{x}}\} = [\mathbf{M}]^{-1}\left(\{\mathbf{f}\}^{\text{ext}} - \{\mathbf{f}\}^{\text{int}}\right) \tag{6.34}$$

The external nodal forces $\{\mathbf{f}\}^{\text{ext}}$ and mass matrix $[\mathbf{M}]$ can also be obtained by inserting the shape functions in the continuous virtual work equation. The mass matrix which results is non-diagonal however. This poses a difficulty in an explicit time integration scheme as it requires an inversion of the mass matrix. In explicit time integration of structural equations a lumped mass matrix is normally used which is diagonal. Zienkiewicz *et al.* (2005a) describes several methods for lumping the mass matrix but for the linear 3 node triangular elements considered in this study, lumping is trivial by assigning a 3$^{\text{rd}}$ of the mass or every element to each node. The FE model is used in this study both in a structure-only simulation as well as in a FSI simulation in which it is combined with the flow solver using an Immersed Boundary Method (IBM). In the structure-only situation only pressure loads are considered. For the linear 3 node triangular elements considered in this study evaluation of the external nodal forces is trivial as well by assigning a 3$^{\text{rd}}$ of the pressure load on the element face to each node. In the FSI case the time integration is performed by the flow solver. The structural nodes are immersed in and are advected by the fluid which gives updated nodal positions every

time step. The nodal masses can be included in the fluid solver by locally increasing the fluid density as discussed in section 6.4. The internal nodal forces are determined by evaluating Equation 6.33 based on the updated nodal positions. As the nodal mass has been transferred to the flow solver in the FSI situation, determination of the external nodal forces is straight forward by

$$\{\mathbf{f}\}^{\text{ext}} = \{\mathbf{f}\}^{\text{int}} \tag{6.35}$$

These external forces have to be delivered by the fluid flow and are therefore supported in the fluid flow as body forces which are used in the next time step of the time integration of the fluid flow.

When used in the FSI situation, enough dampening is considered to be present in the fluid flow such that no additional dampening seems required. For the structure-only situation some dampening needs to be included in order to dampen structural oscillations which arise once the structure is loaded. A widely used method is to apply a linear dampening matrix which calculates additional nodal dampening forces by the product of a dampening matrix [**C**] with the column matrix of the nodal velocities.

$$\{\mathbf{f}\}^{\text{damp}} = [\mathbf{C}]\{\dot{\mathbf{x}}\} \tag{6.36}$$

Often the so-called Rayleigh dampening is used which uses a dampening matrix [**C**] which is a linear combination of the mass matrix [**M**] and stiffness matrix [**K**]

$$[\mathbf{C}] = \alpha[\mathbf{M}] + \beta[\mathbf{K}] \tag{6.37}$$

It can be shown that in a linear approximation, which holds for small vibrations, a modal decomposition of the momentum equation is possible which requires the dampening matrix to be a linear combination of the mass and stiffness matrix. For the dampening coefficient ζ of the i^{th} mode then holds

$$\zeta_i = \frac{1}{2\omega_i}(\alpha + \beta\omega_i^2) \tag{6.38}$$

with modal frequency ω_i. This indicates that when structural dampening is used with $\beta > 0$, an over-critically damped response might result for the higher frequency modes. This might be advantageous when using an implicit time integration as it damps higher frequencies which are not of interest which would otherwise require a small time step to resolve. The overcritical dampening is problematic in a explicit time integration however as it limits the time step due to the viscous transport time involved, similar to the time step limitation by viscosity in the flow solver as discussed in section 6.2. Furthermore stiffness matrices are not available as they are not required in an explicit time integration. In explicit time integration only the so-called mass damping is employed. The coefficient α is determined by first estimating the lowest modal frequency from a step response simulation of using a model without dampening before calculating α from Equation 6.38 by $\alpha = 2\zeta_1\omega_1$ with an assumed dampening coefficient of 0.7 which give a nicely damped response.

6.3.2. ROTATION FREE TRIANGULAR SHELL ELEMENT

As discussed in section 4.3 the use of thin plate theory seems to be a reasonable approximation for the modelling of the structural deformation of the diaphragm. However, many FE plate models have both translational as well as rotational degrees of freedom, (Zienkiewicz and Taylor, 2005). This approach is incompatible with the anticipated IMB as the fluid model only allows for support of forces not of moments related to the rotational degrees of freedom. A plate model only involving translational degrees of freedom is therefore sought. The method used in this study is based on the rotation-free triangular shell elements described by Oñate and Zárate (2000). Oñate and Zárate (2000) describe a rotation free FE shell model which combines FV discretization techniques with FE discretization techniques by using a patch of 4 triangular elements as the basic element for deriving the relationship between the nodal displacements and the nodal forces. The Kirchhoff-Love theory is used in the derivation of the model such that it applicable for thin shells which is considered reasonable for the diaphragm deformation analysis as mentioned before. First the Basic Plate Triangle (BPT) will be discussed which applies for flat plates. Then the Basic Shell Triangle (BST) will be discussed which is an extension of the BST for curved shells which furthermore includes in-plane or membrane deformation by combining it with a Constant Strain Triangle (CST). The derivation as described by Oñate and Zárate (2000) assumes small displacements and strains which is not the case for the diaphragm deformation analysis in this study. Changes to the BST triangle formulation are described which are required for the large displacements present in this study.

BASIC PLATE TRIANGLE (BPT)

The constitutive moment-curvature and curvature-deflection relationships according the Kirchhoff-Love theory for a flat plate in the xy-plane with a deflection w in z-direction as shown in Figure 6.6 were mentioned before in section 4.3 but are repeated here for clarity.

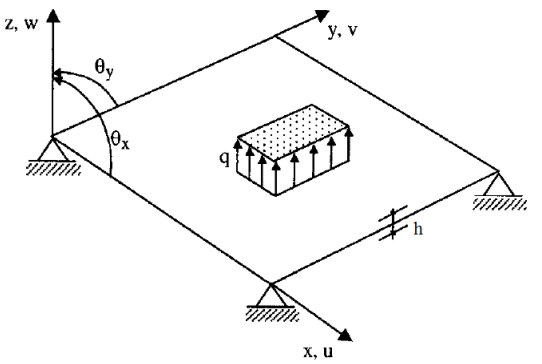

Figure 6.6: Plate model sign convention, (Oñate and Zárate, 2000), Copyright ©2000 John Wiley & Sons, Ltd, reprinted with permission.

Constitutive equation

$$\{\mathbf{m}\} = [\mathbf{D}]\{\boldsymbol{\kappa}\} \tag{6.39}$$

Curvature deflection equation

$$\{\boldsymbol{\kappa}\} = \{\mathbf{L}\}w \tag{6.40}$$

with surface curvature $\{\boldsymbol{\kappa}\}$, deflection to curvature operator $\{\mathbf{L}\}$, moment $\{\mathbf{m}\}$ and plate rigidity $[\mathbf{D}]$ defined as:

$$\{\boldsymbol{\kappa}\} = \left[\kappa_x, \kappa_x, \kappa_{xy}\right]^T \tag{6.41}$$

$$\{\mathbf{L}\} = \left[-\frac{\partial^2}{\partial x^2}, -\frac{\partial^2}{\partial y^2}, -2\frac{\partial^2}{\partial x \partial y}\right]^T \tag{6.42}$$

$$[\mathbf{D}] = \frac{Eh^3}{12\left(1-\nu^2\right)}\begin{bmatrix} 1 & \nu & 0 \\ \nu & 1 & 0 \\ 0 & 0 & \frac{1-\nu}{2} \end{bmatrix} \tag{6.43}$$

with Elastic modulus E, Poisson's ratio ν and plate thickness h. The plate geometry is discretized using a triangular mesh with elements with a linear interpolation of the deflection within each element. A patch of 4 elements as shown in Figure 6.7 is used for deriving the force displacement relationships within a patch.

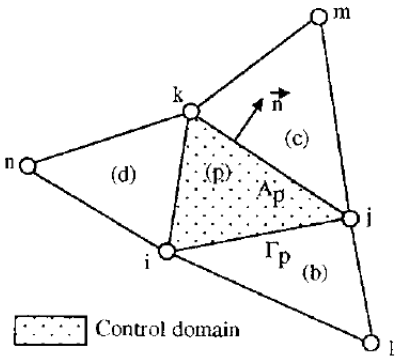

Figure 6.7: Patch of 4 elements, (Oñate and Zárate, 2000), Copyright ©2000 John Wiley & Sons, Ltd, reprinted with permission.

A constant curvature and constant moment within the central element p is assumed such that

$$\{\mathbf{m}\}_p = [\mathbf{D}]_p\{\boldsymbol{\kappa}\}_p \tag{6.44}$$

The constant element curvature can be obtained by taking the area integral of the right-hand side of Equation 6.40, but it requires the evaluation of second derivatives of the deflection w. These second derivatives are zero when a triangular element with linear interpolation of the deflection is used. The deflection of the other nodes in the patch

needs to be included to evaluate the curvature in the central element. The area integral of the curvature deflection relationship can be transformed into a boundary integral by applying Gauss's theorem which relates the 'flux' of the gradient of the deflection w on the cell boundary Γ_p to the cell center curvature value $\{\boldsymbol{\kappa}\}_p$

$$\{\boldsymbol{\kappa}\}_p = \frac{1}{A_p}\int_{A_p}\{\mathbf{L}\}w\,\mathrm{d}A = \frac{1}{A_p}\int_{\Gamma_p}[\mathbf{T}]\nabla w\,\mathrm{d}\Gamma \tag{6.45}$$

with

$$[\mathbf{T}] = \begin{bmatrix} -n_x & 0 & -n_y \\ 0 & -n_y & -n_x \end{bmatrix}^T \tag{6.46}$$

This step of transforming a area integral to a boundary integral in order to evaluate boundary fluxes is typical for a FV discretization. In the boundary integral of Equation 6.45 no second derivatives need to be evaluated any more, only the gradient of the deflection at the 3 boundary edges is required. The issue is that the gradient is constant and only defined within each triangular element and is discontinuous at the boundary. For evaluating the boundary integral, a simple averaged value of the neighbouring elements is used as suggested by Oñate and Zárate (2000). When the linear interpolation functions $[\mathbf{N}]^{(e)}$ are inserted in Equation 6.45, and averaging of the gradient across the boundary is applied, a linear relationship between the patch curvature and the nodal defections $\mathbf{w}_p$ of the 6 nodes in the patch results.

$$\{\boldsymbol{\kappa}\}_p = \frac{1}{A_p}\int_{\Gamma_p}[\mathbf{T}]\nabla[\mathbf{N}]^{(e)}\{\mathbf{w}\}^{(e)} = \mathbf{B}_p\{\mathbf{w}\}_p \tag{6.47}$$

To obtain a relationship between the nodal deflections and the nodal forces the principle of virtual work can be applied

$$\{\delta\mathbf{w}\}_p^T\{\mathbf{f}\}_p = \int_{A_p}\delta\{\boldsymbol{\kappa}\}_p^T\{\mathbf{m}\}_p\,\mathrm{d}A_p \tag{6.48}$$

which after inserting Equation 6.44 and Equation 6.47 gives

$$\{\mathbf{f}\}_p^{\mathrm{int}} = [\mathbf{B}]_p^T[\mathbf{D}]_p\{\boldsymbol{\kappa}\}_p A_p \tag{6.49}$$

Note that Equation 6.47, Equation 6.48 and Equation 6.49 are similar to Equation 6.32, Equation 6.31 and Equation 6.33 but use the curvature $\boldsymbol{\kappa}$ and moment $\mathbf{m}$ as the generalised strain and generalised stress respectively. Equation 6.47 could be inserted in Equation 6.49 to obtain a stiffness matrix as is done by Oñate and Zárate (2000), but is left in the more general form as this allows the use of a non-linear relationship between the nodal displacements and the patch curvature as is required in this study and because no stiffness matrix is required for the explicit time integration used in this study. For the flat plate case, the FE discretization relates the nodal deflection w in the z-direction to the nodal forces in z-direction resulting in the so-called Basic Plate Triangle (BPT) element.

BASIC SHELL TRIANGLE (BST)

Oñate and Zárate (2000) describe the changes to the BPT element which are required for the use in a generally curved shell. This element includes the bending deformation of the shell as well as the in-plane membrane deformation which is included by combining the element with the Constant Strain triangle (CST) element. The resulting element is called the Basic Shell Triangle (BST). The shell bending moments are no longer related to the shell curvature but to the change in shell curvature as the shell can already have an initial curvature in its unloaded shape. The change in curvature is furthermore not related to the nodal deflections of the patch nodes in a single direction but related to nodal displacements of the patch in 3 dimensions. Oñate and Zárate (2000) use a local coordinate system in each triangle of the patch as shown in Figure 6.8 for the derivation of FE description.

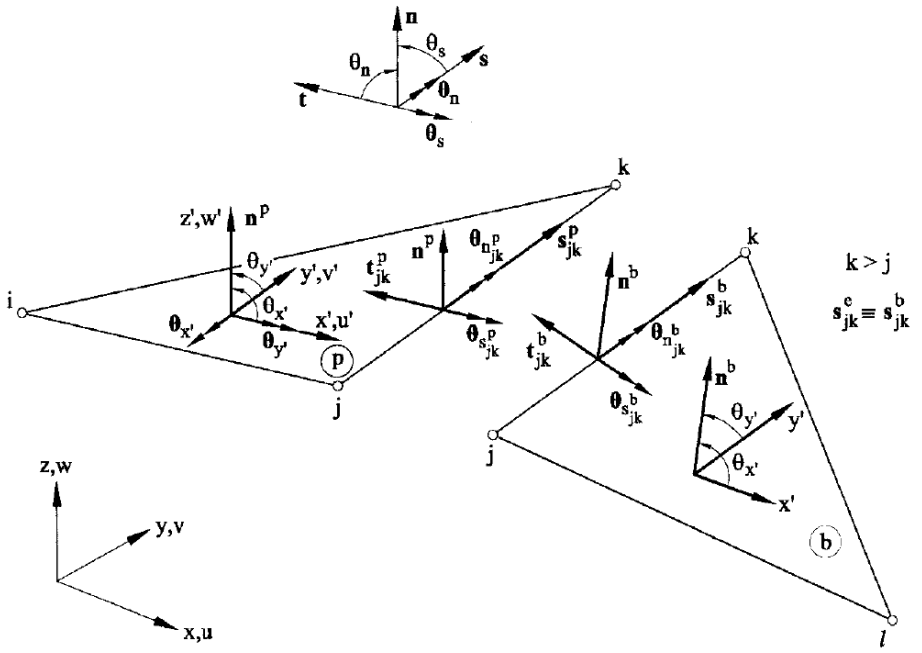

Figure 6.8: Definition of global and local and side coordinate systems, (Oñate and Zárate, 2000), Copyright ©2000 John Wiley & Sons, Ltd, reprinted with permission.

The local coordinate system is used to determine the deflection gradient in each triangle similar to what was done for the BPT element. A deflection gradient represents a local rotation of the shell which is constant within a triangular element. The local rotation of the element is equal to the gradient of the deflection, $\theta_{x'} = \partial w'/\partial x'$ and $\theta_{y'} = \partial w'/\partial y'$, which can be expressed as a function of the tangential and normal side rotations θ_s and θ_n defined in a side coordinate system aligned with an edge of the triangle. For evaluating the boundary integrals, the side rotations of both triangles on an edge are averaged. These side rotations can again be expressed in terms of the local nodal de-

flections of the individual triangles in the patch using the linear shape functions in each triangle by evaluating Equation 6.47. The nodal deflections are then expressed in different local coordinate system for each element by $\{\mathbf{w}\}'_p$. Evaluation of Equation 6.47 then gives the local deflection to local curvature matrix $[\mathbf{S}]_p$

$$\{\delta\boldsymbol{\kappa}\}'_p = [\mathbf{S}]_p\{\delta\mathbf{w}\}'_p \tag{6.50}$$

However, the variation in element curvature $\{\delta\boldsymbol{\kappa}\}'_p$ is then still expressed in terms of the variation of the $4\times 3 = 12$ local nodal deflections expressed in 4 different local coordinate systems in $\{\mathbf{w}\}'_p$. These local deflections can be expressed in terms of the $3\times 6 = 18$ global nodal displacements of the 6 nodes in the patch, $\{\mathbf{u}\}'_p$, using a 18×3 transformation matrix $[\mathbf{C}]_p$.

$$\{\mathbf{w}\}'_p = [\mathbf{C}]_p\{\mathbf{u}\}'_p \tag{6.51}$$

This is then used to define the global displacement to curvature matrix $[\mathbf{B}]_{b_p}$.

$$[\mathbf{B}]_{b_p} = [\mathbf{C}]_p[\mathbf{S}]_p \tag{6.52}$$

In a small displacement situation the global displacement to curvature matrix $[\mathbf{B}]_{b_p}$ can be used to directly relate the patch curvature to the nodal displacements such that an element stiffness matrix can be obtained. Here it is left in a form similar to Equation 6.49 as the model is used here for describing large displacements of the diaphragm within an explicit time integration. This gives for the internal nodal forces

$$\{\mathbf{f}\}^{\text{int}}_{b_p} = [\mathbf{B}]^T_{b_p}[\mathbf{D}]_p\{\boldsymbol{\kappa}\}'_p A_p \tag{6.53}$$

In Equation 6.53 the patch curvature $\{\boldsymbol{\kappa}\}'_p$ is defined in the local coordinate system of the central element. The internal nodal forces $\{\mathbf{f}\}^{\text{int}}_{b_p}$ are defined in global coordinates as $[\mathbf{B}]_{b_p}$ includes the transformation from local to global coordinates. The algebra involved in deriving the BST element is quite involved but is fully worked out by Oñate and Zárate (2000).

CONSTANT STRAIN TRIANGLE (CST)

For including the membrane deformation a standard Constant Strain Triangle (CST) with plane stress conditions is used for which holds

$$\{\mathbf{f}\}^{\text{int}}_{m_p} = [\mathbf{B}]^T_{m_p}[\mathbf{D}]_m\{\boldsymbol{\epsilon}\}'_m A_p \tag{6.54}$$

with

$$[\mathbf{D}]_m = \frac{Eh}{1-\nu^2}\begin{bmatrix} 1 & \nu & 0 \\ \nu & 1 & 0 \\ 0 & 0 & \frac{1-\nu}{2} \end{bmatrix} \tag{6.55}$$

and

$$\{\boldsymbol{\epsilon}\}'_m = [\mathbf{B}]'_0\{\mathbf{u}\}'_m \tag{6.56}$$

The membrane strain $\{\boldsymbol{\epsilon}\}'_m$ is evaluated in a local coordinate system using the in-plane displacements $\{\mathbf{u}\}'_m$ in that local coordinate system and a displacement to strain matrix $[\mathbf{B}]'_0$ defined in the local coordinate system which is evaluated on the original undeformed element indicated by the subscript 0. $[\mathbf{B}]_{m_p}$ is derived from the local in-plane to membrane strain matrix $[\mathbf{B}]'_m$ for which holds

$$\{\delta\boldsymbol{\epsilon}\}'_m = [\mathbf{B}]'_m\{\delta\mathbf{u}\}'_m \tag{6.57}$$

The in-plane nodal displacements in the local coordinate system are related to the patch nodal displacements in the global coordinate system by the transformation matrix $\mathbf{L}_p$ by

$$\{\delta\mathbf{u}\}'_m = [\mathbf{L}]_p\{\delta\mathbf{u}\}_p \tag{6.58}$$

which gives the definition for $[\mathbf{B}]_{m_p}$

$$[\mathbf{B}]_{m_p} = [\mathbf{B}]'_m[\mathbf{L}]_p \tag{6.59}$$

$\{\mathbf{f}\}^{\text{int}}_{m_p}$ is defined in global coordinates as the displacement to strain matrix $[\mathbf{B}]^T_{m_p}$ in Equation 6.54 includes a transformation from local coordinates to global coordinates.

6.3.3. UPDATED LAGRANGIAN FORMULATION

The element as derived in Oñate and Zárate (2000) uses infinitesimal strain theory and small displacement theory which allows the derivation of a constant coefficient stiffness matrix which directly relates the nodal displacements to the internal nodal forces. However, for the diaphragm deformation analysis the small displacement assumption doesn't hold obviously as the displacement of the central plate is between 20 and 30% of the diaphragm diameter. A linear relationship between nodal displacements and internal nodal forces by a constant coefficient stiffness matrix does no longer hold and the relationship becomes strongly non-linear. However, most of the non-linearity is due to the so-called geometric non-linearity and only to a limited extent due to non-linearity in the material behaviour as discussed in section 4.3. The geometric non-linearity is caused by large displacements, rotations and deformation of the structural elements. Here a co-rotational frame of reference is used for every element in which the local deformation is evaluated which are the local element membrane strain $\{\boldsymbol{\epsilon}\}'_m$ and the local change in patch curvature $\{\boldsymbol{\kappa}\}'_p$. Then the infinitesimal strain constitutive model is used to evaluate the membrane stresses and bending moments in the local co-rotational coordinate system.

At the start of every time step the nodal positions are given from the last time step. A so-called updated Lagrangian formulation, (Belytschko *et al.*, 2000), is used for obtaining the internal nodal forces by evaluating Equation 6.53 and Equation 6.54 in the deformed configuration which can be summed to give the patch internal nodal forces in global coordinates

$$\{\mathbf{f}\}^{\text{int}}_p = \{\mathbf{f}\}^{\text{int}}_{b_p} + \{\mathbf{f}\}^{\text{int}}_{m_p} \tag{6.60}$$

The local deflection to local curvature matrix $[\mathbf{S}]_p$ is evaluated in the local co-rotational coordinate systems of each triangle in the patch. $[\mathbf{S}]_p$ can be updated every time step but this is not strictly required as it only depends on the shape of the individual triangle and not its orientation in space or otherwise stated it is invariant under rigid body translation and rotation of the individual triangles. When the in-plane membrane strain variation is not too significant within a single time step, updating $[\mathbf{S}]_p$ is not required every time step. Update of the transformation matrix $[\mathbf{C}]_p$, and thereby the global displacement to curvature matrix $[\mathbf{B}]_{b_p}$, is required more often, for example every time step, such that $[\mathbf{B}]_{b_p}$ represents the actual global displacement to curvature matrix belonging to the nodal positions of the deformed configuration. The curvature in the element local coordinate system $\{\boldsymbol{\kappa}\}'_p$ is directly evaluated by calculating the normal side rotations θ_n from the face normals of the patch triangles in the deformed configuration. The tangential side rotations θ_s are absent as the side coordinate system remains aligned to the element edge in the deformed configuration when using an updated Lagrangian formulation, further simplifying the evaluation of the local patch curvature. Furthermore the element area A_p is updated every time step which is also used to update the element thickness h in $[\mathbf{D}]_p$ using an incompressibility condition for the element volume. This procedure includes all geometrically non-linearities in the evaluation of $\{\mathbf{f}\}^{\text{int}}_{b_p}$ in Equation 6.53 while still using a linear small strain constitutive model. The same update procedure applies to the evaluation of the nodal forces in Equation 6.54 related to the membrane strain in the element.

6.3.4. CONTACT MODEL

Next to the Fluid Structure Interaction between the flexible structure and the fluid flow, a structure-structure interaction between the flexible diaphragm and the rigid housing wall is possible as well. Especially at the end of the suction stroke, the diaphragm can come close to the rear wall of the diaphragm housing and make contact with it. A relatively simple contact model based on the so-called penalty method as described by Belytschko *et al.* (2000) is used. Both the deformable structure as well as the potential contact surfaces are represented by a triangular mesh. The rigid contact surfaces are checked for penetration by the FE nodes every time step. When a positive penetration is detected, a restoring force, $\{\mathbf{f}\}^{\text{contact}}$, proportional to the penetration depth is applied in the vertex or node normal direction of the structural mesh. This vertex or node normal is the average of the face normals of the triangles which share that node. No friction is included in this simple contact model. The procedure to check for penetration is further clarified with the help of Figure 6.9.

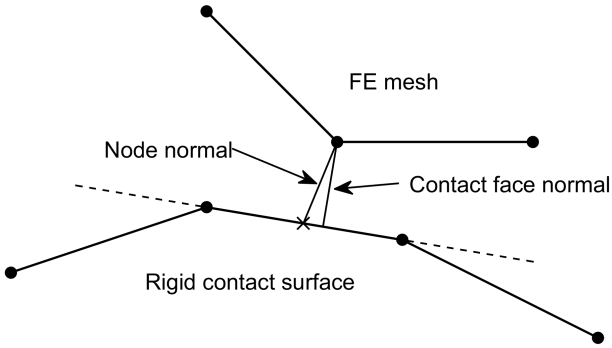

Figure 6.9: Penetration check in 2D situation

To verify whether a node has penetrated a specific triangle of the rigid contact surface, the intersection point × of the node normal with the plane through the triangle face, indicated by the dashed line in Figure 6.9, is determined first. Then it is evaluated whether the intersection point lies inside or outside of the rigid contact triangle. When it lies inside the triangle, the distance from the rigid contact triangle face to the node is evaluated by projecting the intersection point to node vector on the rigid contact triangle face normal vector. Only when a negative distance, hence positive penetration, is found, a contact condition is determined and a restoring force proportional to the penetration depth is applied on the node in the node normal direction of the triangular FE mesh. The procedure described so-far would require the evaluation of the contact condition of every node with every rigid contact triangle which would represents a huge computational burden. In order to speed up the contact calculation a contact detection algorithm has been developed which significantly reduces the number of faces to check for penetration. The procedure is further clarified with the help Figure 6.10 and follows the following steps:

1: Subdivide the computational domain in rectangular sub-domains
2: For every sub-domain list the triangle centres of the rigid contact surface that reside in that sub-domain
3: Subdivide the computational domain in a 2^{nd} series of rectangular sub-domains of equal side length but staggered with respect to the sub-domains which hold the rigid contact triangles.
4: **for all** nodes of FE mesh
5: Determine in which sub-domain of the 2^{nd} series the node resides
6: Gather the previously generated lists of rigid contact triangles whose center resides in the 8 (in 3D or 4 in 2D) neighbouring and overlapping sub-domains which hold the rigid contact triangles.
7: Determine the distance between the node and the listed triangle centres and select those who are within a small search radius of a few mesh sizes
8: Determine the intersection coordinates of the node normal and planes through the individual triangles

9: Select the rigid contact triangles which have intersection coordinates within the triangle
10: Determine the distance between node and rigid contact triangle face by projecting the intersection point to node vector on rigid contact face normal vector
11: Select the shortest distance, when the node normal crosses multiple faces, and determine whether the node has penetrated the nearest face by evaluating the sign of the shortest distance
12: When a node has penetrated the contact body, set a restoring force in the opposite direction of the node normal and scale it proportional with the penetration depth
13: **end**

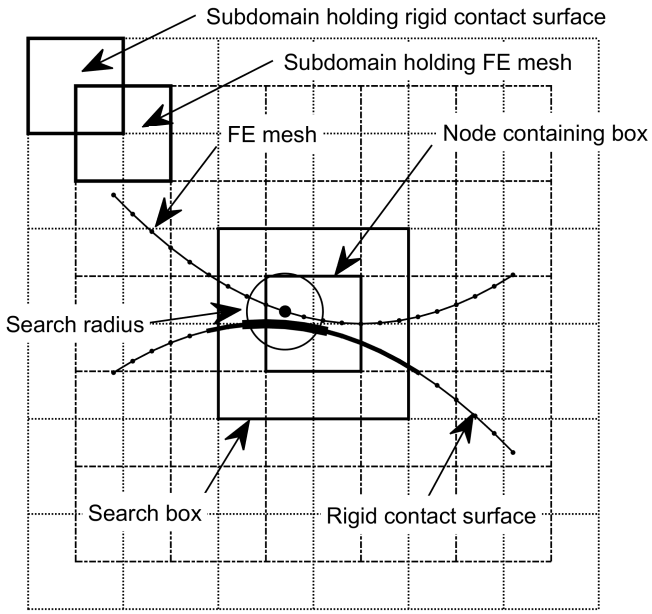

Figure 6.10: Contact search algorithm in 2D situation

The initial rectangular search domain has twice the dimensions of a single sub-domain but it is guaranteed to include all triangle centres which lie within a distance of half the sub-domain size from the node whose contact condition is evaluated. While proceeding in the contact detection algorithm the number of triangles which remain a candidate for potential penetration are successively reduced. The computational complexity of the calculation increases while proceeding, but the calculation only has to be applied on a successively reducing number of candidate penetrations, thereby limiting computational effort. The procedure described above evaluates the penetration of the rigid contact surface by the nodes of the FE mesh. However, the nodes of the FE mesh lie on the mid-surface of the shell model and not on its actual contact surface. In order to correct

for this, a surface point is placed on the contacting side of the FE mesh placed half the local shell thickness away from the actual node in the direction of the node normal. Instead of checking for the penetration by the actual node, the penetration by the surface point is evaluated.

The contact stiffness poses an additional stability limit which can reduce the allowable time step when it is selected too high, (Belytschko *et al.*, 2000). The contact stiffness should not be selected much higher than the in-plane nodal stiffness of node which is roughly Eh. The actual normal stiffness of the diaphragm is roughly EA_p/h which means that it is roughly equal to the in-plane stiffness when the element size is of similar size as the plate thickness. In this study the minimum of both conditions is used.

6.3.5. DISPLACEMENT AND DEFORMATION CONSTRAINTS

The outer rim of the diaphragm is clamped between the cover and the pump chamber housing thereby constraining any displacement of the outer edge of the diaphragm. In the explicit time integration used in this study, this displacement constraint is simply imposed by excluding the constrained nodes at the outer edge from the temporal integration, thereby maintaining their position. Next to the outer edge, the central plate in the diaphragm and the connected monitoring rod pose additional constraints on the displacement and deformation of the diaphragm in this central region. The central plate prohibits any deformation of the diaphragm and the monitoring rod only allows translation in rotation around the monitoring rod axis. These constraints can be included in the model quite easily by using penalty forces on the structural nodes when the displacement or deformation differs from the constraints imposed by the central plate and the monitoring rod using a method similar as described by Peskin and McQueen (1980). The z-position of the central plate position is determined every time step by averaging the z-coordinates of the structural nodes which are constrained by the central plate. The undeformed nodal positions of the constrained nodes are determined subtracting the z-coordinate of the central plate for the nodal positions. A penalty force $\{\mathbf{f}\}^{\text{constraint}}$ is then applied on the constrained nodes in the opposite direction of the displacement of the nodes with respect to the undeformed central plate position.

6.3.6. TEMPORAL INTEGRATION

Although the structural model and its temporal integration finally has to be merged with the flow solver, a temporal integration of the structure-only model is described here as well. This is used for structure-only evaluations and gives insights in the stability limits which play a role the FSI case as well. Explicit temporal integration is used in this study as it finally has to be combined with and explicit flow solver. The discrete momentum equation which needs to be solved is

$$[\mathbf{M}]\{\ddot{\mathbf{x}}\} - \{\mathbf{f}\}^{\text{int}} = \{\mathbf{f}\}^{\text{ext}} = \{\mathbf{f}\}^{\text{fluid}} + \{\mathbf{f}\}^{\text{contact}} + \{\mathbf{f}\}^{\text{constaints}} \tag{6.61}$$

which holds both for a single element as well as for the complete system. The global system force vector can be assembled from the element, or in this case patch, force vectors by a so-called assembly or scatter operation

$$\{\mathbf{f}\} = \{\mathbf{f}\}^{\text{ext}} - \{\mathbf{f}\}^{\text{int}} = \sum_e [\mathbf{L}]_e^T \{\mathbf{f}\}_e^{\text{ext}} - \sum_p [\mathbf{L}]_p \{\mathbf{f}\}_p^{\text{int}} \tag{6.62}$$

in which $[\mathbf{L}]_e$ is the element connectivity matrix and $[\mathbf{L}]_p$ is the patch connectivity matrix which are a boolean matrices which link the element or patch or nodal indices to the global nodal indices. Note the difference between the patch and the element connectivity as the patches of 4 triangular elements are overlapping each other. The mass matrix can be assembled by summing over the element contributions but then both permutation of rows and columns is required as the inertial force is a product of mass and acceleration and which element vectors are both permuted in the assembly process.

$$[\mathbf{M}] = \sum_e [\mathbf{L}]_e^T [\mathbf{M}]_e [\mathbf{L}]_e \tag{6.63}$$

As mentioned before, a diagonal or lumped mass matrix $[\mathbf{M}]$ is used in the FE discretization. The inversion of a diagonal mass matrix is trivial as the diagonal elements of the inverted mass matrix $[\mathbf{M}]^{-1}$ are simply the reciprocal values of the diagonal elements of the mass matrix $[\mathbf{M}]$. Integration of Equation 6.61 then simplifies to applying Newton's second law on each individual node. For the triangular shell elements the diagonalization of the mass matrix is trivial by assigning $\frac{1}{3}$ of the element mass to each node. In a regular mesh the global nodal mass is then the summed contribution of $\frac{1}{3}$ of element masses of the 6 surrounding elements.

A basic explicit Euler method could be used for the time integration of the nodal positions $\mathbf{x}$ of the diaphragm using Newton's second law:

$$\{\mathbf{v}\}^{n+1} = \{\mathbf{v}\}^n + [\mathbf{M}]^{-1} \{\mathbf{f}\}^n \Delta t \tag{6.64}$$

$$\{\mathbf{x}\}^{n+1} = \{\mathbf{x}\}^n + \{\mathbf{v}\}^n \Delta t \tag{6.65}$$

using nodal velocities $\{\mathbf{v}\}$, nodal forces $\{\mathbf{f}\}$ and nodal masses $[\mathbf{M}]$. Use of the basic Euler method is not recommended as it is known to add energy to the system and can easily become unstable, Scherer (2010). An improvement is described by Cromer (1981) who uses the velocity at the new time level to update the position which is called the Euler-Cromer method which is energy conserving.

$$\{\mathbf{v}\}^{n+1} = \{\mathbf{v}\}^n + [\mathbf{M}]^{-1} \{\mathbf{f}\}^n \Delta t \tag{6.66}$$

$$\{\mathbf{x}\}^{n+1} = \{\mathbf{x}\}^n + \{\mathbf{v}\}^{n+1} \Delta t \tag{6.67}$$

Both the basic explicit Euler and the Euler-Cromer method are first-order accurate. A simple change by using the velocity at intermediate time levels makes the method second-order accurate which is then called the Leap-frog method, (Scherer, 2010):

$$\{\mathbf{v}\}^{n+1/2} = \{\mathbf{v}\}^{n-1/2} + [\mathbf{M}]^{-1} \{\mathbf{f}\}^n \Delta t \tag{6.68}$$

$$\{\mathbf{x}\}^{n+1} = \{\mathbf{x}\}^n + \{\mathbf{v}\}^{n+1/2} \Delta t \tag{6.69}$$

Leap-frog is similar to the Velocity-Verlet method, (Scherer, 2010), which updates the velocity in 2 half time steps such that velocity data is also available at the integer time intervals as used for the position. Both Leap-frog as well as Velocity-Verlet are referred to as the central difference method by Belytschko *et al.* (2000) who identifies them as the most widely used time integration methods for explicit structural dynamics simulations. The Leap-frog method is used further in this study as there is no reason for having the nodal velocities as an output at the same time level as the positions. The first update of the velocity uses a half time step when starting with initial conditions at the same time level $n = 0$. It can be seen that apart from this start-up, the Leapfrog has the same update structure as the Euler-Cromer method and is therefore just as expensive as the basic explicit Euler method but is both energy conserving and second-order accurate.

6.3.7. STABILITY CRITERIA

As the Leap-frog method is explicit, it has a time step limited by stability requirements. A stable time step is limited by the highest natural frequency in the system by, Scherer (2010)

$$\Delta t \leq \frac{2}{\omega_n} \tag{6.70}$$

For a continuum Belytschko *et al.* (2000) indicate that for low order elements this is equivalent to

$$\Delta t \leq \frac{\Delta_e}{c_e} \tag{6.71}$$

with element size Δ_e and speed of sound within the element $c_e = \sqrt{\frac{K_e}{\rho_e}}$. This stability limit can therefore be seen as a CFL condition limiting the time step to the propagation time of a mechanical wave over a single mesh spacing. For the shell model used in this study, the highest natural frequency ω_n has to be estimated. The highest natural frequency can be estimated by considering the motion of a single structural node in the model while all other nodes are constrained. For the natural frequency ω_n of single degree of freedom mass spring system holds:

$$\omega_n = \sqrt{\frac{k_n}{m}} \tag{6.72}$$

with nodal stiffness k_n and nodal mass m. The nodal stiffness in the shell model results from the superposition of 3 structural deformation modes; the in-plane or membrane stiffness, the out of plane bending stiffness and when considering contact, a contact stiffness as is described later. The question is how these individual stiffness's scale with the element dimension Δ_e and the shell thickness h. From a dimensional analysis of the force displacement relationship of the membrane deformation, Equation 6.54, it follows that the nodal membrane stiffness k_m scales proportional with the elastic modulus E and the shell thickness h but that it is independent on the element size Δ_e

$$k_m \sim Eh \tag{6.73}$$

For the nodal bending stiffness k_b it similarly follows from Equation 6.53 that it is proportional with the shell thickness to the power 3 and inversely proportional with the element size Δ_e squared

$$k_b \sim \frac{Eh^3}{\Delta_e^2} \tag{6.74}$$

The nodal contact stiffness k_c is assumed to be proportional with the stiffness across the shell thickness which is inversely proportional to the shell thickness and proportional with element surface area, hence proportional with the element size squared.

$$k_c \sim \frac{E\Delta_e^2}{h} \tag{6.75}$$

The nodal mass in the shell model scales proportional with the shell density, the shell thickness and element area, hence element size squared

$$m \sim \rho h \Delta_e^2 \tag{6.76}$$

For the natural frequency related to the individual nodal stiffness's then holds

$$\omega_m = \sqrt{\frac{k_m}{m}} \sim \sqrt{\frac{E}{\rho}} \Delta_e^{-1} \tag{6.77}$$

$$\omega_b = \sqrt{\frac{k_b}{m}} \sim \sqrt{\frac{E}{\rho}} h^2 \Delta_e^{-2} \tag{6.78}$$

$$\omega_c = \sqrt{\frac{k_c}{m}} \sim \sqrt{\frac{E}{\rho}} h^{-1} \tag{6.79}$$

From the scale analysis of the individual stiffness's it follows that the contact stiffness is dominant when using large elements sizes, the membrane stiffness might be dominant at intermediate element sizes, depending on the proportionality constant which applies and that the nodal bending stiffness is dominant when using small element sizes. The nodal natural frequency scales inversely proportional with the element size when the nodal membrane stiffness is dominant. The time step restriction is then proportional with the element size, similar as in a continuum. When using very small elements however, the natural frequency and hence the time step restriction is dominated by the bending stiffness and the time step restriction becomes proportional with the element size squared which makes it very restrictive for small element sizes. An order of magnitude estimation of this transition can be made by equating the proportionality relationships derived above ($k_m = k_b = k_c$) which then indicates that the bending stiffness becomes dominant when the element size is of the same order as the shell thickness. When the bending stiffness becomes too restrictive in the time step it might be better to use either a continuum description using solid elements instead of a shell elements or to use a thick plate model which limits the out of plane stiffness by including shear deformation. This nodal shear stiffness scales similar as the membrane stiffness such that a time step

restriction proportional with the elements size results. The anticipated element size of $O(\Delta_e) = 10^{-2}$ m is of the same order as the diaphragm thickness. The use of the thin shell model might then not be overly restrictive but when performing mesh refinement it must be anticipated that the time step restriction becomes dominated by the bending stiffness which might prohibit large mesh refinements. An estimate of the time step restriction is made by amusing that the membrane stiffness is still dominant. With a elastomer density of $O(\rho) = 10^3\,\mathrm{kg/m^3}$, an elastic modulus of $O(E) = 10^6$ Pa and a typical element size of $O(\Delta_e) = 10^{-2}$ m this gives a time step limit of $O(\Delta t) = O(\Delta_e/\sqrt{\frac{E}{\rho}}) = 0.1 - 1$ ms.

6.4. FLUID STRUCTURE INTERACTION

The interaction between the flow model and the structural model needs to be included in order to model the Fluid Structure Interaction (FSI) between the fluid flow and the immersed elastic structure. Next to the interaction between the fluid flow and the elastic structure, interaction between the fluid flow and the immersed rigid housing needs to be included as well. Both are included using an Immersed Boundary Method (IBM). For the flexible structure an IBM using feedback forcing is used while for the interaction with the rigid housing and IBM with direct forcing is used, (Mittal and Iaccarino, 2005).

6.4.1. IBM WITH FEEDBACK FORCING FOR FLEXIBLE STRUCTURES

The interaction between the immersed flexible diaphragm and the fluid flow is modelled using an IBM which uses so-called feedback forcing, (Mittal and Iaccarino, 2005), which was originally developed by Peskin, (Peskin, 1977, Peskin and McQueen, 1989, Peskin, 2002). In this method the fluid flow is solved on a fixed Eulerian grid in which a Lagrangian mesh of the deformable structure is immersed. The fluid flow advects the immersed nodes of the deformable structure. External nodal forces are required to balance the internal nodal forces generated by the deformation of the structure. These external nodal forces are to be supported in the fluid as body forces when they are not resulting from contact with the rigid contact surfaces or from deformation constraints by the central plate and monitoring rod. When considering the FSI, the nodal forces are not represented as column matrices in Voigt notation but as Cartesian tensors, indicated by the omission of the brace, {}. For the elastic forces $\mathbf{f}_e$ acting on the fluid holds

$$\mathbf{f}_e = \mathbf{f}^{\text{int}} + \mathbf{f}^{\text{contact}} + \mathbf{f}^{\text{constraints}} \tag{6.80}$$

The elastic force tensor $\mathbf{f}_e$ represents the discrete elastic forces acting on the fluid at the nodal positions of the Lagrangian structural mesh. The Lagrangian forces represent impulse forces on the Eularian grid obtained by the product of the elastic force tensor $\mathbf{f}_e$ with the Dirac delta function δ. The fluid body force per unit volume $\mathbf{b}_e$ due to the elastic forces can then be obtained by integrating over the deformed and immersed structural domain Ω

$$\mathbf{b}_e\,\mathrm{d}V = \int_\Omega \mathbf{f}_e \delta\left(|\mathbf{x}_f - \mathbf{x}_s|\right)\mathrm{d}\Omega \tag{6.81}$$

in which δ is the Dirac delta function which has a unity value when the distance between the structural position $\mathbf{x}_s$ and the Eulerian fluid position $\mathbf{x}_f$ is zero and has a

zero value elsewhere. The structural nodes are immersed in and advected by the fluid flow with velocity $\mathbf{v}_f$ such that the velocity of a structural nodes $\mathbf{v}_s$ is given by

$$\mathbf{v}_s(\mathbf{x}_s) = \mathbf{v}_f(\mathbf{x}_s) = \int_\Omega \mathbf{v}_f(\mathbf{x}_f)\,\delta(|\mathbf{x}_f - \mathbf{x}_s|)\,\mathrm{d}\Omega \tag{6.82}$$

The Lagrangian structural nodes generally don't correspond to the computational points or cell centres on the Eulerian grid. When evaluated on a discrete grid, a continuous approximation of the Dirac delta function δ is required. This distribution or interpolation function which approximates approximates δ is required to distribute the nodal forces to the surrounding Eulerian fluid points and interpolate the fluid velocities to the structural nodes. The support width of the distribution function should furthermore be wide enough such that no jumps in the body forces are generated when the structural nodes move through the fluid grid. The Dirac delta function δ is approximated in 3D by the product of 3 one dimensional functions , ϕ

$$\delta(\mathbf{x}) \approx \phi\left(\frac{x}{\Delta_x}\right)\phi\left(\frac{y}{\Delta_y}\right)\phi\left(\frac{z}{\Delta_z}\right) \tag{6.83}$$

In this study a basic cosine function is used as was originally used by Peskin (1977)

$$\phi(r) = \begin{cases} \frac{1}{4}\left(1+\cos\left(\frac{\pi r}{2}\right)\right) & \text{if } |r| \le 2 \\ 0 & \text{if } |r| > 2 \end{cases} \tag{6.84}$$

with $r = x/\Delta_x$, $r = y/\Delta_y$ or $r = z/\Delta_z$ being the distances between the structural nodes and the fluid points scaled with the fluid grid spacing. The function according Equation 6.84 is continuous such that it avoids jumps in the distributed forces or interpolated velocity when the structural nodes move through the fluid grid and has a finite support width which is nice from a computational efficiency point of view. Furthermore conservation of momentum is assured as

$$\sum_j \phi(r-j) = 1 \tag{6.85}$$

for all real r and integer j which means that the sum of the discrete body forces equals the discrete nodal force which was distributed. The interpolation function according Equation 6.84 will interpolate smooth functions with second-order accuracy but because the velocity field across the boundary is generally not smooth across the boundary, the spatial accuracy of this IBM is generally only first-order, (Peskin, 2002).

The used time integration of the fluid structure interaction model is quite similar to the Leap-frog method which was described for explicit integration of the structure-only equations. Update of the velocity of the flow field, and therefore of the velocities of the structural nodes as well, is done with a explicit first-order method as described in section 6.2 which is similar as velocity update in the Leap-frod method shown in Equation 6.68. These flow velocities are used to obtain the interpolated nodal velocities of the structure according Equation 6.82. These nodal velocities are then used to update the position of the structural nodes using the position update in the Leap-frog method shown in Equation 6.69. As the integration of the nodal acceleration is included in the

temporal integration of the momentum equations according Equation 6.3, any structural nodal mass $\mathbf{M}_s$ which has to be included, needs to be included in Equation 6.3 as well. When the immersed structure is neutrally buoyant no additional mass of the structure is present as it is already accounted for by fluid density. When any excess nodal mass needs to be included, it can be included by locally changing the fluid density for which the same distribution function δ can be used, (Peskin, 2002).

$$\rho \, \mathrm{d}V = \rho_f \, \mathrm{d}V + \int_\Omega \frac{\rho_s - \rho_f}{\rho_s} \mathbf{M}_s \delta \left(|\mathbf{x}_f - \mathbf{x}_s| \right) \mathrm{d}\Omega \tag{6.86}$$

STABILITY CRITERIA

A similar time step restriction based on the highest natural frequency in the structural model as present in the explicit time integration of the structure-only equations applies in the FSI situation as well, next to the time step restrictions which apply for the explicit integration of the Navier-Stokes equations. The stiffness's in the FSI model obviously scale similar as in the structure-only model, but the mass scaling is a bit different. When using a mass-less immersed boundary method, no structural mass is present but some part of the surrounding fluid acts as an added nodal mass. When the structural mesh size is proportional to the fluid grid size it seems logical to assume a effective fluid mass m_f which scales with the fluid density ρ_f and the grid size Δ_f to the power 3

$$m_f \sim \rho_f \Delta_f^3 \tag{6.87}$$

For the natural frequency related to the individual nodal stiffness's as described in subsection 6.3.7 then holds

$$\omega_m = \sqrt{\frac{k_m}{m_f}} \sim \sqrt{\frac{E}{\rho}} h^{0.5} \Delta_f^{-1.5} \tag{6.88}$$

$$\omega_b = \sqrt{\frac{k_b}{m_f}} \sim \sqrt{\frac{E}{\rho}} h^{1.5} \Delta_f^{-2.5} \tag{6.89}$$

$$\omega_c = \sqrt{\frac{k_c}{m_f}} \sim \sqrt{\frac{E}{\rho}} h^{-0.5} \Delta_f^{-0.5} \tag{6.90}$$

A time step restriction proportional to the fluid grid and structural mesh size to the power 1.5 and 2.5 results for a nodal stiffness dominated by respective membrane and bending stiffness, hence more restrictive than in the structure-only case where the exponents 1 and 2 respectively apply. This has also been observed in some undocumented numerical experiments by the author. When the immersed structure has a higher density, the time step limitation moves more towards the proportionality derived for the structure-only case as the nodal mass scales with the mesh size squared for a shell element. The stability limit can be tempered a bit by artificially increasing the nodal mass locally, which can be done in areas with low fluid and hence structure velocities, such as near the clamping area of the diaphragm.

6.4.2. IBM WITH DIRECT FORCING FOR RIGID STRUCTURES

In the previous section the fluid structure interaction between the flexible immersed boundary and the fluid flow is described. This approach is used to model the interaction between the deformable diaphragm and the fluid flow. The interaction between the rigid housing and the fluid flow needs to be modelled as well. One could consider to use the same IBM as used for the flexible structure with an increased stiffness of the structural model in order to mimic its rigidity. However this will put severe restrictions on the allowable time step. In order to circumvent this restriction, a direct forcing IBM as described by Fadlun *et al.* (2000) is used. In this method the time discretized Navier-Stokes equations as given by Equation 6.3 are used as a starting point. On the boundary of and within the immersed rigid structure, the velocity at the new time level $\mathbf{v}^{n+1}$ is known. This is simply the velocity of the immersed rigid structure at the new time level $\mathbf{v}_b^{n+1}$ which is identically zero in this study as it represent the rigid stationary pump chamber. The body force required to enforce the fluid flow velocity to the velocity of the immersed structure can be obtained from Equation 6.3 which gives

$$\mathbf{b_r}^n = \rho^n \frac{\mathbf{v}_b^{n+1} - \mathbf{v}^n}{\Delta t} + \nabla \cdot \left(\rho^n \mathbf{v}^n \mathbf{v}^n\right) + \nabla p^{n+1} - \nabla \cdot \boldsymbol{\tau}^n - \mathbf{b}_e^n - \mathbf{b}_g^n \tag{6.91}$$

Note that the body force term $\mathbf{b}^n$ in Equation 6.3 is split here into a body force term $\mathbf{b}_e^n$ representing the presence of the elastic immersed structure, a body force term $\mathbf{b}_g^n$ representing the gravitational load and a body force term $\mathbf{b}_r^n$ representing the presence of the rigid immersed structure. The required body force $\mathbf{b}_r^n$ can not be explicitly calculated from Equation 6.91 is it contains the pressure at the new time level p^{n+1}. An estimate of the pressure at the new time level has to be made, for which the pressure at the current time level p^n is used in this study which is most straight forward and allows an explicit evaluation of $\mathbf{b}_r^n$. As the determination of the body force does not include any dynamic process it does not place any additional limitations of the allowable time step.

The forcing described above would only be correct when the fluid points on which the forcing is applied lie exactly on the boundary of the immersed rigid structure. For a curved geometry this does generally not hold and it can never hold when using a staggered grid as the control volumes for the individual flow direction don't coincide. Fadlun *et al.* (2000) evaluated three interpolation methods for determining the required forcing term:

Staircase approximation. The simplest method is to consider a fluid point either to be part of the fluid flow such that it gets no forcing or consider it to be part of the immersed rigid structure and such that it gets a full forcing according Equation 6.91. The immersed rigid structure is then represented as a staircase which is different for every flow direction in case of the staggered grid used in this study. This makes the approximation of the geometry somewhat diffuse. The convergence study by Fadlun *et al.* (2000) indicates that this approach gives less than first-order spatial convergence.

Scaling of body force. An improvement is obtained by scaling the body force in Equation 6.91 with the volume fraction of the fluid cell which is occupied by the im-

mersed rigid structure. The convergence study by Fadlun *et al.* (2000) indicates that this approach gives a first-order spatial convergence.

Linear interpolation. A further improvement is possible when the velocity of the first point next to the boundary in the fluid is determined such that a linear interpolation of the velocity in the fluid towards the boundary gives the correct velocity of the immersed rigid structure. From this velocity the forcing is calculated with Equation 6.91. Instead of the first point in the fluid, the first point in the rigid boundary could be used as well. The convergence study by Fadlun *et al.* (2000) indicates that this approach gives a second-order spatial convergence.

In this study the second method using the scaling of the body force is used as this is relatively simple to implement and has the same order of spatial convergence as the IBM used for the flexible immersed structure.

6.5. IMPLEMENTATION

MATLAB® IMPLEMENTATION

The numerical model as described in this chapter has been developed from scratch and has been implemented in the high-level programming environment Matlab® a product of MathWorks®, MathWorks (2016). Matlab® was initially selected as the author had some previous programming experience in Matlab®. It was initially regarded as an ideal programming environment for getting familiar with the implementation of numerical procedures and for the prototyping parts of the numerical model but not necessary most suitable for the final implementation of an efficient numerical model. When developing the code however, it turned out that the computational performance is not that bad at all when a few basic tricks for speeding up the Matlab® code are included. The most important ones are:

- *Pre-allocation* of arrays. Memory has to be re-allocated when an array grows within e.g. a `for`-loop. This re-allocation can be prevented by initializing a array of the often known end size of the array.
- *Vectorizing* of array operations can be used instead of performing identical serial operations on elements in an array in a `for`-loop. The vectorized operations can be handled by the processor in parallel within a single process. Note that this is different from parallel processing where different processes are handled in parallel by parallel processors or computational cores.
- Use of *logical indexing*. A subgroup of an array which fulfils a logical condition can be created by using a vectorized version of the logical condition for indexing in the array. This vectorized version of the logical condition in essence creates a boolean mask which is used to select entities in the array.
- Use *built-in* functions based on pre-compiles code. Matlab® is an interpreted code which means that a code is executed line by line without being compiled in advance as is done with C or Fortran code for example. Many basic function are however built-in the computational core of Matlab® and are pre-compiled. Use

of these built-in functions is often faster than interpreted versions implemented in Matlab® code. Examples are Fast Fourier Transform, multi dimensional array convolution and the `triangulation` and `griddedInterpolant` classes for operations on 2D and 3D triangulated data and interpolation of gridded data receptively.

- *Avoid repetitive calls* to sub-functions by vectorization or *in-lining* of simple functions. As Matlab® is an interpreted language repetitive function calls within, e.g. for element wise operation in a `for`-loop, can be costly. When the function accepts or can be changed to accept arrays, repetitive call are eliminated. When the function only performs simple basic operations it is faster to not use a sub-function at all and code the sub-function in-line of the calling function.

All these tricks have been used when implementing the numerical model but most essential is obviously the vectorization of array operations which has been used extensively. Although not used in this study further improvement of the computational efficiency within Matlab® is possible by explicitly program parallel processing, computation on a GPU and and use of pre-compiled C, C++ or Fortran subroutines by using so-called MEX (Matlab EXecutabe)-functions. Further advantages experienced while developing the code were the high-level programming characteristics such omission of the need for variable declaration, the versatile data types and structures, the integrated graphics environment and code profiling tools, large user community and the large amount of open-source toolboxes.

For the field data of the flow solver multidimensional arrays is used whose indices (i,j,k) correspond to the physical indices of the structured numerical grid. Implementation of discrete grid operations is therefore straight forward by using (vectorized) array indexing. As most of the operations in the flow solver are basic addition, subtraction, multiplication and division operations on a structured grid, a rather efficient flow solver results by properly vectorizing the code. The operations on the unstructured FE mesh are somewhat more computationally intensive per FE element are mainly involve many small vector matrix multiplications on FE element level. Some of these operations, such as cross and inner product operations used in geometry calculations, have been vectorized, but other operations still required the use of `for`-loops.

DESCRIPTION REFERENCE MODEL

The numerical model has been configured and parametrized to correspond to the experimental set-up described in chapter 7. This reference model is used as a basis for a parameter study described in chapter 8. Settings of some characteristics used in the reference model are shown in Table 6.1.

Table 6.1: Setting of characteristics in reference FSI model

Characteristic	**Setting**
Stroke volume	10 litre
Stroke rate	100 spm
Diaphragm displacement volume at zero stroke volume	2 litre
Diaphragm clamping diameter	454 mm
Diameter propelling fluid port	125 mm
Diameter suction and discharge port	100 mm
Gravitational acceleration	$9.81\,\mathrm{kg\,m\,s^{-2}}$
Density propelling fluid	$900\,\mathrm{kg/m^3}$
Newtonian viscosity propelling fluid	40 mPa s
Density pumped liquid	$1000\,\mathrm{kg/m^3}$
Newtonian viscosity pumped liquid	1 mPa s
Elastic modulus diaphragm rubber	2.7 MPa
Poisson ratio diaphragm rubber	0.5
Size of computational domain	$0.5 \times 1 \times 0.5$ m
Number of fluid cells (excl. ghost cells)	$64 \times 128 \times 64 = 524{,}288$
Fluid cell size	$7.81 \times 7.81 \times 7.81$ mm
Number of structural nodes	14077
Number of structural elements	27744
Typical edge length of structural elements	4 mm
Advection scheme	TVD with UMIST limiter
Eddy viscosity model	None (ILES)
Maximum time step when not limited by CFL condition	0.5 ms

A visual impression of the geometry, fluid grid and structural mesh is shown in Figure 6.11. Here one can recognise the rectangular fluid domain in which the fluid volume is immersed. The majority of the computational volume is solid as only 14% of the computational volume actually contains fluid. For the solid and fluid geometry only full cells are shown which are respectively 100% solid or 100% fluid. The approximation of the boundary of the fluid domain might seem rather coarse but its actual representation is more smooth due to the used immersed boundary method. The immersed boundary method as implemented scales the body forces with the volume fraction of the cell which is solid which gives a first-order approximation of the true fluid-solid interface. This is somewhat shown by the fluid-solid interface represented by an isosurface of the 50% volume faction calculated from the 3D array containing the volume fractions. The triangular structural mesh of the diaphragm on the other hand is very fine with a typical edge length of approximately 50% of the fluid cell size which follows from the requirement for a leak free boundary with the implemented immersed boundary method with feedback forcing as described by Peskin (2002). The rear wall contact surfaces also consists of a triangular mesh for which a mesh size similar to the structural mesh was chosen.

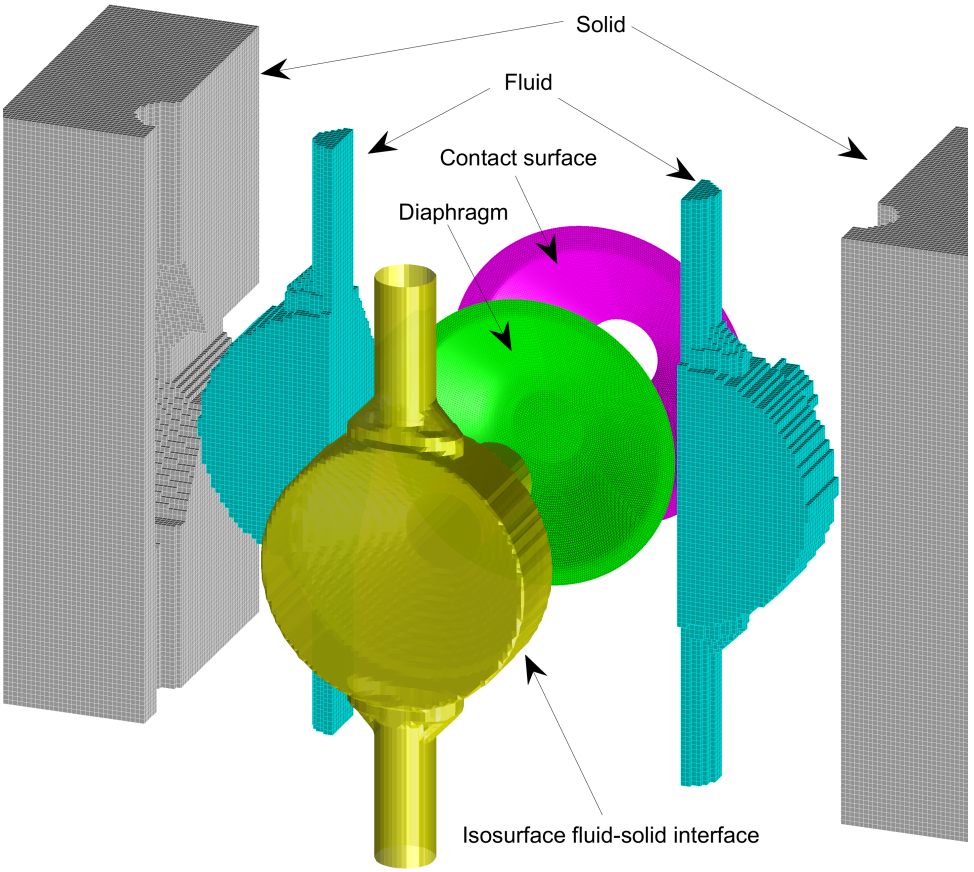

Figure 6.11: Visual impression of 3D geometry, fluid grid and structural mesh used in reference model

BOUNDARY CONDITIONS

Boundary conditions for the momentum equations of the fluid flow have been applied to the edges of the fluid domain, which are of the free-slip wall, no-slip wall, inflow or outflow type whose implementation is described in section 6.2. On the boundary of the computational domain 4 different areas can be identified with each their specific boundary conditions:

1. Boundary of computational domain cutting through the immersed rigid solid of housing. Here a free-slip wall boundary condition is used. This makes sure no fluid is leaving or entering the computational domain in this area of the boundary, while leaving the constraint of the tangential components, which are internal points in a staggered grid, up to the direct forcing generated by immersed rigid solid.

2. Propelling fluid port. During the discharge stroke an inflow boundary condition is used which is switched to an outflow boundary condition during the suction stroke.

3. Suction port. During the discharge stroke a no-slip wall boundary condition is used which is switched to an inflow boundary condition during the suction stroke.

4. Discharge port. During the discharge stroke an outflow boundary condition is used which is switched to an no-slip wall boundary condition during the suction stroke

On the inflow boundary condition a velocity profile is used for the boundary normal component while the boundary tangential components are set to zero. The outflow boundary condition uses a zero gradient or homogeneous Neumann boundary condition for all velocity components with a subsequent scaling of the boundary normal component such the volumetric outflow matches the volumetric inflow such that the integral of the divergence of the flow velocity in the domain is zero. A homogeneous Neumann boundary condition is used for the pressure in the Poisson equation on the entire boundary of the fluid domain. The following velocity profile was used for the velocity component normal to the boundary for the inflow on the circular ports with radius R at radius r from the centre of the port.

$$v_n(r) = v_{max} \frac{(R^m - r^m)}{R^m} \tag{6.92}$$

Here a exponent of $m = 10$ was used which gives a flat top profile with a 99% boundary layer thickness of $\delta = 0.37R$ which is roughly 2 to 3 grid spacings in the reference model depending on which port is considered. A single grid spacing corresponds to a 80 to 90% boundary layer thickness. This profile gives a short entrance effect. When the profile is assumed to be uniform, $m >> 10$, large errors are made in the interpolated velocity on the port edge which introduces an entrance effect. When the profile is more gradual, $m << 10$, it deviates to much from the profile which develops downstream, thereby also introducing an entrance effect. To choose m such that the boundary layer thickness of the entrance profile is a few fluid cells thick, seem to be reasonable therefore. The inflow profile is sinusoidally varied in time. However this requires a volume fluctuation which starts from the volume behind the diaphragm in its unstressed state. When operating at higher stroke rates, collision with the rear wall is very likely to happen. In an actual piston diaphragm pump and in the experimental set-up this is prohibited by the diaphragm stroke control system which fills or relieves small amounts of propelling fluid when the monitoring rod connected to the central plate in the diaphragm travels outside its allowable operating limits. A stroke control system has been implemented in the numerical model as well which sets sinusoidal flow to zero when it is in its suction stroke and when the diaphragm is outside its operating limit. This effectively increases the volume behind the diaphragm but it can take a few strokes before stable operation is achieved which then consumes valuable computational time. When the required additional volume is known at forehand, it is more efficient to change the stroke volume of the first discharge stroke in the programmed profile.

GEOMETRY GENERATION

The developed program can be freely configured for different flow simulations. All the setting for the FSI solver are set in a parameter file which also includes some geometrical parameters. The geometry of the pump chamber and diaphragm can either be loaded from a STL-file which holds a triangulation of the surface enclosing the fluid domain and a triangulation of the mid-surface of the diaphragm, or it can be generated parametrically within the program. A basic geometric toolbox has been developed which allows the parametric generation of triangulated surfaces of solid objects such as a cylinder, a block or cuboid and a general revolve of a line around an axis. Representation of a solid in a regular grid can be done by a process often referred to as voxelization. The voxelized geometry is simply a 3D boolean array which indicates which points of the 3D grid are within the surface triangulation. With this boolean array it is straight-forward to perform some basic Constructive Solid Geometry (CSG) operations such as union, intersection and difference.

PROGRAM PROCEDURE

The procedure followed by the program can be summarized as follows

1: Load model parameter file
2: Initialize all flow field arrays, $[\mathbf{v}, p, \rho, \mu, \mathbf{b}_e, \mathbf{b}_s]$
3: Load or generate triangulated surface enclosing fluid domain
4: Immerse fluid domain surface in computational domain of the flow solver and determine for every computational cell the solid volume fraction
5: Load or generate triangulated surface representing mid-surface of the initial diaphragm shape including initial nodal positions, velocities and masses and element features such as face area, element thickness, face normal and element connectivity
6: Initialize local element membrane strain $\{\boldsymbol{\epsilon}\}'_m$, local patch curvature $\{\kappa\}'_p$, displacement to membrane strain matrix $[\mathbf{B}]_{p_b}$ and displacement to curvature matrix $[\mathbf{B}]_{p_m}$ before calculating the internal nodal force $\{\mathbf{f}\}^{\text{int}}$ by Equation 6.53 and Equation 6.54.
7: Load or generate triangulated surface representing rigid contact surface and initialise nodal contact force matrix $\mathbf{f}^{\text{contact}}$
8: Initialize randomly distributed passive maker particles in fluid domain for flow visualization
9: Initialize time $t = 0$ and iteration counter $n = 0$
10: **while** $t < t_{max}$ and $n < n_{max}$
11: Increase iteration counter n = n+1
12: Set fluid type tag of every computational cell in computational domain of flow solver deepening on cell centre position relative to diaphragm surface by ray tracing algorithm in z-direction.
13: Set fluid density in each p-cell based on fluid type tag and increase density due to immersed boundary mass by Equation 6.86
14: Set fluid viscosity in each p-cell based on both fluid type tag and local shear rate depending on rheological or turbulence model used
15: Compute time step Δt by Equation 6.19 and user defined limits and increase time $t = t + \Delta t$. Use $\Delta t = \Delta t/2$ when $n = 1$ for starting the Leap-frog time integration with staggered velocity and position updates.

16: Apply boundary conditions for flow solver by setting values in ghost cells of computational domain of flow solver according subsection 6.2.4
17: Calculate fluid body forces $\mathbf{b}_e$ generated by immersed flexible structure by evaluating Equation 6.81 using Equation 6.80, Equation 6.83 and Equation 6.84.
18: Calculate convective, pressure gradient, viscous and gravitational body force terms of Navier-Stokes equations in Equation 6.3 using the FV discretization described in subsection 6.2.2.
19: Calculate the fluid body force generated by the immersed rigid structure by Equation 6.91 using the previously calculated convective, pressure gradient,viscous and body force terms.
20: Calculate intermediate velocity $\mathbf{v}^*$ from Equation 6.5.
21: Calculate right hand side of Poisson equation in Equation 6.7.
22: Solve Poisson equation of Equation 6.7 with homogeneous Neumann boundary conditions using multigrid solver discussed in subsection 6.2.5.
23: Update intermediate velocity $\mathbf{v}^*$ to new velocity $\mathbf{v}^{n+1}$ by Equation 6.6.
24: Advect unconstrained nodes of immersed structure by interpolating the fluid velocities to the structural nodes using Equation 6.82 followed by integration of their position with Equation 6.69. Use $\Delta t = 2\Delta t$ when $n = 1$ for starting the Leap-frog time integration with staggered velocity and position updates.
25: Advect passive maker particles by interpolating the fluid velocities to the passive marker particles using tri-linear interpolation followed by integration the position of their position with Equation 6.69. Use $\Delta t = 2\Delta t$ when $n = 1$ for starting the Leap-frog time integration with staggered velocity and position updates.
26: Update the local element membrane strain $\{\boldsymbol{\epsilon}\}'_m$, local patch curvature $\{\kappa\}'_p$, displacement to membrane strain matrix $[\mathbf{B}]_{p_b}$ and displacement to curvature matrix $[\mathbf{B}]_{p_m}$ before updating the internal nodal force $\{\mathbf{f}\}^{\text{int}}$ by Equation 6.53 and Equation 6.54.
27: Calculate nodal constraint forces $\{\mathbf{f}\}^{\text{constraint}}$ due to stiffening effect and motion constraints of central plate and monitoring rod
28: Check for penetration of rigid contact surface and calculate external nodal contact forces according procedures in subsection 6.3.4
29: Combine all internal and external nodal forces in single nodal force matrix which are to be supported in fluid flow
30: Display and save data when required
31: **end**

In the next chapter an experimental set-up for determining deformed diaphragm shapes will be described. Also some experimental results will be described which will then be used in the subsequent chapter to validate the numerical model described in this chapter.

7

EXPERIMENTS

The objective of this study is to develop an experimentally validated numerical model for predicting the operation condition induced diaphragm deformation. The developed numerical Fluid-Structure-Interaction (FSI) model is described in chapter 6. In this chapter the experimental part of this study is described.

7.1. INTRODUCTION

The objective of the experimental part of this study is to provide experimental data of the diaphragm deformation which can be used to validate the numerical model described in chapter 6 which was developed as part of this study. Previous work on experimental determination of pump diaphragm deformation was performed by Schlücker (1993) as described in chapter 3. The set-up used by Schlücker (1993), as shown in Figure 7.1, used a laser triangulation sensor to measure the axial displacement of the diaphragm in the Z-direction at a specific XY location. Based on the assumption that the diaphragm motion is reproducible from stroke to stroke, the diaphragm shape can be reconstructed by gathering the axial diaphragm positions of all the XY locations measured at a specific piston position. Fluid momentum loading was not considered as the experimental set-up only included the propelling fluid while the pump fluid was absent. The PTFE diaphragm was only clamped to the pump chamber and only air was present on the pumped fluid side of the diaphragm in-between the laser triangulation sensor and the diaphragm. In this study the inclusion of the pumped fluid is essential as it is the main source of the fluid momentum loading present in the pump chamber. The fluid momentum loading is important when considering the larger piston diaphragm pumps as used in the mining and mineral processing industries as shown by the dimensional analysis and field experience data presented in chapter 5.

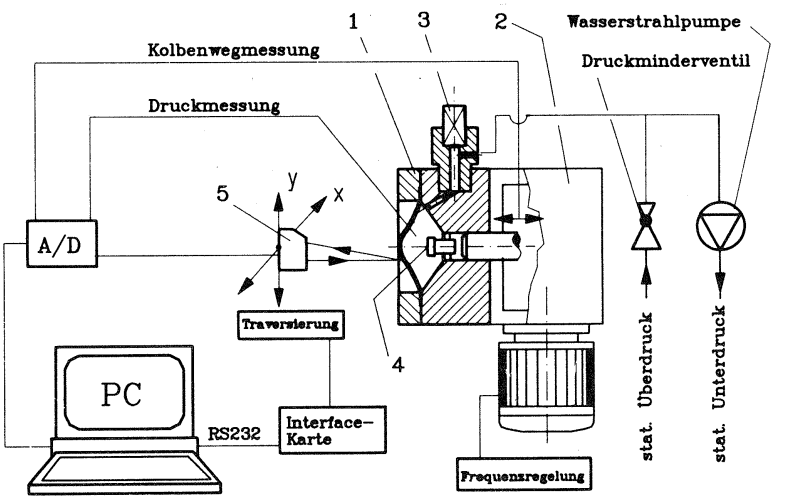

Figure 7.1: Experimental set-up for determining PTFE diaphragm deformation as used by Schlücker (1993), reprinted with permission

For a complete deformed diaphragm shape determination only optical techniques seem suitable. Next to 3D reconstruction using sequential 1D diaphragm displacement measurements acquired on a 2D measuring grid as used by Schlücker (1993), 3D reconstruction could be done using multiple simultaneously acquired 2D images acquired with multiple high-speed cameras with different viewing angles. The advantages of such an approach are the instantaneous acquisition of a complete instantaneous diaphragm shape and the possibility to track material points on the diaphragm surface. The former is mainly advantageous when the diaphragm deformation is not reproducible from stroke to stroke which was not expected. The latter could be advantageous when the local deformation gradients or strain on the diaphragm surface is to be determined. Although the surface strain is of interest, a full diaphragm strain state determination would still not be possible as the surface strain consists of both membrane as well as bending strains which can not be determined from a single surface strain measurement. Despite the advantages, the high cost, complexity and the expected limits in robustness of the multiple camera approach let to the decision to perform the 3D reconstruction using sequentially measured diaphragm displacements on a 2D measuring grid as was done by Schlücker (1993). This method only allows the determination of the deformed shape and does not track material points on the surface and can therefore not be used to determine surface strains. For the objective of validating the numerical FSI model however, determination of the deformed shape suffices. This method furthermore assumes, and therefore requires, a reproducible diaphragm motion for stroke to stroke which was expected to be present.

For determining basic design parameters of the experimental set-up, the dimensional analysis described in chapter 5 can be used. The dimensional analysis showed that the pumped slurry in most applications is non or slow settling such that it behaves as a homogeneous fluid. The dimensional analysis furthermore showed that the forces due to turbulent stresses are of a much lower magnitude than the forces due to fluid momentum. It was also shown that viscous stresses are only important to be considered when pumping paste type slurries with yield stresses in the range of 100 to 1000 Pa. As most piston diaphragm pump applications handle slurries with a yield stress lower than 100 Pa, inclusion of high viscous fluids in the experimental set-up is not a strong requirement. The lower relevance of the 2 phase character, the turbulence and rheology of the pumped slurry allowed the use of water as the pumped fluid which is nice when optical methods are to be used for determining the deformation shape of the diaphragm. The dimensional analysis furthermore indicated that the FSI mechanism in the pump chamber is in essence defined by 3 main dimensionless numbers being the dimensionless stroke volume, the dimensionless stroke rate and the dimensionless hydrostatic pressure. Independent variation of these 3 dimensionless parameters over the range of interest would be advantageous. The most straight forward method for varying the dimensionless stroke volume and stroke rate is to design a set-up with a variable stroke volume and variable stroke rate. A variable dimensionless density difference is less straight forward however. By replacing the propelling fluid and/or the pumped fluid by air, a large density difference can be enforced over the diaphragm however. This density difference is of similar order of magnitude as the density difference between the propelling fluid and a mineral concentrate such as iron ore concentrate with a mixture density of 2300 kg/m^3. The size the diaphragm used in the experimental set-up can not be much smaller than what is used in practice as the dimensionless hydrostatic pressure includes the dimension of the diagram the size. In this study a diaphragm size with a nominal stroke volume of 10 litre was selected which is a common size used in practice and has a dimension which is approximately 50 % of dimension of the largest size diaphragm currently used. This allows the generation of hydrostatic pressure which is smaller than what could be present in the largest diaphragm, but which is of similar order of magnitude and is as large as what is considered practical and reasonable from a cost point of view. This allows the generation of realistic hydrostatic pressure loads which can be used to validate the numerical FSI model without covering the full range of hydrostatic pressures encountered in practice. It is noted however that the approach of replacing the propelling fluid and/or pumped fluid with air does not independently scale the dimensionless hydrostatic pressure as the fluid momentum load, represented by the dimensionless stroke rate, is significantly affected by the low density of the air. Experimental data can be provided for validating the hydrostatic pressure loading in the numerical model but no data can be provided for the combination of a high hydrostatic load and a high fluid momentum load as is present is some practical applications. However, when the numerical model is capable of handling the individual effects, its capability of handling the combined effect seems plausible.

7.2. MATERIALS AND METHODS

7.2.1. EXPERIMENTAL SET-UP

The basic characteristics of the experimental set-up, which design was inspired by the set-up used by Schlücker (1993), are shown in Figure 7.2. The set-up basically consists of a Hydraulic Power Unit (HPU) (1) which supplies hydraulic power to a high response proportional valve (2) which drives a hydraulic cylinder (3) in a closed loop position control to perform a reciprocating motion. The hydraulic cylinder drives a larger diameter piston which displaces propelling fluid in and out of the pump chamber (4) thereby displacing the diaphragm which is mounted in the pump chamber. Self-acting non-return valves connect the pump chamber a water loop (5) and enable a positive displacement pump acting. The pump chamber cover has a transparent PMMA window which enables visual observation of the diaphragm. In front of the pump chamber a numerically controlled servo electric XY table is positioned on which a laser triangulation sensor (6) is mounted. The laser triangulation sensor successively measures the displacement of the diaphragm in Z-direction on different XY locations. A Supervisory Control And Data Acquisition (SCADA) (7) provides supervisory control of the individual devices and performs data acquisition of relevant signals. As the piston displacement is measured simultaneously, reconstruction of a specific deformed diaphragm shape is possible by gathering all diaphragm positions measured at a specific piston position from the successively measured diaphragm displacements.

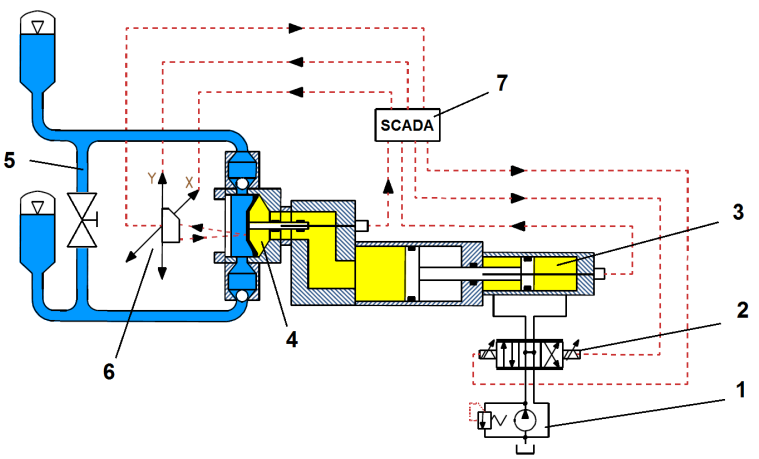

Figure 7.2: Sketch of experiments set-up

Further details of the experimental set-up are as follows:

1. Hydraulic Power Unit (HPU) consisting of a tank mounted 140 cc variable displacement axial plunger pump with 45 kW, 1500 rmp electric motor and an auxiliary system for cooling and filtration purposes. The variable displacement axial plunger pump is equipped with an electronic flow, power and pressure controller which enables to use of the HPU as a fixed pressure source up to a maximum of 28 MPa.

Furthermore, the HPU provides leakage compensation for the propelling fluid by adding or relieving small amounts of propelling liquid when the diaphragm operates outside its allowable limits using 2 solenoid actuated hydraulic valves (not shown). The hydraulic power unit is controlled using a PLC which communicates to the SCADA system using a Profibus protocol.

2. **High response proportional hydraulic valve** with closed-loop position controller which controls the oil flow to the hydraulic cylinder. The digital controller communicates to the SCADA system using a Profibus protocol for start and stop commands and uses a analogue signal for the position reference of the hydraulic cylinder which is generated within the SCADA system.

3. **Hydraulic differential cylinder** with 500 mm stroke, 63 mm piston and 45 mm rod equipped with a magneto-restrictive position sensor with a digital SSI interface to the digital position controller. A 400 mm piston is connected to the rod of the hydraulic cylinder which displaces the propelling fluid. In combination with the 28 MPa hydraulic pressure a maximum pressure in the pump chamber of 695 kPa can be generated. In this experimental set-up the usable stroke is limited to 100 mm which results in a maximum stroke volume of 12.5 litre.

4. **Pump chamber** with a 52 Shore A NBR diaphragm of 10 litre nominal stroke volume. The pump chamber is equipped with a self-acting spring loaded (15 kPa) all-metal non-return suction and discharge valves. The diaphragm has a central metal plate to which a monitoring rod is connected in which a magneto-restrictive position sensor is mounted which has an analogue interface to the data acquisition system. The clamping diameter of the diaphragm is 454 mm. The pump chamber cover includes a 60 mm thick PolyMethyl MethAcrylate (PMMA, also known as Acrylic glass or by the trade names as Plexiglass or Perspex) plate with a clamping or support diameter of 454 mm as well.

5. **Water loop** consisting of DN125 steel piping with PN16 flanges, a suction and discharge air vessel of 300 litre nominal volume each and a knife-gate valve for throttling the flow between discharge and suction side of the loop. The air vessels absorb the volume fluctuation in the loop due to the piston displacement by compression and expansion of the air volume which is roughly 250 litre each. The throttle valve can be used for generating a clear difference between the suction and discharge pressure but has been used in the fully open condition during most experiments. The air vessels have a visual indication of the water level and can be pre-loaded with compressed air. The design pressure of the loop is 1000 kPa.

6. **Numerically controlled servo electric XY table** with a laser triangulation sensor, type Mirco-epsilon optoNCDT 1700/ILD 1700-500. The laser triangulation sensor successively measures the diaphragm position in Z-direction on different XY-locations. Each axis has an encoder equipped AC motor which drives a screw spindle and is controlled by a electric drive consisting of both a position controller as well as a frequency converter. The drive communicates to the SCADA system using a Profibus protocol.

7. Supervisory Control And Data Acquisition (SCADA) system consisting of Programmable Automation Controller (PAC) (National Instruments CompactRIO) and a desktop PC. The PAC performs the data acquisition and the supervisory control of all devices while the desktop PC is used as the Human Machine Interface (HMI). On both the PAC as well as the PC, National Instruments LabVIEW programs run. The HPU can be started from the PC by the user and settings such a hydraulic system pressure, stroke rate and stroke volume can be changed manually by the user within the HMI-program. In the HMI-program a list of XY coordinates can be uploaded from a text file which are then sequentially up-loaded to the position controllers of the X and Y axis. The coordinates are uploaded at timed intervals which allows the measurement of the diaphragm displacement in Z-direction at a certain XY position for several strokes before continuing to the next XY position. Once the measurement is started manually from the HMI-program the following signals are logged continuously at a measurement rate of 1000 Hz:

1. Position hydraulic cylinder
2. Position diaphragm cone plate
3. Diaphragm position with laser triangulation sensor
4. X position of the XY table
5. Y position of the XY table

The measurements can further be followed in real-time using a scope function in the HMI-program.

7.2.2. OPERATING PROCEDURE

During an experiment, XY coordinates are uploaded to the drives of the XY table at prespecified timed intervals. When the drive receives a new position, the XY table moves to a new position which is maintained until a new position is received by the drive. The timed interval can be adjusted and is set such that several strokes are measured before continuing to a new position. Diaphragm shapes have been measured by using either a coarse grid of 276 points with a spacing of roughly 20 mm or fine grid of 1037 points with a spacing of roughly 10 mm as shown in Figure 7.3. The timed intervals contained typically 5 to 10 stokes which with a stroke rate in the range of 50 to 150 stokes per minute gives a duration of a measurement cycle for a specific operating condition in the order of an hour when using 1037 points. Because of accessibility constraints of the laser triangulation sensor only one half of the diaphragm has been measured which was considered not to be an issue because of symmetry considerations.

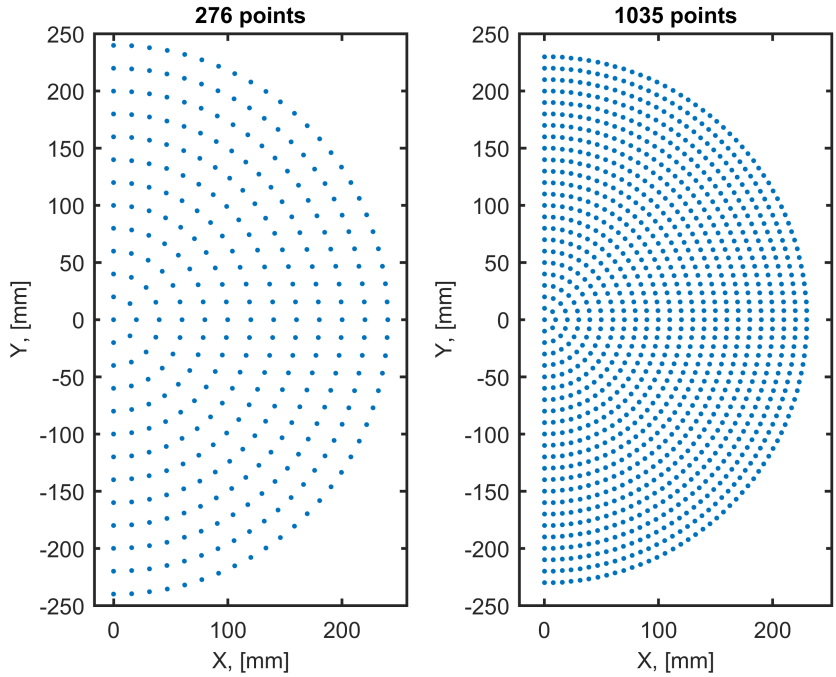

Figure 7.3: Measurement grids used

The operating procedure for the execution of a diaphragm shape measurement for a certain operating condition requires the following steps:

1: Power on system and start HMI-program on desktop
2: Jog XY table to center line of pump chamber
3: Load list of XY coordinates from text file
4: Start hydraulic power unit
5: Set stroke rate, stroke volume, diaphragm fill and relieve positions and sampling rate (up to 1000 Hz)
6: Start cylinder motion
7: Start data acquisition
8: Start automatic sequencing of XY positions
9: When finished, stop data acquisition and save data file
10: Continue to new operating condition (step 5) or stop test rig.

7.2.3. PROCESSING OF EXPERIMENTAL RESULTS

REFRACTION CORRECTION

Laser triangulation sensors are normally used to measure the distance to an object with air in-between for which they are calibrated. The objective in this study is to measure the distance to the pump diaphragm with air, PMMA and water in between. A correction

for the refraction of the laser beam is required because of the triangulation principle used within the sensor. The basic working principle of a laser triangulation sensor is shown in Figure 7.4. A laser beam is transmitted from a laser transmitter and reflected on an object surface in a diffuse way which generates a visual spot on the object. The diffusely reflected laser beam is focused by a lens on a light sensitive device such as a Charge Coupled Device (CCD) sensor. The sensor can determine the location of the focus point of the reflected beam and thereby the angle between the transmitted beam and the reflected beam. From this angle the location of the object can be determined by triangulation.

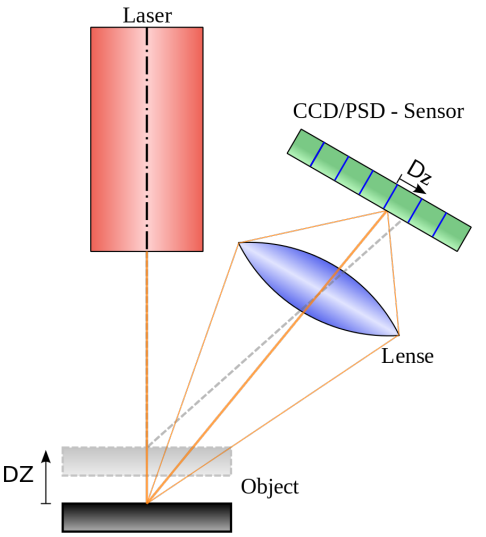

Figure 7.4: Principle of laser triangulation sensor

As the angle of the reflected beam is of interest, refraction of the reflected beam when crossing the water-PPMA and PMMA-air interfaces needs to be considered. Refraction is the change in direction of propagation of a wave due to a change in its transmission medium as shown in Figure 7.5 and is described by Snells law, (Giancoli, 1993)

$$\frac{\sin(\theta_1)}{\sin(\theta_2)} = \frac{v_1}{v_2} = \frac{n_2}{n_1} \tag{7.1}$$

which states that the ratio of the sine of the angles of incidence, θ_1, and refraction θ_2 is equivalent to the ratio of phase velocities v_i in the two media, or equivalent to the reciprocal of the ratio of the indices of refraction n_i as shown in Figure 7.5.

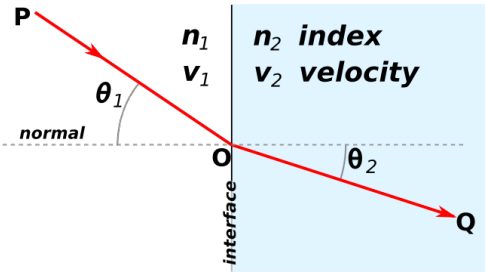

Figure 7.5: Refraction of light

The transmitted laser beam is considered to be perpendicular to the interface planes such that no refraction occurs. The reflected beam which is received by the sensor crosses the interface planes at an angle and will therefore be refracted. The sketch in Figure 7.6 shows how the measurement error due to the refraction arises and gives basis for a geometric determination of this error.

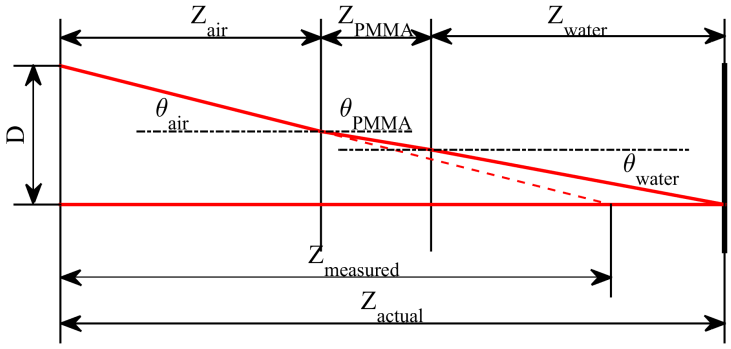

Figure 7.6: Meaurement error induced by refraction

The refraction indices for air, PMMA and water are respectively 1.003, 1.489 and 1.333, (Giancoli, 1993). The following set of equations describes the geometric relationship shown in Figure 7.6.

$$\frac{D}{Z_{\text{measured}}} = \tan(\theta_{\text{air}}) \tag{7.2}$$

$$\frac{\sin(\theta_{\text{PMMA}})}{\sin(\theta_{\text{air}})} = \frac{n_{\text{air}}}{n_{\text{PMMA}}} \tag{7.3}$$

$$\frac{\sin(\theta_{\text{water}})}{\sin(\theta_{\text{PMMA}})} = \frac{n_{\text{PMMA}}}{n_{\text{water}}} \tag{7.4}$$

$$D = Z_{\text{air}}\tan(\theta_{\text{air}}) + Z_{\text{PMMA}}\tan(\theta_{\text{PMMA}}) + Z_{\text{water}}\tan(\theta_{\text{water}}) \tag{7.5}$$

$$Z_{\text{actual}} = Z_{\text{air}} + Z_{\text{PMMA}} + Z_{\text{Water}} \tag{7.6}$$

With known distances Z_{measured}, D, Z_{air} and Z_{PMMA} and refractive indices n_{water}, n_{PMMA} and n_{air}, the equations successively give θ_{air}, θ_{PMMA}, θ_{water}, X_{water} and Z_{actual}. Although the correction is non-linear, it can be shown that the deviation from a linear correction in the measurement range of interest is approximately 0.1% F.S. which is similar to the linearity of the sensor itself. Instead of applying the theoretical correction model, a linear fit through the data of a calibration measurement is used. The calibration measurement is executed by simultaneously measuring the central plate of the diaphragm with the laser triangulation sensor and with the magneto-restrictive position sensor within the monitoring rod while the diaphragm is moving.

3D DEFORMED SHAPE RECONSTRUCTION IN TIME DOMAIN

During a measurement the mentioned signals are continuously logged. The processing of the raw data file for reconstructing the 3D deformed shapes of the diaphragm consists of the following steps:

Cut log file in waveform measurements per XY position. The log file includes the periods in which the XY-table is moving from one position to the other which are identified by a non-constant X or Y position measurement. The period in-between with constant X and Y then belongs to a single XY position. The measurement data of a single XY location is then copied into a data structure which has an record of a waveform of several strokes per XY location.

Repair laser triangulation measurement. From time to time spikes are present in the laser triangulation measurement which are attributed to debris particles present in the pumped water which interrupt a correct diaphragm position measurement. A measurement correction script has been developed which recognizes these spikes, cuts them from the measurement and interpolates the missing data points.

Time Synchronous Averaging (TSA). The diaphragm motion per XY position is measured for several strokes, typically 5 to 10 strokes. From the hydraulic cylinder position measurement the Bottom Dead Center (BDC) of the piston is determined which is used to cut the waveform measurement per XY location into single stroke waveforms. The waveform of a single stroke is then re-sampled using a fixed number of samples per stroke which then allows the averaging of the waveforms over the individual strokes. Before re-sampling a FFT-based low pass filter is applied which removes all frequencies above the Nyquist frequency in order to prevent aliasing. This so-called TSA algorithm filters out the non-synchronous components such that only the harmonic components of the measurement remain.

Reconstruct diaphragm shape. The TSA algorithm produces a waveform per XY position with a fixed number of equally spaced samples per waveform which can be organized in a 2D array Z_{ij} with i the index in the 1D angle array φ_i and j the index in the 1D X-position and Y-position arrays X_j and Y_j. The deformed diaphragm shape at a specific angle φ_i can be reconstructed by gathering all samples with index i from Z_{ij}. The XY-data points can be triangulated using a Delaunay triangulation which is then used in combination with the Z-data points to plot the deformed shape as a 3D triangular mesh.

It should be noted that the XY positions are fixed and that no material or Lagrangian points on the diaphragm are tracked. Material vectors are therefore not tracked during a measurement. The measurement only captures the diaphragm Z-position in a fixed Eulerian XY-grid. Although the material points primarily have a Z-translation, some X and Y translation is present as well. This means that only the deformed shape of the diaphragm is determined and not necessarily its local deformation as this requires material vectors in the deformed configuration to be related to material vectors in the un-deformed configuration. The primary objective of the experimental set-up is to provide diaphragm deformation shape data which can be use to validate the numerical FSI model developed in this study. This validation can then not be based on comparison local deformation quantities but must be based on comparison of deformed diaphragm shapes.

SPECTRAL ANALYSIS OF DIAPHRAGM DEFORMATION SHAPES

A lot of insight is gained from visually observing the deformed diaphragm shapes, especially when observing animations of the diaphragm deformation which show sequential deformed diaphragm shapes. However quantitative analysis of these shapes is somewhat limited, especially when local deformation quantities can not be determined because of the Eulerian measurement grid. Both the periodicity of the diaphragm motion and the wave-like deformation shapes observed in the 3D reconstructed shapes indicate that spectral or frequency domain analysis could be used to quantify the effects which are observed visually. The displacement of propelling fluid by the piston is programmed as a sinusoidal profile. The geometrically non-linear structural response and the non-linear fluid flow dynamics result in a periodic motion of the diaphragm which contains higher harmonics of the fundamental forcing frequency of the piston. The frequency content is evaluated by decomposing a periodic waveform of a diaphragm position measurement on a specific XY-location into a Fourier series using a Fast Fourier Transform (FFT) algorithm. For the XY-locations with index j this gives

$$Z_j(\varphi) = \frac{A_{0j}}{2} + \sum_{i=1}^{N/2} A_{ij} \sin(i\varphi + \Delta\varphi_i) \tag{7.7}$$

with i now indicating the harmonic instead of the index in the 1D angle array and N is the number of samples in the φ direction. The diaphragm displacement waveforms are cut at the BDC of the piston position with an integer number of strokes in order to ensure its periodicity such that the Fourier-series can be determined without using a window function. The frequency content of a compete diaphragm motion is determined by scaling and mapping all the spectra on a single spectrum. The spectra are first scaled by the maximum amplitude in the individual spectra. Then the maximum amplitude of a specific harmonic over all XY-locations is determined. The resulting scaled and mapped spectrum $\hat{A}_j$ is then defined as

$$\hat{A}_i = \max_j \left(\frac{A_{ij}}{\max_{i,j}(A_{ij})} \right) \tag{7.8}$$

The scaled and mapped spectra $\hat{A}_i$ consist of a 1D array for each experimental operating condition and can be combined in a 2D array $\hat{A}_{ik}$ for all experimental operating

conditions k which allows comparison of the frequency content as a function of experimental operating conditions.

So far the spectral analysis has been restricted to the time, or pump cycle angle dimension. A spectral analysis in the spatial directions is possible as well. In a rectangular domain expansion in Fourier-series could be used but this is does not make sense for the circular diaphragm. It is more logical to transform the x, y and z coordinates of the diaphragm to cylindrical coordinates r, θ and z such that a diaphragm shape can be expressed as a function of polar coordinates.

$$z = f(r, \theta) \tag{7.9}$$

The diaphragm shape is periodic in the circumferential direction with a fundamental period of 2π as this period fully describes the shape in the circumferential direction. Because of this periodicity, the shape can be expressed by a Fourier series expansion in the circumferential direction. The phase shift $\Delta\varphi_i$ in Equation 7.7 has to vanish as the deformation is assumed to be symmetric across the YZ plane, which is actually imposed by only measuring half of the diaphragm. In the radial direction however, a Fourier-series does not make sense as the shape is not periodic in the $[0, a]$ interval with a the radius of the diaphragm. Expansion in radial direction using Bessel function seems to be the correct choice as is done for obtaining analytical solutions for differential equations in cylindrical coordinates, such as the vibrating circular plate problem, (Asmar, 2000). For the expansion in the radial direction a Fourier-Bessel series is therefore used for which holds (Weisstein, 2015)

$$f(r) = \sum_{m=1}^{\infty} A_n J_m\left(\frac{\alpha_{mn}}{a} r\right) \tag{7.10}$$

were J_m is a Bessel function of the first kind of order m with positive roots α_{mn} with coefficients A_n which can be found by

$$A_n = \frac{2}{[J_{m+1}(\alpha_{mn})]^2} \int_0^a r f(r) J_m\left(\frac{\alpha_{mn}}{a} r\right) \mathrm{d}r \tag{7.11}$$

In Figure 7.7 Bessel functions of the first kind of order 0, 1 and 2 are shown.

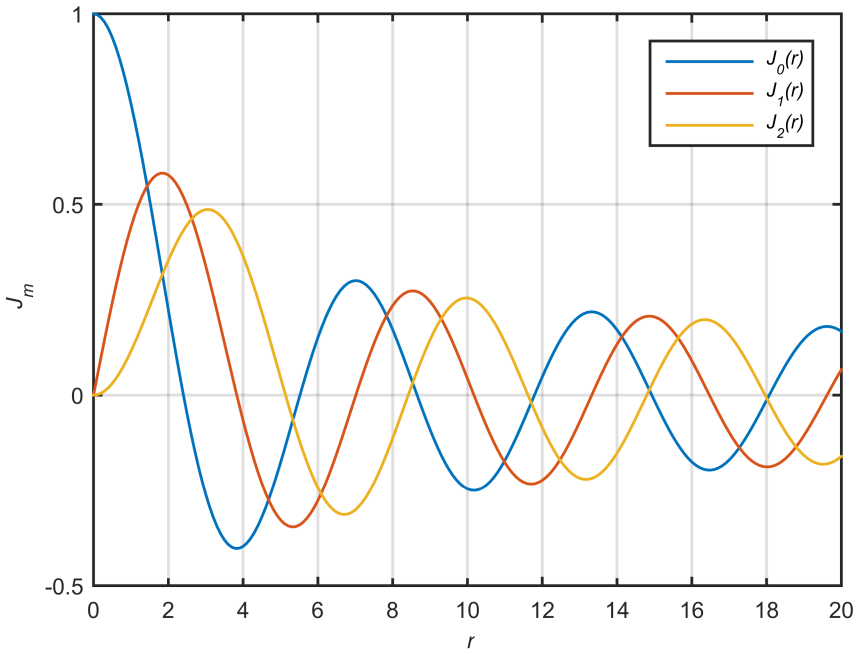

Figure 7.7: Bessel function of the first kind of order 0, 1 and 2

In a circular symmetric situation the 0^{th} order Bessel function is generally used in the expansion. When the shape in the circumferential direction is expanded with trigonometric functions, the order of the Bessel function is related to the harmonic m of the trigonometric function in the circumferential direction according

$$f(r,\theta) = \sum_{m=0}^{\infty} \sum_{n=1}^{\infty} A_{mn} J_m\left(\frac{\alpha_{mn}}{a} r\right) \sin(m\theta) \tag{7.12}$$

A single real coefficient array A_{mn} results by assuming symmetry across the YZ-plane. The shape represented by a single coefficient of the coefficient array A_{mn} is called a mode shape. The modes shapes represented by $m = 0,1,2$ and $n = 1,2,3$ are shown in Figure 7.8

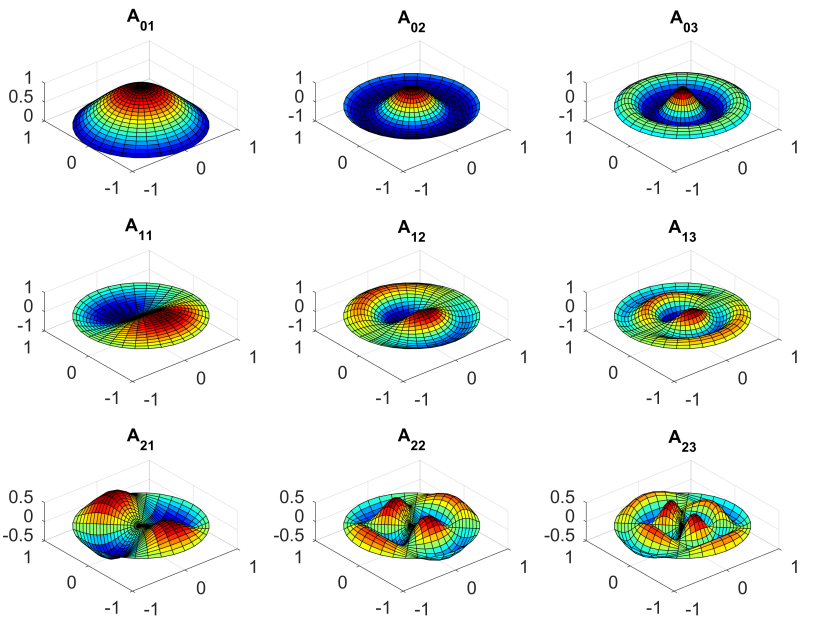

Figure 7.8: Modes represented by A_{mn}

It is the author's understanding that any function in cylindrical coordinates $z = f(r,\theta)$ on a finite domain $[0,a]$ with $z(a) = 0$. can be decomposed in the individual modes shown Figure 7.8. A mathematical proof of this is beyond the author's mathematical capability and understanding of Bessel functions such that this can only be postulated here. A single deformed diaphragm shape can then be represented by the coefficient array A_{mn} whose coefficients are a function of the pump cycle angle φ. During the motion of the diaphragm these coefficients change. In a linear analysis of a vibrating membrane each mode has a single frequency as these are the eigen modes of the membrane, Asmar (2000). But in the non-linear motion of the diaphragm in this study, the contribution of each mode varies periodically in time but not with a single frequency but according to a periodic function, containing multiple frequencies which can again be represented by a Fourier series expansion per mode or individual coefficient in A_{mn}. In order to get an impression of the spatial frequency content of the diaphragm motion, the maximum value of each coefficient in A_{mn} during a pump cycle is determined according

$$\hat{A}_{mn} = \max_{\varphi}\left(A_{mn}(\varphi)\right) \tag{7.13}$$

7.3. RESULTS

7.3.1. OPERATIONAL ISSUES

LASER TRIANGULATION MEASUREMENT

While commissioning the experimental set-up, as described by Schut (2011), several operational issues surfaced with respect to the laser triangulation measurement:

PMMA plate deflection. The original cover design had a 20 mm thick PMMA plate with support diameter of 454 mm. This resulted in a plate centre deflection of 0.03 to 0.04 mm/kPa. The level of plate deflection and the accompanied curvature would introduce too much error in the laser measurement because of changing refraction conditions due to the dynamic pressure fluctuations in the pump chamber. Also the stresses in the plate were not considered acceptable from a fatigue point of view. The plate thickness was therefore increased to 60 mm which reduced the deflection with a factor 27 and the stress levels with a factor 9.

Laser reflection. When the transmitted laser beam crosses the air-PMMA and PMMA-water interfaces it is partially reflected. The sensing element in the laser triangulation sensor observes the reflective spots when they lie within the measurement range of the sensor. A completely faulty position is then evaluated by the sensor which is somewhere in-between the reflective spot on the interfaces and the actual diaphragm position. The solution was found by simply placing the start of the measurement range within the water area such the that the reflective spots on the air-PMMA and PMMA-water interfaces are not observed by the sensor. The reflection in the interfaces furthermore decreases the intensity of the transmitted light, limiting the use of the sensor in less optimal conditions as described below.

Sensor quality. Initially a low-cost laser triangulation sensor (Balluf 26K-LB04) was used which had limitations in non optimal conditions which result when the diffusively reflected laser beam has a lower intensity. The intensity of the diffusively reflected laser beam is lowered by

- Reflection at the interfaces
- Absorption on the diaphragm surface depending on the color of the diaphragm
- Attenuation in the transmitting medium by absorption by the transmitting medium itself or by scattering by debris particles in the transmitting medium
- The angle of incidence on the diaphragm surface

The limitations of the sensor have been evaluated in a bench-top experiment by measuring the limiting angle of incidence. These bench-top experiments showed that the higher performance Micro-epsilon OptoNCDT1700/ILD 1700-500 sensor suffered less from these non-optimal conditions. It was for example able to measure a black rubber sheet up to an angle of incidence of 45 degree with PMMA in between while the Balluf sensor only allowed rotation up to 20 degree. The Mirco-epsilon sensor was therefore selected for further use in the experimental set-up.

Corrosion. When the light travels through the diverse media its intensity is attenuated by both absorption and scattering effects. The absorption coefficient of air, PMMA and clear water is negligible, but scattering by the presence of corrosive particles in the water has shown to decrease the light intensity of the reflected spot the diaphragm to an extent that it could no longer be observed by the laser triangulation sensor. The original design of the experimental set-up used carbon steel components which quickly corroded, prohibiting correct measurements. Solution was found by galvanizing the pump chamber and loop components and using stainless steel non-return valves.

Diaphragm color. The original color of the diaphragm is black. Preliminary bench-top experiments showed that the rubber could be observed by the sensor with both PMMA and water in between. However, experiences in the full scale experimental set-up showed that the absorption of the light by the black surface limited the intensity of the reflected spot and therefore the ability of the sensor to measure in non-optimal conditions such as non-clear water and non-zero angle of incidence on the diaphragm surface. Improvement was found by applying a thin (15 µm) grey PTFE coating (ERIKS-PTFE-SP10020) which increased the allowable rotation angle from 45 degree to 85 degree in a bench-top experiment. The coating has a negligible impact on the diaphragm deformation as the thickness of the coating is negligible compared to the diaphragm thickness. The durability of the coating was limited however due to the limited elasticity of the PTFE coating.

PUMP CHAMBER CAVITATION

Dynamic pressure fluctuations develop in the pump chamber during operation of the experimental set-up. Is must be guaranteed that these pressure fluctuations stay a save amount above the vapour pressure in order to prevent cavitation. When the water in the pump chamber cavitates, vapour bubbles will form which prohibit the visibility in the pump chamber and therefore the ability to measure the diaphragm shape. Due to the unsteady flow conditions, pressure fluctuations are generated in the experimental set-up. A pre-load pressure is required to keep the minimum pressure level during these pressure fluctuations above the vapour pressure. An estimation of the pressure fluctuations can be made using a 1D incompressible flow analysis of the suction line for which holds

$$\Delta p = L\dot{Q} + RQ \text{ with } L = \frac{\rho l}{A} \text{ and } R = f(Q) \tag{7.14}$$

with flow rate Q, hydraulic inductance L, hydraulic resistance R, fluid density ρ, fluid column length l and fluid column cross sectional area A. The flow in the suction and discharge line follows the displacement of the piston which is programmed to have a sinusoidal profile for which holds

$$Q = \frac{V_s}{2}\omega \sin(\omega t) \tag{7.15}$$

$$\dot{Q} = \frac{V_s}{2}\omega^2 \cos(\omega t) \tag{7.16}$$

The non-return valves connect a positive flow towards the discharge line and a negative flow to the suction line. The volume fluctuation generated by the piston is absorbed in the air vessels. The pressure fluctuation in the air vessel in only a few % of the mean pressure as the stroke volume is only a few % of the air volume in the air vessels. As the pressure fluctuation in the air vessels is small compared to the dynamics pressure drop in suction and discharge line a constant velocity can be assumed in the line between the suction and discharge air vessels. The pressure fluctuation in the pump chamber can then be evaluated directly by applying Equation 7.14 on the suction line while assuming a constant pressure in the suction air vessel.

The hydraulic drive allows adjustable stroke volumes V_s up to 12.5 litre and adjustable stroke rate ω up to 150 strokes per minute or 15.7 rad/s. This gives a maximum instantaneous flow rate of 0.098 m^3/s and a maximum fluid acceleration of 1.54 m^3/s^2. The suction and discharge line have an effective length of approximately 2 m and an internal diameter of 128 mm which gives a fluid inductance L of 156 $kPa\,s^2/m^3$ which gives a maximum acceleration pressure of 240 kPa. The estimated resistance at the maximum flow velocity of 7.64 m/s is only 6.8 kPa when assuming a Darcy-Weisbach friction factor of 0.015. Although it is recognized that friction in unsteady flow can be significantly higher than in steady-flow, see e.g. Wylie and Streeter (1993), it is clear that the acceleration pressure is dominant in generating pressure fluctuations in the pump chamber. The unsteady analysis indicates that an absolute suction pressure of 250 kPa would be enough to prevent vaporous cavitation as the vapour pressure of water at room temperature is only 2 kPa. Next to vaporous cavitation one has to make sure that dissolved gas is not released during the low pressure phases of the pump cycle as the released gas bubbles will also limit the visibility. When assuming air saturation at ambient pressure, a gauge suction pressure of 250 kPa would be required which is an absolute suction pressure of roughly 350 kPa depending on the actual ambient pressure. With a pressure amplitude of roughly 250 kPa the maximum gauge pressure at the end the suction stroke and beginning of the discharge stroke, should be limited to roughly 500 kPa. This is lower the maximum gauge pressure of 695 kPa which the hydraulic cylinder can generate. However, while operating the experimental set-up is was found that the widest operating range was obtained with a gauge pre-load pressure of 350 kPa which gave an operating limitation of 125 strokes per minute when operating with a stroke volume of 8 litre. The operating limit scaled proportional with $V_s\omega^2$ as expected, but is much more restrictive than predicted. When decreasing the pre-load pressure, cavitation was more pronounced and when increasing the pre-load pressure, deterioration of the tracking behaviour of the hydraulic cylinder was observed indicating that it was operating against its load limitation. A pressure fluctuation with an amplitude of 350 kPa is estimated from these observations as this corresponds to the 350 kPa pre-load which drops to the ambient saturation pressure and rises to the 700 kPa gauge load limit. This is roughly 3 times higher than what is predicted by the theoretical analysis. The reason for this deviation is not fully clear, but aspects which are considered to play a role are delayed valve closing and opening causing increased fluid column acceleration upon valve opening, under-predicted fluid column inductance and higher fluid acceleration due tracking corrections of servo hydraulic controller upon stroke reversal. Determination of the exact reasons requires more investigation, mainly using dynamic pressure measurements in the chambers of

the hydraulic cylinder and in the pump chamber but this has not been pursued further within this study and the operating limitations were taken as is.

7.3.2. QUASI-STATIC EXPERIMENTS

Several quasi-static experiments have been performed. In these quasi-static experiments a low stroke rate was used which does not generate any significant fluid momentum such that only static effect are included in the diaphragm deformation. Quasi-static experiments are preferred as static experiments are hard to reproduce because of hysteresis in the diaphragm deformation due to monitoring rod friction and buckling effects. The hydrostatic pressure load on the diaphragm is an important static load, next to the volumetric displacement of the piston. The hydrostatic load on the diaphragm can be adjusted by changing the propelling and pumped fluids by using air instead of oil and water respectively. For all 4 combinations of fluid types, quasi-static experiments have been executed using the experimental conditions shown in Table 7.1.

Table 7.1: Experimental conditions quasi-static experiments. All experiments performed with 10 litre stroke volume at 16 strokes per minute (except 8 spm for Meas. ID 3s), a fill position of 14 mm from the rear wall and a measuring grid of 276 points

Meas. ID	**Propelling fluid**	**Pumped fluid**	$\Delta\rho$, [$\mathbf{kg/m^3}$]
1s	Air	Water	-1000
2s	Mineral oil	Water	-100
3s	Air	Air	0
4s	Mineral oil	Air	900

In Figure 7.9 the reconstructed deformed diaphragm shapes obtained from the quasi-static experiments are shown. The effect of the density difference is most prominent halfway the suction and discharge strokes at respectively 90° and 270° of the pump cycle. With a negative density difference the upper half of the diaphragm bulges out while for the positive density difference the lower half bulges out. At the end of stroke positions, the effect of the hydrostatic pressure difference is less pronounced, most likely due to a more stable diaphragm shape. When the density difference is small or absent, as is the case in the 2 middle rows, buckling is observed in the beginning of the discharge stroke at 45° into the pump cycle. At the start of the discharge stroke the diaphragm is compressed in circumferential direction which initiates a buckling deformation in circumferential direction shown by the formation of lobes in the circumferential direction. When a significant density difference is present, a single lobe is formed on the upper or lower half of the diaphragm which leads the volumetric displacement of the diaphragm without initiating a buckling deformation.

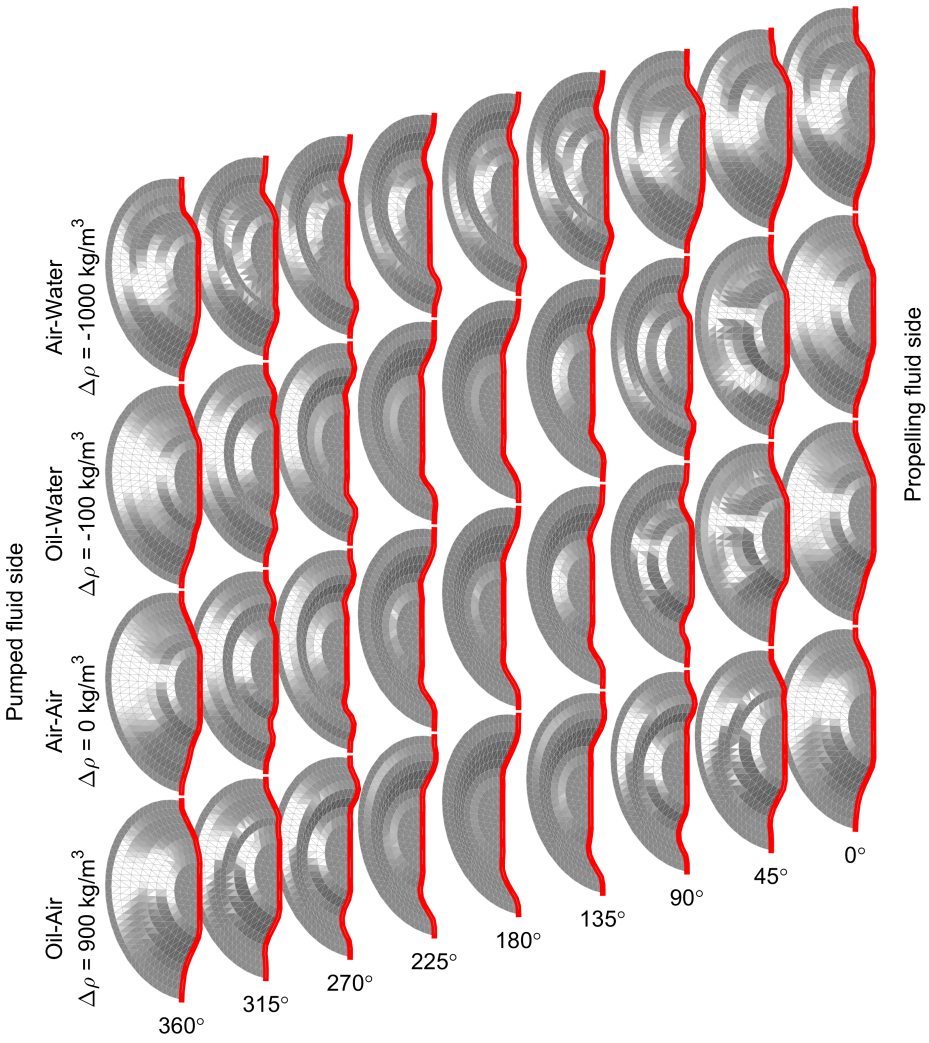

Figure 7.9: Reconstructed deformed diaphragm shapes obtained from quasi-static experiments with different density differences across diaphragm following top-down sequence of Table 7.1. Deformed diaphragm shapes shown from start of discharge stroke on the right with 45° intervals to end of suction stroke on the left.

Although a piston stroke volume of 10 litre was used in al quasi-static experiments, less volumetric displacement resulted for the air-water case (1s) shown in the top row of Figure 7.9. The volumetric displacement of the piston can be derived directly from the measured piston position, the volumetric displacement of the diaphragm can be obtained from the triangulated surfaces of the reconstructed diaphragm shapes. In Figure 7.10 the diaphragm displacement is shown as a function of the piston displacement.

The diaphragm displacement very accurately follows the piston displacement in the experiments with oil as the propelling fluid as it is linked to the piston displacement with an virtually incompressible fluid. When air is used as the propelling fluid, a more compressible fluid links the diaphragm displacement to the piston displacement. Any significant pressure variation then result in a volume variation of the propelling fluid. For the oil-water case (2s) with a small density difference, the volume variation of the propelling fluid is relatively small. For the air-water case (1s) however, a large volume fluctuation of approximately 3 litre is present in the propelling fluid. A large hysteresis loop is observed with horizontal sections which indicates a constant diaphragm displacement while varying the piston displacement. This is most likely due to friction in the monitoring rod. In the air-water case a high density difference in present across the diaphragm which creates a moment on the central plate around the X-axis which is to be balanced by contact forces in the monitoring rod guide. In the air-water case this contact is not lubricated resulting in high static friction which requires a pressure differential across the diaphragm to overcome. In a reciprocating motion the sign of this pressure differential changes upon velocity reversal of the central plate resulting in a pressure fluctuation in the propelling fluid. When using air as the propelling fluid this fluctuation causes significant volume fluctuation of the propelling fluid resulting is significant tracking error of the diaphragm displacement.

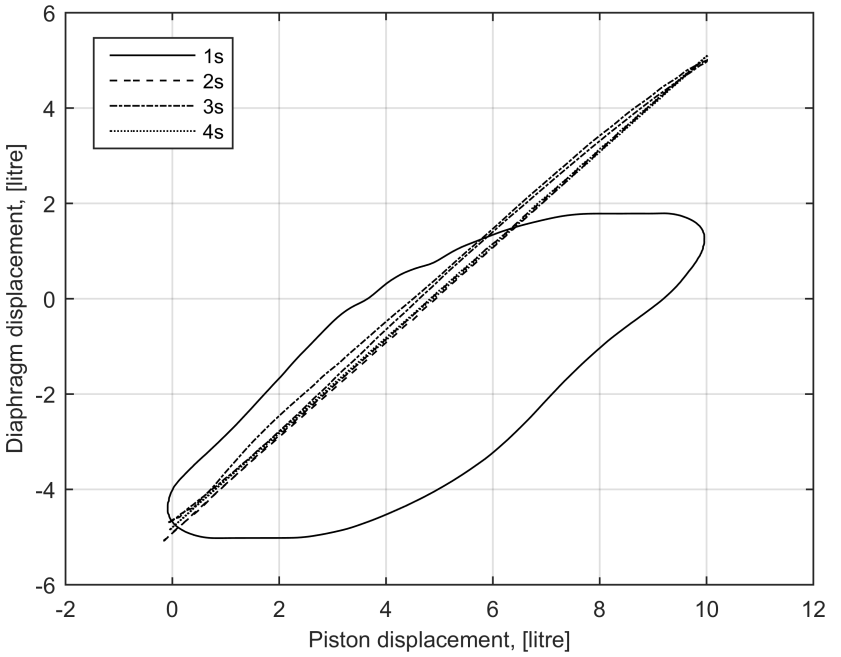

Figure 7.10: Diaphragm displacement versus piston displacement volume in quasi-static experiments

7.3.3. DYNAMIC EXPERIMENTS

Next to the quasi-static experiments a large number of dynamic experiments have been conducted at higher stroke rates where the fluid momentum loading becomes important to consider. The use of air as the propelling fluid in combination with water as the pumped fluid resulted in large tracking errors of the diaphragm with respect to the piston displacement because of propelling fluid compressibility by the large fluctuations of the chamber pressure due to the unsteady flow conditions, similar to what was observed in the quasi-static experiments with air-water due to the increased monitoring rod friction. As the asymmetry of the fluid flow is most prominent on the pumped fluid side, only dynamic oil-water experiments are described here. In Table 7.2 the experimental conditions of 46 dynamic experiments are shown.

Table 7.2: Experimental conditions dynamic experiments. All experiments performed with mineral oil as propelling fluid and water as pumped fluid. For each operating conditions experiments with a fill position of 14 and 34 mm from the rear wall were performed

Meas. ID	Stroke rate, [spm]	Stroke Volume, [litre]	Fill position, [mm]	Number of points
1	50	10	14	276
2	50	10	34	276
3	63	7.9	14	276
4	63	7.9	34	276
5	63	10	14	276
6	63	10	34	276
7	80	6.3	14	276
8	80	6.3	34	276
9	80	7.9	14	276
10	80	7.9	34	276
11	80	10	14	276
12	80	10	14	1035
13	80	10	34	276
14	100	5	14	276
15	100	5	34	276
16	100	6.3	14	276
17	100	6.3	34	276
18	100	7.9	14	276
19	100	7.9	34	276
20	100	10	14	276
21	100	10	14	1035
22	100	10	34	276
23	100	10	34	1035
24	125	3.1	14	276
25	125	3.1	34	276
26	125	4	14	276
27	125	4	34	276
28	125	5	14	276
29	125	5	34	276
30	125	6.3	14	276
31	125	6.3	34	276
32	125	7.9	14	276
33	125	7.9	14	1035
34	125	7.9	34	276
35	140	6.3	14	276
36	140	6.3	14	1035
37	140	6.3	34	276
38	150	2.5	14	276
39	150	2.5	34	276
40	150	3.1	14	276
41	150	3.1	34	276
42	150	4	14	276
43	150	4	34	276
44	150	5	14	276
45	150	5	14	1035
46	150	5	34	276

RECONSTRUCTED DEFORMATION SHAPES

The reconstructed deformed diaphragm shapes of 2 dynamic experiments (Meas. ID 2 and 23) with 10 litre stroke volume are shown in Figure 7.11. In the bottom row the results obtained at 50 strokes per minute are shown. In the middle row the results obtained at 100 strokes per minute are shown. In the top row a smoothed version of the results obtained at 100 strokes per minute are shown obtained using the trigonometric and Bessel function interpolation as described in subsection 7.2.3.

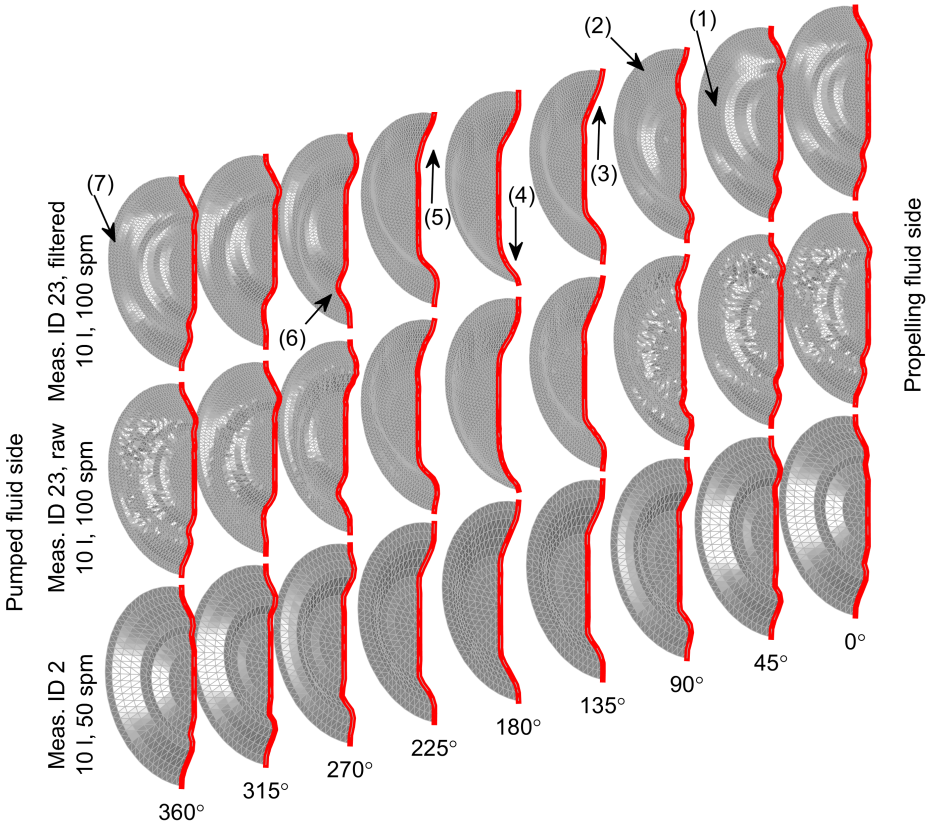

Figure 7.11: Reconstructed deformed diaphragm shapes obtained from dynamic experiments with 10 litre stroke volume. Bottom row shows results obtained at 50 strokes per minute (Meas. ID 2), middle row shows results obtained at 100 strokes per minute (Meas. ID 23) and top row shows smoothed version of middle row using trigonometric and Bessel function interpolation as described in subsection 7.2.3. Deformed diaphragm shapes shown from start of discharge stroke on the right with 45° intervals to end of suction stroke on the left.

The deformed diaphragm shapes obtained at 50 strokes per minute (spm) are more

or less axisymmetric while those obtained at 100 spm are significantly asymmetric. The buckling deformation as observed in the quasi-static experiments is not observed in the 50 spm experiment, indicating a slight preferential asymmetrical deformation induced by the asymmetric fluid momentum loading. The reconstructed deformed diaphragm shapes obtained at 100 spm have a non-smooth surface in some areas of the diaphragm. This is most likely due to not completely reproducible deformed diaphragm shapes from stroke to stroke. Using the trigonometric and Bessel function interpolation, smooth deformed diaphragm shapes can be obtained. However, some non-reproducible higher order deformation shapes could be removed by the smoothing process, but these can't be reconstructed from the sequential measurements anyway. At the end of the suction stroke and at the beginning of the discharge stroke at 315° and 360°, contact of the upper part of the diaphragm with the rear wall of the pump chamber is observed while the lower half bulges out somewhat. During the start of the discharge stroke at 45 degree, most of the diaphragm displacement is covered by the sides of the diaphragm at the 9 o'clock position (1). The lobe formed at the 9 o'clock position grows towards the 12 o'clock position and seems to peel the upper part of the diaphragm from the rear wall. At the middle of the discharge stroke, at 90°, most of the diaphragm displacement is covered by the upper part of the diaphragm (2). Towards the end of the discharge stroke a top-down-top oscillation of the propelling fluid volume behind the diaphragm is observed which bulges out on the 12 o'clock position at the end of the suction stroke at 135° (3), on the 6 o'clock position at the stroke reversal point at 180° (4) and bulges out on the 12 o'clock position in the beginning of the discharge stroke at 225° (5). Towards the end of the suction stroke a strong asymmetric deformation shape which bulges out at the 6 o'clock position is formed at 270° (6) and 315°. This is considered to be caused by the low pressure created by the high velocity jet entering the pump chamber during the suction stroke through the inlet port of the pump chamber. At the end of the suction stroke, when no inlet velocity is present, the lobe at the 6 o'clock positions rolls towards the 9 o'clock position (7) before it continues to roll to the 12 o'clock position during the beginning of the discharge stroke as discussed above. The deformation behaviour at 100 spm is clearly much more dynamic than at 50 spm as it shows waves rolling over the diaphragm surface which are absent at 50 spm. These waves create additional diaphragm deformation and hence additional strain which is most severe near the clamped edge of the diaphragm.

SPECTRAL ANALYSIS

Phenomenological analysis of the diaphragm deformation is possible by observing the 3D reconstructed deformed diaphragm shapes, preferably in an animation showing the diaphragm motion. However quantitative analysis of and comparison between different 3D deformed diaphragm shapes is difficult. As the motion of the diaphragm is periodic in time and in circumferential direction and shows wave-like patterns, a spectral analysis is used for further quantitative analysis of the deformed diaphragm shapes. In this spectral analysis the diaphragm motion and deformed shapes are decomposed in Fourier and Fourier-Bessel series as discussed in subsection 7.2.3. First a frequency analysis in the time direction of the axial displacement of the diaphragm at individual measurement location is performed using Equation 7.7. A typical amplitude spectrum of a diaphragm displacement measurement is shown in Figure 7.12.

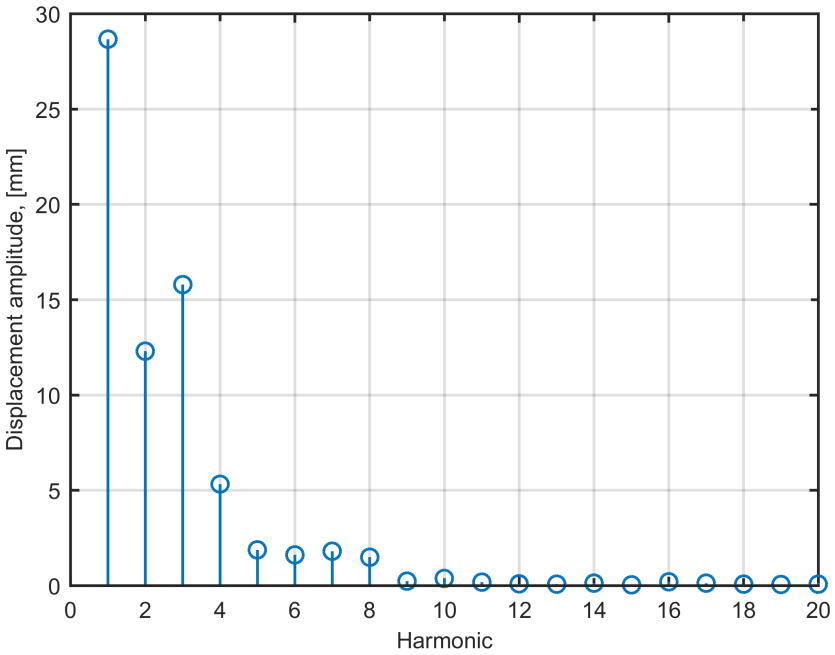

Figure 7.12: Typical amplitude spectrum diaphragm displacement spectrum. Meas. ID 23: 10 litre stroke volume at 100 strokes per minute, spectrum shown for X = 0 mm and Y = -160 mm

Although the piston displacement is following a sinusoidal profile, higher harmonics are observed in the displacement of the diaphragm indicating a non-linear response. Figure 7.12 shows a significant contribution to diaphragm displacement up to the 8^{th} harmonic. In order to determine the frequency content of a complete diaphragm motion, all amplitude spectra of the individual XY locations of a single experiment are scaled and mapped on a single amplitude spectrum using Equation 7.8. The first harmonic has the highest amplitude in all the mapped spectra. In order to give an impression of the frequency content of all the mapped spectra, the highest harmonic i is determined for each mapped spectrum which has an amplitude $\hat{A}_i$ larger than respectively α = 50, 20, 10, 5 2 or 1 % of the maximum amplitude in that mapped spectrum, max($\hat{A}_i$). In Figure 7.13 the distribution of these highest harmonics i is shown.

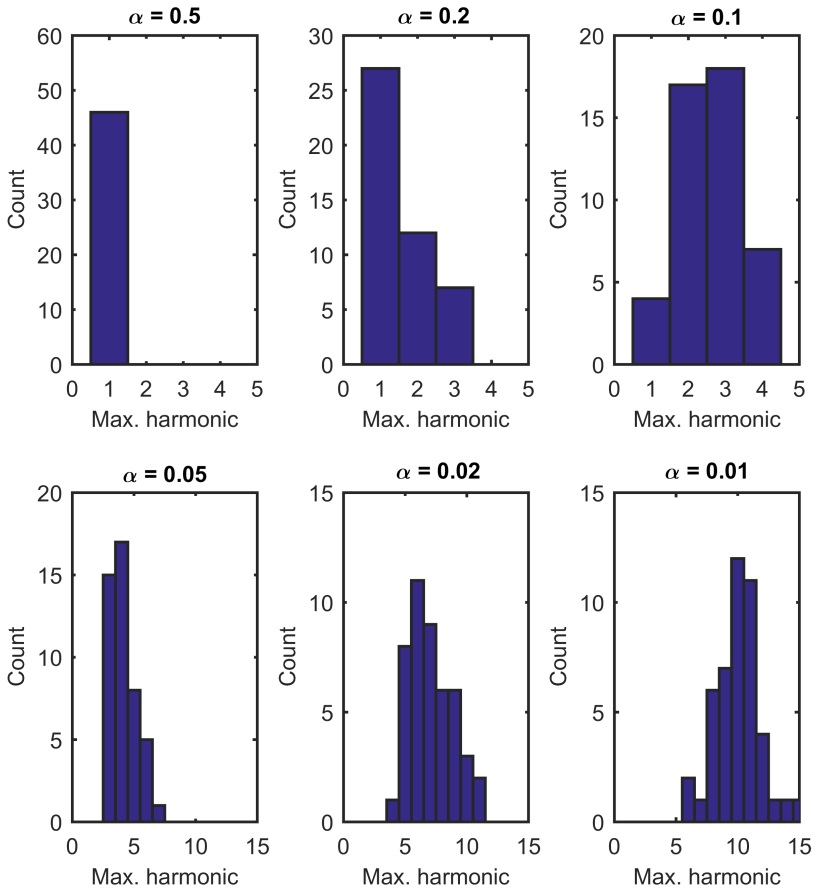

Figure 7.13: Distribution of harmonics in scaled and mapped diaphragm displacement spectra $\hat{A}_i$. For each spectrum the maximum harmonic i is determined which satisfies $\hat{A}_i > \alpha \max(\hat{A}_i)$

The maximum harmonic is the first fundamental for all situations. Harmonics higher than the 1st can have a significant amplitude as shown by the 20 and 10 % amplitude distributions which include higher harmonics up to the 4th harmonic. Harmonics higher than the 4th have a less significant contribution as shown by the 5, 2 and 1 % amplitude distributions. The 1% amplitude contains harmonics up to the 15th which is considered the limit of the relevant harmonic content of all the diaphragm displacement measurements. The harmonic content of the diaphragm displacement is depending on the operating conditions as it correlates well with flow rate as can be seen in Figure 7.14.

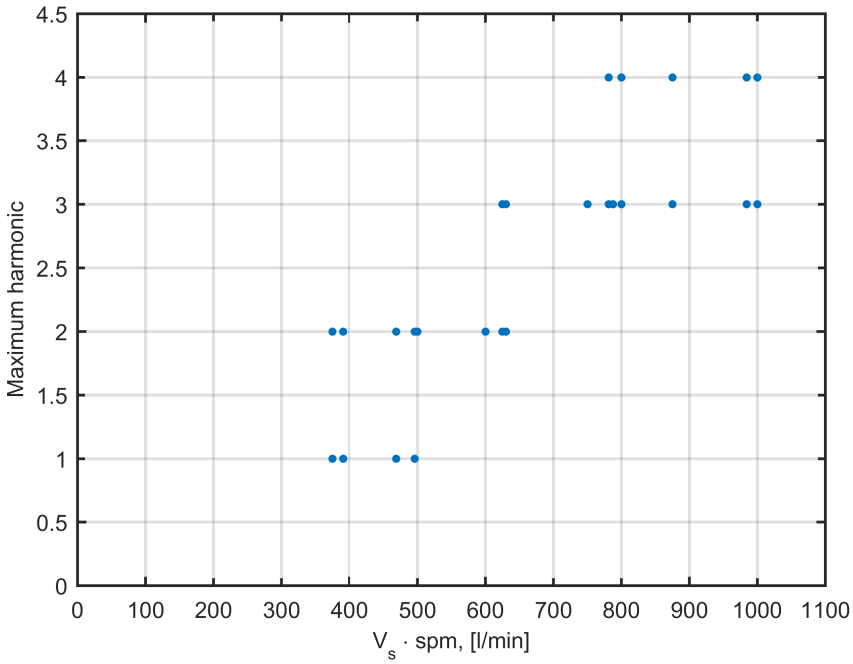

Figure 7.14: Correlation between flow rate and the highest harmonic with an amplitude larger than 10 % of the maximum amplitude in the spectrum

Next to the frequency analysis of the measured axial diaphragm displacement, a spectral analysis of the deformed shapes has been performed. This spatial spectral analysis uses a Fourier series expansion in the circumferential direction and a Fourier-Bessel series expansion in the radial direction using Equation 7.10, Equation 7.11 and Equation 7.12 which results in coefficient matrix $\mathbf{A}_{mn}$ with circumferential modes m and radial modes n. During the diaphragm motion, the value of the coefficients in A_{mn} change. The spectral content of the diaphragm motion in spatial directions is evaluated by determining the maximum values of the coefficients in A_{mn} during a pump cycle according Equation 7.13. A typical result is shown in Figure 7.15.

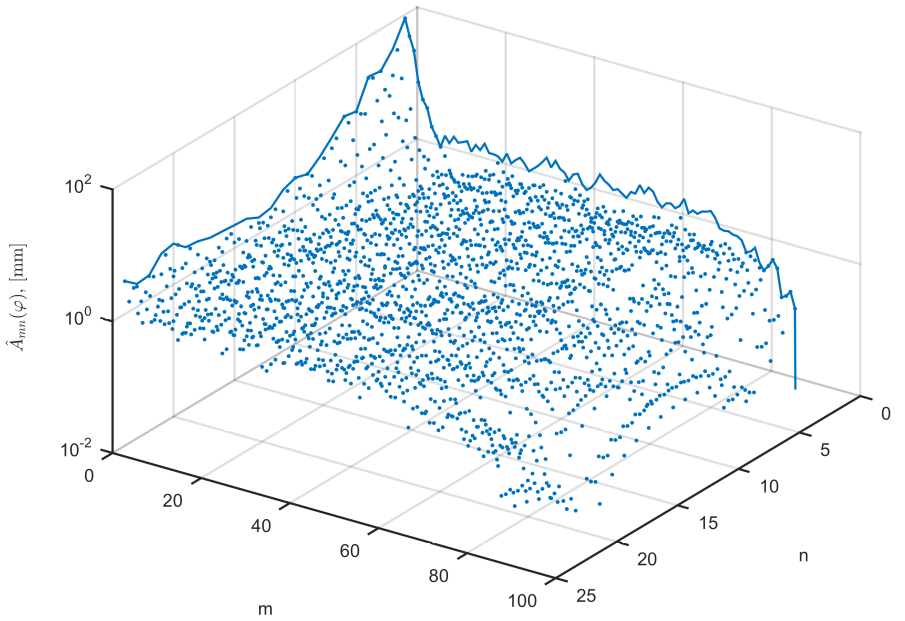

Figure 7.15: Maximum values of mode coefficients $\hat{A}_{mn}$ during pump cycle with enveloping curves for 10 litre stroke volume at 100 strokes per minute (Meas. ID 23)

The maximum coefficient shown in Figure 7.15 is of $O(\hat{A}_{mn}) = 100\,\text{mm}$ for $m = 0$ and $n = 1$. The noise platform is around 1 mm or 1 %. The coefficients which rise above this noise platform are within the range $m < 10$ and $n < 10$ which seems to hold for all dynamic measurements performed. These values are therefore used as the cut-off values when applying the spectral analysis for smoothing of the deformed diaphragm shapes as is done in the top row of Figure 7.11. In static measurements this noise platform is roughly an order of magnitude lower with a value around 0.1 mm or 0.1 %. The increased noise platform is considered to be caused by a not exactly reproducible diaphragm motion for all strokes within a measurement sequence. In order to evaluate the spatial frequency content of the diaphragm shape in radial and circumferential direction, the maximum index n and m are determined respectively which have a value higher than 10 % of the maximum value at $m = 0$ and $n = 1$. These maximum values are again plotted as a function of the flow rate in Figure 7.16 in order to evaluate whether a correlation is present.

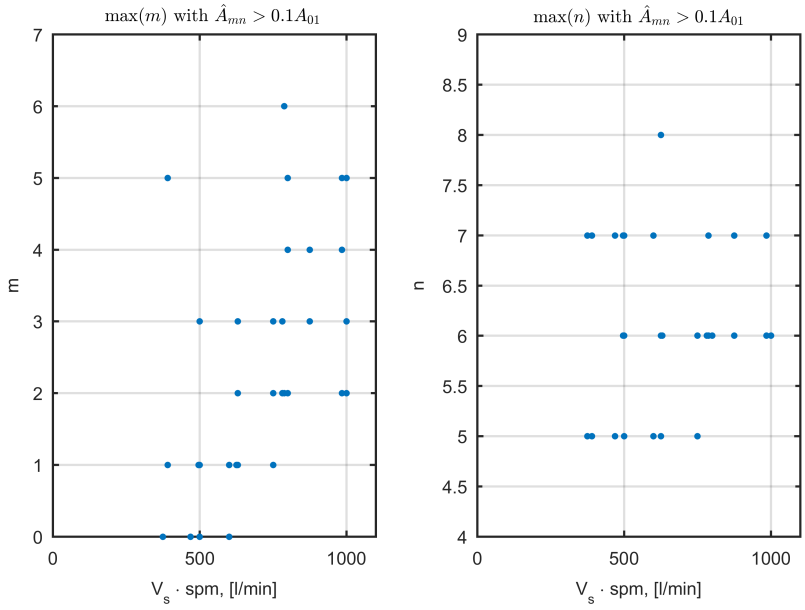

Figure 7.16: Maximum indices m and n in $\hat{A}_{mn}$ which have a value higher than 10 % of $\hat{A}_{01}$

The number of expansions n in the Fourier-Bessel series with a coefficient higher that 10 % of $A_{\text{max},0,1}$ is between 5 and 8 but does not seem to correlate with the flow rate. The number of harmonics m in the circumferential direction on the other hand does correlate with the flow rate. The correlation shows a higher contribution from higher harmonics with increasing flow rate which indicates a more dynamic motion of the diaphragm with increasing flow rate which matches the observations for the 3D animations of the diaphragm motion.

7.4. DISCUSSION, CONCLUSIONS AND RECOMMENDATIONS

7.4.1. DISCUSSION

After resolving the initial operational issues, the laser triangulation measurement has show to be a robust method for determining local diaphragm displacements. The approach using sequentially measured diaphragm displacements on different XY locations worked very well in the quasi-static and low stroke rate experiments as the diaphragm deformation was very reproducible from stroke to stroke resulting in smooth reconstructed diaphragm shapes. The higher stroke rate measurement showed the presence of higher order harmonics in both the time as well as the circumferential direction which correlated well with the flow rate. In the higher stroke rate situations some non-reproducibility on the diaphragm deformation was observed which resulted in more noisy reconstructed diaphragm shapes. Whether this is an inherent to the flow rates situation is not clear. The non-reproducibility could be caused by non-reproducibility of the vortex production or turbulent flow field in the pump chamber whose energy content increases with the sec-

ond power of the flow rate. But the limitations in the tracking behaviour of the servo hydraulic drive and the operation near the cavitation limit are expected to contribute as well. Improvement of the tracking performance of the hydraulic drive and a further increase in the pre-load pressure of the experimental set-up to provide a higher margin against cavitation are required to eliminate these uncertainties and to allow operation at higher stroke rates than obtained so-far. This would require either a hydraulic drive with a much higher load rating or some form of hydraulic balancing should be used to balance the pre-load in experimental set-up such that the hydraulic drive only has to provide power for acceleration of the fluid column in the experimental set-up. Another approach is be to use a crank mechanism with a high inertia drive for improving accuracy of the piston motion. When such improvement would be implemented one could evaluate whether the non-reproducible diaphragm behaviour remains or not. The approach of reconstructing the deformed diaphragm shapes from sequentially measured diaphragm displacement shape reconstruction becomes less suitable when the non-reproducible behaviour turns out to be inherent for high flow rate operation. Then an instantaneous determination of deformed diaphragm shape, for example by using the multiple camera technique, is required. This approach is expected to have its limitation however, with respect to robustness, accuracy, obtainable depth of field in combination with frame rate, exposure and luminance restrictions.

7.4.2. CONCLUSIONS

The following conclusions can be drawn from the operational experience with the experimental set-up and the obtained experimental results

- Refraction of the reflected laser beam needs to be corrected which can be done using a theoretical model or a calibration experiment
- Cavitation in the pump chamber needs to be excluded to allow visual observation of the diaphragm. A suction pressure 3 times higher than the acceleration pressure based on the piston acceleration is required to eliminate cavitation in the pump chamber. This is higher than anticipated and limits the operating range which can be covered by the hydraulic drive.
- Quasi-static and low stroke rate experiment showed very reproducible diaphragm displacement which enabled accurate reconstruction of deformed diaphragm shapes.
- In higher stroke rate experiments some non-reproducibility was observed which resulted in more noisy reconstructed diaphragm shapes. Filtering of the reconstructed deformed diaphragm shapes in the spectral domain using Fourier and Fourier-Bessel series allows the removal of the spatial noise and results in smooth deformation shapes
- Spectral analysis of the reconstructed deformed diaphragm shapes using Fourier and Fourier-Bessel series showed an increase of the higher order harmonics in time and circumferential direction with increasing flow rate.

7.4.3. RECOMMENDATIONS

Recommendations for improvements of the experimental set-up are:

- Improve tracking performance of servo hydraulic drive of experimental set-up at higher stroke rates such that a wider operating range of the set-up is possible.
- Investigate non-reproducibility of the diaphragm deformation in experimental set-up further. First an improvement of the hydraulic drive is required as the increase in non-reproducible behaviour coincides with the start of the reduced tracking performance of the hydraulic drive. When non-reproducibility remains, instantaneous determination of deformed diaphragm shapes using camera techniques could be considered.

8

RESULTS AND VALIDATION OF NUMERICAL MODEL

8.1. INTRODUCTION

In this chapter the performance of the numerical model developed in this study is quantified. The numerical results are validated with the experimental results obtained from the experimental set-up developed within this study. A sensitivity study of some parameters in the numerical model is performed. Next some numerical simulation results are shown which are obtained using industrially relevant fluid parameter values of slurry density and yield stress. Based on the results, the strengths an weaknesses of the developed model are discussed and guidelines for use and directions for future research are given.

8.2. OVERVIEW NUMERICAL SIMULATIONS

Several numerical simulations have been conducted. A reference case with a stroke volume of 10 litre at 100 strokes per minute was selected which was used as a basis for some parameter studies. The numerical approach followed by the numerical model has been discussed in chapter 6 and specific characteristics of the reference case were shown in Table 6.1. Numerical simulations with variations on this reference case were conducted for validation by experimental results and for evaluating the influence of some specific parameters. The variations conducted are summarized as follows:

- Quasi-static simulations with and without hydrostatic pressure load using structure-only model
- High stroke rate (reference case) and low stroke rate using FSI model
- Effect of elastic modulus using FSI model
- Effect of advection scheme and turbulence model

- Effect of fluid grid and structural mesh size
- Effect of slurry density and yield stress

The quasi-static simulations are validated using the quasi-static experiments shown in Table 7.1 with the air-air and oil-air loading with measurement ID 3s and 4s. The reference case is validated using the dynamic experiment with measurement ID 23 as shown in Table 7.2. For the low stroke rate case, the dynamic experiment with measurement ID 2 with 10 litre stroke volume at 50 strokes per minute was selected. The simulation variations focussing on the effect of elastic modulus, advection scheme, turbulence model and mesh and grid size are all compared with the results of the dynamic experiment of the reference case with measurement ID 23. The validation of the effect of the slurry density and yield stress can not be validated with the available experimental results and is presented here to show the relevance of the parameters and as an example of future use of the model in studying practical situations. Variation of some important parameters with respect to the reference case are shown in Table 8.1.

Table 8.1: Variations of important parameters with respect to the reference model (ID 3 in bold) which characteristics are shown in Table 6.1.

ID	f [spm]	ρ_1 [kg/m^3]	ρ_2 [kg/m^3]	# cells [$\cdot 10^3$]	E [Mpa]	Adv. Scheme / Turb. Model	τ_y [Pa]
1	60	0	0	(*)	2.7	-	-
2	60	900	0	(*)	2.7	-	-
3	**100**	**900**	**1000**	**524**	**2.7**	**TVD**	**0**
4	50	900	1000	524	2.7	TVD	0
5	100	900	1000	524	2.2	TVD	0
6	100	900	1000	524	3.4	TVD	0
7	100	900	1000	524	4.2	TVD	0
8	100	900	1000	524	2.7	UD	0
9	100	900	1000	524	2.7	HD	0
10	100	900	1000	524	2.7	TVD+WALE	0
11	100	900	1000	66	2.7	TVD	0
12	100	900	1000	221	2.7	TVD	0
13	100	900	1000	1769	2.7	TVD	0
14	100	900	2300	524	2.7	TVD	0
15	100	900	1000	524	2.7	TVD	100
16	100	900	1000	524	2.7	TVD	1000

(*) Structure-only model with 2611 nodes

8.3. QUASI-STATIC STRUCTURE-ONLY SIMULATIONS

8.3.1. APPROACH

In the fluid structure interaction model a flow solver and a structural solver are merged together. In this section the structural solver is validated with some quasi-static exper-

iments. From the dimensional analysis of the FSI problem it follows that next to the piston displacement volume, hydrostatic and fluid momentum loads, and to a lesser extent viscous fluid loads, are present on the diaphragm. However, the fluid momentum and viscous loads are considered absent in low speed operation. In this situation only the piston displacement and the hydrostatic fluid loads due to density differences across the diaphragm need to be evaluated. The volumetric piston displacement will then give a uniform pressure loading on the diaphragm and the hydrostatic fluid load will only add a constant pressure gradient in the gravitational direction. These load cases can be evaluated without the use of a flow solver and only require the structural model which enables its validation without the added complexity of the flow solver. This also allows an isolated evaluation of the effect of the hydrostatic pressure load on the diaphragm due to density differences between propelling and pumped fluid. Validation is possible using the quasi-static experiments in which the propelling fluid and/or pumped fluid were replaced by air. A situation without a hydrostatic load is simulated in the experimental set-up by using air for both the propelling as well as the pumped fluid. A situation with a hydrostatic load was simulated by using mineral oil as the propelling fluid while using air as the pumped fluid. These cases respectively refer to measurement ID 3s and 4s in Table 7.1.

Although the explicit dynamic structural model described in chapter 6 is most suited for simulation of dynamic situations, it can also be used for a quasi-static simulation when sufficient damping is added and when the load is applied sufficiently slow such that any damping and inertial loads in the model are small compared to the internal and external loads due to respectively the internal stresses and externally applied pressure. This approach is also referred to as dynamic relaxation, (Belytschko *et al.*, 2000). Here a simple mass proportional damping as discussed in section 6.3 has been used, whose damping constant α is scaled such that a well damped ($\zeta \approx 0.5$) step response is achieved. A simulation at a stroke rate of 60 spm or 1 Hz is considered quasi-static as a lowest natural frequency of the structural model of approximately 17 Hz was determined from the simulation of a step response.

In the experiments, the volumetric displacement of the diaphragm is prescribed by the displacement of the piston. In the numerical model however, a pressure load needs to be applied to the diaphragm. Because of the snap-through behaviour of the diaphragm a simple pressure load which increases in time won't work. The volumetric displacement needs to be given as a constraint to the diaphragm deformation and the pressure has to follow from that. This effect has been included in the structural model by including a lumped hydraulic capacitance in the structural model. Every time step the volume behind the diaphragm V_d is calculated and the difference with the volume based on the piston displacement V_s is determined. Based on this difference a uniform pressure load is applied on the surface of the diaphragm which is proportional with this volume difference by scaling it with a reference volume V_0, and multiplying it with some bulk modulus K.

$$p = \frac{V_d - V_s}{V_0} K \tag{8.1}$$

The bulk modulus has been set such that the difference between the diaphragm and

piston displacement volume remains small, less than 1%, without limiting the time step of the simulation. A time step limitation could arise as the lumped hydraulic capacitance adds stiffness to the model. The average volume between the piston and the diaphragm is used as the reference volume V_0, a practical value of the bulk modulus which can then be used is 1 MPa, which represents an air volume pre-loaded at approximately 700 kPa when assuming adiabatic compression ($K = \gamma p$). The FE mesh used has 2611 nodes, hence 7833 Degrees Of Freedom (DOF)) and 5046 elements, which is approximately 2 times the number of nodes for regular triangular mesh. The nodes on the outer edge, which represents the centre of the O-ring of the diaphragm, are constraint in all directions and the nodes outside the clamping diameter are constrained in the axial direction only such that radial slip in the diaphragm clamping is possible to some extend. Trials which different constraint conditions around this diaphragm clamping such as fully constraining all nodes outside the clamping diameter or adding some flexibility to the axial constraint, did not give significantly different results.

8.3.2. RESULTS AND VALIDATION QUASI-STATIC SIMULATIONS

OIL-AIR LOADING

In Figure 8.1 numerically and experimentally obtained 3D deformed diaphragm shapes for the oil-air loading are compared. The lower part of the diaphragm sags due to the higher hydrostatic pressure on the propelling fluid side. The numerically obtained deformed shapes resemble the experimental obtained ones quite well.

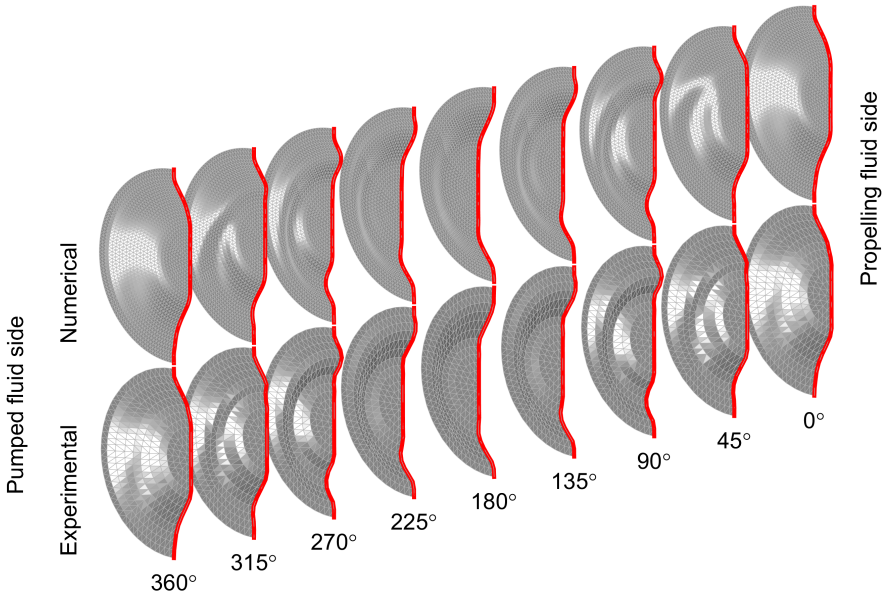

Figure 8.1: Comparison of numerically (top) and experimentally (bottom) obtained 3D deformed diaphragm shapes for quasi-static oil-air loading with a density difference of 900 kg/m^3. Numerical results obtained with structure-only model with lumped parameter fluid capacitance enabling control of displacement volume. Experimental conditions according Table 7.1, measurement ID 4s. Deformed diaphragm shapes shown from start of discharge stroke on the right with 45° intervals to end of suction stroke on the left.

To validate the agreement further, 2D cross sections are shown in Figure 8.2 for different piston positions at 45° intervals. As can be seen the agreement between the experimental and numerical results is quite good.

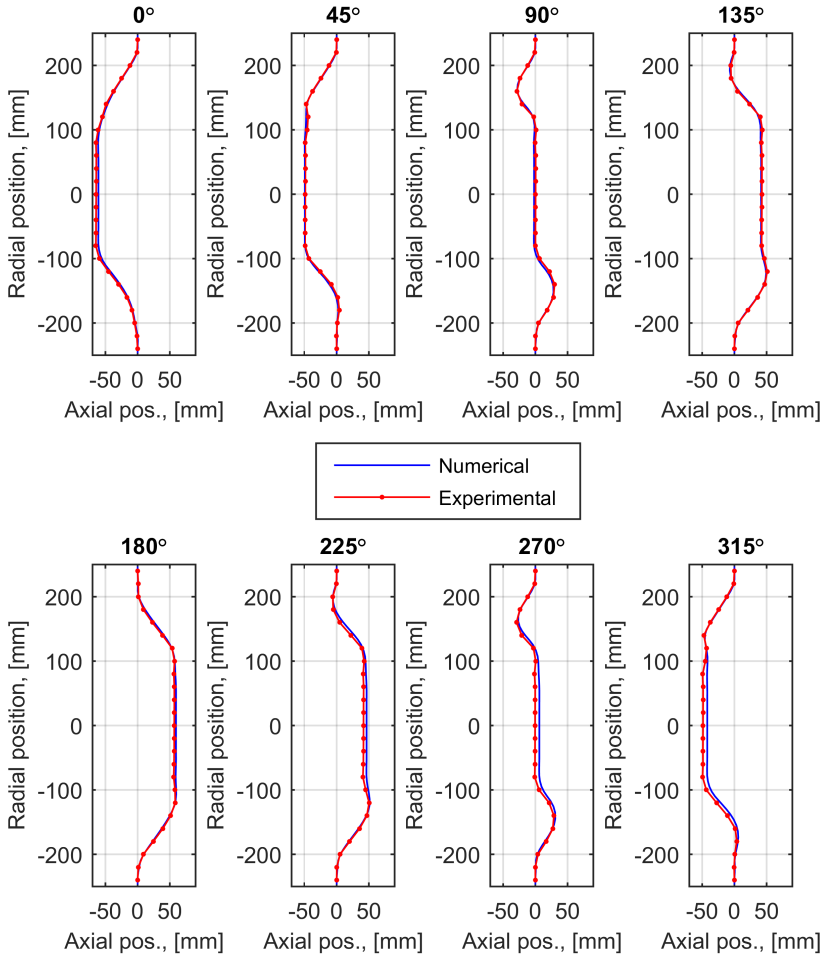

Figure 8.2: Comparison numerical (blue) and experimental (red) results in 2D cross sections in vertical plane at 45° intervals for quasi-static oil-air loading with 900 kg/m^3 density difference. Numerical results obtained with structure-only model with lumped parameter fluid capacitance enabling control of displacement volume. Experimental conditions according Table 7.1, measurement ID 4s.

AIR-AIR LOADING

In Figure 8.3 numerically and experimentally obtained 3D deformed diaphragm shapes for the air-air loading are compared. The numerically obtained deformed shapes resemble the experimental obtained ones quite well. The numerically obtained deformation shapes are axisymmetric for the major part of the pump cycle, except at 45° into the discharge strokes where formation of buckling lobes is observed. The buckling lobes are observed in the experimentally obtained deformed shapes as well. The buckling lobes in the numerical results are periodic every 60° and align with the periodicity in the FE mesh. The buckling lobes in the experimental result are not completely periodic and only 5 of them seem to form.

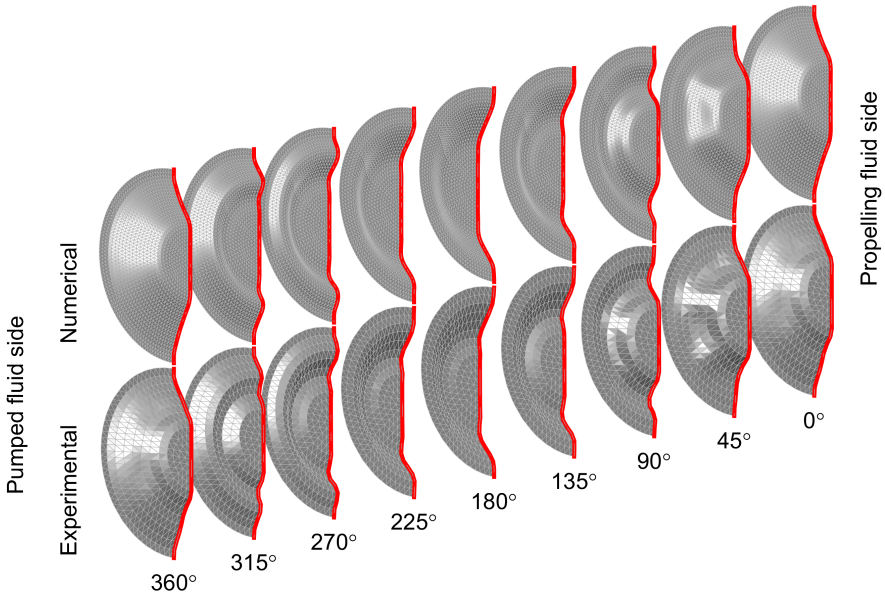

Figure 8.3: Comparison of numerically (top) and experimentally (bottom) obtained 3D deformed diaphragm shapes for quasi-static air-air loading without a density difference. Numerical results obtained with structure-only model with lumped parameter fluid capacitance enabling control of displacement volume. Experimental conditions according Table 7.1, measurement ID 3s. Deformed diaphragm shapes shown from start of discharge stroke on the right with 45° intervals to end of suction stroke on the left.

For further validation, 2D cross sections are shown in Figure 8.2 for different piston positions at 45° intervals. For most piston positions the agreement is quite good, but at the end of the suction stroke at 315°, a larger difference between the numerical and experimental results is observed. Here the diaphragm approaches a snap-through point and the response in the experiments is different from what is predicted by the numerical model. What is exactly causing this difference is not known, but the accuracy of the modelling of the bending stiffness near the central metal plate could be limited and the absence of the shear deformation in the thin plate model might play a role here as well. In the last 45 degrees of the suction stroke only 15% of the stroke volume is left to be displaced, while the diaphragm centre still has to travel approximately 30% of its stroke. At the start of this last part of the suction stroke, the annular area of the diaphragm is convex when looking in the positive axial direction, but has to snap to a concave shape in order to compensate for the excess displacement volume of the central plate of the diaphragm. The deformation behaviour of the diaphragm near this snap-though point is most likely more dependent on the local bending and potentially shear stiffness near the central plate than during is the rest of the stroke. During the discharge stroke the annular area of the diaphragm is concave when looking in the positive axial direction, while during the suction stroke it is largely convex.

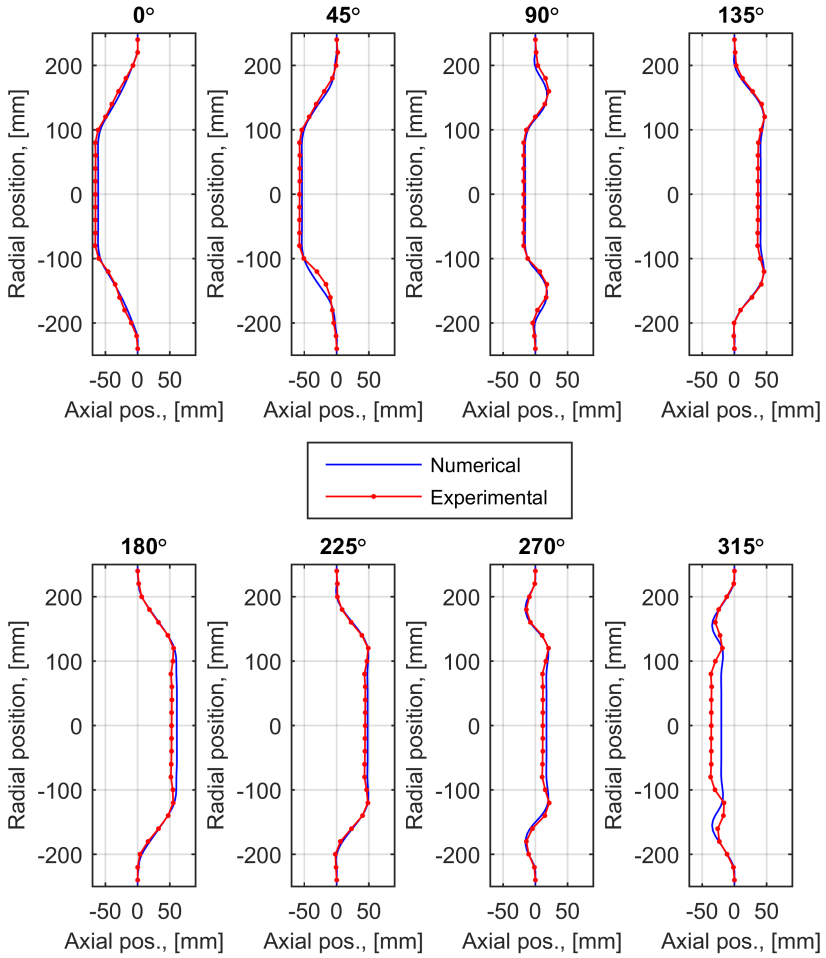

Figure 8.4: Comparison numerical (blue) and experimental (red) results in 2D cross sections in vertical plane at 45° intervals for quasi-static air-air loading without density difference. Numerical results obtained with structure-only model with lumped parameter fluid capacitance enabling control of displacement volume. Experimental conditions according Table 7.1, measurement ID 4s.

The difference in concave and convex shape can also be recognized when the position of the centre of the diaphragm is plotted as a function of the displaced volume, as can be seen in the left plot of Figure 8.5. The central plate is continuously lagging behind the annular area as shown by the hysteresis loop. The steep slope at the end of the suction stroke in the curve of the numerical results (1) indicates a large displacement of the central plate with only a small displacement volume, hence an abrupt snap-through at the end of the suction stroke. This abruptness is not present to the same extent in the experimental results. In the right plot of Figure 8.5 the path of the central plate is plotted as a function of stroke volume for the for the case with the hydrostatic pressure loading. Here hardly any hysteresis loop can be seen, indicating similar concave and convex de-

formation during the suction and discharge stroke. In Figure 8.1 and Figure 8.2 one can see that the hydrostatic pressure loading generates a concave deformation shape of the annular area in the lower section of the diaphragm which gradually turns to a convex deformation shape in upper section of the diaphragm. During the deformation cycle the lower section stays largely concave and the upper section largely convex.

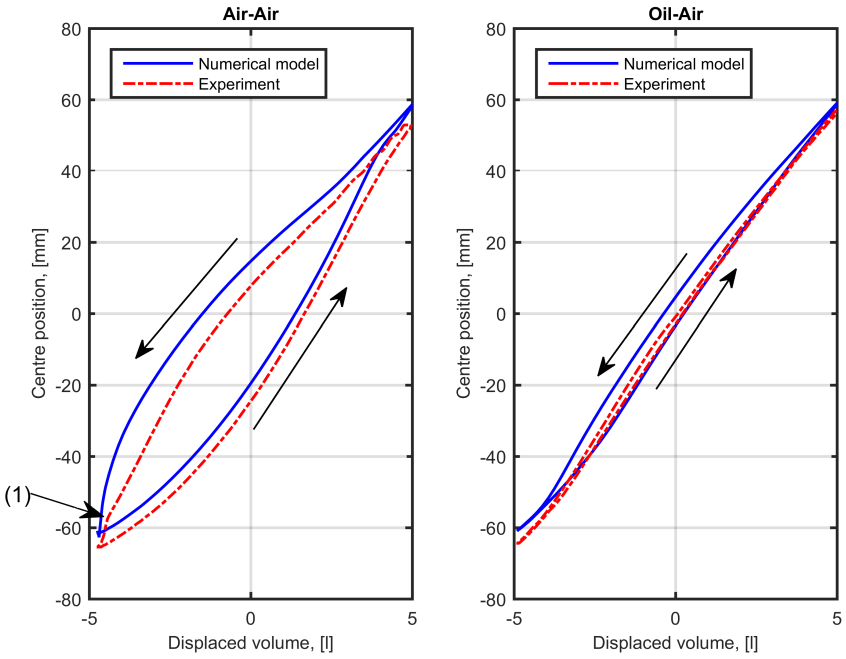

Figure 8.5: Path dependency of diaphragm deformation shown by path of diaphragm central plate versus the displaced volume for quasi-static case without (left) and with (right) a hydrostatic loading. Numerical results obtained with structure-only model with lumped parameter fluid capacitance enabling control of displacement volume. Experimental conditions according Table 7.1, measurement ID 4s and 3s respectively.

The highly non-linear deformation behaviour of the diaphragm and its snap-though behaviour is further shown by the pressure load versus volumetric displacement of the diaphragm curve shown in Figure 8.6. The pressure load is calculated in the numerical model according Equation 8.1 while applying the volumetric displacement. Both the curve with (oil-air) and the curve without (air-air) hydrostatic load show a highly non-linear pressure versus volumetric displacement behaviour with a negative slope between the local maximum and minimum, indicating a negative stiffness hence buckling or snap-through behaviour. The pressure load versus volumetric displacement curves are not identical for the discharge and suction stroke. For the air-air case this can be explained by the different deformation shapes in the discharge and suction stroke at similar volumetric displacement. For the oil-air case the deformation shapes are more or less identical and implying another reason for the difference in the pressure load curve

during the discharge and suction stroke. The difference can be explained by the mass proportional dampening which is used in the structural model. This introduces a nodal dampening force term which is proportional with the nodal velocity itself, independent on deformation rate of the diaphragm material. The velocities of the nodes in the centre of the diaphragm and the dampening constant are of such magnitude that they can explain the difference in the pressure load curve. The curves are expected to map on each other for very load strokes rates but this would require extremely long simulation times when using the explicit dynamic structure-only model which requires a small time step for stability reasons.

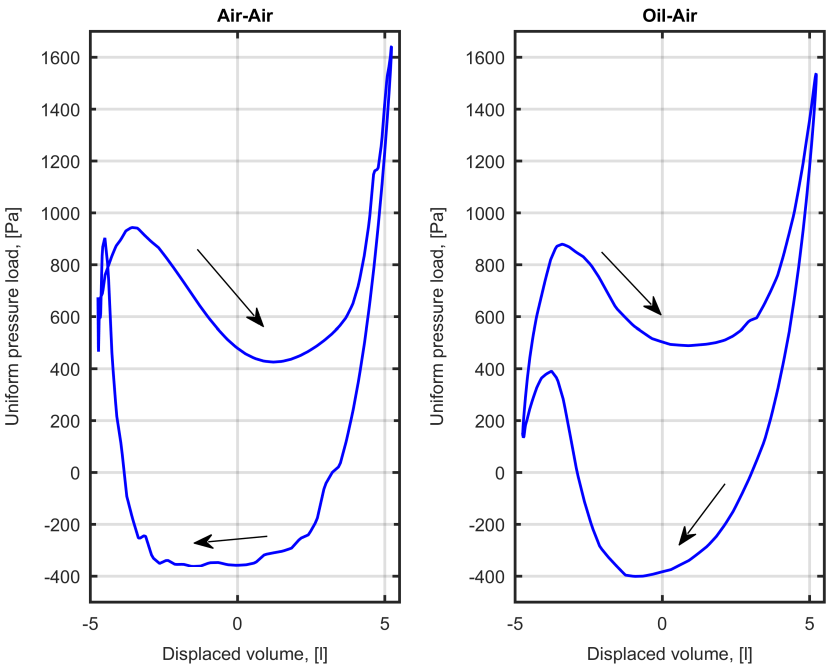

Figure 8.6: Pressure load on diaphragm as function of volumetric displacement obtained from quasi-static structure-only numerical model without hydrostatic load (air-air on left) and with hydrostatic load (oil-air, right). Numerical results obtained with structure-only model with lumped parameter fluid capacitance enabling control of displacement volume. Experimental conditions according Table 7.1, measurement ID 3s and 4s respectively.

8.4. HIGH AND LOW STROKE RATE VALIDATION OF FSI MODEL

In this section the fluid structure interaction model is validated with experimental data obtained at a high and a low stroke of respectively 100 and 50 strokes per minute. In both cases a stroke volume of 10 litre is used which is considered the static displacement volume limit. The measurement ID's of the experimental results according Table 7.2 are 23 and 2 respectively. The stroke rate of 100 strokes per minute was selected as this was the highest stroke rate which could be obtained in the experimental test rig with the 10

litre stroke volume before encountering cavitation issues. The 10 litre at 100 strokes per minute is the reference case whose characteristics are described in Table 6.1.

8.4.1. STABILITY ISSUES

In section 6.2 and section 6.4 the presence of stability limits in the flow solver and the FSI model due to the explicit time integration were discussed. In the flow solver the time step is limited by the characteristic diffusion time across a fluid cell and the characteristic advection time across a fluid cell also referred to a the CFL limit. In the FSI model an additional limit due to the mechanical natural frequencies is to be considered as well. This mechanical natural frequency limit is dominated by the bending stiffness for smaller mesh sizes as discussed in section 6.3 and section 6.4. Absolute values of the alowable time step with respect to the diffusion and CFL limit can be evaluated directly according Equation 6.19, which is not possible for the mechanical frequency as it is unknown how much added fluid mass needs to be included. This limit was therefore determined empirically by trial-and-error. Although the stiffness of the diaphragm changes drastically during its deformation, the element stiffness's are expected to remain relatively constant such that the empirically determined time step limit by the mechanical natural frequency should remain relatively constant as well. During initial simulations it was found however that the structural mesh gradually became distorted. The distortion had a high-low variation every other element, especially near areas with high local flow velocities. The distorted element finally became unstable, prohibiting any longer duration simulation of several strokes. A solution was found to use a more stringent CFL limitation in the fluid cells which are used for interpolating the immersed boundary points. Finally a global CFL limit of 0.8 was used and local CFL limit of 0.2 was used near the immersed flexible boundary.

8.4.2. RESOLVED FLOW FIELDS REFERENCE CASE

The deformed diaphragm shapes are a result of the fluid structure interaction between the diaphragm and the fluid flow on both sides of the diaphragm. For a better understanding of the FSI mechanisms some observations of the resolved flow field are discussed first.

In Figure 8.7 contour plots are shown which show the magnitude of the velocity in the XZ-plane on 45° intervals for the reference case with 10 litre stroke volume at 100 stroke per minute using the TVD scheme with UMIST flux limiter without eddy viscosity model. At 0° no flow is entering or leaving the computational domain but still a rather large recirculation is present on the pumped fluid side of the diaphragm. During the discharge stroke the diaphragm is displaced towards the right and in the 2nd half of the discharge stroke a toroidal vortex forms on the propelling fluid side of the diaphragm which is still present at the stroke reversal point at 180 degrees. At the end of the discharge stroke a higher velocity region forms on the top side of the diaphragm near the discharge port which causes the top side to lead with respect to the bottom side. Around the stroke reversal a top down oscillation of the propelling fluid is seen which creates additional bending near the camped edge of the diaphragm compared to a more symmetrical deformation obtained without asymmetrical fluid loads. This is best seen in a 3D animation but can be recognized in the 135, 180 and 225 degrees contour plot where

the oscillation is respectively top-down-top. During the suction stroke a high velocity jet is entering the housing. Much higher velocities are present in the housing during the suction stroke than in the discharge stroke as the fluid flow does not follow the rapid geometric expansion of in the housing.

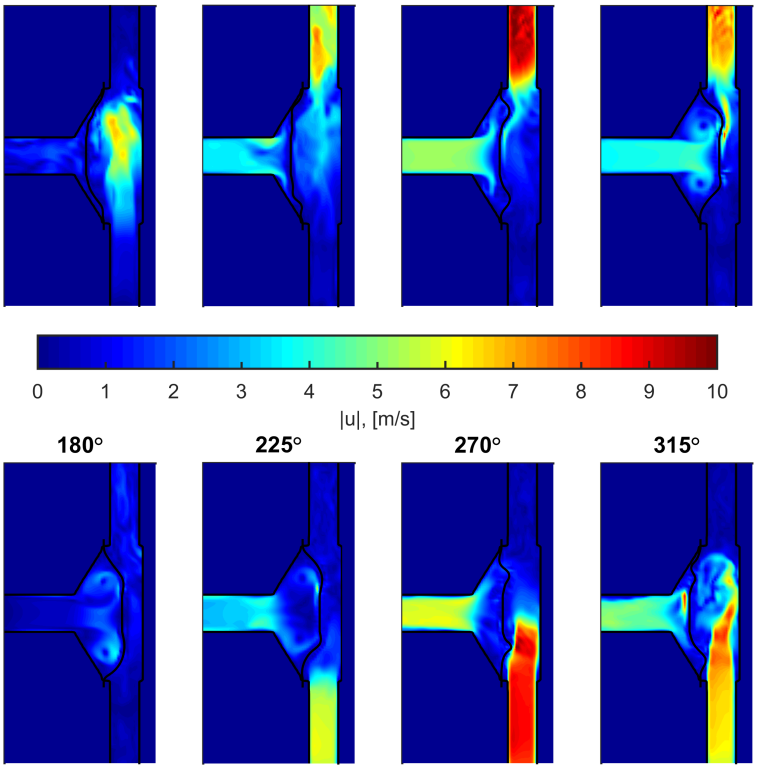

Figure 8.7: Contour plots of magnitude of velocity in XZ-plane on 45° intervals for FSI reference case according Table 6.1 with 10 litre stroke volume at 100 strokes per minute using TVD scheme with UMIST flux limiter without eddy viscosity model

The high velocity present in the suction port continues in the housing as a jet where it forms rather complex vortex structures. These vortex structures can be visualized using the so-called Q-criterion which is the second invariant of the velocity gradient tensor which indicates the balance between the rotation rate and the rate-of-deformation as shown by Dubief and Delcayre (2000) and discussed in section 4.1. In areas where Q is positive, the rotation of the flow dominates over the deformation or shear of the flow. A vortex can then be identified by a zone in which the Q-criterion is larger than some threshold value. The Q-criterion is used for visualizing vortex structures by plotting iso-surfaces of a specific Q-value. In Figure 8.8 the vortex structure at 315 degrees is shown. Although a vorticity free inflow boundary is used, vortex structures rapidly form when the fluid from the suction port can expand in the housing. As can be seen in Figure 8.8

relatively small vortices with a core diameter of a few grid cells are resolved by the model.

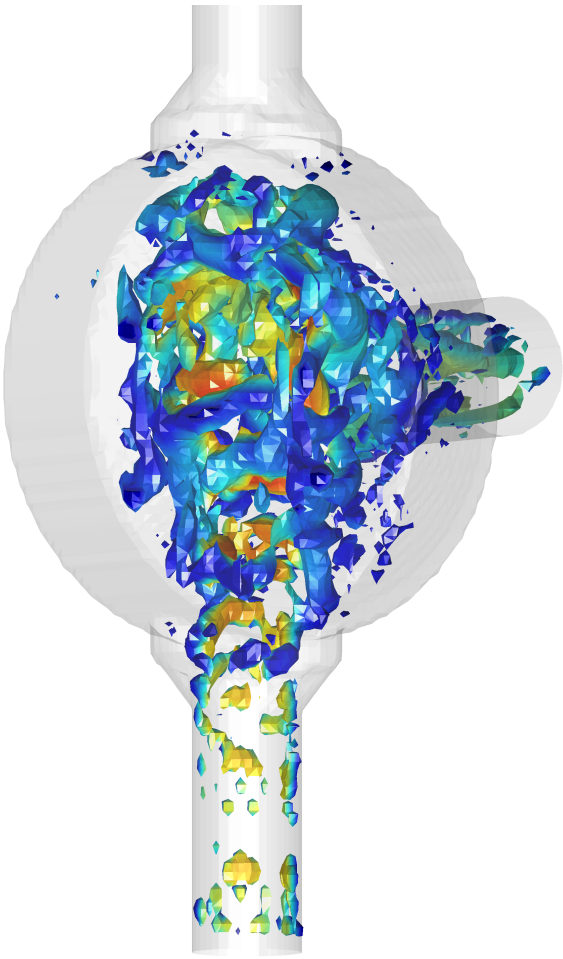

Figure 8.8: Vortex structure at 315 degrees shown by isosurfaces of Q-criterion at $Q = 1000s^{-2}$ for FSI reference case according Table 6.1 with 10 litre stroke volume at 100 strokes per minute using TVD scheme with UMIST flux limiter without eddy viscosity model. Isosurface is coloured with the magnitude of the velocity

8.4.3. DEFORMED DIAPHRAGM SHAPES REFERENCE CASE

In Figure 8.9 the numerically and experimentally obtained 3D deformed diaphragm shapes for the reference case of 10 litre stroke volume at 100 strokes per minute are compared. Although the hydrostatic pressure difference is rather low in this case, a rather extreme asymmetrical deformation can be observed. This asymmetrical deformation is a result of the additional fluid momentum loading on the diaphragm at the higher stroke rate compared to the quasi-static case shown before. The phenomenological deformation behaviour of the diaphragm observed in the experimental results is replicated by the numerical model. At the beginning of the discharge stroke at 45°, the top of the diaphragm

is near the rear wall and a lobe on the side around the 9 o'clock position is present (1). Halfway the discharge stroke at 90°, this side lobe moves to the top position (2). Around the end of the discharge stroke and the beginning of the suction stroke at 135°, 180° and 225°, a top-down-top oscillation of the fluid around the diaphragm is observed (3)-(4)-(5). During the suction stroke a lobe on the lower half of the diaphragm is formed, most likely due the low pressure created by the high velocity jet entering the pump chamber via the suction port. However, a sharp fold is observed in the lower half of the diaphragm in the numerical results (6) which is not present in the experimental results. Furthermore higher order surface waves are observed in the numerical results (7) which are not present in the experimental results.

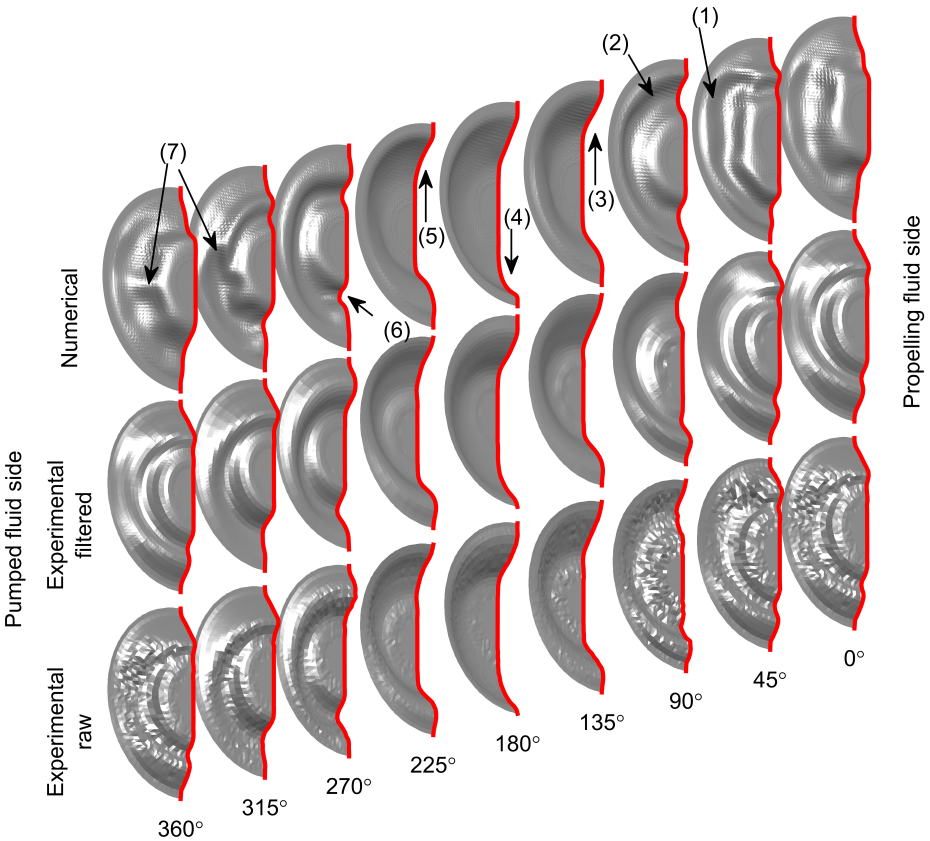

Figure 8.9: Comparison of numerically (top) and experimentally (bottom) obtained 3D deformed diaphragm shapes for reference case with 10 litre stroke volume at 100 strokes per minute. Numerical results obtained with FSI model according Table 6.1. Experimental conditions according Table 7.2, measurement ID 23. Bottom row shows raw experimental data and middle row shows filtered experimental data. Deformed diaphragm shapes shown from start of discharge stroke on the right with 45° intervals to end of suction stroke on the left.

In Figure 8.10 2D cross sections of the experimental and numerical deformed di-

aphragm shapes are compared at 45° intervals in the pump cycle. Near the end of the discharge and the beginning of the suction stroke at 135°, 180° and 225°, the comparison is quite good. In the other positions some differences between the experimental and numerical results can be seen. The main source for the observed differences is considered to be the buckling or snap through behaviour of the diaphragm. This results in unstable deformation shapes of the diaphragm which can bifurcate into different shapes as a result of relatively small differences in the model compared to the experimental set-up.

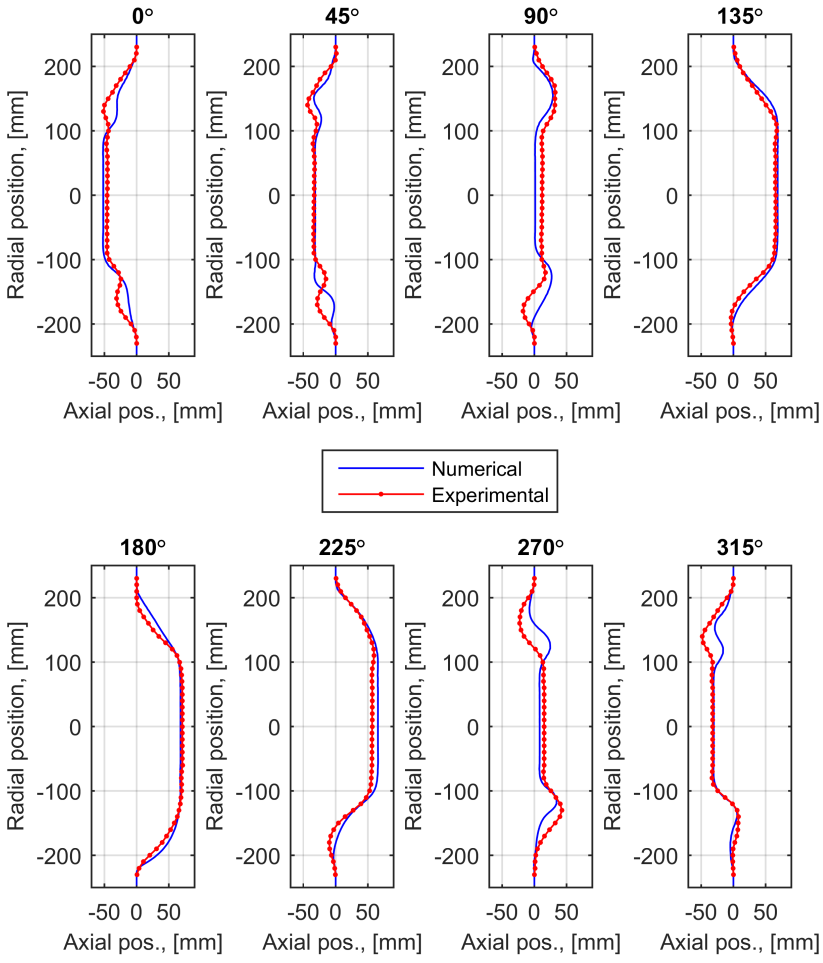

Figure 8.10: Comparison of numerical and experimental results in 2D cross sections in vertical plane at 45° intervals for FSI reference case of 10 litre stroke volume at 100 strokes per minute. Numerical results obtained with FSI model according Table 6.1. Experimental conditions according Table 7.2, measurement ID 23.

8.4.4. DEFORMED DIAPHRAGM SHAPES LOW STROKE RATE CASE

Next to the reference case of 10 litre at 100 strokes per minute a low speed case of 10 litre stroke volume at 50 strokes per minute was simulated and validated with experimental

results. In Figure 8.11 the numerically and experimentally obtained 3D deformed diaphragm shapes are compared. An asymmetric deformation shape is observed in the numerical results while the experimental results show largely axisymmetric deformation shapes. The asymmetry in the numerical results is mainly formed at the end of the suction stroke at 315° where the upper part of the diaphragm is leading the volumetric displacement while the lower part lags behind by forming a lobe. Higher order surface waves as observed in the numerical results for 100 strokes per minute are not observed in the numerical results for this 50 strokes per minute case.

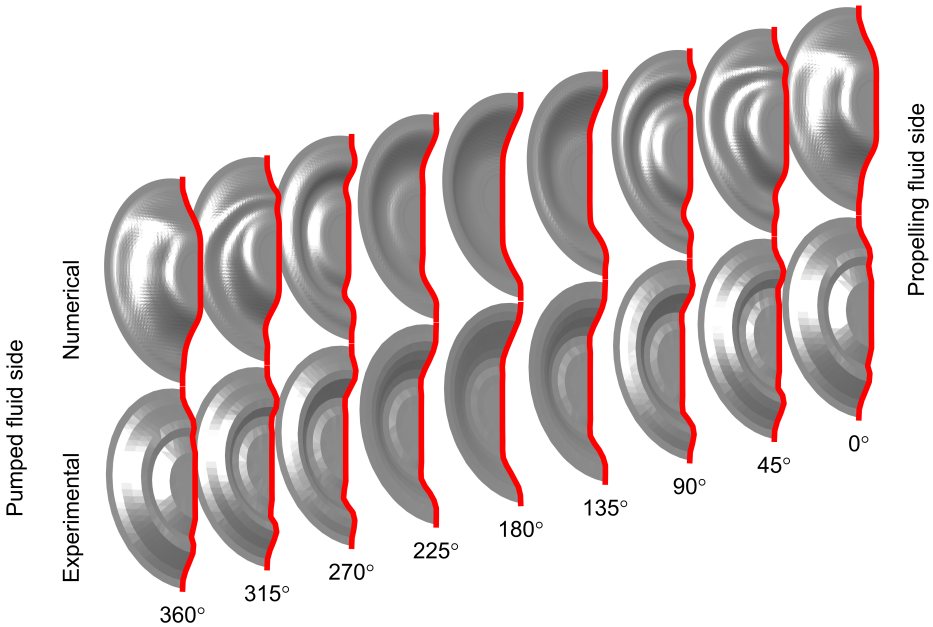

Figure 8.11: Comparison of numerically (top) and experimentally (bottom) obtained 3D deformed diaphragm shapes for 10 litre stroke volume at 50 strokes per minute. Numerical results obtained with FSI model according Table 6.1 with 50 spm and 1.1 litre initial diaphragm displacement. Experimental conditions according Table 7.2, measurement ID 2. Deformed diaphragm shapes shown from start of discharge stroke on the right with 45° intervals to end of suction stroke on the left.

In Figure 8.12 2D cross sections of the experimental and numerical deformed diaphragm shapes at 50 strokes per minute are compared at 45° intervals in the pump cycle. The deformed shape at the end of the discharge stroke at 180° is reproduced quite accurately by the model. During the rest of the suction stroke a larger displacement of the central part of the diaphragm is observed in the numerical results. At the end of the suction stroke this leads to the formation of a concave lobe in the positive axial direction in the lower half of the diaphragm. In the experimental results the curvature in both the upper and lower half remains convex during the entire discharge and suction stroke, different from the quasi-static results. The stroke length of the central part of the diaphragm is approximately 20 mm longer in the numerical results approaching the rear

wall. The diaphragm fill position in both the experimental cases with 100 and 50 stroke per minute, with measurement ID 23 and 2 respectively, were equal at 34 mm from the rear wall. The initial diaphragm displacement volume at zero piston displacement as set by the propelling fluid fill and relieve system in the experiment was 1.1 litre for the 50 strokes per minute case compared to 2 litre for the 100 strokes per minute case. These initial diaphragm displacement volumes have been used in the numerical model. The numerical model seems to have difficulties with smaller initial diaphragm displacement volumes which causes the central plate to be dragged more towards the propelling fluid port during the last part of the suction stroke. Similar issues were experienced when validating the experimental cases with a diaphragm fill position of 14 mm from the rear wall. These issues are most likely a result of the lack of any fluid grid resolution between the diaphragm and the rear wall when the diaphragm is approaching the rear wall. Fluid grid refinement is required to improve this situation.

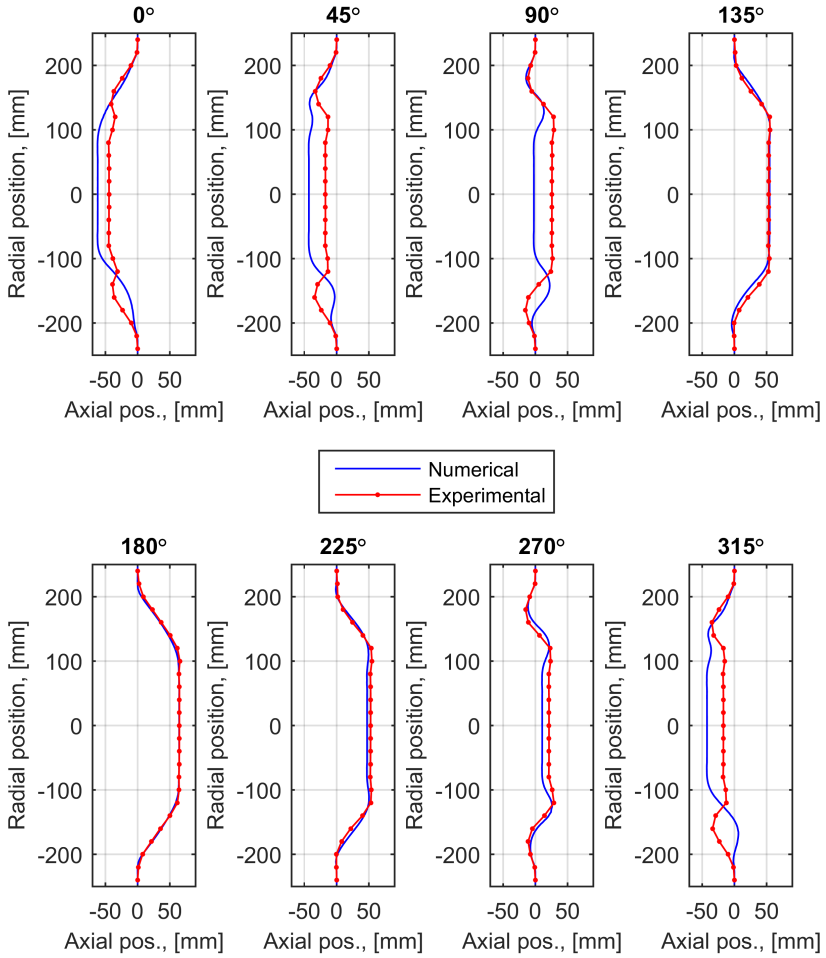

Figure 8.12: Comparison experimental and numerical results in 2D cross sections in vertical plane at 45° intervals for 10 litre stroke volume at 50 strokes per minute. Numerical results obtained with FSI model according Table 6.1 with 50 spm and 1.1 litre initial diaphragm displacement. Experimental conditions according Table 7.2, measurement ID 2.

8.5. EFFECT OF ELASTIC MODULUS

The elastomer of the diaphragm is characterized with its hardness which can be used to estimate the elastic modulus of the rubber, (Gent, 2001). In the experiments a diaphragm with a specified hardness of 52 Shore A has been used, which gives an elastic modulus of 2.7 MPa. The allowable variation however is ± 5°. When converted to an elastic modulus this gives a range of 2.2 to 3.4 MPa which is 80 to 125% of the average value. When considering the dimensionless stroke rate, this range would corresponds to a stroke rate variation of roughly ± 10% as the dimensionless stroke rate scales with the square root of the elastic modulus. A parameter study using elastic moduli of respectively 2.2, 2.7,

3.4 and 4.3 MPa has been conducted.

In Figure 8.13 3D deformed diaphragm shapes obtained from the parameter study are shown. The phenomenological behaviour is the same for all situations. It seems however that higher order surface waves are more prominent for lower elastic moduli shown in the top rows. The sharp fold at the lower part of the diaphragm halfway the suction stroke at 270° is no longer observed in the 4.2 MPa case. Phenomenologically the 4.2 MPa case seems to resemble the experiential results most closely. The sharp fold and the higher order surface waves are not observed in the experimental results which suggest a too flexible deformation behaviour of the diaphragm in the reference model with the 2.7 MPa elastic modulus.

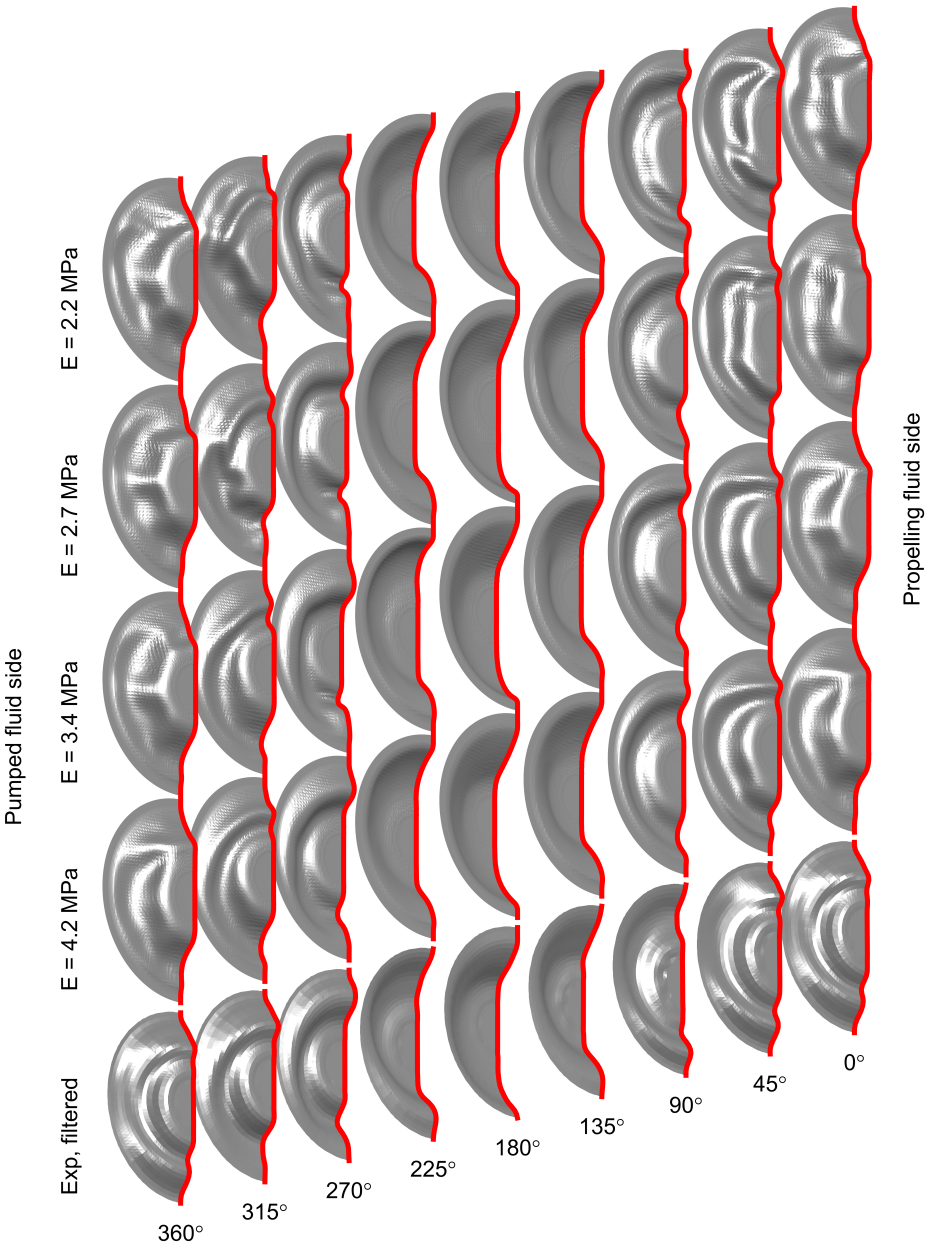

Figure 8.13: Effect of elastic modulus on numerically obtained 3D deformed diaphragm shapes as a variation of the reference case with 10 litre stroke volume at 100 strokes per minute according Table 6.1. Experimental conditions according Table 7.2, measurement ID 23. From top to bottom; $E = 2.2$ MPa, $E = 2.7$ MPa, $E = 3.4$ MPa, $E = 4.2$ MPa, filtered experimental results. Deformed diaphragm shapes shown from start of discharge stroke on the right with 45° intervals to end of suction stroke on the left.

In Figure 8.14 the influence of the elastic modulus on the numerically obtained diaphragm shapes in 2D cross sections is shown. It can be seen that the variation in the elastic modulus, which is within the allowable range for the diaphragm rubber (2.2 to 3.4 MPa), can already give variations in the numerically obtained diaphragm deformation shape which are of similar magnitude as the differences observed between the experimentally and numerically obtained deformation shapes. In some situations the lower elastic modulus gives a better comparison with the experimental results as for example in lower lobe at 90° and the upper lobe at 315° where the 2.7 MPa case is most close. But in other situations the higher elastic modulus gives a better comparison such as in the upper lobe at 270° where the 3.4 MPa case is most close and in the lower lobe at 270° where the 4.2 MPa case is most close, although outside the allowable hardness range for the diaphragm. Some of the observed differences between the experimentally and numerically obtained deformation shape could therefore be explained by the deviation or variation of the elastic modulus in the experimental set-up from the one used in the numerical model. As the numerical results seem quite susceptible to differences in elastic modulus, approximations introduced by use of the shell model based on thin flat plate theory and the use of the small strain constitutive model could be contributing to the observed differences as well.

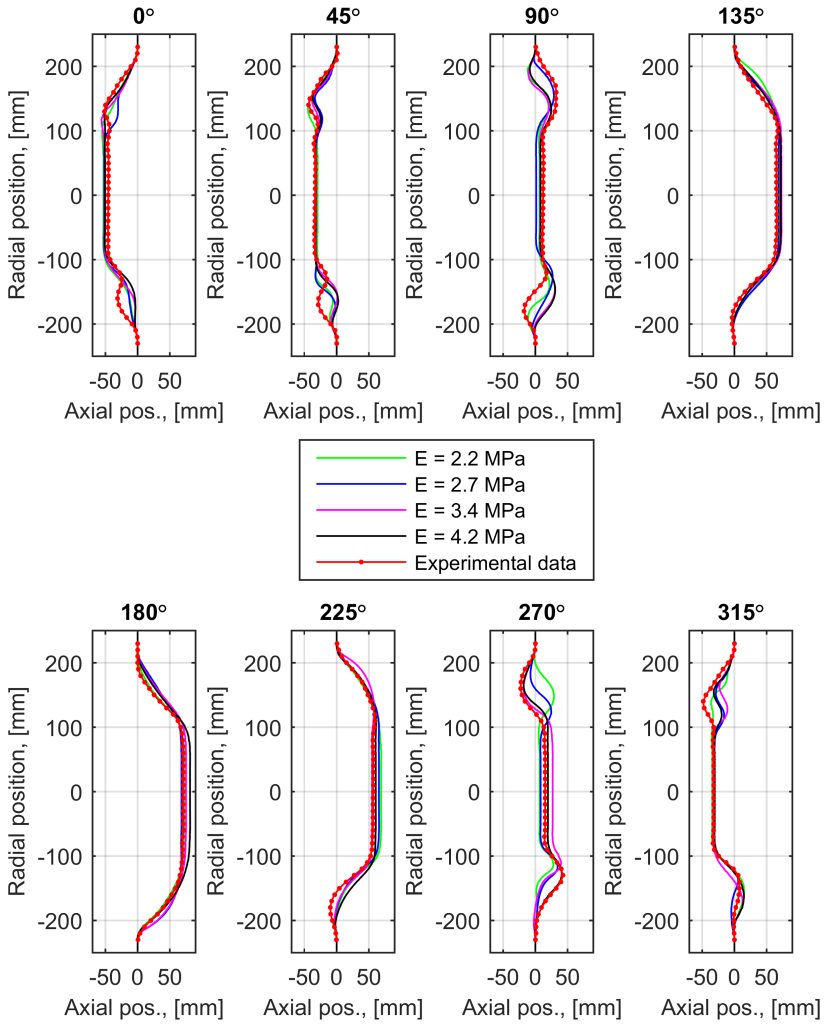

Figure 8.14: Effect of elastic modulus on 2D deformation shapes. Comparison of experimental and numerical results in 2D cross sections in vertical plane at 45° intervals for 2.2, 2.7 (reference case), 3.4 and 4.2 MPa.

8.6. EFFECT OF ADVECTION SCHEME AND TURBULENCE MODEL

Next to deviations of the structural model from reality, deviation of the modelled flow field from reality might be causing differences between the numerically and experimentally obtained deformed diaphragm shapes. One aspect is the ability of the flow model to capture the vortical structures and turbulent aspects of the fluid flow. Based on a dimensional analysis it was argued that the viscous and turbulent stresses in the fluid flow were negligible compared to the hydrostatic and inertial pressure. This relaxes the need for accurate modelling of turbulence and might allow the use of low order diffusive up-

wind schemes in this case. The following variations of the reference model have been evaluated in order to evaluate the effect the different advection schemes and the use of an eddy viscosity model whose background is described in section 6.2.

1. Upwind differencing of advection term in the momentum equation without eddy viscosity model
2. Hybrid differencing of advection term in the momentum equation which uses central differencing when the local grid Peclet number is smaller than 2 and uses upwind differencing when it is higher than 2 without eddy viscosity model
3. A Total Variation Diminishing (TVD) scheme for the advection term in the momentum equation using the UMIST flux limiter without using eddy viscosity on top of the molecular viscosity model (reference model)
4. A Total Variation Diminishing (TVD) scheme for the advection term in the momentum equation using a UMIST flux limiter in combination with the WALE SGS eddy viscosity model

All these approaches can be seen as some sort of Large Eddy Simulations (LES) as no Reynold Averaged Navier Stokes (RANS) turbulence models are used while the grid is too coarse to capture the smallest turbulent scales such that it can not be considered a Direct Numerical Simulation (DNS) either. Some form of additional dissipation is required to keep the numerical model stable as the smallest turbulent scales at which the dissipation take place are not resolved. In the first 3 cases the additional dissipation comes from the numerical scheme such that these approaches can be viewed as a form of Implicit Large Eddy Simulation (ILES) while the latter uses a physically based eddy viscosity model such that it is a form of an explicit LES.

8.6.1. RESOLVED FLOW FIELDS

As the different approaches impact the modelled flow field the resolved flow field are discussed first. The resolved flow fields of the reference model which uses the TVD scheme with UMIST flux limiter without eddy viscosity model, have been discussed in section 8.4. The resolved flow fields of the other approaches are discussed below.

UPWIND DIFFERENCING WITHOUT EDDY VISCOSITY MODEL

In Figure 8.15 contour plots of the magnitude of the velocity in the XZ-plane on 45° intervals obtained using upwind differencing are shown. When comparing the contour plots with Figure 8.7 one can see that the velocity field is more smooth when using upwind differencing. The smaller scale vortices are dissipated by the higher numerical dissipation of the upwind scheme.

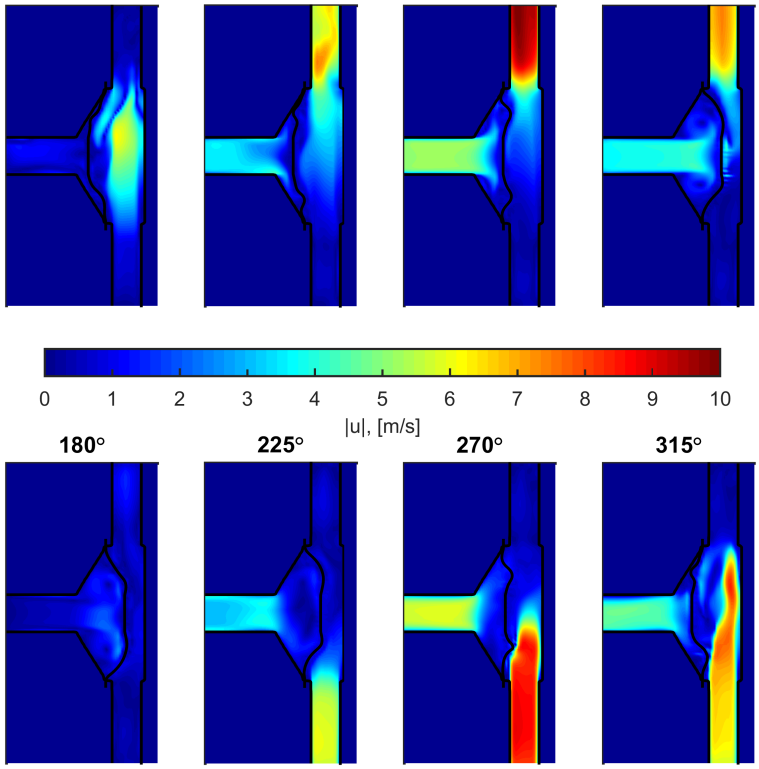

Figure 8.15: Contour plots of magnitude of velocity in XZ-plane on 45° intervals for FSI reference case according Table 6.1 with 10 litre stroke volume at 100 strokes per minute using upwind differencing without eddy viscosity model

The reduced level of detail of the captured vortices is also shown in Figure 8.16 where the isosurface of the Q-criterion is shown at 315 degrees. Only the largest vortices are captured when using upwind differencing. However, the smaller scale vortices don't seem that relevant for the diaphragm deformation as the obtained diaphragm deformation shapes don't differ that much as will be shown in the next section.

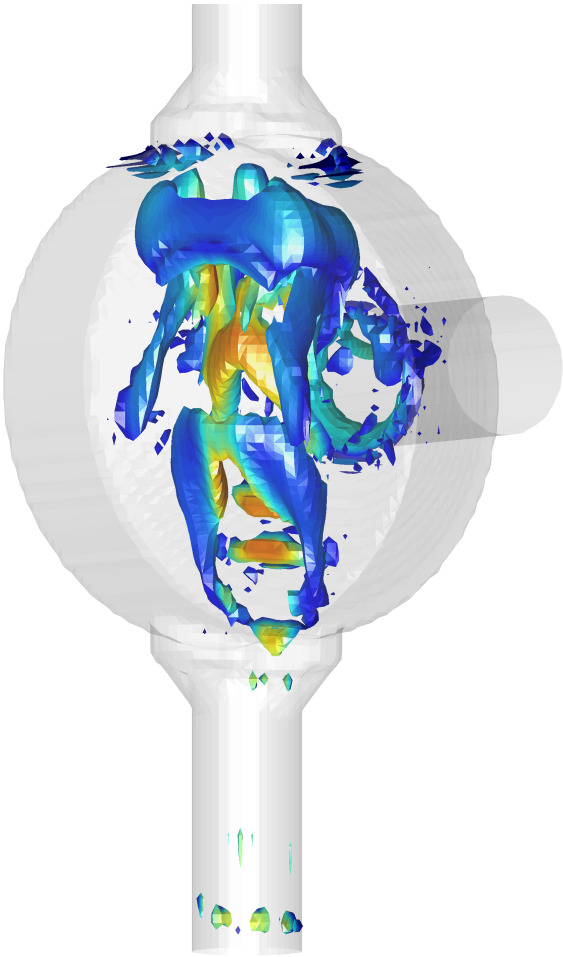

Figure 8.16: Vortex structure at 315 degrees shown by isosurfaces of Q-criterion at $Q = 1000s^{-2}$ for FSI reference case according Table 6.1 with 10 litre stroke volume at 100 strokes per minute using upwind differencing without eddy viscosity model. Isosurface is coloured with the magnitude of the velocity

The resolved flow fields when using hybrid differencing are almost exactly equal when using the upwind differencing and are therefore not discussed. This can be explained by the fact that the grid Peclet number is mostly higher than 2 which effectively switches the hybrid scheme to the upwind mode.

TVD SCHEME WITH WALE EDDY VISCOSITY MODEL

The vortical structures obtained with the TVD scheme with UMIST flux limiter with and without the WALE SGS eddy viscosity model show some differences when comparing Figure 8.17 with Figure 8.8. The vortical structure obtained when using the WALE SGS eddy viscosity model seems a bit more smooth and less chaotic than the one obtained without the WALE SGS eddy viscosity model.

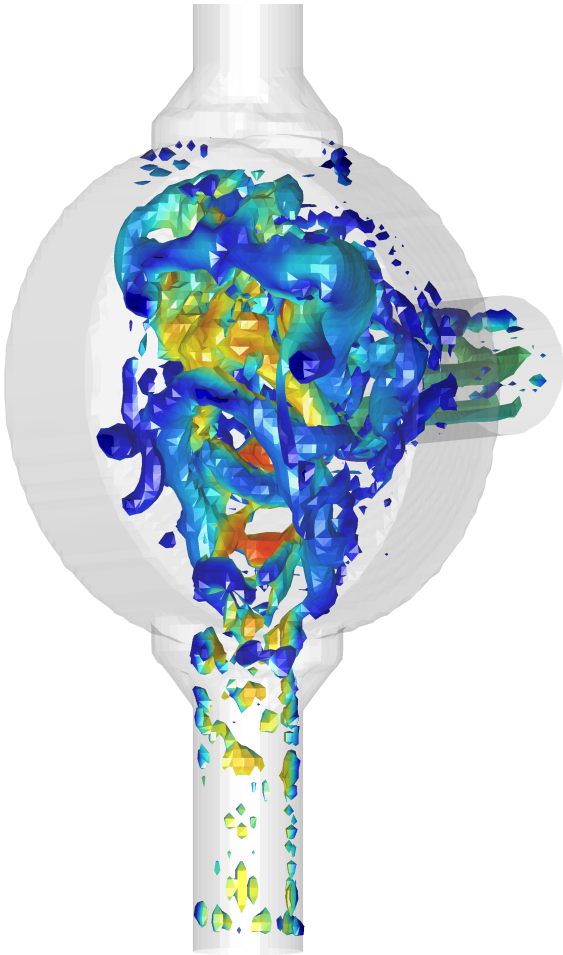

Figure 8.17: Vortex structure at 315 degrees in FSI reference case with the WALE SGS eddy viscosity model shown by isosurfaces of Q-criterion at $Q = 1000s^{-2}$. Isosurface is coloured with the magnitude of the velocity

8.6.2. DEFORMED DIAPHRAGM SHAPES

In Figure 8.13 3D deformed diaphragm shapes obtained with the different advection schemes and turbulence models are shown. Although some differences can be observed, the differences are small and no clear trend in the differences is observed.

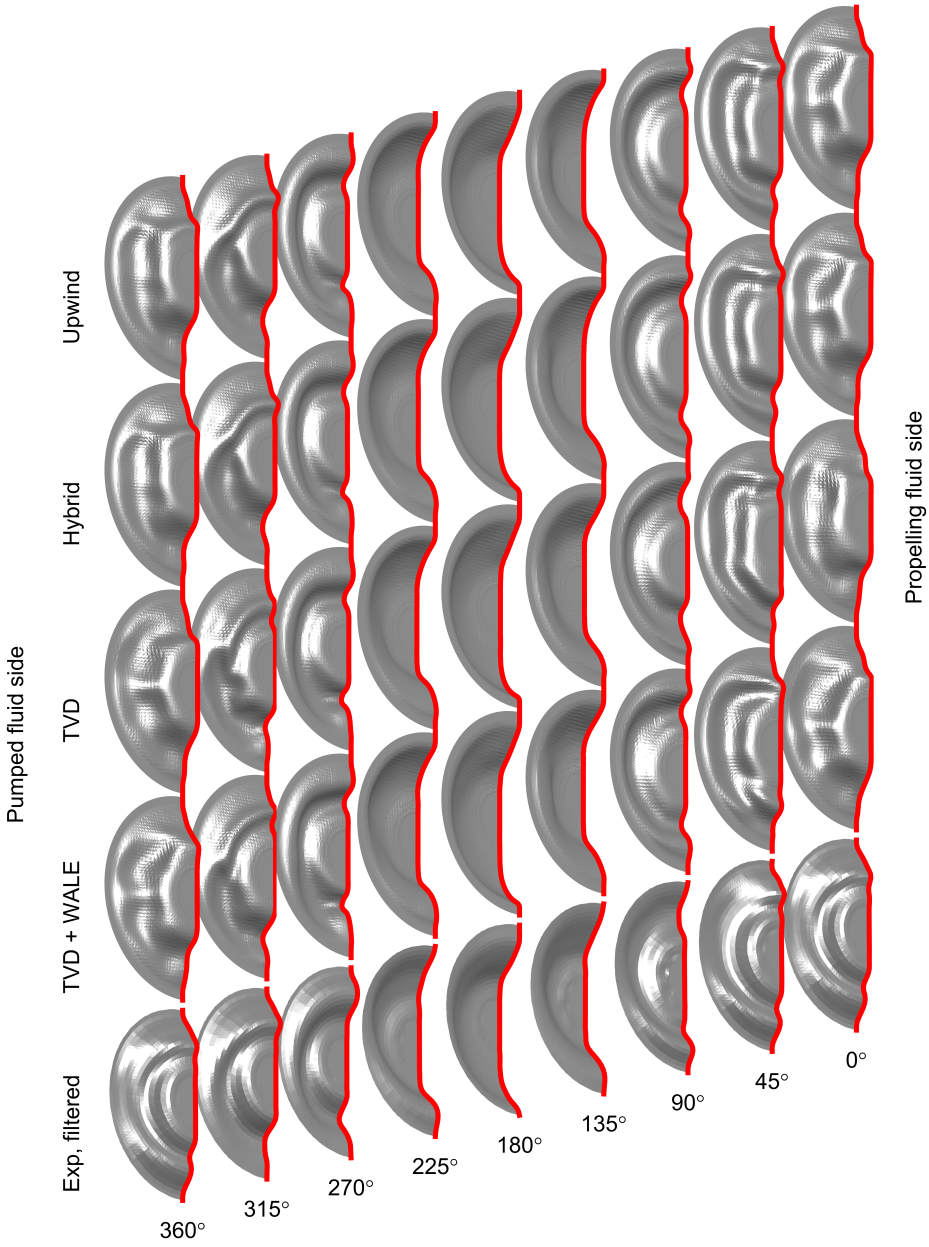

Figure 8.18: Effect of advection scheme and turbulence model on numerically obtained 3D deformed diaphragm shapes for reference case with 10 litre stroke volume at 100 strokes per minute according Table 6.1. Experimental conditions according Table 7.2, measurement ID 23. From top to bottom; upwind differencing, hybrid differencing, TVD scheme with UMIST flux limiter, TVD scheme with UMIST flux limiter and WALE SGS eddy viscosity model and filtered experimental results. Deformed diaphragm shapes shown from start of discharge stroke on the right with 45° intervals to end of suction stroke on the left.

Cross sections of the obtained diaphragm deformation shapes are shown in Figure 8.19 where they are compared with the experimental results. The differences between the 4 approaches are rather small. The upwind and hybrid differencing are almost exactly equal which can be explained by the fact that the grid Peclet number is mostly higher than 2 which effectively switches the hybrid scheme to the upwind mode. The 2 TVD schemes with and without the eddy viscosity model give slightly different results than the upwind and hybrid scheme but don't differ much from each other.

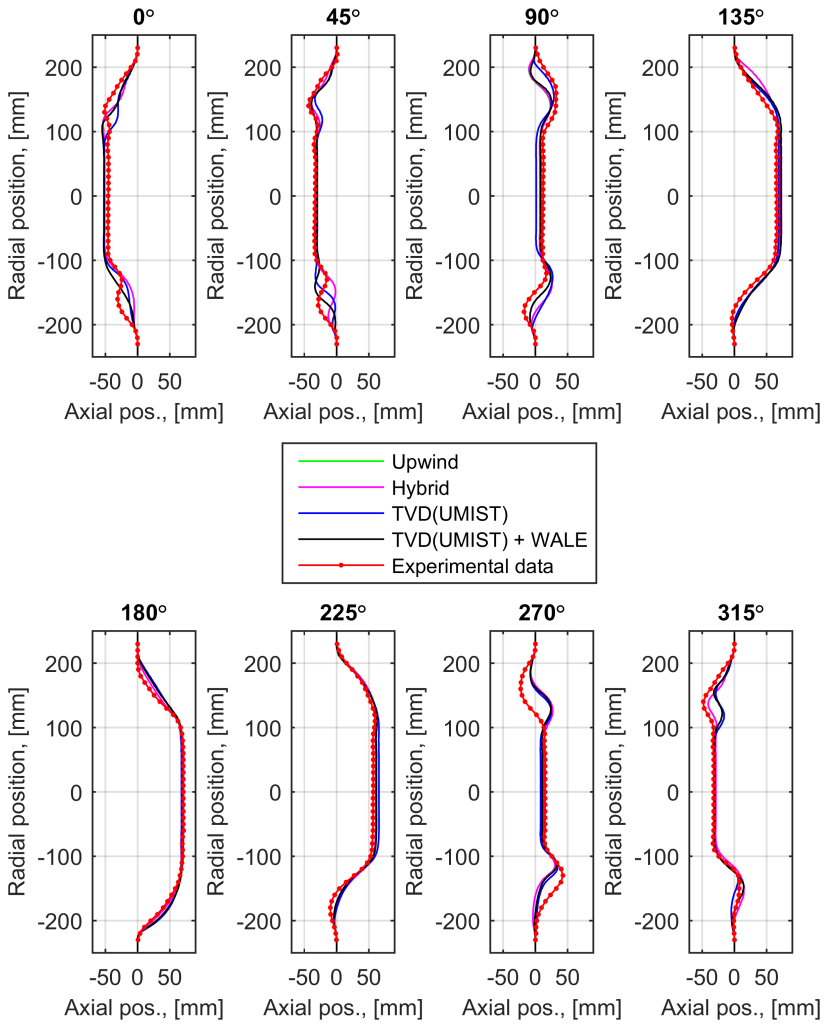

Figure 8.19: Effect of advection scheme and use of turbulence model on deformation shapes. Comparison experimental and numerical results in 2D cross sections in vertical plane at 45° intervals for upwind differencing, hybrid differencing, TVD scheme with UMIST flux limiter, TVD scheme with UMIST flux limiter and WALE SGS eddy viscosity model and experimental results (filtered).

8.7. EFFECT OF FLUID GRID AND STRUCTURAL MESH SIZE

The reference model uses a Cartesian fluid grid with 64x128x64 = 524,288 fluid cells and a structural FE model with 14077 nodes. The effect of mesh and grid size was evaluated by using respectively 32, 48, 64 and 96 fluid cells in the X-direction, while proportionally scaling the fluid grid and structural mesh spacing in other directions.

In Figure 8.20 3D deformed diaphragm shapes obtained with the different fluid grid and structural mesh sizes are shown. The deformed shapes obtained with the 2 intermediate grid sizes, the reference case and one step coarser with respectively 64 and 48 fluid cells in the X direction, are more or less similar. Higher order surface waves are more prominent near the end of the suction stroke and the beginning of the discharge stroke for the reference case. The coarsest grid size is considered too coarse as the central part of the diaphragm is dragged towards the propelling fluid port, most likely as no fluid cells remains in-between the diaphragm and the rear wall at the end of the suction stroke. The finest grid shows violent higher order behaviour but this is caused by instabilities due to mesh distortion. Simulations at this finest grid level need to be re-run which were not completed at the the time of writing as they take roughly 500 hours of computational time.

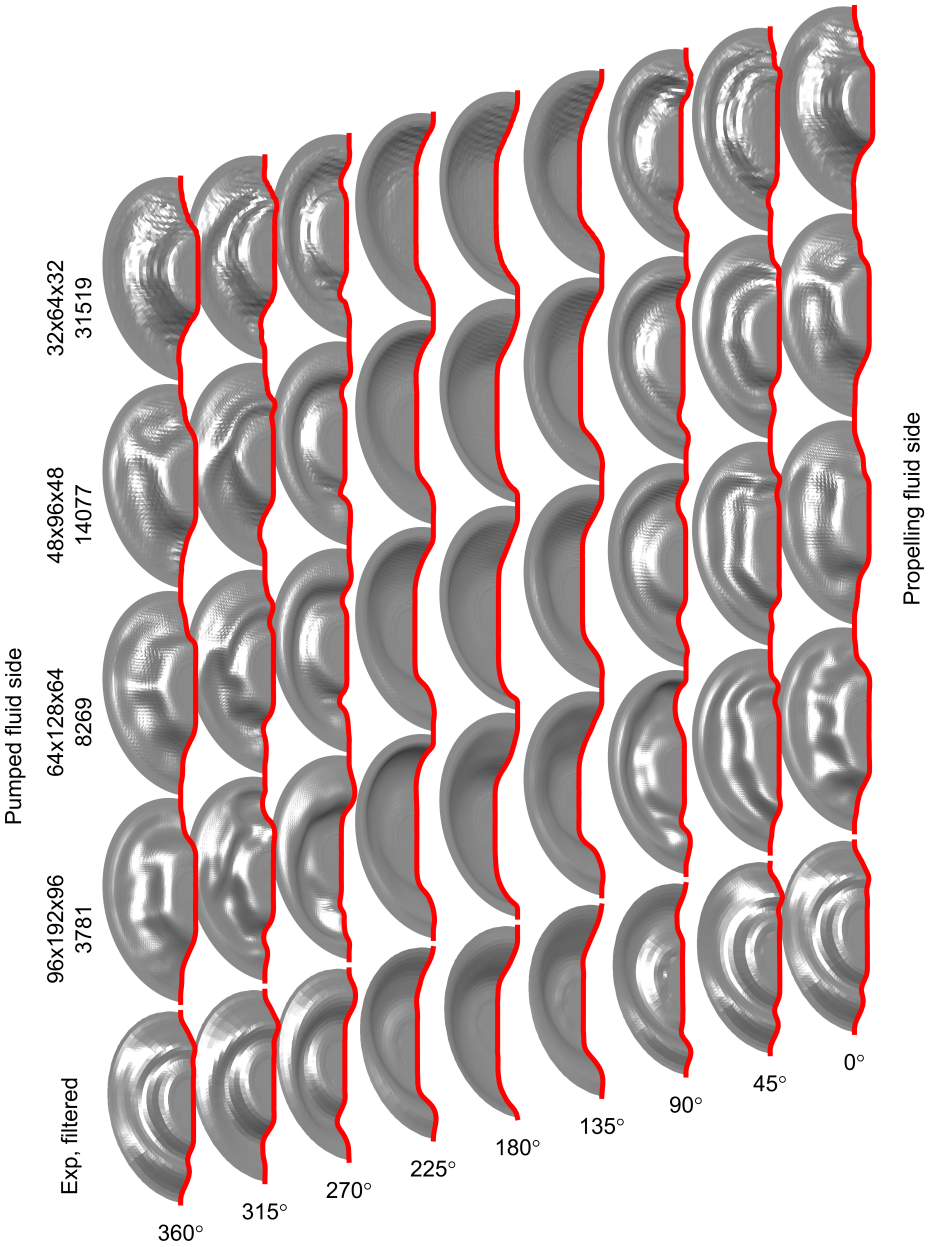

Figure 8.20: Effect of grid and mesh size on numerically obtained 3D deformed diaphragm shapes for reference case with 10 litre stroke volume at 100 strokes per minute according Table 6.1. Experimental conditions according Table 7.2, measurement ID 23. From top to bottom; 32x64x32 fluid cells and 3781 structural nodes, 48x96x48 fluid cells and 8269 structural nodes, 64x128x64 fluid cell and 14077 structural nodes, 96x192x96 fluid cells and 31519 structural nodes and filtered experimental results. Deformed diaphragm shapes shown from start of discharge stroke on the right with 45° intervals to end of suction stroke on the left.

Cross sections of the obtained diaphragm deformation shapes are shown in Figure 8.21 where they are compared with the experimental results. The 2D cross sections at 0° also show how the central part of the diaphragm is dragged towards the propelling fluid port for the coarsest grid size, again suggesting the relevance of the ratio between the grid size to the fill position of the diaphragm. The deformed shape of the coarsest mesh halfway the discharge stroke at 90° also shows the largest deviation from the experimental data. The 2 intermediate mesh sizes show similar deformation for the majority of the stroke but have some differences in the lower half of the diaphragm at 45° into the discharge stroke. The finest mesh size does not give an improvement as the numerical results are contaminated with instabilities. A re-run of the finest grid model is required with more stringent time step limitations as mentioned before. Convergence of the solution is has not been obtained so-far. Convergence of the resolved flow fluid is not expected anyway as smaller turbulent scales are resolved when refining the fluid grid size. It is expected however that the structural solution converges on a much coarser grid level. However, so-far no convergence of the deformation shapes has been obtained.

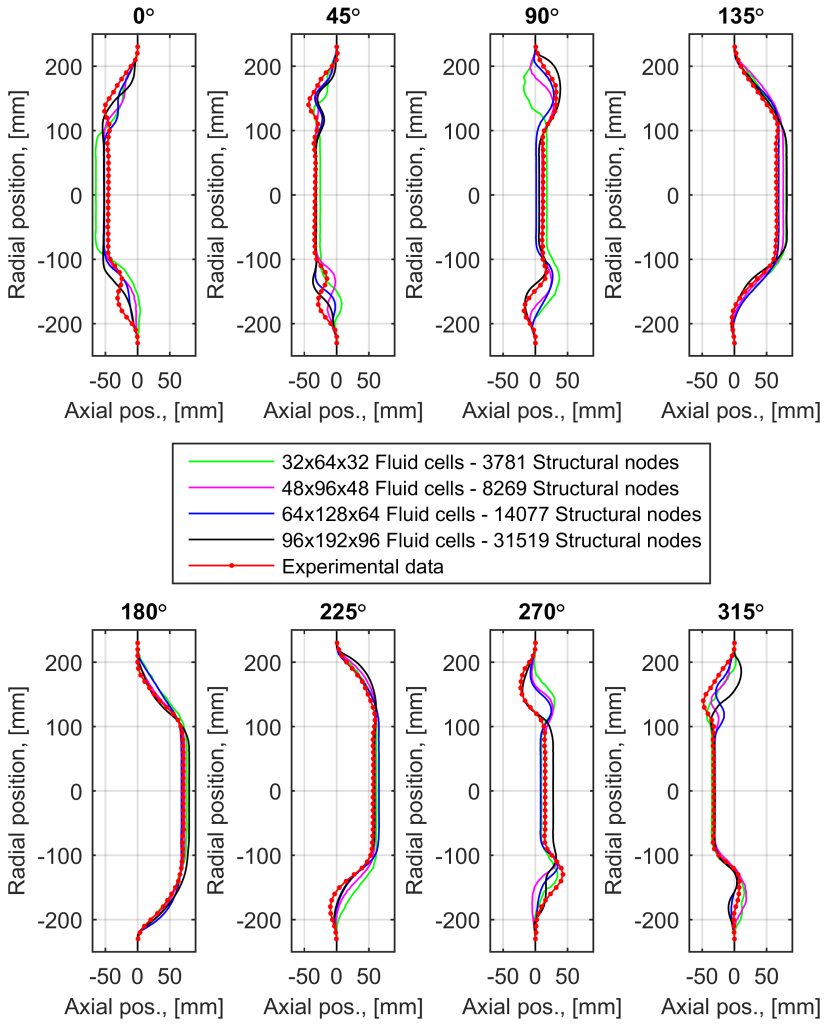

Figure 8.21: Effect of fluid grid and structural mesh size on deformation shapes. Comparison numerical and experimental results in 2D cross sections in vertical plane at 45° intervals.

8.8. EFFECT OF SLURRY DENSITY AND YIELD STRESS

All previous parameter studies could be validated with experimental results as they concentrated on water as the pumped fluid. The final objective of the numerical model is to predict diaphragm deformation shapes in actual operational conditions using slurry as the pumped fluid. As discussed in section 5.2 the settling characteristics of the fine particle slurries encountered in practical piston diaphragm pump applications are less relevant in this study which allows the slurry to be modelled as a homogeneous mixture with uniform fluid properties. The differences with water are then the difference in the mixture density and the mixture rheology. The density is an important parameter as it both

scales the fluid momentum loads as well as the hydrostatic fluid loading as discussed in chapter 5. The mixture density in slurry applications can be significantly different from water, with the most extreme values encountered in iron concentrate pipelines where mixture densities up to 2300 kg/m^3 are encountered. The mixture rheology is of less concern for most slurries as the viscous and turbulent stresses are of much lower magnitude than fluid momentum load. In section 5.3 it was estimated that viscous effect are only important to be considered when handling highly viscous paste slurries with Bingham yield stress levels in the range of 100 to 1000 Pa, as encountered in some tailing disposal applications. In this section the isolated effect of slurry density and slurry yield stress are evaluated with 3 variations on the reference case; one with a mixture density of 2300 kg/m^3, one with a yield stress of 100 Pa and one with yield stress of 1000 Pa. Further details of the fluid parameters used in these 3 variations are shown in Table 8.2.

Table 8.2: Variations of fluid parameters for evaluating the effect of fluid density and yield stress

ID	ρ_2, [kg/m^3]	τ_y, [Pa]	μ_∞, [mPa s]
14	2300	0	20
15	1000	100	200
16	1000	1000	2000

For the 2 situations with a yield stress, a limiting Newtonian fluid viscosity of 100 Pa s was used for shear rates approaching 0 as discussed in section 4.1. This in order to obtain acceptable time steps in the explicit time iteration whose time step is limited by the characteristic diffusion time for these highly viscous cases as discussed in section 6.2.

8.8.1. RESULTS

In Figure 8.22 3D deformed diaphragm shapes obtained with the different fluid properties are shown. In the top row with the high mixture density of 2300 kg/m^3 the formation of an extreme lobe in the upper part of the diaphragm is observed halfway the discharge stroke at 90° (1). Here the diaphragm is not only bending while forming the lobe but is ballooning as well. At the end of the discharge stroke the elastic energy stored in the ballooned section is released causing an oscillation which forms a convex lobe in the positive axial direction in the upper part of the diaphragm at the 180° position (2). More extreme lobe formation is also observed in the lower half of the diaphragm when approaching the end of the suction stroke at 315° (3).

The results for the 100 Pa yield stress case don't differ much from the reference case with water as the pumped fluid indicating the lower relevance of the slurry rheology for yield stresses lower than 100 Pa. The results for the 1000 Pa yield stress case however do differ from the reference case with water as the pumped fluid. Here a more extreme lobe formation in the upper half of the diaphragm is observed halfway the discharge stroke at 90° (4) as well.

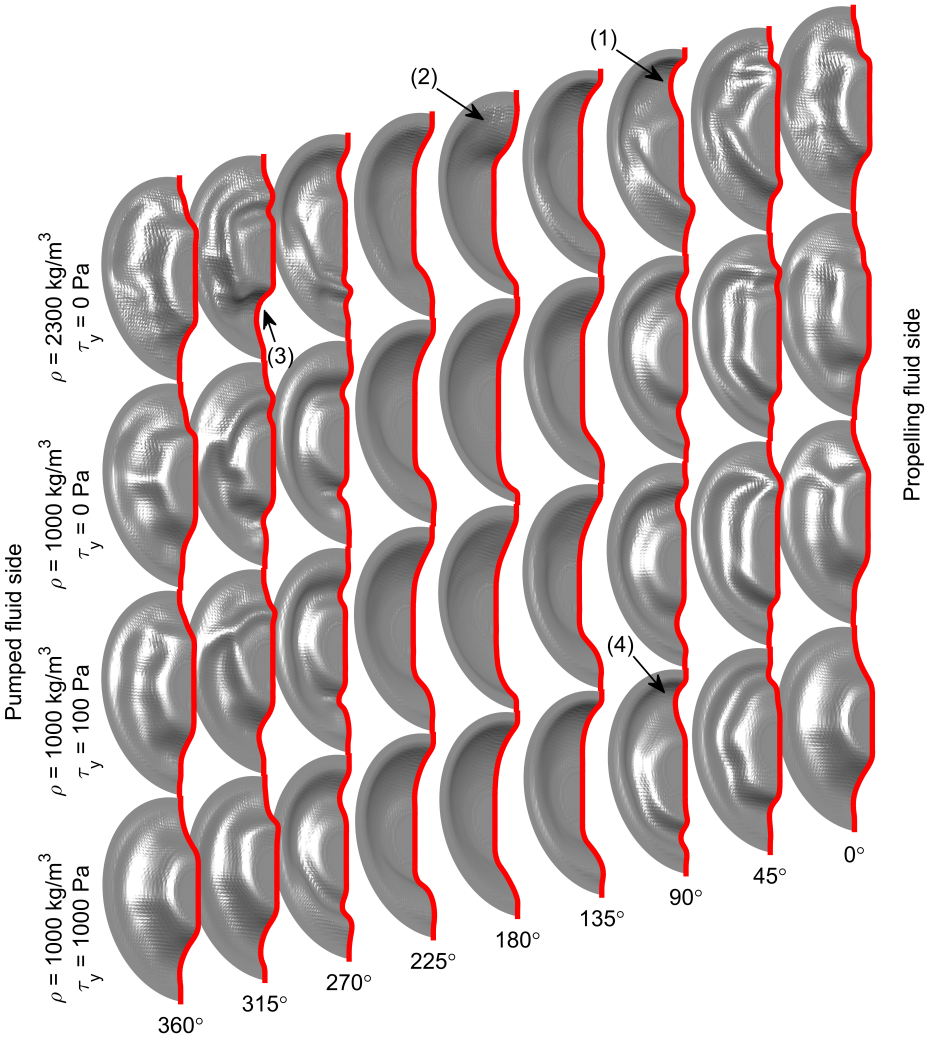

Figure 8.22: Effect of slurry properties on numerically obtained 3D deformed diaphragm shapes for reference case with 10 litre stroke volume at 100 strokes per minute accordingTable 6.1. From top to bottom; slurry density 2300 kg/m^3, slurry density 1000 kg/m^3 (reference case), yield stress 100 Pa, yield stress 1000 Pa. Deformed diaphragm shapes shown from start of discharge stroke on the right with 45° intervals to end of suction stroke on the left.

Cross sections of the obtained diaphragm deformation shapes are shown in Figure 8.23. The small differences between the reference case and the 100 Pa yield stress case are observed more clearly and quantitatively in these 2D cross sections. The ballooning of the upper part of the diaphragm at the 90° position is clearly observed for the 2300 kg/m^3 density and 1000 Pa yield stress cases and is most extreme for the 2300 kg/m^3 density case. Both the sharp bending around the diaphragm clamping edge as well as

the ballooning on the upper part of the diaphragm creates high strain levels in the diaphragm. Such high strain levels will most likely result in diaphragm fatigue failures in a continuous duty application. At the end of the discharge stroke the fluid momentum which generates the ballooning decreases and the elastic energy stored in the ballooned section is released. For the high density case this results in a oscillation of the upper part of the diaphragm observed by the concave shape in the positive axial direction at 135° which turns convex at 180° and back to concave again at 225°. For the 1000 Pa yield stress case the ballooned section does not oscillate as the fluid then would have to be sheared in the opposite direction which would require a directional change of the shear stress which would require a shear stress change of at least twice the 1000 Pa yield stress. For the 1000 Pa yield stress case it is furthermore observed that the stroke length of the central part of the diaphragm is somewhat longer as it seems to be dragged more towards the rear wall in the second half of the suction stroke.

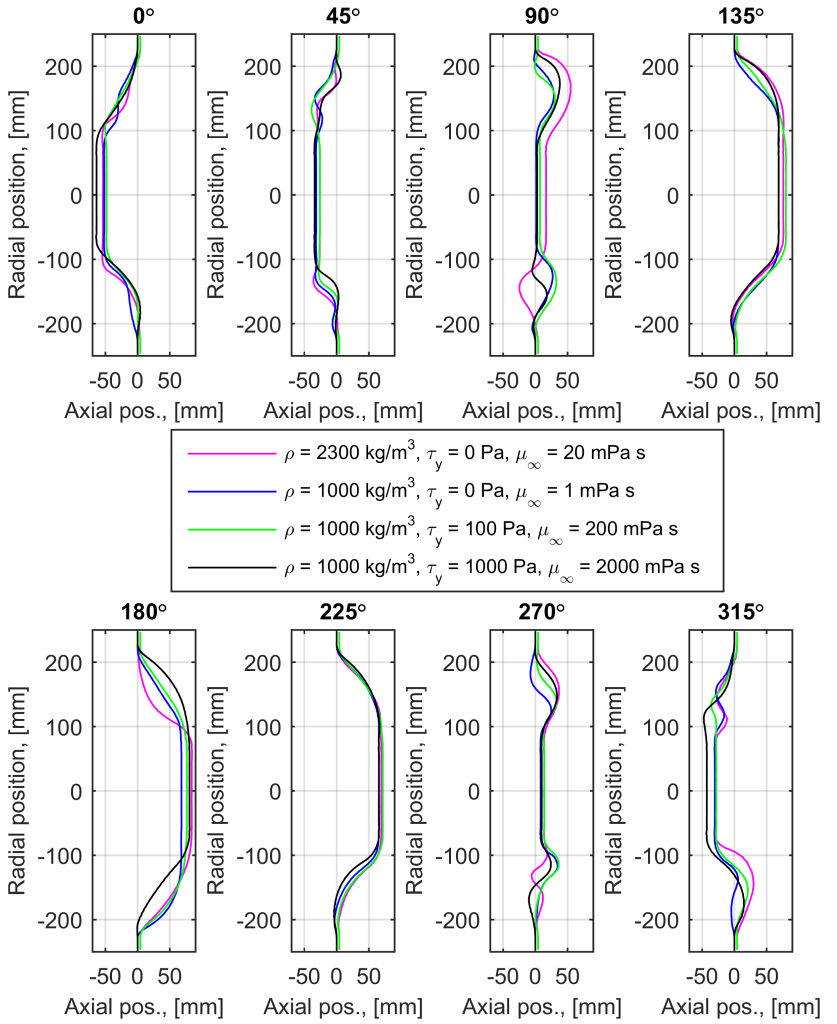

Figure 8.23: Effect of slurry properties on deformation shapes. Comparison numerical and experimental results in 2D cross sections in vertical plane at 45° intervals.

8.9. DISCUSSION

In this chapter the results of the numerical FSI model developed in this study were validated with experimental results, focussing on a single operating condition. In some situations the model was able to reproduce the experimental results quite accurately while in other situations some differences between the numerical results and the experimental results were observed.

8.9.1. QUASI-STATIC STRUCTURE-ONLY RESULTS

The quasi-static simulations using the structure-only model reproduced the experimental results quite well, especially when an hydrostatic pressure difference across the diaphragm is present. When no hydrostatic pressure difference across the diaphragm is present, a difference was observed between the numerical results and the experimental results at the end of the suction stroke. In the numerical results a more abrupt snap-though at the end of the suction stroke was present than in the experimental results. The snap-through behaviour was further identified in the pressure load versus volumetric displacement plots in Figure 8.6 by the local maxima and minima with the negative slope, hence negative stiffness, in-between them. Exact reproduction of the snap-though events is difficult as these events are influenced by small changes in local stiffness of the diaphragm and can be quite dynamic, especially the one at the end of the suction stroke for the air-air loading case, limiting the validity of the quasi-static approach. However, the quasi-static results showed that when an asymmetric load is present on the diaphragm, a less abrupt and more reproducible diaphragm deformation is present. The asymmetric loads result in preferential asymmetric deformation modes with less steep negative stiffness's than in the symmetric loading case. Next to limitations in the quasi-static structure-only modelling approach, modelling assumptions in the structural model could play a role as well in explaining the differences between the numerically and experimentally obtained deformed diaphragm shapes. The structural model uses shell model based on the Kirchhoff thin plate model which does not include transverse shear deformation of the shell. For the low order deformation modes this was considered a correct assumption, but around the snap-through points shear deformation might be more important. Shear deformation will lower the local stiffness of the diaphragm, which might be relevant especially when higher order modes are formed in the diaphragm during the snap-through events.

8.9.2. FSI RESULTS

When validating the FSI results at the high stroke rate of 100 strokes per minute and the low stroke rate of 50 strokes per minute, more differences were observed between the experimental and the numerical results than in the quasi-static situations described above.

In the low stroke rate case, an asymmetric deformation shape was observed in the numerical results which was not present in the experimental results. It is expected that the asymmetric deformation in the numerical model is effected by the limitation in fluid grid resolution between the diaphragm and the rear wall of the pump chamber when the diaphragm is approaching the rear wall. Fluid momentum loads on the pumped fluid side are considered to be small in this low stroke rate case, but the fluid momentum loads on the propelling liquid sides can be higher when the diaphragm is approaching the rear wall and fluid has to be squeezed out of the gap between the diaphragm and the rear wall. When the gap becomes small any fluid cell grid resolution is lost here which forces the structural nodes to party follow flow velocity in the gap as they are advected using an interpolation function which uses an interpolation domain with a radius of 2 fluid cells. Fluid grid refinement would be required for improving the near wall behaviour.

In the high stroke rate case, higher order deformation modes were observed in the

numerical results than in the experimental results. Whether these higher order modes are completely absent in the experimental result is not clear, as the reconstructed diaphragm deformation shapes showed an increased level of spatial noise due to non-reproducibility in the raw experimental data. When these higher order modes are not periodic from stroke to stroke, they will be filtered out by the Time Synchronous Averaging (TSA) algorithm used in the processing of the sequentially measured diaphragm displacements. However, limitations in the numerical model could cause these differences as well. The following limitations of the numerical model could explain the observed differences:

Small deformation assumptions in shell model The shell model used is based on small deformation theory which results in nodal forces in the FE mesh which are proportional with the change of curvature of an FE element. It was argued before that the curvature was not that important in the evaluation of the element stiffness despite the non-linear stress and strain distribution across the thickness of the shell as the deviations from the linear distribution would largely cancel out when evaluating the stiffness of an element. In retrospect it must be concluded that it is not as much the initial curvature but the change of curvature which limits the uses of a linear shell model. The deviations from the linear stress distribution might cause a deviation from the linear stiffness behaviour earlier than expected due to non-linear material behaviour, mainly in compression. When bending a plate, the compression of the concave side is limited for large changes in the radius of curvature which then requires significant stretching of the mid-surface of the plate. This non-linear effect is not captured correctly by the linear shell model used. A model which includes this stiffening effect, would limit the formation of sharp bends and folds and would therefore result in a more smooth deformation shape with less contribution of higher order deformation modes.

Fluid grid size It was shown that vortices are formed on the pumped fluid side which roll over the surface of the diaphragm. The interpolation function used for advecting the structural nodes uses an interpolation domain with a radius of 2 fluid cells. This interpolation domain might extend quite far into the flow domain on the pumped fluid side for coarser fluid grid sizes and thereby transferring part of the motion of the rolling vortices to the diaphragm. This might result in the formation of higher order deformation modes in diaphragm deformation shapes of the numerically obtained results which are not observed in the experimental results. A finer fluid grid size would limit the extension of the interpolation domain to a smaller boundary layer between the pumped fluid domain and the diaphragm. This would allow more freedom of the flow with less transfer of the motion of the vortices to the diaphragm as the smaller boundary layer has less velocity fluctuations than in the core of the flow domain.

Deviation in elastic modulus The numerical experiments with a higher elastic modulus showed a reduction of the contribution of higher order deformation modes and elimination of the sharp fold formation on the lower half of the diaphragm halfway the suction stroke which is more close to the experimental observations.

The allowable variation in hardness of the diaphragm could already explain some of the differences observed between the numerical and experimental results as the allowable variation in the hardness specification largely covers the variation in elastic modulus in the numerical experiments. The smaller difference between the numerical and experimental results when using a higher elastic modulus could also point to limitations of the linear shell model in representing the correct stiffness for large changes in curvature as discussed above.

Accurate modelling of viscous and turbulent stresses and limitation of numerical dissipation is considered of lower importance, indicated by the relatively small differences between the deformed diaphragm shapes obtained using the different advection schemes and the limited impact of the WALE turbulence model on the deformed diaphragm shapes. Also the small effect of a pumped fluid with a 100 Pa yield stress on the deformed diaphragm shapes indicates the lower relevance of viscous effects.

Although some differences were observed between the numerical and experimentally obtained deformed diaphragm shapes halfway the suction and discharge stroke, the differences at the end of the discharge stroke were relatively small. In these phases of the pump cycle the diaphragm is stretched most, eliminating much of the complexity of the snap-though behaviour and the higher order deformation modes. Stretching of the diaphragm is most critical from a durability point of view as the stretching causes high localized strain levels near the clamped edge and the central plate of the diaphragm which are the known failure locations of the diaphragm. The model is therefore considered to give valuable and quantitatively correct results at these phases in the pump cycle and is therefore considered to be a suitable design tool, also in its current state. When the most extreme stretching occurs half way the suction or discharge stroke, as is the case in the numerical experiment using a high density slurry as the pumped fluid, the model is considered to be suitable as a design tool as well.

8.9.3. SUGGESTED MODEL IMPROVEMENTS

Some limitations of the numerical model have been discussed above, here some suggestions are given for future improvements of the model.

Shear deformation in shell model In retrospect it could be concluded that shear deformation might be more important than initially assumed. Especially at snap-through points and for higher order deformation modes, the neglect of shear deformation might no longer be valid. Inclusion of shear deformation in the rotation free triangular shell model as used in this study has been described by Oñate and Zárate (2010) and Zárate and Oñate (2011). The inclusion of the shear deformation could not only improve the deformation behaviour but will also relax the restriction on the time step posed by the scaling of the element stiffness with element size as described in section 6.3 and is considered to be required when further grid refinement is considered.

Large deformation shell model The use of infinitesimal deformation theory in deriving the shell elements formulations used in this study are not representing the deformation behaviour of the diaphragm correctly when small radii of curvature

or folds are formed in the diaphragm. A more proper treatment of the large deformation shell kinematics and the inclusion of a non-linear material model in the rotation free triangular shell model used in this study is described by Oñate and Flores (2005) and Flores and Oñate (2005).

3D solid model for diaphragm Next to the improvements in the shell models described above, a 3D solid model could be used as the structural model of the diaphragm. This approach requires a very fine structural mesh as a proper treatment of the bending deformation requires the use of several FE elements across the thickness of the diaphragm. The structural deformation is then forced to be incompressible as the FE nodes are immersed and advected in an incompressible fluid flow. For an elastomeric material this is a correct physical representations but the combination of 2 incompressibility constraints might pose some numerical difficulties with respect to element locking, see e.g. Belytschko *et al.* (2000). A benefit of this approach would be the ability to include all geometric details of the diaphragm, which could give more accurate strain levels, especially near the clamped edge and the central plate.

Grid refinement The resolution of the fluid grid is considered too coarse when the diaphragm is working close to the rear wall. A reasonable number of fluid cells should be between the diaphragm and the rigid walls of the pump chamber when significant fluid velocities are present in-between. This is not only important for correctly describing the details of the flow in such regions but also to allow shear between the fluid flow and the diaphragm which is limited to some extent when the interpolation domain for the advection of the structural nodes covers a significant part of the fluid domain in-between the diaphragm and the rigid wall. The higher order modes observed in the numerical results could also be introduced by a relatively large interpolation domain with respect to the size of the fluid domain in-between the diaphragm and the rigid wall. The reference model however, which uses a 64x128x64 fluid grid with 524,288 fluid cells, is considered to be the current practical limit as a simulation of 5 strokes takes a couple of days to complete while running on a single CPU in the current implementation.

Reduction of computational time For grid refinements to be practical, a reduction of the computational time of an order of magnitude is required. One improvement direction is trying to reduce the number of inactive fluid cells which are in the rigid structure. In the reference model used in this study, only 14 % of the computational domain is occupied by fluid while the rest is in the rigid solid domain but places a burden on the flow solver as the Navier-Stokes equations are solved in the entire computational domain, including the rigid solid domain. An improvement might be possible by stretching the grid spacing of the structured grid outside the pump chamber in the regions of the propelling fluid port and the in and outlet ports. This results in a non-equidistant grid but a reduction of the number of fluid cells in the order of 40 % is considered feasible. This requires changes in the flow solver code to handle non-equidistant grids. More advanced approaches could use a more local grid refinement in the pump chamber using an octree fluid

cell structure or block structured grid refinement. These changes result in unstructured fluid grids and would require a complete re-coding of the flow solver. Next to reducing the number of fluid cells in the rigid solid domain, further performance improvements of the FSI solver are required. Significant improvements are considered possible by using parallel computing. In the explicit time integration scheme, the update for every fluid cell and structural node is independent from other fluid cells and structural nodes enabling a relatively straight forward and efficient implementation of parallel computing. Only the Poisson solver is implicit, but the red-black Gauss-Seidel smoother, which is responsible for 70 % of the computational time of the Poisson solver, allows parallel updates of all red and black points in the grid. Large speed improvements could also be obtained when implementing certain computations on a Graphical Processing Unit (GPU) which allows many parallel computations due to the very high number of computational cores on a GPU which can be in the range from hundreds to thousands of computational cores. The complete numerical model is now implemented in the high level programming environment Matlab®. Parallel CPU computing and GPU computing is also possible within the Matlab® environment using the parallel and possibly distributed computing toolboxes. Next to parallel computing, implementation of the most computationally intensive pieces of code in C^{++} and calling them from the Matlab® program as MEX-functions could also give some improvement in computational speed. By combining the above mentioned improvements an improvement in computational speed of several factors up to an order of magnitude is considered feasible, but requires considerable effort in further optimizing the code of the numerical model.

9

CONCLUSIONS AND RECOMMENDATIONS

9.1. CONCLUSIONS

DIMENSIONAL ANALYSIS

The following conclusions can be drawn from the dimensional analysis of the Fluid Structure Interaction (FSI) mechanism in piston diaphragm pumps described in the in chapter 5.

- Quasi-static structure-only analysis which are used in current state of the art diaphragm deformation analysis approaches are unsuitable for analysing diaphragm deformation behaviour when fluid momentum loading is dominant as the forces due to unsteady fluid acceleration are of similar magnitude as the convective fluid acceleration.
- Both the dimensional analysis as well an the numerical results have shown that the effect of viscous and turbulent stresses on the deformed diaphragm shapes is limited, only for slurries with visco-plastic behaviour with a yield stress larger than 100 Pa it is important to consider viscous effects.
- Main aspects of the FSI in piston diaphragm pumps can be described using 4 dimensionless numbers; the dimensionless stroke volume, the dimensionless stroke rate, the dimensionless hydrostatic pressure and the density ratio.
- All field experiences with reduced diaphragm life can be explained when representing the field experience data in dimensionless form. This indicates that all field experiences with reduces diaphragm life are caused by too high fluid loads due to a combination of hydrostatic and fluid momentum loads.
- A robust diaphragm selection guideline can be derived by enveloping the dimensionless parameters of the field experience data in which no issues with reduced

diaphragm life have been encountered. A practical approach of this enveloping can be done by drawing enveloping curves in a 2D plot of the corrected dimensionless stroke volume versus the corrected dimensionless stroke rate. The dimensionless hydrostatic pressure difference and the dimensionless effective flow area in the pump chamber were used in the corrections respectively. The enveloping curve then consists of a limit on the corrected dimensionless stroke volume and a limit on the corrected dimensionless flow rate which the product of the corrected dimensionless stroke volume and stroke rate.

EXPERIMENTS

An experimental set-up has been developed for experimental determination of diaphragm deformation shapes which are used for validation of the numerical model developed in this study. The experimental set-up used a single chamber piston diaphragm pump with a servo hydraulic drive which allows variation of both stroke volume and stroke rate. The pump chamber had a transparent cover which enabled the visual observation of the diaphragm deformation. A laser triangulation sensor mounted on a numerically controlled XY table was used to sequentially measure the diaphragm displacements on a XY grid. Using the simultaneously measured piston position, 3D deformed diaphragm shapes can be reconstructed. Summarized results and conclusions from the experiments are:

- Refraction of the reflected laser beam needs to be corrected which can be done using a theoretical model or a calibration experiment
- Cavitation in the pump chamber needs to be excluded to allow visual observation of the diaphragm. A suction pressure 3 times higher than the acceleration pressure based on the piston acceleration is required to eliminate cavitation in the pump chamber. This is higher than anticipated and limits the operating range which can be covered by the hydraulic drive.
- Quasi-static and low stroke rate experiment showed very reproducible diaphragm displacement which enabled accurate reconstruction of deformed diaphragm shapes.
- In higher stroke rate experiments some non-reproducibility was observed which resulted in more noisy reconstructed diaphragm shapes. Filtering of the reconstructed deformed diaphragm shapes in the spectral domain using Fourier and Fourier-Bessel series allows the removal of the spatial noise and results in smooth deformation shapes
- Spectral analysis of the reconstructed deformed diaphragm shapes using Fourier and Fourier-Bessel series showed an increase of the higher order harmonics in the time and circumferential direction with increasing flow rate.

NUMERICAL MODEL

A numerical FSI model has been developed within this study for modelling the interaction between the deformation of the pump diaphragm and the fluid flow on both sides of the pump diaphragm. The summarized results and conclusions from the numerical experiments and the validation with the experimental results are:

- Quasi-static deformation shapes are reproduced quite accurately using the quasi-static structure-only numerical model, especially when a hydrostatic pressure difference is present across the diaphragm.
- The quasi-static results show snap-though behaviour of the diaphragm deformation which complicates the exact reproducibility of the experimental results by the numerical model.
- Higher order modes are observed in the numerical results of the FSI model, especially halfway the discharge and suction stroke, which are not present in the experimental results.
- Some of the higher order modes might be present in the experimental set-up might not be fully periodic such that they are filtered out by the Time Synchronous Averaging (TSA) algorithm and the spatial filtering.
- Differences between the numerical and experimentally obtained deformed diaphragm shapes are also considered to be caused by limitations in the numerical model which are:
  - Small deformation assumption used in shell model which does not reproduce the bending stiffness increase for large changes in radius of curvature which could limit the formation of the higher order deformation modes and sharp folds which are generated by the numerical model but are not observed in the experimental data.
  - Limitations in fluid grid size limit shearing of the fluid from the diaphragm surface when the interpolation domain of the interpolation function used for the advection of the structural nodes covers a significant part of the fluid domain in-between the diaphragm and the rigid wall of the pump chamber,
  - The elastic modulus assumed in the numerical model might deviate from the one present in the diaphragm in the experimental set-up as the allowable hardness variation represents a ±25% variation of the elastic modulus. This range of elastic moduli generated variation of the numerically obtained deformed diaphragm shapes of the same order as the differences observed between the experimentally and numerical results.
- The rheology of the slurry is only important to consider when the slurry yield stress is larger than 100 Pa. As most practical slurries have a yield stress less than 100 Pa, the slurry density is often the only relevant fluid parameter to consider.

9.2. RECOMMENDATIONS

The recommendations for the application of the gained knowledge and future research is as follows:

DIAPHRAGM SELECTION

- Use diaphragm selection rules derived from enveloping problem free dimensionless field experience data when no experimentally validated numerical FSI results are available.
- Operators and engineering companies should challenge pump manufacturers to show how their equipment falls within the manufacturers dimensionless experience envelope or what has been done to safely move outside this experience envelope.
- Use developed numerical FSI model to evaluate and optimize diaphragm selection rules by evaluating specific field experiences with and without reduced diaphragm life
- Use developed numerical FSI model to optimize geometry of diaphragm and pump chamber such that current limits on dimensionless stroke volume and flow rate can be increased

EXPERIMENTAL SET-UP

- Improve tracking performance of servo hydraulic drive of experimental set-up at higher stroke rates such that a wider operating range of the set-up is possible.
- Investigate non-reproducibility of the diaphragm deformation in experimental set-up further. First an improvement of the hydraulic drive is required as the increase in non-reproducible behaviour coincides with the start of the reduced tracking performance of the hydraulic dive. When non-reproducibility remains, instantaneous determination of deformed diaphragm shapes using camera techniques could be considered.

NUMERICAL MODEL

- Implement shear deformation behaviour in shell model
- Implement large deformation and non-linear material behaviour in shell model
- Implement 3D hyper-elastic solid model
- Make flow solver suitable for non-equidistant grids which allows stretching of the structured fluid grid to reduces number of inactive fluid cells in rigid solid domain
- Make computationally intensive parts of numerical model suitable for parallel computing on multiple CPU's
- Make computationally intensive parts of numerical model suitable for parallel computing on GPU
- Implement computationally intensive parts of numerical model in C^{++} and call code from the Matlab® program using MEX-functions
- After optimizing the computational performance run model on finer grid and revalidate the results using experimental data

- Use numerical model to evaluate specific field experiences with and without reduced diaphragm life to evaluate and gain confidence in the predictive capability of numerical model in practical slurry applications. When sufficient confidence is gained, use numerical model to optimize diaphragm and housing geometry.

REFERENCES

ANSI/HI, *6.1-6.5-1994: Reciprocating power pumps,* (1994).

W. Eifler, E. Schlücker, U. Spicher, and G. Will, *Küttner Kolbenmaschinen* (Vieweg+Teubner Verlag, 2009).

F. Habashi, *A short history of hydrometallurgy,* Hydrometallurgy **79**, 15 (2005), teaching and Learning Hydrometallurgical Science and Engineering-Part I.

R. van Rijswick, J. Kuenen, J. Sloesen, and A. Wilmsen, *GLORES, the gateway to piston diaphragm pumps for high volume applications,* in *Hydrotransport 18* (BHR Group, Rio de Janeiro, Brazil, 2010) pp. 463–473.

R. van Rijswick, *Pressure pulsation analysis of crankshaft positive displacement pumps,* in *Hydrotransport 17* (SAIMM and the BHR Group, Cape town, South Africa, 2007) pp. 219–230.

R. van Rijswick, *Alcan gove pulsation and vibration analysis,* Visit report WEIR Minerals Netherlands b.v. (2008).

S. Georgiadis, *Beitrag zur Berechnung de Beanspruchung kreisrunder Metallmembranen mit grosser Auslenkung*, Ph.D. thesis, Universität Erlangen-Nürnberg (1988).

L. Völkl, *Einspanneffekte an Membranen von Membanpumpen und -verdichtern*, Ph.D. thesis, Universität Erlangen-Nürnberg (1992).

E. Schlücker, *Zur Optimierung kreisrunder Plastomermembranen für oszillierende Verdrängerpumpen*, Ph.D. thesis, Universität Erlangen-Nürnberg (1993).

W. Schmitt, *Kunststoffe und Elastomere in der Dichtungstechnik* (W. Kohlhammer GmbH, Stuttgart, 1987).

Simrit, *Technical Manual*, Freudenberg Simrit GmbH & Co. KG (2007).

C. Segers, *IR-860307-membraanbeweging van ZPM 1800,* Internal report WEIR Minerals Netherlands b.v. (1986).

R. van Rijswick, A. Talmon, and C. van Rhee, *Fluid structure interaction in piston diaphragm pumps,* in *International Pump Users Forum* (Düsseldorf, Germany, 2012).

R. van Rijswick, A. Talmon, and C. van Rhee, *Fluid structure interaction in piston diaphragm pumps,* in *Hydrotransport 19* (BHR Group, Denver, USA, 2014) pp. 43–56.

R. van Rijswick, A. Talmon, and C. van Rhee, *Fluid structure interaction (FSI) in piston diaphragm pumps,* The Canadian Journal of Chemical Engineering **94**, 1116 (2016).

J. Stroeken, *IR-040301-membraanbelastingkengetallen voor 10 t/m 70ltr,* Internal report WEIR Minerals Netherlands b.v. (2004).

G. Hou, J. Wang, and A. Layton, *Numerical methods for fluid-structure interaction - a review.* Communications in Computational Physics **12**, 337 (2012).

T. Sarpkaya, *A critical review of the intrinsic nature of vortex-induced vibrations,* Journal of Fluids and Structures **19**, 389 (2004).

M. Thiriet, *Biology and Mechanics of Blood Flows, Part II: Mechanics and Medical Aspects* (Springer Science+Business Media, LLC, 2008).

R. Mittal, H. Dong, M. Bozkurttas, F. Najjar, A. Vargas, and A. von Loebbecke, *A versatile sharp interface immersed boundary method for incompressible flows with complex boundaries,* Journal of Computational Physics **227**, 4825 (2008).

O. Zienkiewicz, R. Taylor, and J. Zhu, *The finite element method: its basics & fundamentals*, 6th ed. (Elsevier Ltd., 2005).

O. Zienkiewicz, R. Taylor, and P. Nithiarasu, *The Finite Element Method for Fluid Dynamics*, 6th ed. (Elsevier Ltd., 2005).

J. Ferziger and M. Peric, *Computational methods for fluid dynamics*, 3rd ed. (Springer-Verlag Berlin Heidelberg NewYork, 2002).

C. S. Peskin, *Flow patterns around heart valves: A numerical method,* Journal of Computational Physics **10**, 252 (1972).

C. S. Peskin, *Numerical analysis of blood flow in the heart,* Journal of Computational Physics **25**, 220 (1977).

B. E. Griffith, *Immersed boundary model of aortic heart valve dynamics with physiological driving and loading conditions,* International Journal for Numerical Methods in Biomedical Engineering **28**, 317 (2012).

H. Bungartz and M. Schäfer, *Fluid Structure Interaction II*, edited by H.-J. Bungartz, M. Mehl, and M. Schäfer (Springer Berlin Heidelberg, 2006).

T. Belytschko, W. K. Liu, and B. Moran, *Nonlinear Finite Elements for Continua and Structures* (John Wiley & Sons Ltd, 2000).

F. Nicoud and F. Ducros, *Subgrid-scale stress modelling based on the square of the velocity gradient tensor,* Flow, Turbulence and Combustion **62**, 183 (1999).

Y. Dubief and F. Delcayre, *On coherent-vortex identification in turbulence,* Journal of Turbulence **1**, N11 (2000), http://dx.doi.org/10.1088/1468-5248/1/1/011 .

A. Ugural and S. Fenster, *Advanced Strength and Applied Elasticity*, 3rd ed. (Prentice-Hall PTR, 1995).

C. W. Macosko, *Rheology: Principles, Measurements, and Applications*, 1st ed. (Wiley-VCH, Inc., 1994).

A. Gent, *Engineering with Rubber: how to design rubber components*, 2nd ed. (Hanser, Munich, 2001).

T. C. Papanastasiou, *Flows of materials with yield,* Journal of Rheology **31**, 385 (1987).

H. Versteegh and W. Malalasekera, *An introduction to computational fluid dynamcs* (Pearson education limited, 2007).

F. F. Grinstein, L. G. Margolin, and W. Rider, *Implicit large eddy simulation : computing turbulent fluid dynamics* (Cambridge University Press, 2007).

S. B. Pope, *Turbulent flows* (Cambridge University Press, 2000).

R. Fox and A. McDonald, *Introduction to fluid mechanics*, 5th ed. (John Wiley & Sons, Inc., New York, 1998).

R. Mittal and G. Iaccarino, *Immersed boundary methods,* Annual Review of Fluid Mechanics **37**, 239 (2005), http://dx.doi.org/10.1146/annurev.fluid.37.061903.175743 .

C. S. Peskin and D. M. McQueen, *Modeling prosthetic heart valves for numerical analysis of blood flow in the heart,* Journal of Computational Physics **37**, 113 (1980).

C. S. Peskin and D. M. McQueen, *A three-dimensional computational method for blood flow in the heart i. immersed elastic fibers in a viscous incompressible fluid,* Journal of Computational Physics **81**, 372 (1989).

R. Roark and W. Young, *Formulas for Stress and Strain* (McGraw-Hill, 1983) iSBN 0-07-085983.

O. Zienkiewicz and R. Taylor, *The finite element method for Solid and Structural Mechanics*, 6th ed. (Elsevier Ltd., 2005).

E. Oñate and F. Zárate, *Rotation-free triangular plate and shell elements,* International Journal for Numerical Methods in Engineering **47**, 557 (2000).

K. C. Wilson, G. R. Addie, A. Sellgren, and R. Clift, *Slurry Transport using Centrifugal Pumps*, third edition ed. (Springer Science-I-Business Media, Inc., 2006).

R. Cooke and A. Paterson, *The design of slurry pipeline systems,* Course notes Paterson and Cooke slurry pipeline design course (2008).

R. Cooke, *Thickened and paste tailings pipeline systems: Design procedure – part 1,,* in *Paste 2006*, Paste (Australian Centre for Geomechanics, Limerick, Ireland, 2006).

E. Buckingham, *On physically similar systems; illustrations of the use of dimensional equations,* Phys. Rev. **4**, 345 (1914).

M. T. Heath, *Scientific computing, an introductory survey* (McGraw-Hill, 1997).

E. Fadlun, R. Verzicco, P. Orlandi, and J. Mohd-Yusof, *Combined immersed-boundary finite-difference methods for three-dimensional complex flow simulations,* Journal of Computational Physics **161**, 35 (2000).

P. K. Sweby, *High resolution schemes using flux limiters for hyperbolic conservation laws,* SIAM Journal on Numerical Analysis **21**, 995 (1984), http://dx.doi.org/10.1137/0721062 .

F. S. Lien and M. A. Leschziner, *Upstream monotonic interpolation for scalar transport with application to complex turbulent flows,* International Journal for Numerical Methods in Fluids **19**, 527 (1994).

B. P. Leonard, *Simple high-accuracy resolution program for convective modelling of discontinuities,* International Journal for Numerical Methods in Fluids **8**, 1291 (1988).

B. Leonard, *A stable and accurate convective modelling procedure based on quadratic upstream interpolation,* Computer Methods in Applied Mechanics and Engineering **19**, 59 (1979).

M. Griebel, T. Dornseifer, and T. Neunhoeffer, *Numericall Simulation in Fluid Dynamics* (SIAM, 1998).

P. M. Gresho and R. L. Sani, *On pressure boundary conditions for the incompressible navier-stokes equations,* International Journal for Numerical Methods in Fluids **7**, 1111 (1987).

W. L. Briggs, V. E. Henson, and S. F. McCormick, *A multigrid tutorial*, 2nd ed. (Society for Industrial and Applied Mathematics, 2000).

P. Wesseling, *An Introduction to Multigrid Methods*, corrected reprint. philadelphia: r.t. edwards, inc., 2004 ed. (John Wiley & Sons, Ltd, 1992).

P. Wesseling, *Cell-centered multigrid for interface problems,* Journal of Computational Physics **79**, 85 (1988).

P. O. Scherer, *Computational Physics Simulation of Classical and Quantum Systems* (Springer-Verlag Berlin Heidelberg, 2010).

A. Cromer, *Stable solutions using the euler approximation,* American Journal of Physics **49**, 455 (1981).

C. S. Peskin, *The immersed boundary method,* Acta Numerica , 1 (2002).

MathWorks, *Matlab - the language of technical computing,* www.mathworks.com/products/matlab/ (2016).

D. C. Giancoli, *Natuurkunde voor Wetenschap en Techniek, deel II: Golven en Geluid, Kinetische Theorie en Thermodynamica, Magnetisme, Licht*, 2nd ed. (Academic Service, Schoonhoven, 1993).

N. H. Asmar, *Partial differential equations and boundary value problems* (Prentice Hall, 2000).

E. W. Weisstein, *Fourier-bessel series,* From MathWorld–A Wolfram Web Resource. http://mathworld.wolfram.com/Fourier-BesselSeries.html (2015).

R. Schut, *Experimental determination and analysis of diaphragm deformation and strains in piston diaphragm pumps*, Master's thesis, Delft University of Technology (2011).

E. Wylie and V. L. Streeter, *Fluid Transients in Systems* (Prentice Hall, Inc, 1993).

E. Oñate and F. Zárate, *Extended rotation-free plate and beam elements with shear deformation effects,* International Journal for Numerical Methods in Engineering **83**, 196 (2010).

F. Zárate and E. Oñate, *Extended rotation-free shell triangles with transverse shear deformation effects,* Computational Mechanics **49**, 487 (2011).

E. Oñate and F. G. Flores, *Advances in the formulation of the rotation-free basic shell triangle,* Computer Methods in Applied Mechanics and Engineering **194**, 2406 (2005), computational Methods for Shells.

F. G. Flores and E. Oñate, *Improvements in the membrane behaviour of the three node rotation-free {BST} shell triangle using an assumed strain approach,* Computer Methods in Applied Mechanics and Engineering **194**, 907 (2005).

DANKWOORD/ACKNOWLEDGEMENTS

Het zit erop. Naast dat het schrijven van dit proefschrift ook veel van mijzelf heeft gevraagd zijn er natuurlijk ook een aantal mensen die ik wil bedanken voor hun bijdrage. Dat ik überhaupt ben gaan nadenken over het doen van een promotie onderzoek heb ik aan jou te danken Cees. Jij was het die mij, tijdens het Hydrotransport congres in Kaapstad in 2007, vroeg of ik geen zin had om een promotie onderzoek te gaan doen. Hier ben ik ook nog wel een woord van dank aan Erik van der Kuy verschuldigd aangezien hij voor het eerste contact heeft gezorgd tijdens het congres Diner. Mijn eerste reactie was echter: "Dat academisch geneuzel is niets voor mij". Maar toen jij aangaf dat het doen van een promotie traject in deeltijd, naast mijn baan bij WEIR Minerals op een onderwerp uit de praktijk, ook een optie was, raakte ik snel enthousiast. Na een eerste gesprek op de TU samen met Arno hadden we snel een voorkeur bepaald voor het vloeistof-structuur interactie onderwerp. Het heeft nog een tijd geduurd voordat alle betrokken bij WEIR en thuis overtuigd waren van het nut van het doen van dit promotie traject en voordat alle financiering en contracten rond waren. Maar vol enthousiasme ben in maart 2010 begonnen. Je heb mij gemotiveerd om te beginnen met het schrijven van een eigen flow solver, dit om een gedegen achtergrond in numeriek analyse van stromingen op te doen. Omdat mijn achtergrond hierin beperkt was, was dit een zware opgave en heb me in het begin dan ook vaak afgevraagd waar ik aan begonnen was. Door jou motivatie en eigen ervaring hierin ben ik er toch doorheen gekomen en uiteindelijk hebben we er zelfs voor gekozen om het gehele numerieke model zoals beschreven in dit proefschrift vanaf scratch te ontwikkelen. Verder wil ik je bedanken voor het vertrouwen en de vrijheid die ik heb gekregen in het definiëren en uitvoeren van het onderzoek. Arno jij bent vanaf het eerste gesprek betrokken geweest bij het onderzoek en mijn copromotor geweest tijdens het onderzoek. Ik heb erg genoten van de discussies die we hebben gehad, zeker ook die over Niet-Newtonse slurrie stromingen. Het zijn verder met name jou opmerkingen geweest op het eerste concept van het proefschrift die ervoor gezorgd hebben dat het proefschrift is wat het nu is. Dit heeft er wel voor gezorgd dat ik de structuur en de omvang van het eerste concept behoorlijk overhoop heb gegooid en dat ik thuis moest uitleggen dat ik toch nog niet helemaal klaar was. Maar toch zeker bedankt hiervoor.

Next to my promotor and copromotor I would like to thank all committee members. Thank you for your willingness to read my thesis and be part of my defence committee. I hope you enjoyed reading my thesis.

En dan is er natuurlijk de vakgroep baggertechniek in Delft. Ondanks dat ik er maar 1 dag in de week was, heb ik toch veel gehad aan de interactie binnen de vakgroep en ik ben dan ook altijd met veel plezier naar Delft gekomen. Joep, jij was mijn eerste kamergenoot en was ook met je eigen flow solver bezig. We hebben veel goede discussies

gehad over de numerieke aanpak van stromingsproblemen en de diverse programmeer uitdagingen. Met name jou aanwijzingen met betrekking tot de implementatie van de expliciet Navier-Stokes solver op basis van het boekje van Griebel en de eerst aanzet tot de Multigrid Poisson solver zijn erg belangrijk geweest in de initiële opzet van mijn numerieke model. Daarnaast waren er natuurlijk ook de koffieautomaat discussies, waar ook jij Lynyrd, vaak bij was. Hier werden naast CFD perikelen ook vaak de politiek en de niet-behoudende schema's uit de economie besproken. Ik heb hier leuke herinneringen aan. Na Joep werd jij Rudy, mijn kamergenoot, iemand die net as ik van de Eindhovensche school kwam. Ook wij hebben veel goede discussies gehad, waarvan met name die over de expliciete tijdsintegratie integratie van discrete massa's zinvol voor mij zijn geweest. De laatste periode ben jij Jort, mijn kamergenoot geweest. Ik heb altijd genoten van je nuchtere Hollandse persoonlijkheid en heb je bewonderd om je pragmatische aanpak in je onderzoek. Geert, in jou rol als universitair docent, heb jij mij enorm geholpen om mijn flow solver echt goed werkend te krijgen. Met name om de juiste implementatie van de randvoorwaarden te krijgen. Ook de stap die ik gezet heb om (I)-LES modellen te implementeren komt voort uit onze discussies. Erg bedankt voor deze ondersteuning. Ondanks mijn beperkte aanwezigheid in Delft wil ik toch ook graag de overige AIO's bedanken voor de gezellige sfeer bij de koffieautomaat en tijdens vakgroep diners. Rik, Arno, Xiuhun, Ershad, Frans, Bas en Dave, Bedankt. En niet te vergeten ook jij Sape.

Verder zijn er ook een aantal collega's van WEIR Minerals die ik graag wil bedanken. Als eerste wil ik jou Gregor, bedanken omdat jij mij vanaf het begin gesteund hebt in mijn ambities om een promotie traject in te gaan naast mijn baan bij WEIR. Jij heb ervoor gezorgd dat er steun vanuit het MT was, en dat ik voldoende ruggensteun had als mensen aanspraak op mij wilde maken als dit niet uitkwam zodat ik voldoende tijd vrij kon maken voor het onderzoek, met name in de afrondende fase. Ook van jou heb ik het vertrouwen en de vrijheid gekregen het onderzoek naar eigen inzicht in te richten. Zonder jou steun en vertrouwen had ik dit nooit van de grond gekregen en laat staan af kunnen ronden. Jan-Peter ook jou wil ik bedanken voor de geboden kans om dit promotie onderzoek te doen. Bedankt dat jij de meerwaarde van een deeltijd promotie hebt ingezien en vanuit het bedrijf voor de financiële ondersteuning in dit project hebt gezorgd. Ik heb alleen je initiële advies om niet aan kinderen te beginnen tijdens het promotie onderzoek niet opgevolgd.

Aan het experimentele deel van het onderzoek hebben een aantal mensen bijgedragen die ik graag wil bedanken. Arno bedankt voor het basis ontwerp dat je gemaakt heb van de testopstelling en Joop bedankt voor het uitwerken van alle productie tekeningen hiervan. Luc, bedankt voor het schrijven van de besturingssoftware van de testopstelling. Het geringe aantal problemen dat we met de besturing hebben gehad is een bewijs van de kwaliteit van jouw werk. Geert, jij hebt zorg gedragen dat testopstelling gebouwd werd en in bedrijf genomen kon worden, ondanks de vele open eindjes die er nog waren. Het was goed te weten dat dit bij jou in goede handen was. Van jou zelfstandigheid en organisatie talent kunnen velen nog wat leren. Rolf jij bent als afstudeerder tegen de initiële tekortkomingen van de testopstelling aangelopen, maar hebt deze weten op te lossen of aanbevelingen weten te geven hoe deze op te lossen. Een essentiële stap in het onderzoek. Hiervoor enorm bedankt. Jordy en Fred, jullie hebben

ervoor gezorgd dat de installatie van een galvanische coating kon worden voorzien, hetgeen noodzakelijk was om corrosie uit te sluiten, hiervoor bedankt. Fred jij heb vele uurtjes met opstelling doorgebracht en de meeste experimenten zoals gebruikt in dit proefschrift uitgevoerd. Dit ging niet altijd vanzelf, was het niet een onrustige loop van de aandrijfcilinder, dan was het wel cavitatie in de opstelling of problemen met het opslaan van de meetfiles waardoor we een serie experimenten weer moesten herhalen. Bedankt voor jouw volharding en bereidheid om door te gaan tot het goed genoeg was. Jan, ik heb veel gehad aan de discussies met jou over membraanvervormingen. Jou kennis en ervaring uit de eerdere onderzoeken was erg belangrijk om mee te nemen.

Verder wil ik alle familie en vrienden bedanken voor de interesse die jullie getoond hebben in mijn promotie traject, ook al was het misschien niet altijd geheel duidelijk wat ik aan het doen was en waarom. Pap en Mam jullie ook enorm bedankt voor het vertrouwen dat jullie altijd in mij hebben gehad en de mogelijkheden die ik van jullie heb gekregen. Mam jij staat altijd voor me klaar als ik hulp nodig heb en hebt altijd een luisterend oor. Pap zoals ik reeds in het voorwoord heb aangegeven ben jij het die mij enthousiast heeft gemaakt voor de techniek waardoor ik ervoor gekozen heb om werktuigbouwkunde te gaan studeren. In mijn werkzaamheden als stagiair en als ontwikkelingsingenieur bij WEIR Minerals heb ik onder jouw leiding veel vrijheid en vertrouwen gekregen mijn werkzaamheden zelf te organiseren. De zelfstandigheid die ik hier mee heb opgedaan heeft mij in dit promotie traject enorm geholpen. Verder is natuurlijk de kennis en ervaring die ik van jou heb gekregen op het gebied van zuigermembraanpompen en membraanvervorming, natuurlijk essentieel geweest binnen dit onderzoek. Hiervoor enorm bedankt.

Lars, Niels en Lotte, pappa is nu klaar met het boekje over het hoedje en hoeft niet meer (zo vaak) op de zolder te gaan werken achter de computer. Ondanks dat jullie het niet allemaal even bewust hebben meegemaakt hebben jullie toch wat aandacht van mij moeten missen op de momenten dat ik me met name in het weekend terug moest trekken op de zolder om aan mijn promotie te werken.

Maar mijn grootste dank gaat toch wel uit naar jou Yvonne. Op het moment dat jij net je eigen promotie af aan het ronden was kwam ik met het idee om ook aan een promotie traject te beginnen en wel in deeltijd waarvoor ook een behoorlijk investering van privé tijd voor nodig zou zijn. Ondanks dat je sceptisch was, heb je me wel gedurende het gehele traject gesteund. Toen ik begon waren we nog met zijn tweetjes maar nu zijn we inmiddels met zijn vijven. Ik kan je dus ook niet genoeg bedanken voor de offers die jij hebt gebracht door de volledige organisatie van ons gezin voor jou rekening te nemen. Dit om mij de mogelijkheid te geven me menig avond en weekend terug te trekken om aan mijn promotie te werken. Ondanks dat het erg zwaar was voor jou en dat je het soms ook niet meer zag zitten, heb je me ook enorm geholpen door het afdwingen van het inplannen van vaste promotie momenten zodat er toch enige regelmaat en duidelijkheid was in ons gezin. Ook het commitment dat ik van jou kreeg om mij te ondersteunen om de eindsprint van het schrijven van het proefschrift in te gaan is ongekend. Terugkijkend is dit eigenlijk ook gekkenwerk geweest. Yvonne, ik hou ontzettend veel van jou en ben je ontzettend dankbaar voor jouw ondersteuning tijdens dit promotie traject.

Curriculum Vitæ

Ralph van Rijswick

03-04-1979	Born in Nijmegen, Netherlands.

Education

1991–1997	VWO (pre-university education) Dendron College, Horst
1997-2003	Master of Science in Mechanical Engineering Eindhoven University of Technology

Working Experience

2000-2001	Trainee and part-time Research and Development Engineer WEIR Minerals Netherlands b.v.
2002-2004	Trainee and Development Engineer Bosch Rexroth Hydraudyne b.v.
2004-2009	Research and Development Engineer WEIR Minerals Netherlands b.v.
2009-present	Chief Engineer Piston Diaphragm Pumps WEIR Minerals Netherlands b.v.
2010-2016	PhD Student Dredging Engineering, Delft University of Technology

List of Publications

Journal Papers

1. **R. van Rijswick**, A. Talmon, and C. van Rhee, *Fluid structure interaction (FSI) in piston diaphragm pumps*, The Canadian Journal of Chemical Engineering 94, 1116 (2016).

Conference Papers

5. **R. van Rijswick**, A. Talmon, and C. van Rhee, *3D numerical modelling of fluid structure interaction in piston diaphragm pumps*, in *International Pump Users Forum* (Düsseldorf, Germany, 2016).

4. **R. van Rijswick**, A. Talmon, and C. van Rhee, *Fluid structure interaction in piston diaphragm pumps*, in *Hydrotransport 19* (BHR Group, Denver, USA, 2014) pp. 43–56.

3. **R. van Rijswick**, A. Talmon, and C. van Rhee, *Fluid structure interaction in piston diaphragm pumps*, in *International Pump Users Forum* (Düsseldorf, Germany, 2012).

2. **R. van Rijswick**, J. Kuenen, J. Sloesen, and A. Wilmsen, *GLORES, the gateway to piston diaphragm pumps for high volume applications*, in *Hydrotransport 18* (BHR Group, Rio de Janeiro, Brazil, 2010) pp. 463–473.

1. **R. van Rijswick**, *Pressure pulsation analysis of crankshaft positive displacement pumps*, in *Hydrotransport 17* (SAIMMand the BHR Group, Cape town, South Africa, 2007) pp. 219–230.